

**UTILIZATION OF FUNCTIONALLY GRADED  
MATERIALS IN FEMORAL PROSTHESIS**

**AZIM ATAOLLAHI OSHKOUR**

**FACULTY OF ENGINEERING**

**UNIVERSITY OF MALAYA**

**KUALA LUMPUR**

**2015**

**UTILIZATION OF FUNCTIONALLY GRADED MATERIALS IN  
FEMORAL PROSTHESIS**

**AZIM ATAOLLAHI OSHKOUR**

**THESIS SUBMITTED IN FULFILMENT OF THE  
REQUIREMENTS FOR THE DEGREE OF DOCTOR OF  
PHILOSOPHY**

**FACULTY OF ENGINEERING  
UNIVERSITY OF MALAYA  
KUALA LUMPUR**

**2015**

To

My beloved parents, my wife, my sisters, and my brother for their  
endless love, support, and encouragement

UNIVERSITI MALAYA  
ORIGINAL LITERARY WORK DECLARATION

Name of Candidate: Azim Ataollahi Oshkour (I.C/Passport No: F16425429)

Registration/Matric No: KHA10032

Name of Degree: Doctor of philosophy

Title of Project Paper/Research Report/Dissertation/Thesis (“this Work”):

Utilization of functionally graded materials in femoral prosthesis

Field of Study: Biomechanics

I do solemnly and sincerely declare that:

- (1) I am the sole author/writer of this Work;
- (2) This Work is original;
- (3) Any use of any work in which copyright exists was done by way of fair dealing and for permitted purposes and any excerpt or extract from, or reference to or reproduction of any copyright work has been disclosed expressly and sufficiently and the title of the Work and its authorship have been acknowledged in this Work;
- (4) I do not have any actual knowledge nor do I ought reasonably to know that the making of this work constitutes an infringement of any copyright work;
- (5) I hereby assign all and every rights in the copyright to this Work to the University of Malaya (“UM”), who henceforth shall be owner of the copyright in this Work and that any reproduction or use in any form or by any means whatsoever is prohibited without the written consent of UM having been first had and obtained;
- (6) I am fully aware that if in the course of making this Work I have infringed any copyright whether intentionally or otherwise, I may be subject to legal action or any other action as may be determined by UM.

Candidate’s Signature

Date

Subscribed and solemnly declared before,

Witness’s Signature

Date

Name:

Designation:

## ABSTRACT

Total hip replacement is a highly effective surgical operation that relieves pain and restores the function of a degenerated hip joint. However, with the increasing incidence of total hip replacements, particularly among young patients, and femoral prosthesis implantation, implant designs should consider long-term survival and better performance. Minimizing the mismatch between the prosthesis and bone stiffness to reduce stress shielding and retain interface stresses within acceptable levels, can increase the longevity of total hip replacement and enhance the performance of the prosthesis. A prosthesis with adjustable stiffness may enable prosthetists to match the prosthesis and bone stiffness. Functionally graded materials have attracted much attention in the production of prosthesis with customizable stiffness.

Computational modeling provides a flexible framework to examine the behavior of hip replacements, host bone, and different implant design configurations using a computer instead of conducting expensive and destructive experimental tests. ABAQUS, a finite element software, was used to analyze a femur implanted with different prostheses and determine the circumferential crack behavior in the cement layer of a total hip replacement. The cemented and cementless Charnley femoral prostheses composed of functionally graded materials were initially examined. Finite element analysis was performed on the implanted femur with prostheses made of conventional materials, such as stainless steel, and titanium alloys. Finite element analysis was then conducted on the cementless and cemented functionally graded femoral prostheses with different geometries. Circumferential cracks were located in the cement layer on the internal and external surfaces of the cement at different positions along its length from distal to proximal direction. After numerical studies, an experiment was performed using the composites and functionally graded materials

composed of four metallic phases and two ceramic phases. Physical and compressive mechanical properties were then examined.

Results revealed that a prosthetic material plays a key role on the strain energy density in the proximal metaphysics of the femur and on the stress distribution in the implanted femur constituents. Low-stiffness prostheses resulted in higher strain energy density in the periprosthetic femur. In the femur with functionally graded prostheses, strain energy density proportionally increased with gradient index growth. Stiffer prostheses carried more stress than less stiff prostheses. The increase in gradient index also showed an adverse relationship with the developed stress in the femoral prostheses. However, the developed stress in the bone and cement demonstrated an increasing trend with the increase in gradient index. The internal and external circumferential cracks had no significant interaction. The numerical study on the circumferential crack behavior revealed that  $K_{II}$  was smaller than  $K_I$  and  $K_{III}$ . Higher values of stress intensity factors were obtained at the distal part compared with that at the proximal part of the cement layer. Moreover, experimental results revealed that the abundant metallic and ceramic composites showed better mechanical properties than those of the composites with 40 wt%–60 wt% of the metal and ceramic phases. In addition, compared to pure metals, the functionally graded materials exhibited better mechanical properties, such as low Young's modulus. Functionally graded materials also demonstrated more compressive stress and plastic deformation than the composites with more than 30 wt% ceramic phases.

## ABSTRAK

Penggantian pinggul sepenuhnya adalah pembedahan yang amat efektif dalam mengurangi kesakitan dan memulihkan fungsi sendi pinggul yang rusak. Walau bagaimanapun, dengan merirngketnga kes penggantian pinggul sepenuhnya, terutamanya di kalangan pesakit yang masih muda, dan implantasi prostesis tulang peha, reka bentuk implan harus mempunyai jangka hayat yang panjang dan prestasi yang lebih baik. Meminimumkan ketidakpadanan antara prostesis dan kekakuan tulang untuk mengurangi tegasan pelindung dan mengekalkan tegasan antara muka pada skala yang boleh diterima akan meningkatkan jangka hayat implan penggantian pinggul sepenuhnya dan meningkatkan prestasi prostesis. Prostesis dengan kekakuan boleh laras membolehkan prostetis memadankan kekakuan prostesis dan tulang. Bahan bergred fungsi telah menarik banyak perhatian dalam pengeluaran prostesis dengan kekakuan boleh ubah suai.

Pemodelan berkomputer menyediakan satu rangka kerja yang fleksibel untuk mengkaji sifat penggantian pinggul, tulang perumah, dan konfigurasi reka bentuk implan yang berbeza dengan menggunakan komputer tanpa meggunakan ujian eksperimen berkost tinggi dan merosakkan bahan. ABAQUS, iaitu perisian elemen unsur, telah digunakan untuk menganalisis tulang paha yang diimplan dengan prostesis yang berbeza dan menentakan keretakan lilitan dalam lapisan simen pada implan penggantian pinggul sepenuhnya. Prostesis tulang paha Charnley, bersimen dan tanpa simen, terdiri daripada bahan bergred fungsi, telah diperiksa. Analisis unsur terhingga telah dijalankan ke atas tulang paha yang diimplan dengan prostesis yang diperbuat daripada bahan-bahan konvensional seperti keluli tahan karat dan aloi titanium. Analisis unsur terhingga kemudian dijalankan ke atas prosesis tulang peha tanpa simen dan prosesis tulang peha bergred fungsi bersimen dengan geometri yang berbeza. Keretakan

lilitan ditemui pada lapisan simen pada permukaan dalaman dan luaran simen di kedudukan yang berbeza sepanjang jarak antara arah distal dan proksimal. Selepas kajian numerikal, satu eksperimen telah dijalankan menggunakan komposit dan bahan-bahan bergred fungsi yang terdiri daripada empat fasa dan dua fasa seramik. Sifat mekanikal dan mampatan fizikal kemudiannya dikaji.

Hasil kajian menunjukkan bahawa bahan prostetik memainkan peranan penting dalam ketumpatan tenaga terikan pada metafizik proksimal tulang paha dan agihan tegangan dalam jujuk tulang paha yang diimplan. Prostesis dengan kekakuan rendah menyebabkan ketumpatan tenaga terikan yang lebih tinggi dalam tulang paha periprostetik. Tulang paha dengan prosthesis bergred fungsi, mempunyai ketumpatan tenaga terikan berkadaran meningkat secara berkadaran dengan kenaikan indeks kecerunan. Prostesis yang lebih kaku mempunyai tegasan yang lebih berbanding prostesis kurang kaku. Peningkatan indeks kecerunan juga menunjukkan hubungan yang bertentangan dengan tegasan yang dihasilkan dalam prostesis tulang paha. Walau bagaimanapun, tekanan yang terhasil dalam tulang dan simen menunjukkan trend yang meningkat dengan peningkatan indeks kecerunan. Keretakan lilitan dalaman dan luaran tidak mempunyai interaksi yang signifikan. Kajian numerikal ke atas kelakuan retak lilitan mendedahkan bahawa  $K_{II}$  adalah lebih kecil daripada  $K_I$  dan  $K_{III}$ . Nilai faktor keamatan tegasan yang lebih tinggi diperoleh di bahagian distal berbanding dengan di bahagian proksimal lapisan simen. Tambahan pula, hasil eksperimen menunjukkan bahawa komposit mewah logam dan seramik menunjukkan sifat-sifat mekanikal yang lebih baik berbanding komposit dengan 40 wt% - 60 wt% logam dan fasa seramik. Di berbaring dengan logen tuten, samping itu, bahan-bahan bergred fungsi menunjukkan sifat mekanikal yang lebih baik, seperti modulus Young yang rendah, untuk implan. Fungsi bahan gred juga menunjukkan lebih tegasan mampatan dan perubahbentukan plastik berbanding komposit dengan lebih daripada 30 wt% fasa seramik.



## **ACKNOWLEDGMENTS**

I would like to express my deep gratitude to my supervisors, namely, Professor Ir. Dr. Noor Azuan Abu Osman and Associate Prof. Ir. Dr. Yau Yat Huang, for providing me the opportunity to continue my PhD program. I am also very thankful for their tireless, kind assistance, support, critical advice, encouragement, and suggestions during the study and preparation of the thesis.

I would also like to express my gratitude to Associate Prof. Ir. Dr. Faris Tarlochan and Dr. Sumit Pramanik for the practical experience and knowledge that they imparted to this thesis. I truly appreciate the time they devoted in advising me and showing me the proper direction to continue my research and for their openness, honesty, and sincerity.

I am also thankful to Mr. Mohd Said Bin Sakat, technician of the Department of Mechanical Engineering, Faculty of Engineering, University of Malaya, for his willingness to provide assistance and advice as well as for being my friend.

## TABLE OF CONTENTS

<b>ABSTRACT</b> .....	<b>iv</b>
<b>ABSTRAK</b> .....	<b>vi</b>
<b>ACKNOWLEDGMENTS</b> .....	<b>viii</b>
<b>TABLE OF CONTENTS</b> .....	<b>ix</b>
<b>LIST OF FIGURES</b> .....	<b>xv</b>
<b>LIST OF TABLES</b> .....	<b>xx</b>
<b>CHAPTER 1</b> .....	<b>1</b>
<b>INTRODUCTION</b> .....	<b>1</b>
1.1 Introduction .....	1
1.2 Problem statement.....	2
1.3 Objectives.....	3
1.4 Thesis layout .....	4
<b>CHAPTER 2</b> .....	<b>5</b>
<b>LITERATURE REVIEW</b> .....	<b>5</b>
2.1 Introduction .....	5
2.2 Hip biomechanics.....	5
2.3 Total hip replacement.....	6
2.4 Implant fixation methods .....	8
2.5 Total hip replacement failure .....	10
2.5.1 Osteolysis .....	10
2.5.2 Primary stability .....	11
2.5.3 Stress shielding .....	12
2.5.4 Cement failure.....	13
2.5.5 Debonding.....	14

2.5.6	Implant fracture.....	14
2.6	Material and geometry of artificial hip joint constituents.....	15
2.6.1	Femoral head and acetabular cup.....	15
2.6.2	Femoral prosthesis (Stem) .....	17
2.6.3	Femoral prosthesis geometry .....	17
2.6.4	Femoral prosthesis materials.....	19
2.7	Surface finishing .....	20
2.8	Materials utilized in artificial hip joint components .....	20
2.8.1	Metals.....	20
2.8.2	Polymers.....	21
2.8.3	Ceramics.....	21
2.8.4	Composites.....	24
2.9	Numerical methods in hip joint biomechanics and implant study .....	26
2.10	Load transfer in the proximal femur .....	31
2.11	Bone .....	33
2.12	Summary .....	34
<b>CHAPTER 3 .....</b>		<b>35</b>
<b>MATERIALS AND METHODS .....</b>		<b>35</b>
3.1	Introduction.....	35
3.2	Outline of Methodology.....	35
3.3	Finite element analysis.....	35
3.3.1	Finite element modeling to use functionally graded materials in femoral prosthesis.....	35
3.3.2	Bone modeling .....	38
3.3.3	Prosthesis modeling .....	40
3.3.4	Mesh generation.....	42

3.3.5	Boundary conditions .....	42
3.3.6	Material properties .....	42
3.3.7	Functionally graded material modeling .....	43
3.3.8	Crack modeling .....	45
3.3.9	Validation of finite element models .....	46
3.4	Experimental procedure .....	47
3.4.1	Test Material .....	48
3.4.2	Composite powder preparation .....	48
3.4.3	Test specimen preparation .....	49
3.4.4	Structure characterization .....	49
3.4.5	Physical characterization .....	50
3.4.6	Mechanical characterization .....	50
3.4.6.1	Vickers hardness test .....	50
3.4.6.2	Compressive static test .....	51
3.5	Summary .....	52
<b>CHAPTER 4 .....</b>		<b>53</b>
<b>RESULTS .....</b>		<b>53</b>
4.1	Introduction .....	53
4.2	Finite element analysis .....	54
4.2.1	Longitudinal, radial, and longitudinal–radial FG Charnley femoral prostheses .....	56
4.2.1.1	Strain energy density .....	56
4.2.1.2	Femoral prosthesis stress .....	60
4.2.1.3	Developed stress in the bone .....	64
4.2.1.4	Developed stress in the cement .....	67
4.2.1.5	Interface stresses .....	70

4.2.2	Cementless prostheses with conventional materials .....	72
4.2.2.1	Strain energy density.....	72
4.2.2.2	Developed stress in the prostheses.....	74
4.2.2.3	Developed stress to the bone.....	76
4.2.3	Cementless longitudinal functionally graded femoral prosthesis with different geometries .....	79
4.2.3.1	Strain energy density.....	79
4.2.3.2	Prostheses stress.....	81
4.2.3.3	Bone Stress.....	84
4.2.3.4	Interface stress.....	88
4.2.4	Cementless radial functionally graded femoral prosthesis with different geometries.....	90
4.2.4.1	Strain energy density.....	90
4.2.4.2	Developed stress in prostheses.....	92
4.2.4.3	Developed stress in the bone.....	94
4.2.4.4	Interface Stress.....	98
4.2.5	Cemented prostheses with conventional materials .....	101
4.2.5.1	Strain energy density.....	101
4.2.5.2	Developed stress in the prostheses.....	103
4.2.5.3	Developed stress in the bone.....	104
4.2.5.4	Developed stresses in the cement layer.....	108
4.2.6	Radial and longitudinal cemented functionally graded prostheses .....	111
4.2.6.1	Strain energy density.....	111
4.2.6.2	Developed stress in the prostheses.....	114
4.2.6.3	Developed stress in the bone.....	116
4.2.7	Developed stress in the cement.....	119

4.2.8	Circumferential cracks in cement.....	124
4.2.8.1	Internal circumferential crack .....	124
4.2.8.1.1	$K_I$ behavior .....	124
4.2.8.1.2	$K_{II}$ behavior .....	126
4.2.8.1.3	$K_{III}$ behavior .....	126
4.2.8.2	External circumferential crack .....	128
4.2.8.2.1	$K_I$ Behavior .....	128
4.2.8.2.2	$K_{II}$ behavior .....	129
4.2.8.2.3	$K_{III}$ behavior .....	129
4.2.8.3	Internal–external circumferential crack .....	130
4.2.8.3.1	$K_I$ behavior at the internal and external surfaces .....	131
4.2.8.3.2	$K_{III}$ behavior at the internal and external surfaces .....	135
4.3	Experimental results.....	140
4.3.1	Composite of calcium silicate and hydroxyapatite with metal phases.....	140
4.3.1.1	Structure characterization.....	140
4.3.1.2	Physical properties .....	147
4.3.1.3	Mechanical properties of the composites.....	151
4.3.2	Functionally graded materials .....	154
4.3.2.1	Physical properties .....	154
4.3.2.2	Mechanical properties .....	155
<b>CHAPTER 5</b>	<b>.....</b>	<b>157</b>
<b>DISCUSSION</b>	<b>.....</b>	<b>157</b>
5.1	Introduction.....	157
5.2	Finite element analysis on the utilization of functionally graded material in femoral prosthesis design.....	157
5.3	Existence of circumferential crack in the cement layer .....	162

5.4 Composites and functionally graded materials .....	164
<b>CHAPTER 6 .....</b>	<b>166</b>
<b>CONCLUSION AND RECOMMENDATIONS .....</b>	<b>166</b>
6.1 Conclusions .....	166
6.2 Recommendations .....	168
<b>LIST OF PUBLICATIONS.....</b>	<b>180</b>

## LIST OF FIGURES

Figure 2.1: The hip joint (Stops et al., 2011) .....	6
Figure 2.2: Three typical hip joint diseases: (a) osteoarthritis, (b) necrosis, and (c) neck fracture (Dunne & Ormsby, 2011; Ilesanmi, 2010) .....	7
Figure 2.3: A typical artificial hip prosthesis (Li et al., 2014).....	8
Figure 2.4: Typical cemented and uncemented fixation (Izzo, 2012).....	9
Figure 2.5: Osteolysis after total hip replacement replacement (Bourghli et al., 2010) .	11
Figure 2.6: Load transfer before and after total hip replacement (Joshi et al., 2000).....	13
Figure 2.7: Fractures in a ceramic ball and acetabulum cup (Jenabzadeh et al., 2012)..	14
Figure 2.8: Typical femoral heads and acetabulum cups (Heimann, 2010).....	16
Figure 2.9: A typical total hip replacement (Jun & Choi, 2010).....	17
Figure 2.10: Typical prosthesis geometries with different cross sections and profiles (Ramos et al., 2012) .....	18
Figure 2.11: Schematic illustration of the different classifications of the cementless femoral stem designs. Type 1 is a single wedge, Type 2 is a double wedge, Type 3A is tapered and round, Type 3B is tapered and splined, Type 3C is tapered and rectangular, Type 4 is cylindrical and fully coated, Type 5 is modular, and Type 6 is anatomic. P = posterior and A = anterior (Khanuja et al., 2011) .....	19
Figure 2.12: Scheme of the aging process (Chevalier, 2006) .....	24
Figure 2.13: A typical FGM structure: (a) gradient and (b) graded.....	26
Figure 2.14: Minimum and maximum principal stress distributions on the (a) lateral and (b) medial sides of the stem as a function of the prosthesis Young's modulus (El-Sheikh et al., 2002).....	27
Figure 2.15: A femoral prosthesis with metal core and variable stiffness (Simões & Marques, 2005) .....	28
Figure 2.16: Hollow stems introduced by Gross and Abel (Gross & Abel, 2001) .....	29
Figure 2.17: Different cross-sections and profiles (Bennett & Goswami, 2008; Sabatini & Goswami, 2008).....	30
Figure 2.18: Stem geometry developed by Ramos et al. (2012).....	30
Figure 2.19: Principles of the load transfer mechanism explained with a simplified intramedullary fixation model (Huiskes, 1988) .....	32



Figure 2.20: Bone structure (Juillard, 2011) .....	33
Figure 3.1: General description of the methodology adopted in the study .....	36
Figure 3.2: General description of the finite element analysis adopted in the study .....	37
Figure 3.2: Development of the three-dimensional model of the femur using Mimic <sup>®</sup> software .....	39
Figure 3.3: Three-dimensional models of the femur: (a) anatomical and (b) simplified .....	39
Figure 3.4: Stem models developed using Solidworks .....	40
Figure 3.5: Dimensions of (a) profile, (b) proximal cross-sections, and (c) distal cross-sections .....	41
Figure 3.7: Internal crack geometry and locations of crack in the cement layer at (a) 25, (b) 50, (c) 75, and (d) 100 mm .....	46
Figure 3.8: Flowchart of the experimental procedure .....	47
Figure 3.9: Typical testing of sample .....	49
Figure 3.10: A micro-hardness tester machine .....	51
Figure 3.11: An Instron universal testing machine .....	51
Figure 4.1: Flow chart of result presentation .....	55
Figure 4.2: Strain energies in the spongy portion of the proximal metaphysis of the femur caused by implantation of (a) normal walking–cemented, (b) normal walking–non-cemented, (c) stair climbing–cemented, and (d) stair climbing–non-cemented prostheses. (The legend shows the changes in the radial volume fraction gradient exponent) .....	59
Figure 4.3: Variation in the von Mises stress in the prosthesis as a function of volume fraction gradient exponent in the non-cemented (a) longitudinal and (b) radial prostheses .....	61
Figure 4.4: Stress variations in the longitudinal femoral prosthesis during normal walking at the (a) lateral and (b) medial sides of cemented prosthesis as well as at the (c) lateral and (d) medial sides of the cementless prosthesis .....	61
Figure 4.5: Stress variation in the longitudinal femoral prosthesis in stair climbing at the (a) lateral and (b) medial sides of the cemented prosthesis as well as at the (c) lateral and (d) medial sides of the cementless prosthesis .....	62
Figure 4.6: Stress variation in the femur during normal walking. (a) Maximum principal stress and cemented prosthesis, (b) minimum principal stress and cemented prosthesis, (c) maximum principal stress and cementless prosthesis, and (d) minimum principal stress and cementless prosthesis .....	65

Figure 4.7: Stress variation in the femur during stair climbing. (a) Maximum principal stress and cemented prosthesis, (b) minimum principal stress and cemented prosthesis, (c) maximum principal stress and cementless prosthesis, and (d) minimum principal stress and cementless prosthesis.....	66
Figure 4.8: Stress variation in the cement layers during normal walking [(a) internal and (b) external layers] and stair climbing [(c) internal and (d) external layers] .....	68
Figure 4.9: Stress variation in the cement layers during normal walking [(a) internal and external layers] and stair climbing [(c) internal and (d) external layers].....	69
Figure 4.10: Strain energy density as a function of (a) distal cross section, (b) proximal cross section, (c) profile, and (d) material composition.....	73
Figure 4.11: Variation in the mean von Mises stress variation as a function of (a) distal cross section, (b) proximal cross section, (c) profile, and (d) material composition .....	75
Figure 4.12: Variation in the mean maximum principal stress as a function of (a) distal cross section, (b) proximal cross section, (c) profile, and (d) material composition .....	77
Figure 4.13: Variation in the mean minimum principal stress variation as a function of (a) distal cross section, (b) proximal cross section, (c) profile, and (d) material composition .....	78
Figure 4.14: Variation in the mean strain energy variation for the different (a) distal cross-sections, (b) proximal cross-sections, (c) profiles, (d) interface properties, and (e) gradient indices .....	81
Figure 4.15: Variation in the mean von Mises for the different (a) distal cross-sections, (b) proximal cross-sections, (c) profiles, (d) interface properties, and (e) gradient indices .....	83
Figure 4.16: Variation in the mean maximum principal stress for the different (a) distal cross-sections, (b) proximal cross-sections, (c) profiles, (d) interface properties, and (e) gradient indices .....	86
Figure 4.17: Variation in the mean minimum principal stress for the different (a) distal cross-sections, (b) proximal cross-sections, (c) profiles, (d) interface properties, and (e) gradient indices .....	88
Figure 4.18: Variation in the mean interface stress for the different (a) distal cross-sections, (b) proximal cross-sections, (c) profiles, and (d) gradient indices.....	90
Figure 4.19: Variation in the strain energy density a function of (a) distal cross-section, (b) proximal cross-section, (c) profile, and (d) gradient index .....	92
Figure 4.20: Variation in the von Mises stress as a function of (a) distal cross-section, (b) proximal cross-section, (c) profile, and (d) gradient index .....	94
Figure 4.21: Variation in the maximum principal stress as a function of (a) distal cross-section, (b) proximal cross-section, (c) profile, and (d) gradient index.....	96

Figure 4.22: Variation in the minimum principal stress as a function of (a) distal cross-section, (b) proximal cross-section, (c) profile, and (d) gradient index.....	97
Figure 4.23: Variation in the interface stress as a function of (a) distal cross-section, (b) proximal cross-section, (c) profile, and (d) gradient index.....	100
Figure 4.24: Strain energy density as a function of the (a) distal cross-section, (b) proximal cross-section, (c) profile, and (d) material of the prostheses.....	102
Figure 4.25: Variation in the mean von Mises stress as a function of the (a) distal cross-section, (b) proximal cross-section, (c) profile, and (d) material of the prostheses.....	104
Figure 4.26: Variation in the mean maximum principal stress as a function of the (a) distal cross-section, (b) proximal cross-section, (c) profile, and (d) material of the prostheses.....	106
Figure 4.27: Variation in the mean minimum principal stress as a function of the (a) distal cross-section, (b) proximal cross-section, (c) profile, and (d) material of the prostheses.....	107
Figure 4.28: Variation in the mean maximum principal stress as a function of the (a) distal cross-section, (b) proximal cross-section, (c) profile, and (d) material of the prostheses.....	110
Figure 4.29: Variation in the mean minimum principal stress as a function of the (a) distal cross-section, (b) proximal cross-section, (c) profile, and (d) material of the prostheses.....	111
Figure 4.30: Variation in the strain energy density at the different (a) distal cross-sections, (b) proximal cross-sections, (c) profiles, and (d) gradient indices.....	113
Figure 4.31: Variation in the von Mises stress in various femoral prosthesis type and side at the different (a) distal cross-sections, (b) proximal cross-sections, (c) profiles, and (d) gradient indices.....	115
Figure 4.32: Variation in the maximum principal stress at the lateral side of femur at the different (a) distal cross-sections, (b) proximal cross-sections, (c) profiles, and (d) gradient indices.....	117
Figure 4.33: Variation in the minimum principal stress at the lateral side of the femur at the different (a) distal cross-sections, (b) proximal cross-sections, (c) profiles, and (d) gradient indices.....	119
Figure 4.34: Variation in the maximum principal stress at the different (a) distal cross-sections, (b) proximal cross-sections, (c) profiles, and (d) gradient indices.....	121
Figure 4.35: Variation in the minimum principal stress at the different (a) distal cross-sections, (b) proximal cross-sections, (c) profiles, and (d) gradient indices.....	123
Figure 4.36: $K_I$ variation along the crack front length at different crack locations: (a) 25, (b) 50, (c) 75, and (d) 100 mm.....	125

Figure 4.37: $K_{II}$ variations along the crack front length at different crack locations: (a) 25, (b) 50, (c) 75, and (d) 100 mm .....	126
Figure 4.38: $K_{III}$ variation along the crack front length at different crack locations: (a) 25, (b) 50, (c) 75, and (d) 100 mm .....	127
Figure 4.39: $K_I$ variation along the crack front length at different crack locations: (a) 25, (b) 50, (c) 75, and (d) 100 mm .....	128
Figure 4.40: $K_{II}$ variation along the crack front length at different crack locations (a) 25, (b) 50, (c) 75, and (d) 100 mm .....	129
Figure 4.41: $K_{III}$ variations along the crack front length at different crack locations: (a) 25, (b) 50, (c) 75, and (d) 100 mm .....	130
Figure 4.42: $K_I$ variation along the crack front on the internal surface: (a) $I_{25}$ , (b) $I_{50}$ , (c) $I_{75}$ , and (d) $I_{100}$ interactions with $E_{25}$ , $E_{50}$ , $E_{75}$ , and $E_{100}$ .....	133
Figure 4.43: $K_I$ variation along the crack front on the internal surface: (a) $E_{25}$ , (b) $E_{50}$ , (c) $E_{75}$ , and (d) $E_{100}$ interactions with $I_{25}$ , $I_{50}$ , $I_{75}$ , and $I_{100}$ .....	135
Figure 4.44: $K_{III}$ variation along the crack front on the internal surface: (a) $I_{25}$ , (b) $I_{50}$ , (c) $I_{75}$ , and (d) $I_{100}$ interactions with $E_{25}$ , $E_{50}$ , $E_{75}$ , and $E_{100}$ .....	137
Figure 4.45: $K_{III}$ variation along the crack front on the internal surface: (a) $E_{25}$ , (b) $E_{50}$ , (c) $E_{75}$ , and (d) $E_{100}$ interactions with $I_{25}$ , $I_{50}$ , $I_{75}$ , and $I_{100}$ .....	139
Figure 4.46: X-ray diffraction patterns of the $CaSiO_3$ -Ti sintered composites .....	141
Figure 4.47: X-ray diffraction patterns of $CaSiO_3$ -Ti-55Ni sintered composites.....	142
Figure 4.48: X-ray diffraction patterns of $CaSiO_3$ -Ti-6Al-4V sintered composites...	143
Figure 4.49: X-ray diffraction patterns of $CaSiO_3$ -SS-316L sintered composites .....	144
Figure 4.50: X-ray diffraction patterns of $Ca_{10}(OH)_2(PO_4)_6$ -Ti sintered composites ..	145
Figure 4.51: X-ray diffraction patterns of $Ca_{10}(OH)_2(PO_4)_6$ -Ti-6Al-4V sintered composites.....	146
Figure 4.52: XRD patterns of $Ca_{10}(OH)_2(PO_4)_6$ -SS-316L sintered composites.....	147
Figure 4.53: Variation in shrinkage as a function of weight percentages of (a) calcium silicate and (b) hydroxyapatite .....	148
Figure 4.54: Variation in density as a function of the weight percentages of (a) calcium silicate and (b) hydroxyapatite .....	149
Figure 4.55: Vickers hardness variation as a function of weight percentages of (a) calcium silicate and (b) hydroxyapatite .....	151

## LIST OF TABLES

Table 3.1: CT scan slices .....	38
Table 3.2: Material properties of the implanted femur components.....	43
Table 3.3: Weight percentages of raw powders in the composites.....	48
Table 4.1: von Mises stress on femoral prosthesis (MPa) .....	64
Table 4.2: Maximum and minimum principal stresses on the femur (MPa). .....	67
Table 4.3: Maximum principal stress on the cement (MPa) .....	70
Table 4.4: Interface stresses in cemented prosthesis (MPa) .....	71
Table 4.5: Variation in Young's modulus as a function of calcium silicate weight percentage .....	152
Table 4.6: Young's modulus variation as a function of hydroxyapatite weight percentage .....	152
Table 4.7: Ultimate compressive strength as a function of calcium silicate weight percentage .....	153
Table 4.8: Ultimate compressive strength as a function of hydroxyapatite weight percentage .....	153
Table 4.9: Strain percentage at maximum load as a function of calcium silicate weight percentage .....	154
Table 4.10: Strain percentage at maximum load as a function of hydroxyapatite weight percentage .....	154
Table 4.11: Variation in shrinkage as a function of weight percentages of calcium silicate and hydroxyapatite.....	155
Table 4.12: Variation in density as a function of weight percentages of calcium silicate and hydroxyapatite .....	155
Table 4.13: Compressive Young's modulus as a function of weight percentages of calcium silicate and hydroxyapatite .....	156
Table 4.14: Ultimate compressive strength as a function of weight percentages of calcium silicate and hydroxyapatite .....	156
Table 4.15: Compressive strain percentage at maximum load as a function of weight percentages of calcium silicate and hydroxyapatite.....	156

## LIST OF SYMBOLS AND ABBREVIATIONS

2D	Two-dimensional
3D	Three-dimensional
CMC	Ceramic metal composite
CoC	Ceramic-on-ceramic
CoP	Ceramic-on-polyethylene
CS	Calcium silicate
CT	Computed tomography
FEA	Finite element analysis
FEM	Finite element method
FG	Functionally graded
FGM	Functionally graded material
HA	Hydroxyapatite
LP	Longitudinal prosthesis
LLP	Lateral side of longitudinal prostheses
L-RP	Longitudinal–radial prostheses
LRP	Lateral side of radial femoral prostheses
MCC	Metal ceramic composite
MLP	Medial side of longitudinal prostheses
MoM	Metal-on-metal
MoP	Metal-on-polymer
MRP	Medial side of radial prostheses
PTFE	Polytetrafluoroethylene
RP	Radial prosthesis
SED	Strain energy density
SIF	Stress intensity factor

St	Stainless steel
STD	Standard deviation
THR	Total hip replacement
Ti	Titanium
wt%	Weight percentage
XRD	X-ray diffraction

# CHAPTER 1

## INTRODUCTION

### 1.1 Introduction

Torturous pain and abnormality in hip joint function are outcomes of severe hip joint degeneration or injury. The final recourse but effective procedure to release pain and restore the normal function of the hip joint is total hip replacement (THR). Fractured femoral neck, particularly in the elderly, avascular necrosis, osteoarthritis, rheumatoid arthritis, and developmental dysplasia require THR. Although THR is an operation with good success rate, failure does happen. THR failure in young patients has become a serious problem because of the increasing incidence of revision surgeries. Revision surgeries are complex and costly, but with poor results. Therefore, long-term THR lifespan is the main goal in new prosthesis designs and serves as the motivation for a prosthetist.

Artificial replacements of body organs demand materials with superior characteristics because of the complex loading and chemical conditions of the human body. Therefore, using composite materials has been increasingly popular. Functionally graded materials (FGMs), which are special composite materials, exhibit interesting properties which make them suitable substitutes for the current materials applied in hip prosthesis. Moreover, loads are transferred from the natural hip joint between the pelvis and the femur through the acetabulum to the head and neck of the femur. After THR, loads are transferred through the prosthesis. An optimal prosthesis design should transfer loads between the pelvis and the femur in a way similar to the natural hip joint without causing extremely damaging peak stress or micromotion. Thus, the



performance of FGM-based prosthesis with different geometries was investigated in the present study.

Experimental and numerical approaches should be used to evaluate the performance of orthopedic implants containing FGMs. Mechanical testing of orthopedic prostheses *in vivo* and *in vitro* provides valuable information for the preclinical assessment of their performance. However, experimental methods are costly, time-consuming, and destructive. On the other hand, numerical methods, such as the finite element analysis (FEA), are common stress analysis approaches to examine complex structures and design parameters without expensive prototyping. These methods are particularly suitable for analyzing hip prostheses because *in vivo* testing would not be required if the implant has a negative effect.

## **1.2 Problem statement**

THR is the final recourse but effective procedure to relieve pain and restore the function of a degenerated hip joint. However, THR has a limited lifespan, and revision surgeries are complex with poor results. Therefore, prosthetists have developed new types of prostheses to increase the durability of THR. Aseptic loosening compromises the lifespan of failed THR. Stress shielding, interface stress, crack, and crack propagation into the cement layer are the main causes of aseptic loosening. Therefore, stress shielding and interface stress should be minimized to prolong the longevity of THR. Additionally, crack behavior and propagation should be evaluated. Stress shielding and interface stress are affected by prosthesis design (i.e., material and geometry). The conventional materials [titanium (Ti), Ti alloys, chrome–cobalt (Cr–Co), and stainless steel (St)] used in femoral prosthesis have conflicting effects on stress shielding and interface stress. The conventional materials with lower Young's modulus

induce more interface stress but cause less stress shielding. By contrast, the conventional materials with higher Young's modulus result in more stress shielding and less interface stress. Therefore, the present study was designed to balance between stress shielding and interface stress in order to prolong the lifespan of THR using FGMs in constructing femoral prosthesis with different geometries. In addition, the behavior of circumferential cracks at different positions in the cement layer was analyzed because of the significant role of these cracks in aseptic loosening.

### **1.3 Objectives**

The objectives of this study are as follows:

- i. To evaluate the effects of gradient index and geometry of prosthesis on the stimulated strain energy density (SED) in the proximal metaphysis of the femur.
- ii. To examine the effects of gradient index and geometry of prosthesis on the developed stress in the prosthesis, bone, and cement as well as on the interface stresses.
- iii. To study the existence of circumferential cracks in the cement layer.
- iv. To evaluate mechanical properties of the metal/ceramic composites, ceramic/metal composites, and FGMs.

## **1.4 Thesis layout**

This thesis is divided into six chapters. After the introductory chapter, chapter two presents a critical review of relevant literature and focuses on hip joint biomechanics, THR, failure of THR, and biomaterials. Chapter three outlines the underlying theory and experimental techniques used in the current work, and the results are presented in chapter four. Chapter five discusses the correlation between the obtained results with the existing theory. Finally, chapter six provides the conclusion and recommendations for future studies.

## **CHAPTER 2**

### **LITERATURE REVIEW**

#### **2.1 Introduction**

This chapter presents a brief review on the hip joint and THR. Hip biomechanics, THR, implant fixation methods, THR failure, geometric functions, and materials of the artificial hip joint components, biomaterials, and FEA are also discussed in this chapter.

#### **2.2 Hip biomechanics**

The hip joint is composed of soft and hard tissues. A joint comprises the femoral head, acetabulum, cartilage, and ligaments (Figure 2.1). The hip joint is classified as a ball and socket joint (Polkowski & Clohisy, 2010). The ball and socket joint provides three rotational movements, namely, flexion–extension, abduction–adduction, and internal–external rotation. The femoral head is connected to the femur via the femoral neck. The cartilage supplies a frictionless joint. The stability of the hip joint is supplied by the ligaments and muscles. This structure provides an optimal stability for the stance and bipedal locomotion, but the hip joint endures complex dynamic and static loads (Bowman Jr et al., 2010).

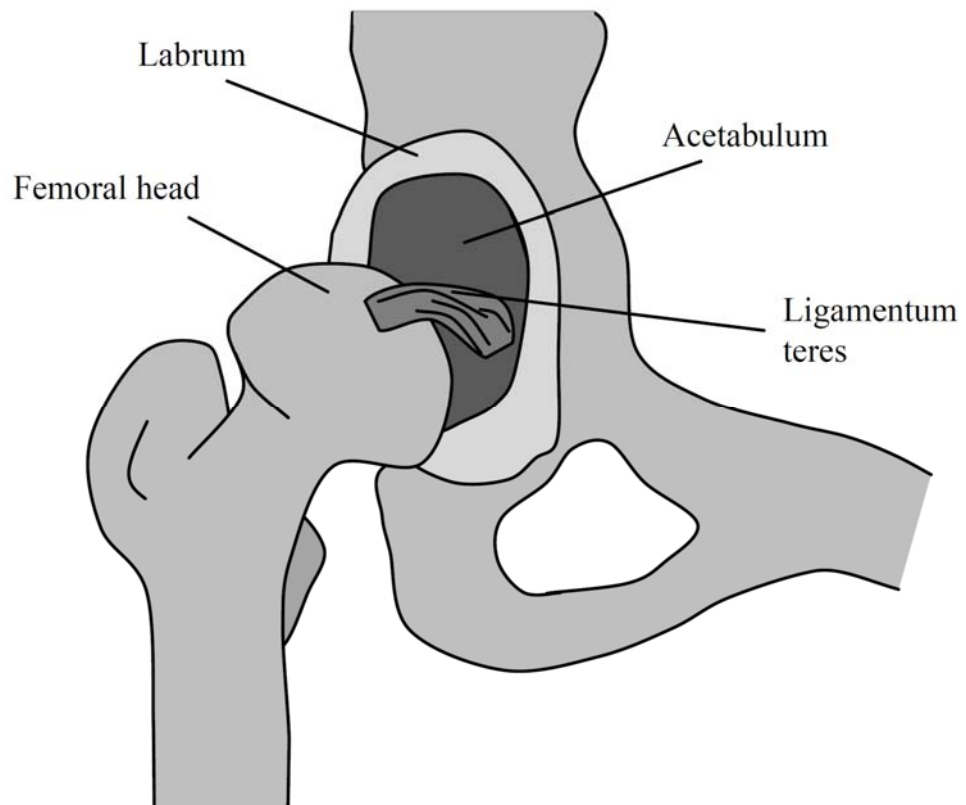


Figure 2.1: The hip joint (Stops et al., 2011)

### 2.3 Total hip replacement

Mechanical injury, chemical process, and/or their combination can cause degeneration and dysfunction in the articular hip joint (Bougherara et al., 2011). The most common causes of hip joint degeneration are osteoarthritis, fracture of the hip, inflammatory arthritis, femoral head necrosis, and rheumatoid arthritis (Figure 2.2).

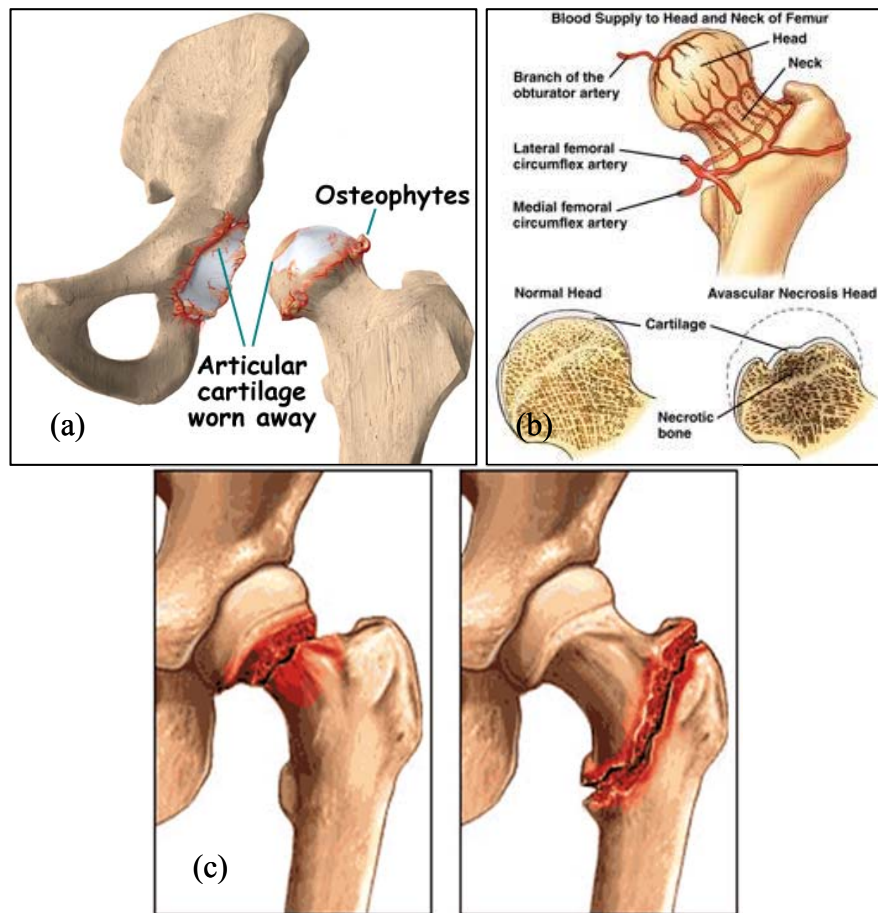


Figure 2.2: Three typical hip joint diseases: (a) osteoarthritis, (b) necrosis, and (c) neck fracture (Dunne & Ormsby, 2011; Ilesanmi, 2010)

The final recourse but the most successful procedure to remedy severely degenerated hip joint is THR (Caeiro et al., 2011). This procedure alleviates the pain and restores the hip joint function. In THR, the natural hip joint is replaced with an artificial hip joint, which consists of the femoral head, acetabular cup (acetabular shell and liner), and femoral prosthesis (stem) (Figure 2.3). The artificial hip joint components are formed in a modular or monoblock structure. A femoral head may also be included in a femoral prosthesis in a monoblock structure.

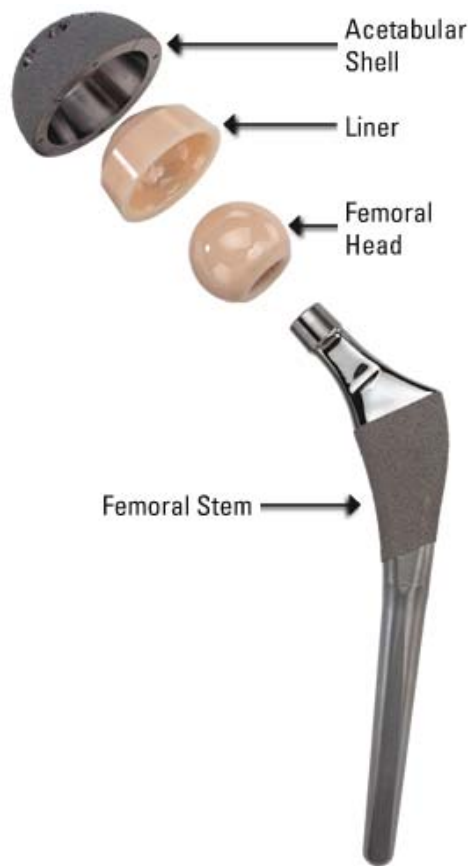


Figure 2.3: A typical artificial hip prosthesis (Li et al., 2014)

## 2.4 Implant fixation methods

The implants are fixed inside the bone with or without cement (Figure 2.4). Cemented prosthesis fixation secures an orthopedic cement prosthesis within the bone. An orthopedic cement is made of polymethylmethacrylate, which is a self-curing and non-adhesive polymeric material (Pal et al., 2013). Therefore, interlocking the spongy bone–cement and cement–implant features provide fixation (Pal et al., 2013). However, in a cementless prosthesis, fixation is performed by press fitting or screwing the components in the bone. This procedure guarantees the primary stability for the in-growth and on-growth of the bone to the implant surfaces, thus providing secondary fixation and long-term durability. Porous and hydroxyapatite (HA) coatings are applied on the surface of a cementless prosthesis to strengthen primary and secondary fixation. Moreover, a hybrid THR is a process when cementless and cemented methods are used

to fix the artificial hip joint components in THR. Bone quality is the most influential criterion in selecting a fixation procedure. Young and more active patients have better bone quality than old and less active patients. Accordingly, a cementless prosthesis is more appropriate for young patients, whereas a cemented prosthesis is more suitable for older patients. Each implant fixation method has advantages and disadvantages. For example, cement provides instant fixation, but a cementless prosthesis bone must grow to secure the prosthesis in the bone. In addition, a cemented prosthesis requires a bigger hole or more reaming inside the bone than cementless prostheses. The revision rate of patients who underwent THR with cemented prosthesis is lower than that of patients with cementless prosthesis.

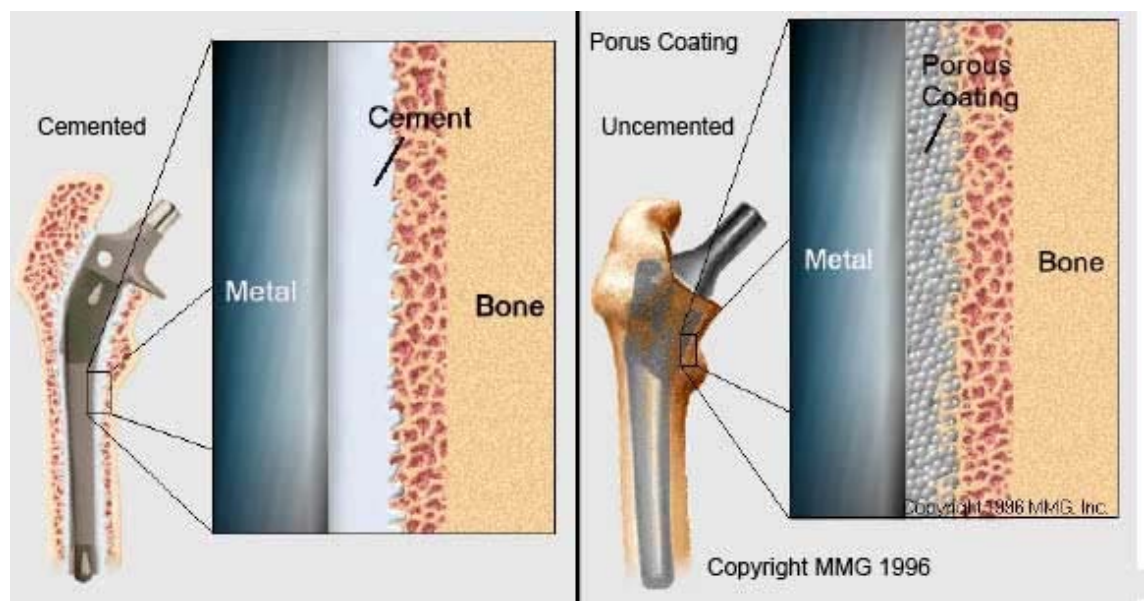


Figure 2.4: Typical cemented and uncemented fixation (Izzo, 2012)



## **2.5 Total hip replacement failure**

Developments in the design, technology, and technical operation increased the success rate of THR. However, THR failure remains a problem, so revision surgery is essential and unpreventable. For example, 10% of all THR surgeries in the USA per year undergo THR revision surgery (Brown & Huo, 2002). Accordingly, the components of the old artificial joint are partially or totally replaced with new components. Mechanical factors are more common causes of THR failure than infection. Aseptic loosening is the most important cause of THR failure (Gross & Abel, 2001). The mechanisms leading to aseptic loosening remain ambiguous. Osteolysis, lack of sufficient primary stability, stress shielding, cement failure, and debonding are some of the main factors that contribute to the development of aseptic loosening and ultimately destruction of THR (Boyle & Kim, 2011; Sivarasu et al., 2011).

### **2.5.1 Osteolysis**

The fretting of the THR joint components against each other releases debris in the joint environment, and the released debris activate the immune system, which causes bone resorption in a biological process known as osteolysis (Figure 2.5) (Bourghli et al., 2010; Fabbri et al., 2011; Suárez-Vázquez et al., 2011). Osteolysis is the main biological factor that causes aseptic loosening. Young patients have higher risk of osteolysis than old patients because of their higher range of activities that release more frictional debris (Beldame et al., 2009; Canales et al., 2010; Yoo et al., 2013). Thus, engineers have developed new designs, coatings, alloys, and bearing surfaces to cope with osteolysis (Canales et al., 2010). The risk of osteolysis in THR with polyethylene component is higher than those with ceramic-on-ceramic (CoC) or metal-on-metal (MoM) joints because of the size and amount of debris (Yoo et al., 2013). A

cross-linked polyethylene has been developed to improve its property against wear and decrease the amount of released particles.

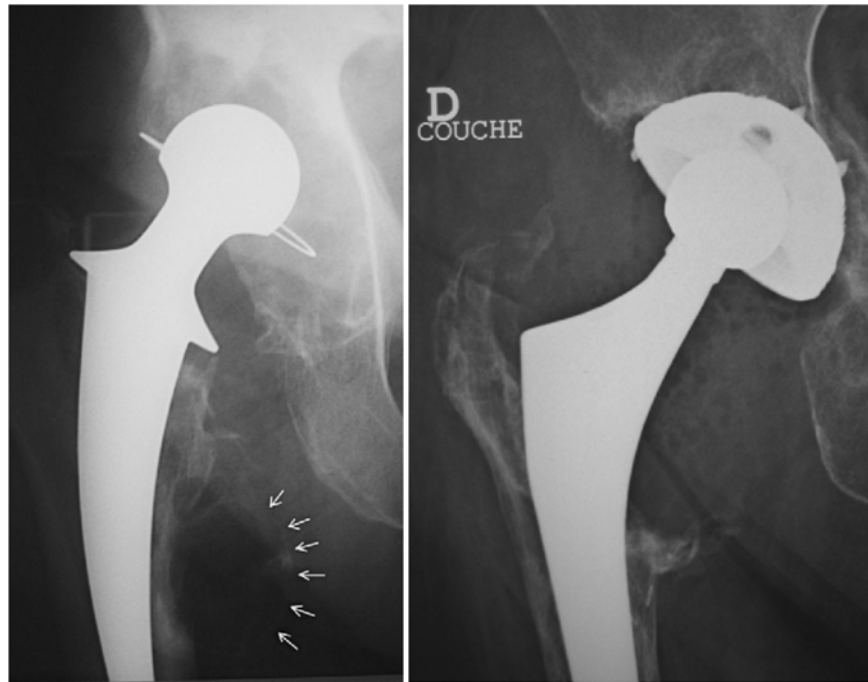


Figure 2.5: Osteolysis after total hip replacement replacement (Bourghli et al., 2010)

### 2.5.2 Primary stability

Primary stability refers to the stability of prosthesis after surgery (Viceconti et al., 2006). This stability is necessary to ensure the short- and long-term THR survival and is more crucial for the cementless prosthesis than the cemented one (Abdul-Kadir et al., 2008). Primary stability is a prior condition resulting in osseointegration and reduced movement at the interfaces of THR (bone–prosthesis and cement–bone) (Cristofolini et al., 2006). Insufficient primary stability will ultimately lead to THR failure because of the excessive motion at its interfaces. Excessive motion prevents the good biological fixation between the bone and the prosthesis by decreasing the bone in-growth into the prosthesis (Hao et al., 2010). Press fitting and proper rasping procedures provide primary stability for cementless prostheses (Varini et al., 2008). Additionally, the expertise of surgeons in selecting femoral prostheses with proper size is crucial to

achieve good primary stability (Varini et al., 2008). In vitro tests and numerical methods have been employed to measure the primary stability of different femoral prostheses (Viceconti et al., 2006). Moreover, intra-operative devices help surgeons to immediately examine the prosthesis stability after surgery (Varini et al., 2008).

### **2.5.3 Stress shielding**

The stress distribution in the femur at the hip joint is altered after implanting a femoral prosthesis because load transfer changes from the joint to the bone as shown in Figure 2.6 (Joshi et al., 2000). The change in stress distribution is due to the mismatch between the prosthesis and bone stiffness (rigidity) (Behrens et al., 2008; Katoozian et al., 2001). Thus, some portions of the bone in THR tolerate less stress compared with the natural bone. This phenomenon is called stress shielding, and rigid prostheses can shield more load transfer from the hip joint to the femur at the proximal metaphysis (Gross & Abel, 2001). Contrary to engineering materials, the bone is a living tissue that can adapt to its mechanical and chemical environment, and it loses its strength because of load absence and stress shielding (Doblaré et al., 2004; Katoozian et al., 2001). Accordingly, excessive stress can develop at the interface of the bone–prosthesis and bone–cement (Gross & Abel, 2001) and cause aseptic loosening, which ultimately results in THR collapse. Therefore, stress shielding should be minimized after THR and stress distribution should be similar to the physiological condition to increase THR durability (Behrens et al., 2008).

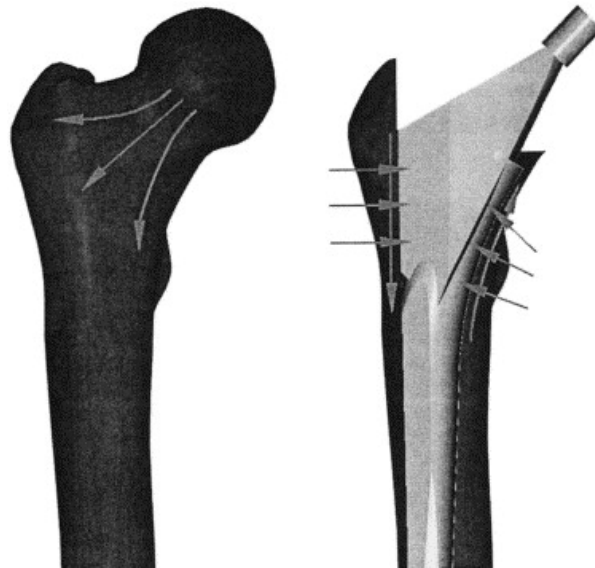


Figure 2.6: Load transfer before and after total hip replacement (Joshi et al., 2000)

#### 2.5.4 Cement failure

Bone cement is a brittle material that provides stability and fixation to the prostheses cemented to the host bone (Janssen et al., 2008; Lewis, 1997). Therefore, cement layer failure results in aseptic loosening (Lai et al., 2009). The strengths of the mechanical bone cement in compressive, tensile, and bending are 75 MPa – 105 MPa, 50 MPa – 60 MPa, and 65 MPa – 75 MPa, respectively. Moreover, the recommended thickness of the cement layer in THR ranges from 2 mm to 5 mm, whereas the cement layer with 5 mm–10 mm thickness is deleterious for the THR lifespan; more cracks are also detected in thinner cement layer (Scheerlinck & Casteleyn, 2006). Cement endures dynamic mechanical repetitive loadings during daily activities (De Santis et al., 2000), and the amplitude of such loadings depends on the type of activity, such as walking, running, or stair climbing. Cyclic loads cause fatigue, which accumulates in the cement layer (Verdonschot & Huiskes, 1997). These loads cause crack initiation and propagation (Waanders et al., 2011; Zivic et al., 2012). In addition, cracks could be initiated during polymerization because of porosities or internal tension and then

propagated in the cement mantle caused by the fatigue loads of daily activities, which ultimately result in cement failure (Achour et al., 2010; Zivic et al., 2012).

### 2.5.5 Debonding

Debonding at the interfaces is another factor that causes aseptic loosening and THR failure. This condition can occur at the cement–prosthesis or cement–bone interface, although most studies have shown the former case (Pérez et al., 2005). Debonding at prosthesis–cement causes higher hoop cement stress and increases the crack densities at the cement (Verdonschot & Huiskes, 1997).

### 2.5.6 Implant fracture

Fracture rarely occurs in the femoral component of THR. The number of fractures in a cemented femoral prosthesis is higher than that in the cementless prosthesis. However, fractures in the ceramic head and acetabulum cup are frequently detected because of the brittleness of ceramics (Figure 2.7).



Figure 2.7: Fractures in a ceramic ball and acetabulum cup (Jenabzadeh et al., 2012)

## **2.6 Material and geometry of artificial hip joint constituents**

The main factors in THR failure are briefly presented in previous sections. Reducing the effect of these factors is the initial step to create a successful design of artificial joint components. According to the literature, the geometry, materials, and surface finishing of the prosthesis are the possible characteristics that should be adjusted to achieve optimal designs. Therefore, the following sections briefly review the materials used and the geometries of artificial hip joint constituents.

### **2.6.1 Femoral head and acetabular cup**

After THR, the femoral head and acetabulum are replaced with MoM, metal-on-polymer (MoP), ceramic-on-polyethylene (CoP), or CoC bearing couples (Figure 2.8). The most commonly used couple joints are MoP and MoM (Catelas et al., 2011). The main criteria for selecting the design and materials for the hip joint bearing are fracture toughness, wear resistance, and frictional properties. Different bearings exhibit varying strengths and weaknesses. In MoP and CoP couple joints, the polymer against ceramic and metal is soft. Therefore, wear occurs in the polymer part of the joint couple. The wearing of polymer and the release of debris into the joint environment primarily cause joint luxation and osteolysis (Tudor et al., 2013). However, the developments in new cross-linked polyethylene can decrease the wear rate and particle sizes (Catelas et al., 2011). Moreover, in designing a process for the MoP couple joint to decrease friction, the artificial femoral head size should be approximately 28 mm to 36 mm, which is considerably smaller than the intact natural femoral head. MoM and CoC have been developed to prevent the release of debris in the joint environment. The second generation of the MoM joint couple with large head and low wear rate is more preferred for THR than the first generation, which shows very weak performance because of the

poor design features and surgical techniques (Molli et al., 2011; Naudie et al., 2004). Improving and optimizing metallurgical approaches (carbon content, method of fabrication, and heat treatment) and geometries (clearance, sphericity, surface finish, functional arc, fixation surface, and head size) enable the second generation of MoM to be superior to the first generation (Molli et al., 2011). Regardless of these advances in producing the MoM couple joint, its exposure to released metal ions because of the articulation wear in the joint remains unsolved (Vendittoli et al., 2011). Thus, CoC couple joints, which have outstanding wear resistance, have been developed as an alternative couple joint for MoP, MoM, and CoP (Al-Hajjar et al., 2013). The CoC couple joint provides a joint with negligible wear because of wettability and wear resistance, thus reducing periprosthetic osteolysis and the release of metal ions in the joint environment (Traina et al., 2013). Contrary to the MoM, MoP, and CoP couple joints, the wear rate in the CoC couple joint does not increase along with the femoral head size (Al-Hajjar et al., 2013). However, the intrinsic brittleness of ceramic materials is the main disadvantage of the CoC couple joints.



Figure 2.8: Typical femoral heads and acetabulum cups (Heimann, 2010)

### 2.6.2 Femoral prosthesis (Stem)

A femoral prosthesis is secured within the femur and connects the upper and lower limbs (Figure 2.9). Accordingly, loads are transferred from the upper limb and hip joint to the lower limb through the femoral prosthesis, so the geometry and material for femoral prosthesis are crucial in the lifespan of THR.



Figure 2.9: A typical total hip replacement (Jun & Choi, 2010)

### 2.6.3 Femoral prosthesis geometry

Four different commercial femoral prostheses are presented in Figure 2.10. The optimal femoral prosthesis geometry can transfer axial and torsional loads without causing destructive stress and excessive micromotion (Scheerlinck & Casteleyn, 2006). In addition to the angle and length of the neck, the geometry of a femoral prosthesis consists of its cross section, profile, and length. Moreover, prosthesis stiffness (rigidity) is a function of the prosthesis geometry and could be optimized by altering the geometry to decrease stress shielding and bone resorption, thus prolonging the THR lifespan. In addition, the developed stress in the cement layer depends on the prosthesis



geometry (Simpson et al., 2009). The stress in the cement and prosthesis can also be reduced by increasing the prosthesis cross section (Gross & Abel, 2001). However, anatomic factors limit the development of a new geometry for femoral prostheses (Ruben et al., 2007).



Figure 2.10: Typical prosthesis geometries with different cross sections and profiles (Ramos et al., 2012)

The initial stability and type of fixation within the cement and bone of the prostheses are affected by the prosthesis geometry (Kleemann et al., 2003). The two designs used to fix a cemented prosthesis inside the cement are shape-closed (composite-beam) and force-closed (loaded-taper) (Scheerlinck & Casteleyn, 2006). In the shape-closed design, stability is provided by interlocking the cement and prosthesis through the rough surface, collars, flanges, and grooves. By contrast, in the force-closed prostheses, the friction and the transfer of forces across the interface maintain the tapered prosthesis into the cement. Moreover, cementless prostheses can be categorized into six groups based on their distinct geometries (Figure 2.11) (Khanuja et al., 2011). Types 1 to 4 are straight femoral prostheses. Types 1 (single-wedge prostheses), 2, and 3 are tapered with more proximal fixation, whereas Type 4 is fully coated with more

distal fixation. Type 5 is a modular prosthesis, and Type 6 is a curved femoral prosthesis with anatomic designs.

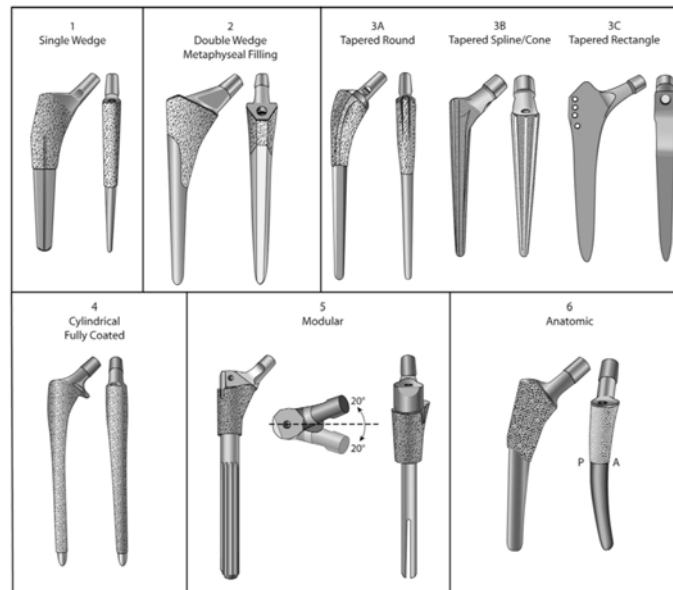


Figure 2.11: Schematic illustration of the different classifications of the cementless femoral stem designs. Type 1 is a single wedge, Type 2 is a double wedge, Type 3A is tapered and round, Type 3B is tapered and splined, Type 3C is tapered and rectangular, Type 4 is cylindrical and fully coated, Type 5 is modular, and Type 6 is anatomic. P = posterior and A = anterior (Khanuja et al., 2011)

#### 2.6.4 Femoral prosthesis materials

Selecting materials for a femoral prosthesis is a complex task, because the implant that would be introduced into the aggressive physiological environment of the human body would be exposed to various biological and mechanical stresses (Enab & Bondok, 2013). The implant material should be biocompatible and resistant against corrosion and wear (Enab & Bondok, 2013). Moreover, the Young's modulus of the prosthesis material directly affects its stiffness and stress shielding. The Young's modulus of the conventional materials (Ti alloy, Cr–Co, and St alloy) applied in femoral prostheses have ten times higher Young's modulus than that of the cortical bone. Thus, the risk of THR failure caused by stress shielding is high.

## **2.7 Surface finishing**

Surface finishing is one of the main factors in the design of implants that significantly affects the longevity of THR (Jamali et al., 2006). The surface finishing (surface roughness) of the head and cup is required to provide good function, whereas the surface finishing of the stem remains debatable (Zhang et al., 2008). The surface finishing of a metallic stem can be smooth-polished surfaces, roughened-blasted surfaces, or geometrically textured surfaces (Crowninshield, 2001).

## **2.8 Materials utilized in artificial hip joint components**

The following section presents a brief review on the materials used in artificial hip joint components. The materials can be classified into four main groups, namely, metals, polymers, ceramics, and composites. Each group has strengths and weaknesses.

### **2.8.1 Metals**

St, Co–Cr–Mo alloys, and Ti alloys are the most commonly used metals for implant designs (Khanuja et al., 2011). St is advantageous in terms of cost and processing availability (Long & Rack, 1998). However, given that St-based prosthesis is prone to corrosion and fracture, Co–Cr–Mo alloys and Ti alloys are more frequently used in prosthesis (Musolino et al., 1996). Co–Cr alloys are stronger than St and Ti alloys and have better corrosion resistance than St (Manicone et al., 2007). Ti alloys have lower Young's modulus, better biocompatibility, and more corrosion resistance than St and Co-based alloys (Long & Rack, 1998). However, Ti alloys have poor shear strength and wear resistance (Long & Rack, 1998).

### **2.8.2 Polymers**

Polymers are long-chain high-molecular weight materials that consist of repeating monomer units (Löser & Stropp, 1999). Orthopedic implants made of polymeric material can be classified into two groups: temporary (bioresorbable or biodegradable) and permanent (long-term implant). Permanent polymeric implants are commonly produced using polyethylene, urethane, and polyketone, whereas temporary polymeric implants consist of polycaprolactone, polylactide, and polyglycolide. Sir John Charnley developed a low-friction joint with a polymeric acetabular cup made of polytetrafluoroethylene (PTFE) and a small metallic femoral head; however, PTFE has been replaced by ultra-high molecular weight polyethylene, which has excellent energy absorption and low coefficient of friction (Long & Rack, 1998; Slouf et al., 2007).

### **2.8.3 Ceramics**

Ceramics are inorganic materials composed of metallic and nonmetallic elements (Asthana et al., 2006; Mackenzie, 1969). Ceramics are widely used in engineering, particularly in the aviation and automotive industries. In addition, ceramic material have good biocompatibility and thus suitable for medical devices and hard tissue replacement. Ceramics, including HA, alumina, and zirconia, have orthopedic applications.

HA, with the chemical formula of  $\text{Ca}_{10}(\text{PO}_4)_6(\text{OH})_2$ , is a crystalline molecule that consists of phosphorus and calcium (Saithna, 2010). HA is the main mineral component (65%) of the human bone (Havlik, 2002). This compound exhibits significant properties such as excellent biocompatibility, bioactivity, nontoxicity, and unique osteoinductivity, for orthopedic applications (Ohgaki & Yamashita, 2003;

Pramanik & Kar, 2013). The brittleness of HA and its lack of mechanical strength limit its application in implants (Aminzare et al., 2012). Therefore, HA can be used as a composite material by reinforcing with other materials or can be applied as a coating on the surface of implants (Aminzare et al., 2012). The HA coat creates a firm fixation by forming a biological bond between the host bone and implant (Singh et al., 2004). Thus, cementless implants coated with HA has higher survival rate than the uncoated implants (Singh et al., 2004).

Calcium silicate (CS) ( $\text{CaSiO}_3$ ) is a highly bioactive material that induces the formation of an HA layer on its surface after soaking in simulated body fluid or human saliva. Hence, CS is an appropriate material for bone filling, implant, and bone tissue regeneration because of its osseointegration properties. However, similar to HA, CS has low fracture toughness and load bearing capacity, thus limiting its application in the human body. Therefore, numerous studies have endeavored to enhance the load bearing capacity and toughness of CS by reinforcing it with other materials such as alumina (Shirazi et al., 2014), carbon nanotube (Borrmann et al., 2004), graphene oxide (Xie et al., 2014), and reduced graphene oxide (Mehrali et al., 2014). In addition, CS is applied as a coating layer on metallic implants to increase their surface bioactivity and to provide a good bond with the bone and a firm fixation.

Alumina is the most stable and inert ceramic material that has been utilized in orthopedic implants (Shikha et al., 2009). Alumina is a polycrystalline ceramic that contains aluminum oxide, which is extremely hard and ranks third after diamonds and silicon carbide, and is also a scratch resistant material (Jenabzadeh et al., 2012). Alumina has a Young's modulus of 380 GPa, which is approximately twice as much as that of St (Hannouche et al., 2005).

Zirconia, a crystalline dioxide ( $ZrO_2$ ) of zirconium, has good chemical and dimensional stability, wear resistance, mechanical strength, and toughness, in addition to the following characteristics: Young's modulus similar to that of St; tensile strength, between 900 MPa and 1,200 MPa; compressive strength, 2,000 MPa (Piconi & Maccauro, 1999). A molecularly stable zirconia can be achieved by mixing it with other metallic oxides, such as MgO, CaO, or  $Y_2O_3$  (Manicone et al., 2007). Despite the difficulty in stabilizing zirconia with  $Y_2O_3$  sintering, this combination presents better mechanical properties than other combinations (Manicone et al., 2007). A biomedical grade of zirconia that has been proposed in 1969 for orthopedic implants and for replacement of Ti and alumina implants has comparable brittleness with that of alumina, thus preventing implant failure (Chevalier, 2006). However, zirconia aging and surface grinding have detrimental effects on its properties and toughness (Figure 2.12) (Kosmač et al., 1999; Luthardt et al., 2002).

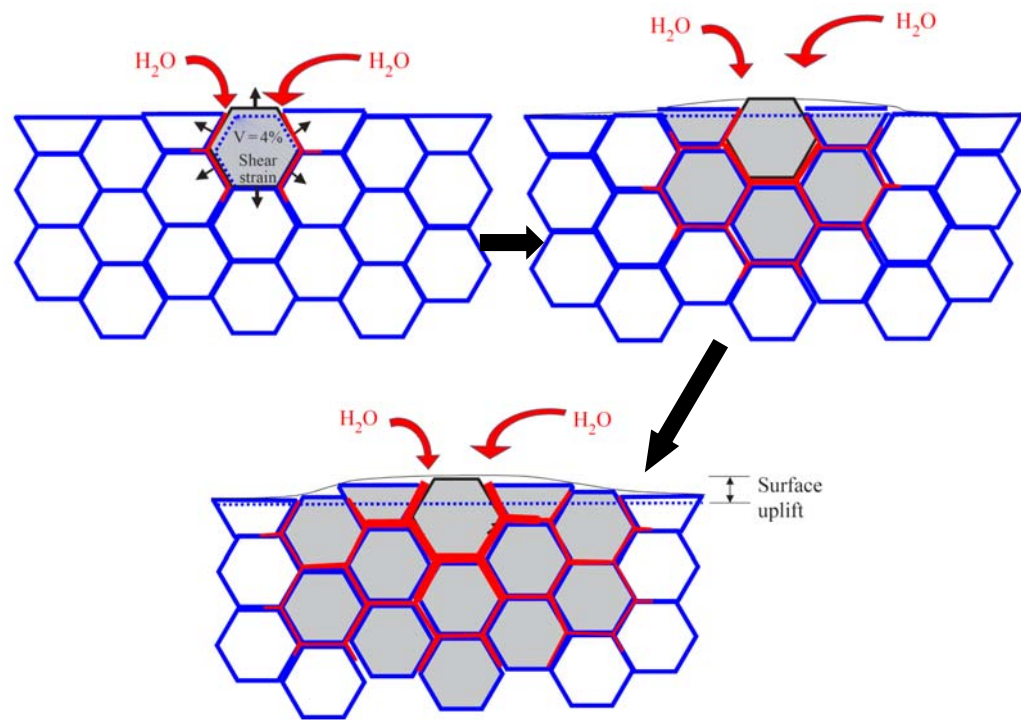


Figure 2.12: Scheme of the aging process (Chevalier, 2006)

#### 2.8.4 Composites

Composites are engineered materials composed of two or more constituents. Currently, composite materials have been used in different fields of engineering, such as biomedical engineering, to produce new devices and implants (De Oliveira Simoes & Marques, 2001). The properties of composites can be modified according to different requirements; moreover, composites overcome the limitation of using single-phase material with the use of combined materials (Evans & Gregson, 1998). Therefore, these materials have better biological and mechanical compatibilities with body tissues and optimal strength and durability (Evans & Gregson, 1998). Orthopedic composites can be classified into polymer composites, ceramic composites, metal composites, and FGMs. In polymer composites, biocompatible polymers are applied as matrix with the reinforced materials (particulates, short or continuous, woven fibers (fabric), and nanofillers), regardless of the curing process (thermoset and thermoplastic). The thermoset polymer composites with low Young's modulus and high strength have been

implemented in femoral prostheses and fixation devices (Scholz et al., 2011). However, their performance in fixation devices is better than that in femoral prostheses (Evans & Gregson, 1998). Moreover, thermoplastic polymer composites have been used in acetabulum cups and artificial knee joint bearing.

Composite materials made of ceramics and metals are categorized based on the matrix and reinforcing materials into ceramic–metal composites (CMCs) and metal–ceramic composites (MCCs). The significant change in mechanical properties is caused by the inclusion of ceramic or metal particles into the metal or ceramic matrixes (Rodriguez-Suarez et al., 2012). Therefore, CMCs and MCCs possess superior stiffness, fracture, fatigue, tribological, and thermal properties to their monolithic ceramic and metal counterparts because of the overlapped strengths and weaknesses of the ceramics and metals (Mattern et al., 2004). Accordingly, conventional and monolithic materials (ceramics and metals) can rapidly change with these composites in various engineering applications such as in aerospace and automobile industries (Sahin, 2005).

FGMs are special groups of composite materials that incorporate continuous change (gradient) or step-wise change (graded) in their microstructure and properties as shown in Figure 2.13 (Miao & Sun, 2009). This concept was obtained from their natural biological structures (Pompe et al., 2003). Adapting materials with specific structural, compositional, morphological, and mechanical properties have emphasized that FGMs can be utilized in the design of new prostheses. The mechanical properties of FGMs can be optimized and controlled by adjusting the volume fraction of each material phase (Nie & Batra, 2010). In addition, the FGM-based implants provide better load bearing capacity, fracture toughness, and wear resistance than their monolithic ceramic or metallic counterparts (Miao & Sun, 2009; Mishina et al., 2008; Zhang et al., 2012).



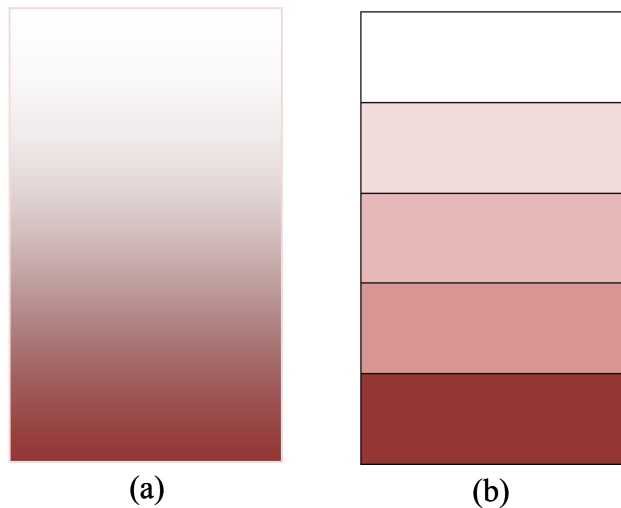


Figure 2.13: A typical FGM structure: (a) gradient and (b) graded

## 2.9 Numerical methods in hip joint biomechanics and implant study

Numerical (computational) methods, such as finite element method (FEM), extended FEM, and boundary element method, are powerful mathematical analysis tools that are widely used in different fields of engineering. Numerical methods are well accepted in biomedical engineering and biomechanics. In the numerical study of implant design, various implant design configurations are considered in a computer rather than performing expensive and destructive experimental tests (Asgari et al., 2004). Accordingly, many researchers have used FEM in analyzing hip joint, hip joint biomechanics, and hip implants. FEM has been used by prosthetists and engineers in the hip implant design to address problems such as implant failure, stress shielding, and bone resorption, which are related to the prosthesis material and design. The materials for prosthesis were discussed by El-Sheikh et al. (2002), Akay and Aslan (1996), Kaddick et al. (1997), Katoozian et al. (2001), Simões and Marques (2005), Kuiper and Huiskes (1997), and Hedia et al. (2004; 2006). Moreover, El-Sheikh et al. (El-Sheikh et al., 2002) examined the stress distribution in the implanted hip components to select the optimal material for femoral prosthesis; the study was conducted by inserting a femoral prosthesis with four different Young's moduli: 25, 100, 196, and 400 GPa. The

prostheses with lower Young's modulus tolerate less stress compared with those with higher Young's modulus as shown in Figure 2.14. Moreover, the developed stresses increase in the bone and cement.

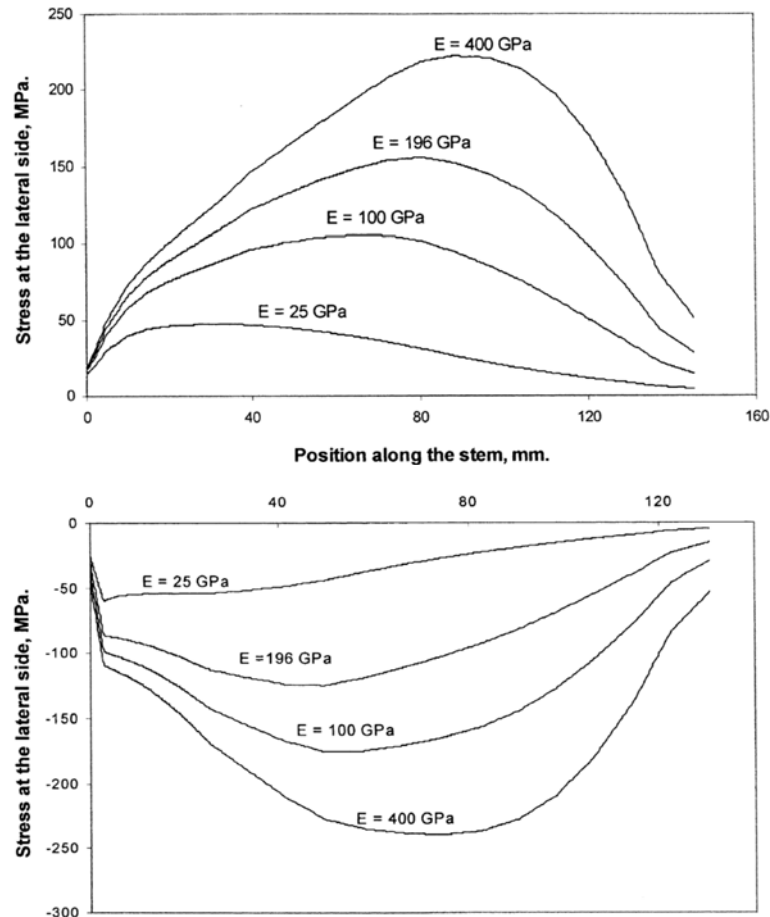


Figure 2.14: Minimum and maximum principal stress distributions on the (a) lateral and (b) medial sides of the stem as a function of the prosthesis Young's modulus (El-Sheikh et al., 2002)

Akay and Aslan (1996), Kaddick et al. (1997), Katoozian et al. (2001), and Simões and Marques (2005) used FEM to determine whether composite materials can replace the conventional materials used in femoral prosthesis. Katoozian et al. (2001) investigated the effect of the fiber orientations in the composites on the stress distribution in the implanted femur components. Moreover, Simões and Marques (2005) used composite materials to construct a prosthesis with metal core and variable stiffness as shown in Figure 2.15. High strain energy was observed in the proximal metaphysis of

the bone, indicating the less stress shielding effect of the prosthesis with tailorable stiffness. However, more principal stress was detected in the bone because of the implantation of the developed femoral prosthesis compared with those of the prostheses composed of conventional materials.

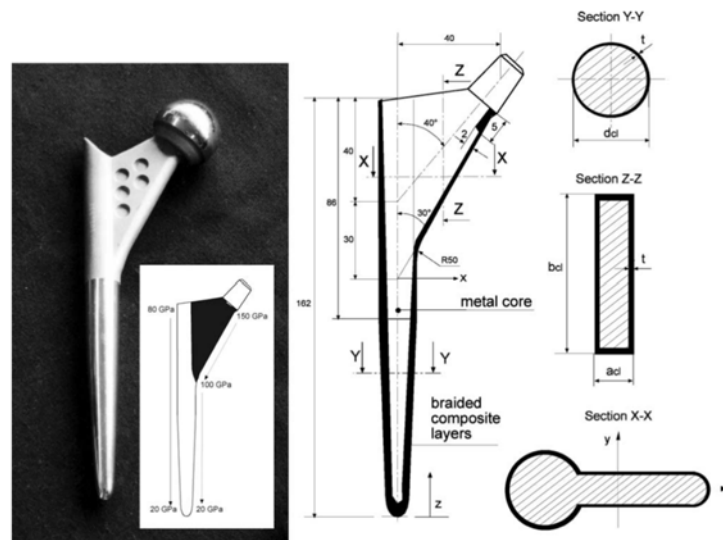


Figure 2.15: A femoral prosthesis with metal core and variable stiffness (Simões & Marques, 2005)

Kuiper and Huiskes (1997) and Hedia et al. (2004; 2006) evaluated the FGM performance in femoral prosthesis using two-dimensional (2D) FEM. The stress shielding, interface stress, and developed stress in the implant decline when FGMs are utilized in the femoral prosthesis. However, the developed stress in the bone and cement increases. Moreover, designing and optimizing the geometry of a femoral prosthesis using FEM were performed by Gross and Abel (2001), Sabatini and Goswami (2008), Bennett and Goswami (2008), and Ramos et al. (2012). Gross and Abel used a hollow stem to decrease prosthesis stiffness (rigidity) and stress shielding as shown in Figure 2.16.

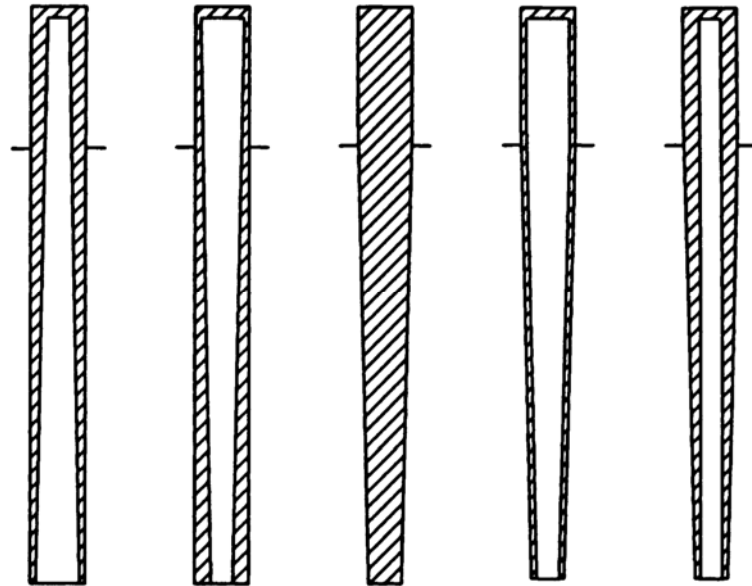


Figure 2.16: Hollow stems introduced by Gross and Abel (Gross & Abel, 2001)

Sabatini and Goswami (2008) and Bennett and Goswami (2008) investigated the effect of the different geometries of prostheses on stress distribution in the implanted femur components. The different cross sections and profiles used in their studies are presented in Figure 2.17.

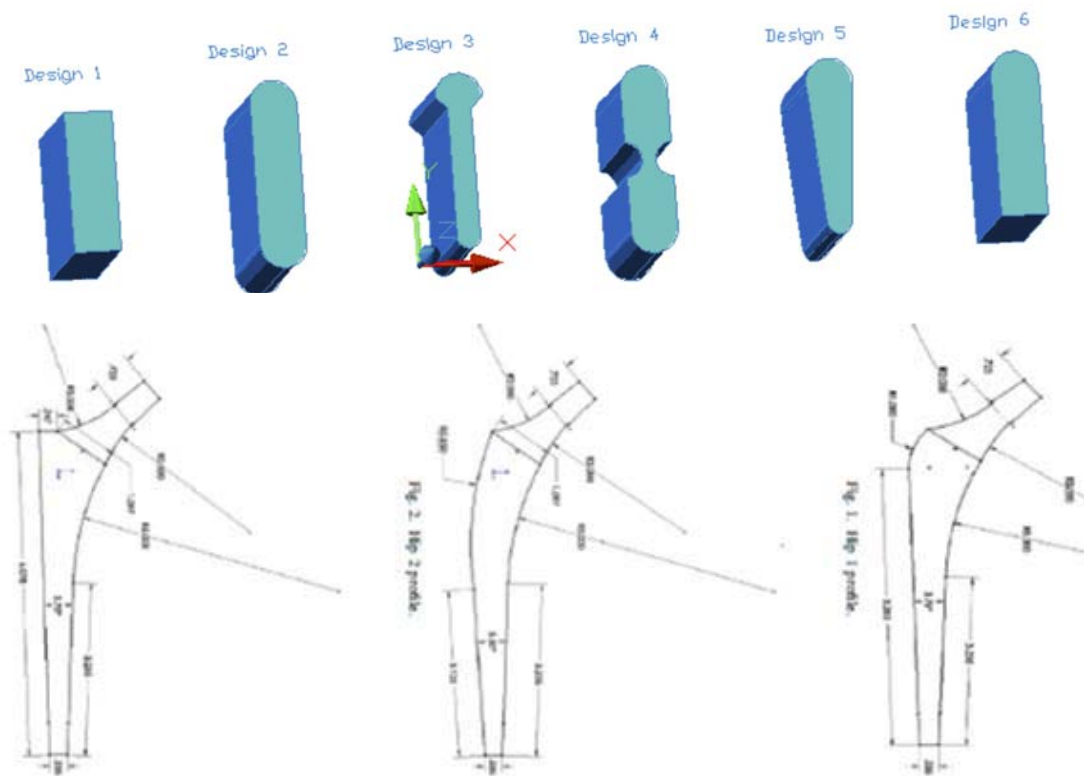


Figure 2.17: Different cross-sections and profiles (Bennett & Goswami, 2008; Sabatini & Goswami, 2008)

Ramos et al. (2012) numerically examined various cemented femoral prostheses with different cross sections and developed a new cemented femoral prosthesis geometry as shown in Figure 2.18. The new design provides 25% less stress in the cement compared with those of conventional prostheses.



Figure 2.18: Stem geometry developed by Ramos et al. (2012)

## 2.10 Load transfer in the proximal femur

All biological tissues have composite structures. This assumption is true for bone–implant combinations. The bone and implant have different material properties. Thus, an interface is required at which the two materials are integrated. One of the most important issues in the bone-implant interfaces is the mechanism of transferring loads from the implant to the surrounding bone. If the two materials are bonded and equal forces are applied with equal strains, Hook’s law and some simple algebra should be used to determine the load shared on each part of the composite structure as shown in Equations (2.1) and (2.2).

$$F_i = \frac{A_i E_i F}{A_i E_i + A_b E_b} \quad (2.1)$$

$$F_b = \frac{A_b E_b F}{A_i E_i + A_b E_b} \quad (2.2)$$

where the subscript  $i$  denotes implant, and  $b$  represents the bone.

As indicated by these analogies for the composite structures and bone–implant configurations, the load transfer mechanism in the femoral hip component exhibits some basic characteristics, regardless of the stem shape and the precise joint load. These basic characteristics can be illustrated by a simplified model of a straight implant mounted on a straight bone tube (Figure 2.19) (Huiskes, 1988).

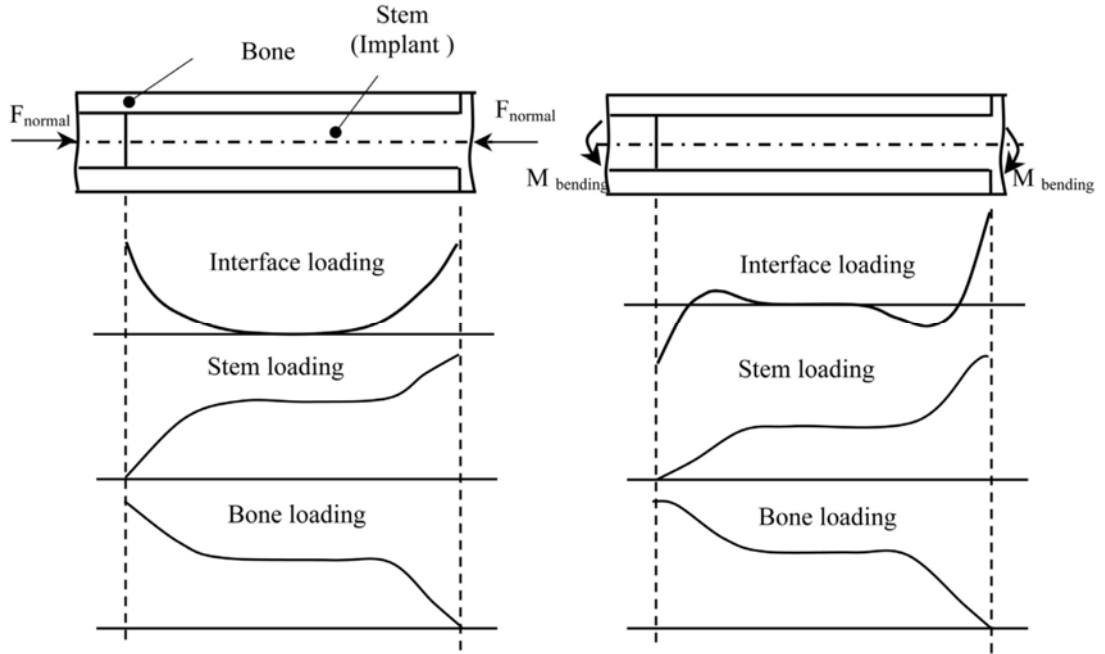


Figure 2.19: Principles of the load transfer mechanism explained with a simplified intramedullary fixation model (Huiskes, 1988)

Figure 2.19 shows that a large load is initially supported by the stem axially and in bending. Afterward, the bone and implant share the load. A high shear stress exists at the interface when the load is transferred. Similar to the previous results of composite bar analysis, a load is shared between the bone and implant with the ratio of implant stiffness to bone stiffness. Higher implant stiffness results in more loads supported by the implant as shown in Equations (2.3) and (2.4).

$$\frac{F_i}{F_{normal}} = \frac{A_i E_i}{A_i E_i + A_b E_b} \quad (2.3)$$

$$\frac{M_i}{M_{bending}} = \frac{I_i E_i}{I_i E_i + I_b E_b} \quad (2.4)$$

where  $F_i/F_{normal}$  is the normal load shared under axial load, and  $M_i/M_{bending}$  is the transverse load shared under bending loads. This finding demonstrates that stress shielding is attributed to high implant stiffness relative to bone stiffness.

The mismatch between the bone and implant stiffness is important for determining stress shielding and interface stress. Higher mismatches between the implant and bone stiffness results in a higher degree of stress shielding because more load is supported by the implant. However, as the implant carries more stress, lower loads should be transferred to the bone, resulting in lower interface stress.

## 2.11 Bone

The skeleton is mostly composed of bony components. Unlike engineering materials, bones are living tissues that can adapt to their mechanical and hormonal environment. Bones are composite materials composed of minerals and collagen with complex and unique mechanical properties. The bone functions are related to age, disease, and use. Moreover, bones are considered FGMs with composition and property dependent on direction and location. Long bones, such as femur, consist of two different bony structures: spongy (cancellous or trabecular) and cortical (compact bone) (Figure 2.20).

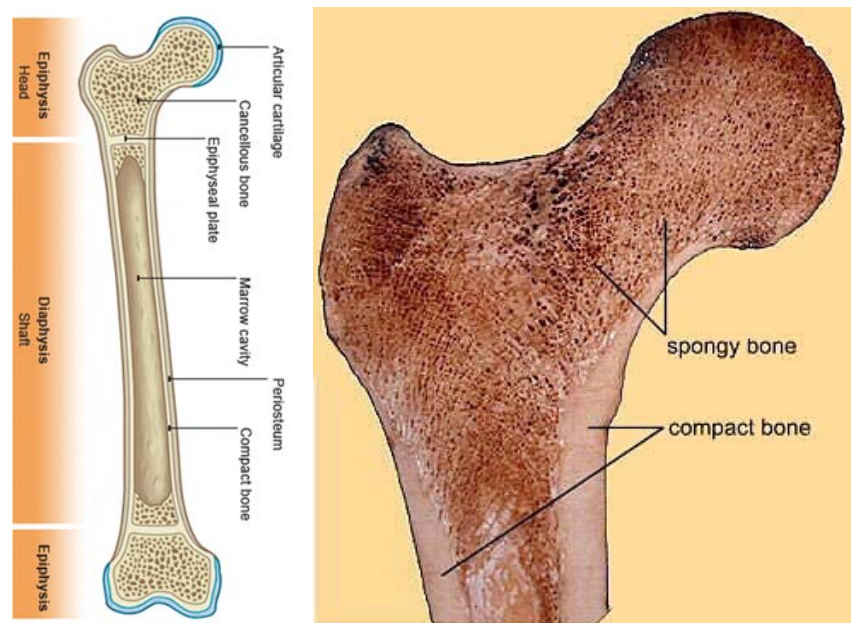


Figure 2.20: Bone structure (Juillard, 2011)



## **2.12 Summary**

This chapter presented a brief review regarding the hip joint and THR. Several studies have been performed to determine the optimal material and geometrical design for femoral prosthesis. However, an optimal hip design remains ambiguous and should be further investigated. Previous studies have focused only on the materials or geometrical design for prosthesis. The increasing incidence of THR involving young patients has motivated the use of FGMs in femoral prosthesis to prolong the lifespan of THR.

## CHAPTER 3

### MATERIALS AND METHODS

#### 3.1 Introduction

This chapter describes the methods performed in the current study. This chapter also presents the strategies developed to serve as guidelines throughout the study and aid in achieving the desired objectives.

#### 3.2 Outline of Methodology

An outline of methodology is presented using a flow chart in Figure 3.1. The outline provides an overview of the whole process and followed by a detailed discussion regarding the procedures and techniques used for FEA and experiment. The main activities in this study include FEA and experimental tests, which are described in this section.

#### 3.3 Finite element analysis

##### 3.3.1 Finite element modeling to use functionally graded materials in femoral prosthesis

A general finite element model was used to evaluate the performance of functionally graded (FG) femoral prostheses. Figure 3.2 presents an FEA flow chart. ABAQUS (ABAQUS Inc., Providence, RI, USA) version 6.10, a finite element software package, was used to determine the performance of FG femoral prostheses.

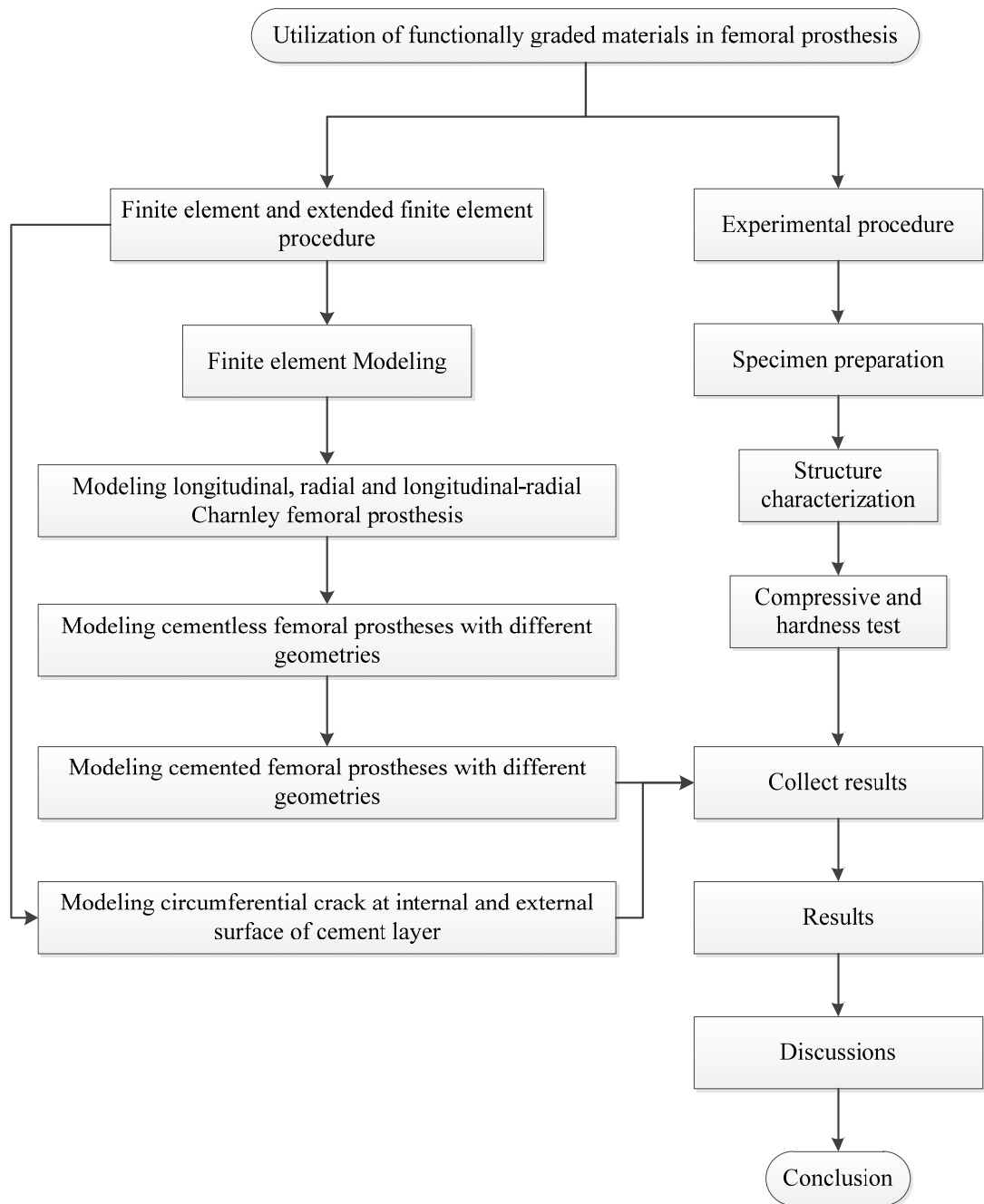


Figure 3.1: General description of the methodology adopted in the study

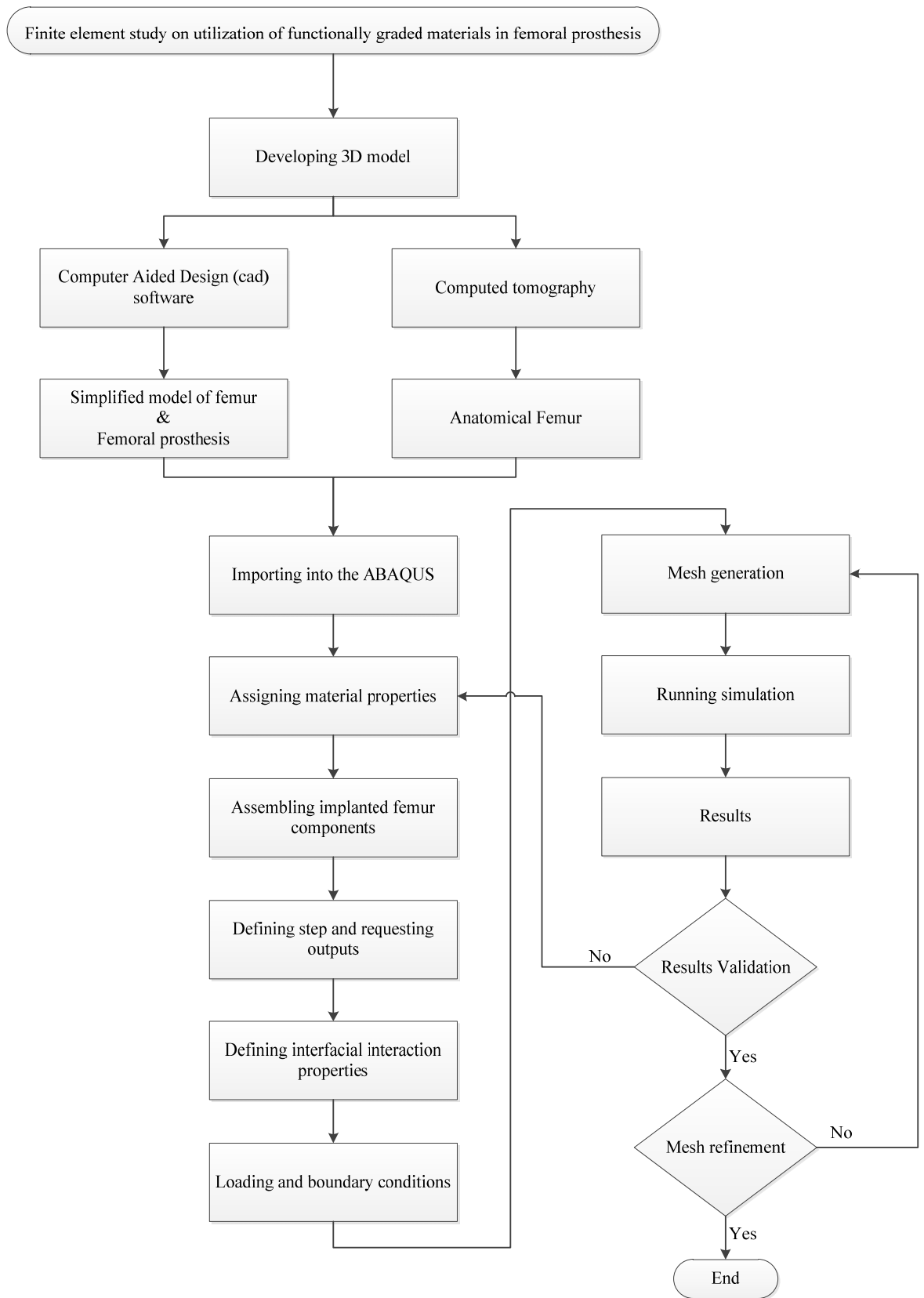


Figure 3.2: General description of the finite element analysis adopted in the study

### 3.3.2 Bone modeling

Computed tomography (CT) images were used to extract three-dimensional (3D) models of an anatomical femur. The properties of the CT scan slices are presented in Table 3.1.

Table 3.1: CT scan slices

Materials	Properties
Width	512 pixels
Height	512 pixels
Pixel size	0.549 mm
Algorithm	B10s
Reduction	1
Field of view	28.10 cm
Gantry tilt	0.000°
Number of slices	988
Slice increment	0.699 mm

The images were captured using a multidetector Siemens unit (Sensation 64; Siemens Medical Solutions, Malvern, PA, USA). The CT images were converted into the Digital Imaging and Communication (DICOM) format and imported to the Mimic<sup>®</sup> software (version 13; Materialise NV, Leuven, Belgium). The femur was identified using tissue-specific threshold values of 148 HU – 1,872 HU (the maximum and minimum threshold values corresponded to the range of grey values to the highlighted pixels). The simplified model of the femur also developed with Solidworks (Solidworks 2012, Dassault Systèmes Solidworks Corp., USA) computer-aided design software. The 3D anatomical model of the femur was developed using Mimic<sup>®</sup> software (Figure 3.3a), whereas the simplified model was constructed using Solidworks (Figure 3.3b).

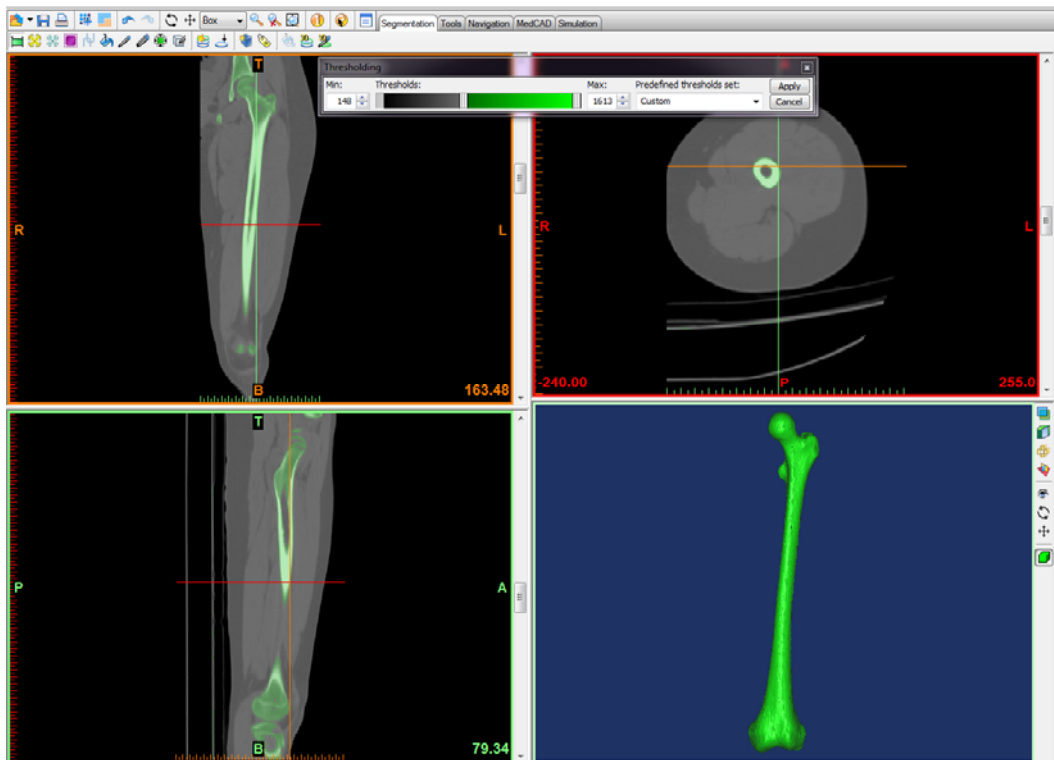


Figure 3.2: Development of the three-dimensional model of the femur using Mimic<sup>®</sup> software

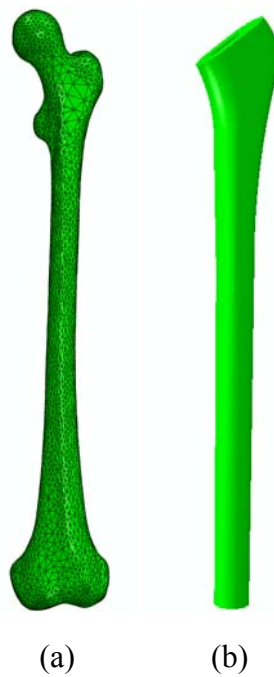


Figure 3.3: Three-dimensional models of the femur: (a) anatomical and (b) simplified

### 3.3.3 Prosthesis modeling

Solidworks (Solidworks 2012, Dassault Systèmes Solidworks Corp., USA) was used to develop a 3D model of the femoral prosthesis. Some of the 3D models of femoral prostheses are presented in Figure 3.4. The models for femoral prostheses with different geometries were developed using Solidworks. The prostheses composed of five distal cross sections, four proximal cross sections, and three profiles (Figure 3.5).

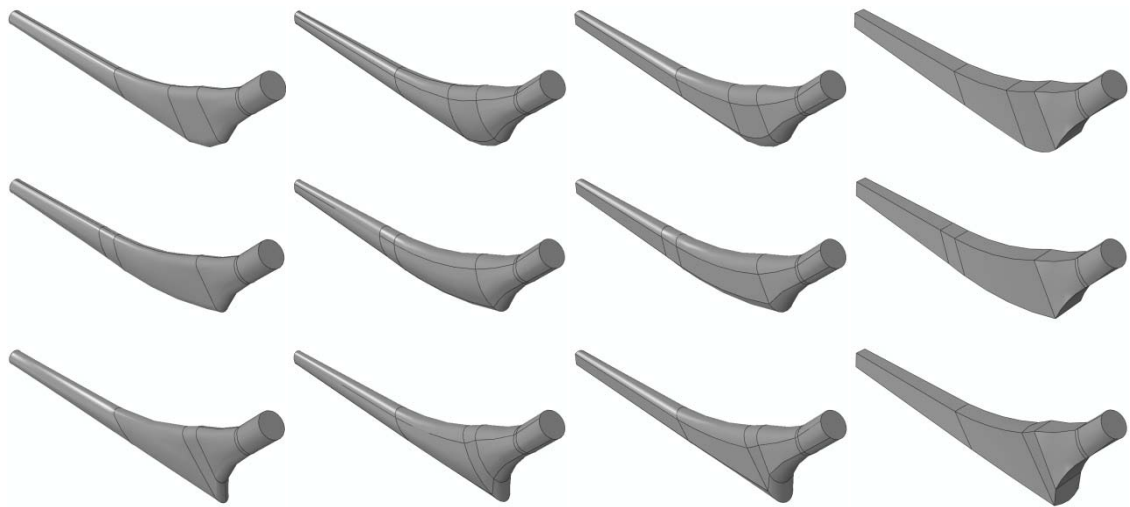


Figure 3.4: Stem models developed using Solidworks

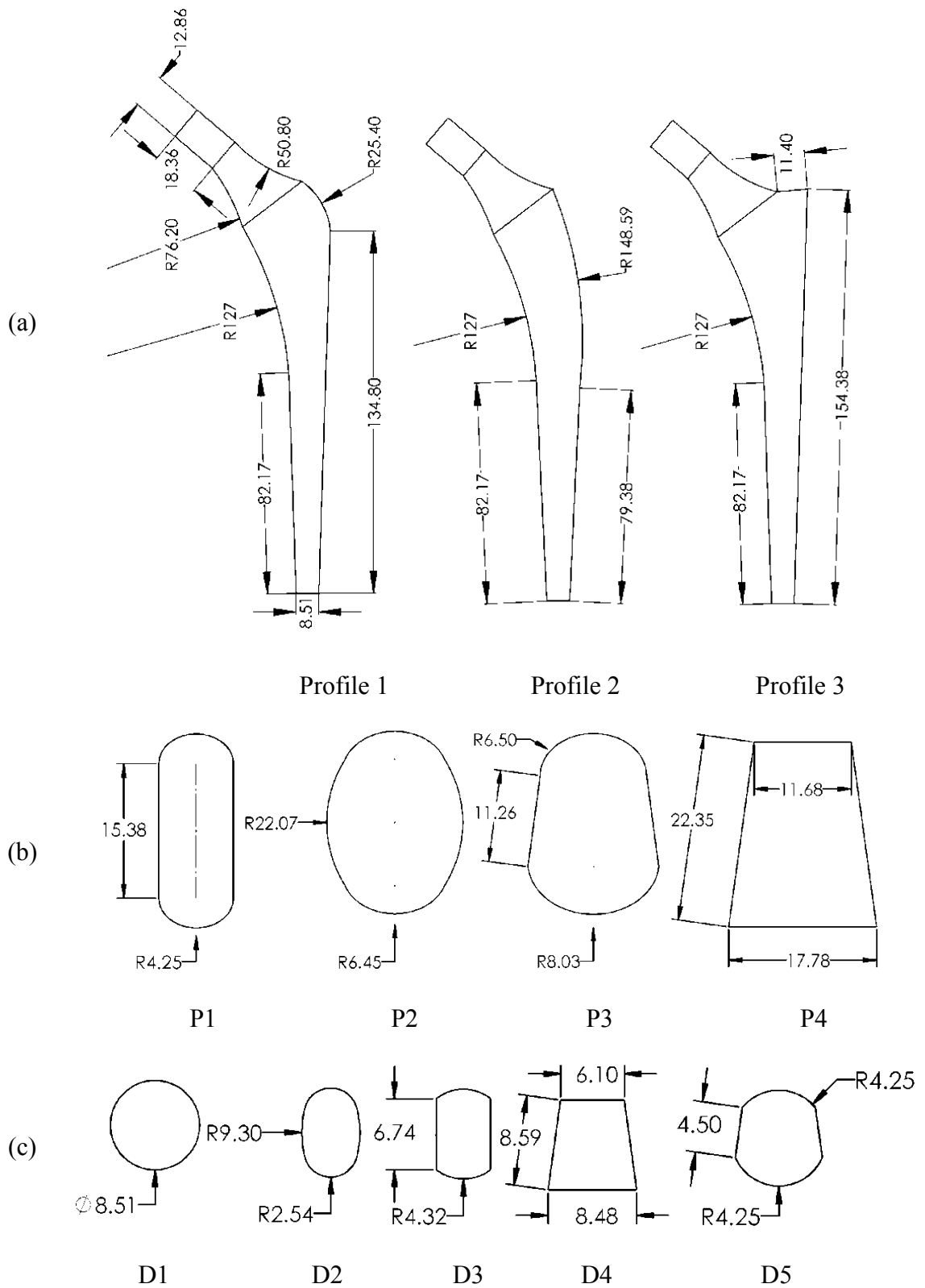


Figure 3.5: Dimensions of (a) profile, (b) proximal cross-sections, and (c) distal cross-sections



### **3.3.4 Mesh generation**

The 3D tetrahedral elements were used to mesh the implanted femur constituents (Ramos & Simoes, 2006). The approximate global sizes to mesh the cement, femoral prosthesis, and femur are 2, 1.5, and 2 mm, respectively.

### **3.3.5 Boundary conditions**

A range of loading conditions from the hip contact force to more complex loading scenarios involving several muscle forces can be used to represent the hip loading conditions. Moreover, two scenarios should be considered at the bone–implant surface for cementless prosthesis implantation. These conditions include non-bonded with friction coefficient and bonded surfaces. The non-bonded condition represents the prior bone in-growth, whereas the bonded surfaces depict the ideal bone in-growth. The desired fixation in cementless prostheses does not immediately occur after surgery. Moreover, the primary stability of a prosthesis can be evaluated by modeling the prosthesis and the straight bone after surgery. In this study, two conditions were considered on the bone–implant surface, namely, non-bonded surfaces with coefficients of friction of 0.4 and bonded surfaces. Friction Coefficients of 0.4 was also considered between the prosthesis and cement.

### **3.3.6 Material properties**

The materials considered in this study for femoral prosthesis are included conventional material (Titanium alloy, Stainless steel and chrome cobalt) and functionally graded material (Titanium alloy-HA and Stainless steel-HA). Ti alloy, St, Cr–Co, and HA are linear isotropic elastic materials. The cortical bone is a transversely

isotropic elastic material, whereas the spongy bone is a linear isotropic elastic material.

The mechanical properties of each material are tabulated in Table 3.2.

Table 3.2: Material properties of the implanted femur components

Material	Plane	E (GPa)	G (GPa)	$\nu$
Cortical bone	Xx	11.5	3.60	0.31
	Yy	11.5	3.30	0.31
	Zz	17.0	3.30	0.31
Spongy bone	-	2.13	-	0.30
HA	-	10.0	-	0.30
Ti alloy	-	110	-	0.30
St	-	220	-	0.30
Cr-Co	-	220	-	0.30

### 3.3.7 Functionally graded material modeling

This study used a piece-wise approach to model FGMs. The mechanical properties of FGMs in the femoral prosthesis varied in the sagittal and transverse planes. The planes were subdivided into partitions with equal heights or thicknesses to distribute the properties to the femoral prosthesis. The material properties were then assigned to each partition using Equation (3.1).

$$P_k = P_a \left( \frac{2K+h}{2h} \right)^n + P_b \left( 1 - \left( \frac{2K+h}{2h} \right)^n \right) \quad -\frac{h}{2} \leq K \leq \frac{h}{2} \quad (3.1)$$

In Equation (3.1),  $P_a$  and  $P_b$  are the material properties in the distal and proximal parts of the femur, respectively. Moreover,  $n$  is the volume fraction gradient exponent (gradient index),  $K$  is the portion height in each longitudinal stem and the thickness for radial prosthesis, and  $h$  is the length or thickness of the prosthesis. The increase in gradient index causes difficulty in FGM production and reduces the strength of prosthesis because of the increase in the HA ceramic phase. Therefore, the maximum

gradient index was limited to 3 in this study. Figure 3.6 illustrates the variation in Young's modulus in the longitudinal and radial prostheses composed of Ti-HA FGM for the gradient indices of 0, 0.1, 0.5, and 1.

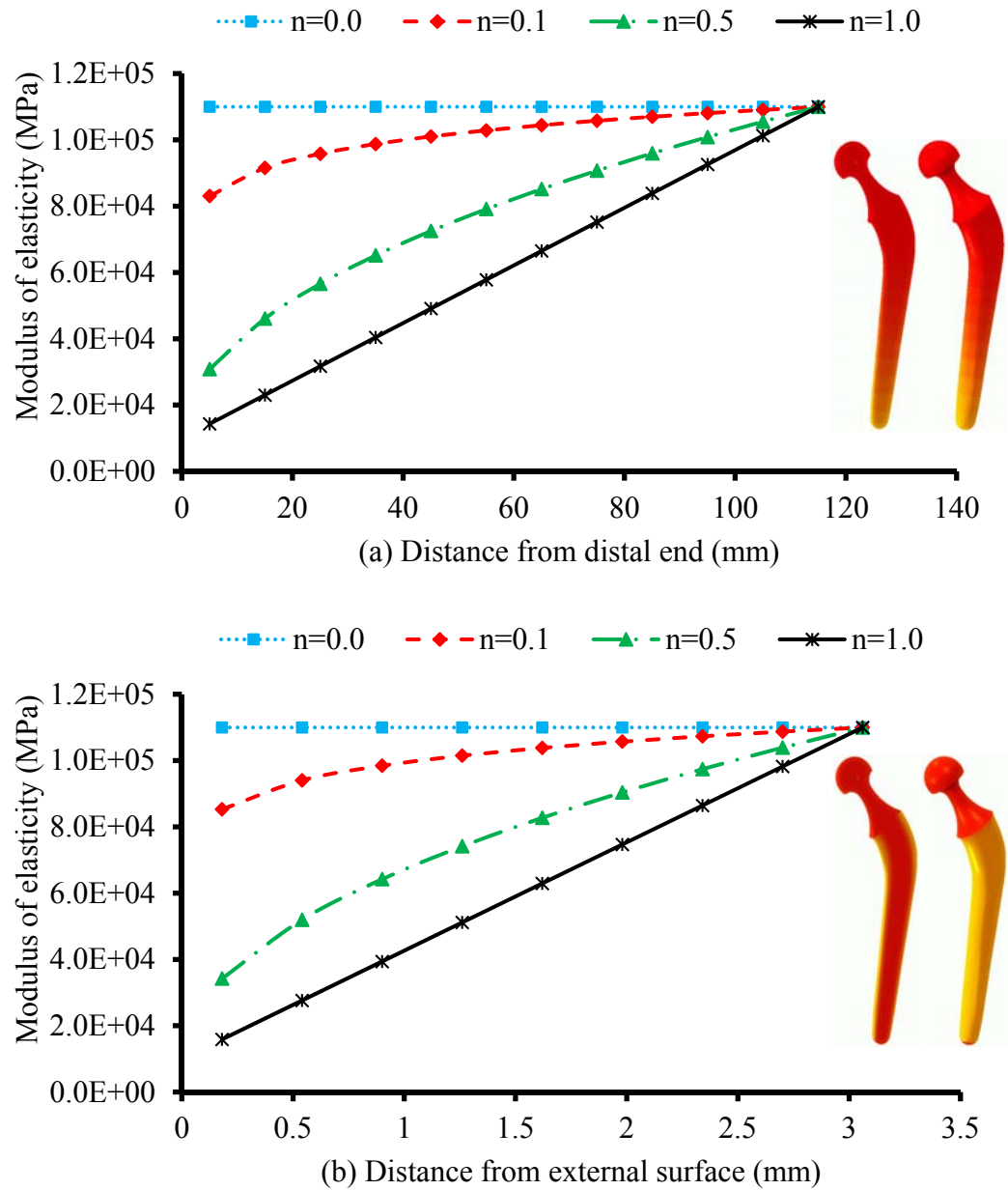


Figure 3.6: Variations in the Young's moduli of the (a) longitudinal and (b) radial prostheses

### 3.3.8 Crack modeling

Three different conditions were considered to assess the crack behavior inside the cement layer. These conditions include the location of cracks along the cement layer, position of cracks on the internal or external surface of the cement layer, and interaction of cracks on each other. The cement layer suffers from normal and shearing stresses, which are applied at the cement layer in hoop and longitudinal directions. Accordingly, the circumferential crack may propagate in the cement layer at different positions. The crack sizes range from micro to macro. In this study, the depths of the internal and external circumferential cracks were assumed to be 0.5 mm within the cement layer of THR. Moreover, the location of the cracks on the internal and external surfaces of the cement layer along the cement length was modified to reveal the places with higher risk of fracture and crack growth rate. Moreover, damage tolerance was based on the likelihood of finding cracks and their estimated propagation rates. Then, the cracks were positioned in the cement with the following distances: 25 (internal crack,  $I_{25}$ ; external crack,  $E_{25}$ ), 50 (internal crack,  $I_{50}$ ; external crack,  $E_{50}$ ), 75 (internal crack,  $I_{75}$ ; external crack,  $E_{75}$ ), and 100 mm (internal crack,  $I_{100}$ ; external crack,  $E_{100}$ ) from the distal end. The models tabulated in Table 1 included the length of the cement with an equidistance of 25 mm from the distal end to the proximal end on its internal and external surfaces. The models also present the relationship between the distance from the distal end and the behavior of stress intensity factor (SIF). An example of an internal crack at different locations is presented in Figure 3.7.

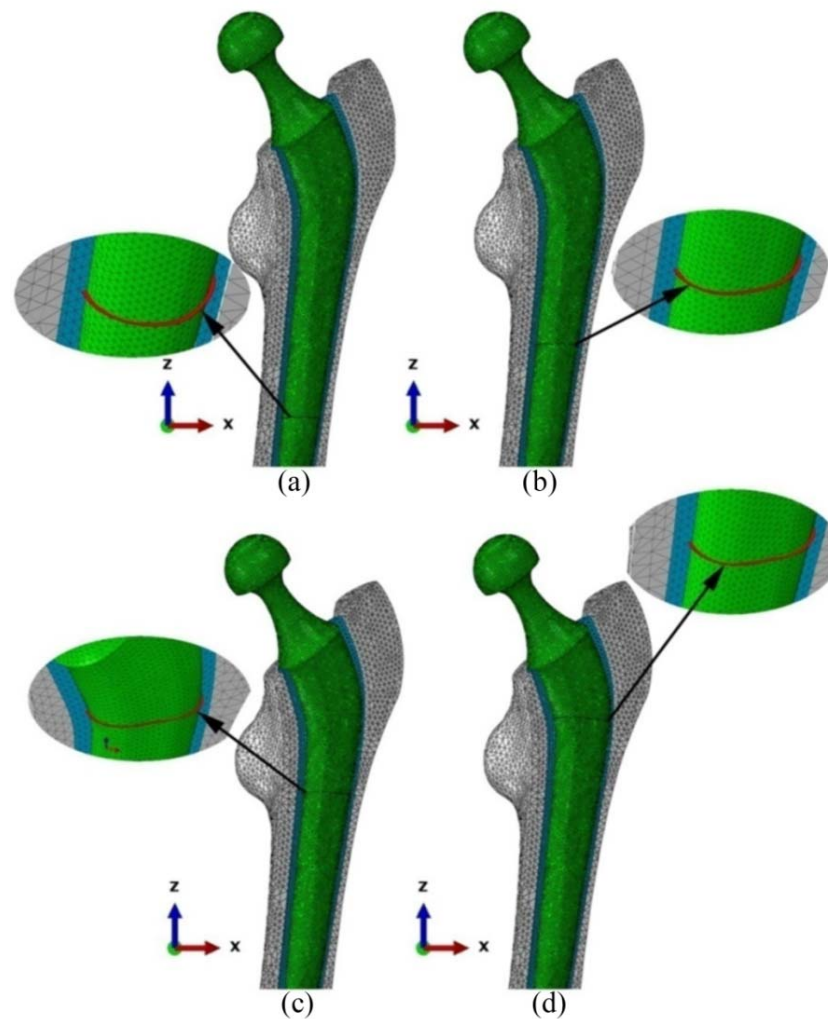


Figure 3.7: Internal crack geometry and locations of crack in the cement layer at (a) 25, (b) 50, (c) 75, and (d) 100 mm

### 3.3.9 Validation of finite element models

After several executions of the model, the errors in the mesh, material model, and boundary conditions were corrected, and the general finite element model was validated. The validation process involved the analysis of the convergence and investigation of the model under various conditions. The convergence of the results was the criterion used for validation. When errors were found during the validation process, a secondary literature survey was conducted to obtain pertinent insights from other studies.

### 3.4 Experimental procedure

Figure 3.8 shows the experimental steps performed in the present study.

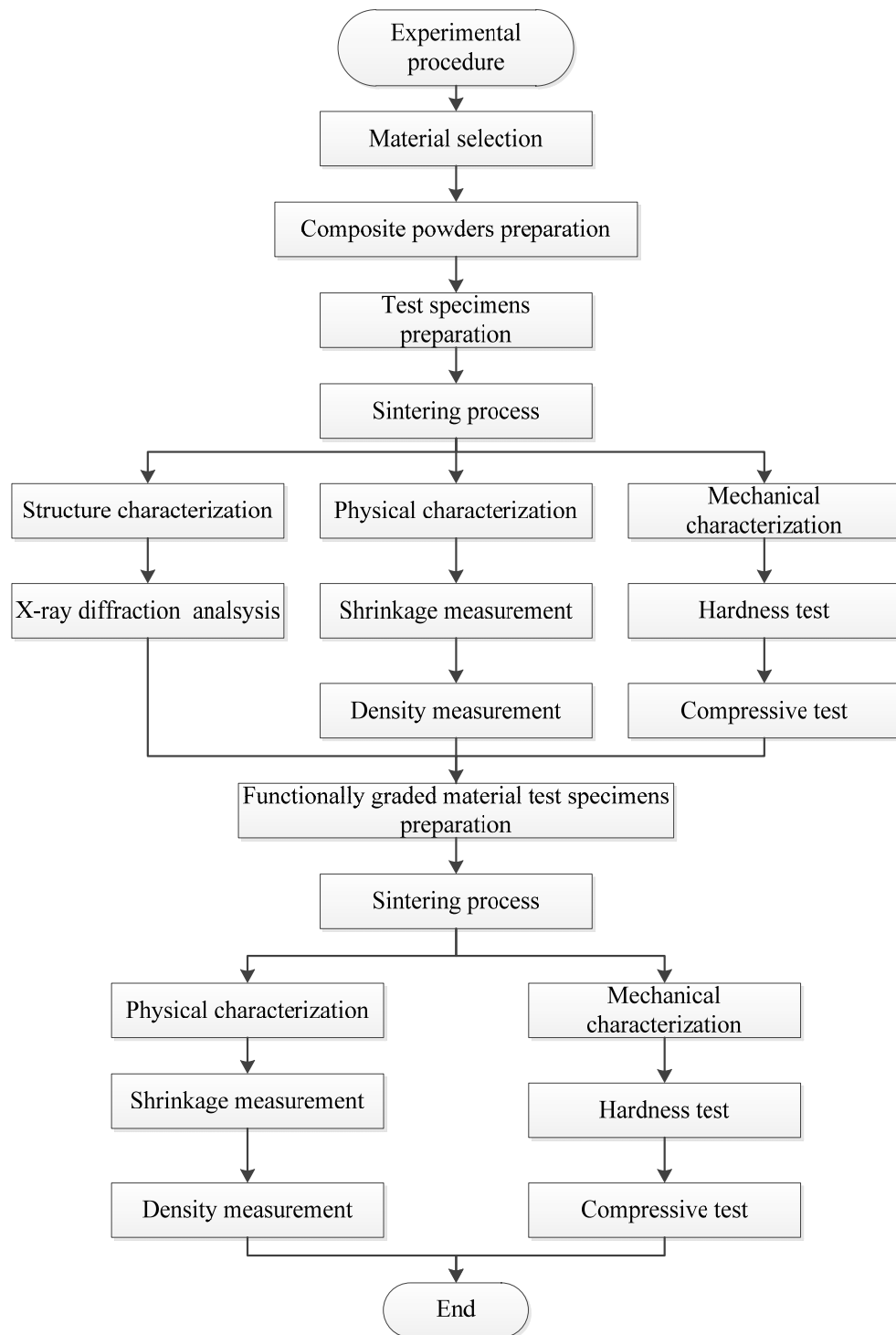


Figure 3.8: Flowchart of the experimental procedure

### 3.4.1 Test Material

Six different raw powders were used in the present study. In addition to two ceramic phases, HA and CS, the powders included four metallic phases: Ti, Ti-6Al-4V, Ti-55Ni, and SS-316L. The metallic phases were 99% pure with particle size  $\leq 45 \mu\text{m}$ , whereas the ceramic phases were  $\geq 90\%$  pure with particle size of approximately  $5 \mu\text{m}$ .

### 3.4.2 Composite powder preparation

Initially, wet ball milling was performed using raw powders at a ball-to-powder weight ratio of 5:1 in ethanol medium at a speed of 300 rpm for 6 h to obtain raw powders with uniform particle sizes. Then, the powders were dried overnight in an oven at  $110 \text{ }^\circ\text{C}$ . The metallic phase was mixed with the ceramic phase at different weight percentage ratios as shown in Table 3.3. The mixture of the powders was homogenized using a horizontal ball mill at 600 rpm for 48 h with ethanol medium. Finally, the mixture of powders was dried overnight (16 h) in an oven at  $110 \text{ }^\circ\text{C}$ .

Table 3.3: Weight percentages of raw powders in the composites

Metal phase content (wt %)	Ceramic phase content (wt %)
100	0
90	10
80	20
70	30
60	40
50	50
40	60
30	70
20	80
10	90
0	100

### 3.4.3 Test specimen preparation

The dried milled powders were compacted at 250 MPa using a manual hydraulic press (GS15011, Graseby Specac) to form green samples. Afterwards, pressureless sintering was performed at 1,200 °C for the composite sample and at 1,200 °C, 1,100 °C, and 1,000 °C for the FGM samples for 3 h in an inert argon gas environment using a vacuum atmosphere furnace (XY1600, Nanyang Xinyu Furnaces). Sintering was conducted to prevent the oxidation of the metal phases. The entire test procedure was performed on each specimen. The specimens were prepared in a cylindrical form with diameter of 6.35 mm and length of 12.7 mm according to the ASTM C 773-8 (Figure 3.9).

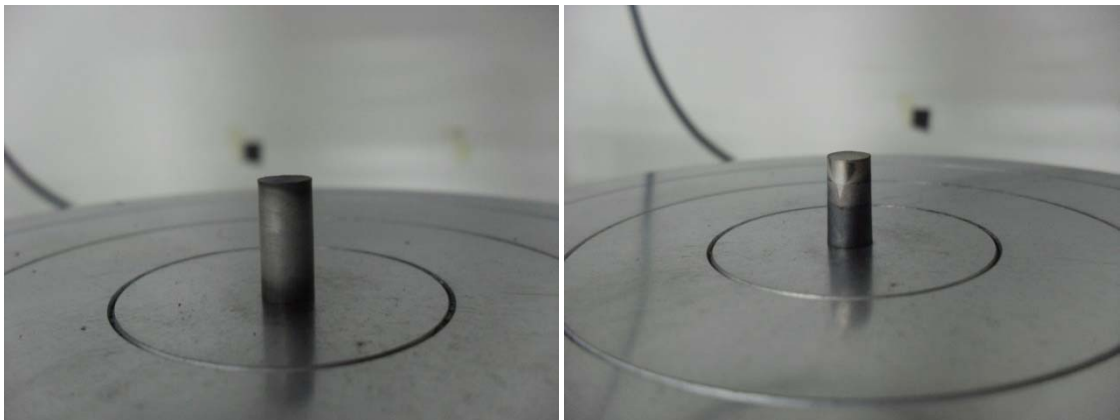


Figure 3.9: Typical testing of sample

### 3.4.4 Structure characterization

X-ray diffraction (XRD) was conducted on the sintered samples using an X-ray diffractometer (Empyrean, PANalytical) to determine and analyze the phase constitution. Scanning angle ( $2\theta$ ) ranged from 20° to 70° using  $\text{CuK}\alpha$  radiation ( $\lambda = 1.54056 \text{ \AA}$ ).



### 3.4.5 Physical characterization

Density ( $\rho$ , g/cc) was measured using Archimedes' principle as discussed in a previous study (Pramanik et al., 2012) and is presented by Equation (3.2), whereas the volume shrinkage ( $\epsilon\%$ ) of the sintered samples was determined with Equation (3.3). A minimum of five identical specimens were obtained. The average and standard deviation (STD) for each sintered sample were determined using the water density of 0.99704 g/mL at 25 °C.

$$\text{Density}(\rho) = \frac{\text{Weight}_{in\ air}}{\text{Weight}_{in\ air} - \text{Weight}_{in\ water}} \times \text{Water density} \quad (3.2)$$

$$\text{Volume Shrinkage percentage}(\delta\%) = \frac{\text{Initial volume} - \text{Final volume}}{\text{Initial volume}} \times 100 \quad (3.3)$$

### 3.4.6 Mechanical characterization

#### 3.4.6.1 Vickers hardness test

Vickers hardness test was conducted on the polished surfaces of the sintered samples using a microVicker's hardness tester (Figure 3.10; AVK-C200, Mitutoyo). The pyramid-shaped diamond indenter was used at a constant load of 5 N for 10 s to obtain a minimum of five indentations from each sample.



Figure 3.10: A micro-hardness tester machine

### 3.4.6.2 Compressive static test

The specimens were subjected to compressive static test at room temperature to determine the compressive elastic modulus ( $E_C$ ) and ultimate compressive strength ( $\sigma_{UCS}$ ) of the composites. The test was conducted using a universal testing machine as presented in Figure 3.11 (4469, Instron). The test was performed under load control condition at a displacement rate of constant cross-head speed of 1 mm/min.



Figure 3.11: An Instron universal testing machine

### 3.5 Summary

This chapter described the overview of the methodology used in this study to achieve the desired objectives. The methodology was divided into two parts: finite element modeling and experimentation. Finite element method included the modeling of longitudinal, radial, and longitudinal–radial Charnley FG femoral prostheses as well as the longitudinal and radial FG femoral prostheses with different geometries. Moreover, the experiments included the preparation of the composites of Ti, Ti–Ni, Ti–6Al–4V, and SS–316L with CS and HA to assess their composition structure and compressive properties as a function of the ceramic phase weight percentage after sintering at 1,200 °C. In addition, FGMs composed of Ti, Ti–Ni, Ti–6Al–4V, and SS–316L with CS and HA were prepared. The FGMs sintered at 1000 °C, 1100 °C, and 1200 °C and their physical and compressive mechanical properties were also assessed.

## CHAPTER 4

### RESULTS

#### 4.1 Introduction

This chapter is divided into two parts: FEA and experimental results. The FEA results obtained using the models are divided into four parts: longitudinal, radial, and longitudinal–radial FG Charnley femoral prosthesis, cementless FG prostheses, cemented FG prostheses, and cemented prostheses with circumferential cracks. The SED at the proximal of the femur was determined to examine the stress shielding level of the prosthesis. The risk of failure of prostheses was examined by assessing the developed von Mises stress. The maximum and minimum principal stresses stimulated to the bone were used as failure criterion. Cement failure was investigated by measuring the maximum and minimum principal stresses induced to the cement. The induced shear interface stresses were used to obtain the risk of failure in the interfaces. Circumferential crack behavior was studied by investigating SIFs, namely,  $K_I$ ,  $K_{II}$ , and  $K_{III}$ , at the crack front. The experimental results are divided into two parts: metal (Ti, Ti–6Al–4V, Ti–55Ni, and SS-316L)–ceramic (CS and HA) composites and FGMs. The experimental results include physical properties, XRD, static compression, and Vickers hardness. Physical properties include shrinkage and density. The experimental results for compressive static test at ambient temperature provide the material properties, including compressive Young’s modulus, ultimate compressive strength, and strain percentage at the maximum load.

## **4.2 Finite element analysis**

This section presents the results of FEA using the implanted femur with different configurations (Figure 4.1). The FEA results were obtained by implanting cementless and cemented FG Charnley femoral prostheses in the anatomical model of the femur. The results of implanting the cementless prostheses with different geometries composed of conventional materials and FGMs were also presented. Moreover, the results of inserting the cemented prostheses made of conventional materials and FGMs with different geometries in the anatomical femur were demonstrated. The results of the presence of the circumferential cracks in the cement layer were discussed at the end of this section.

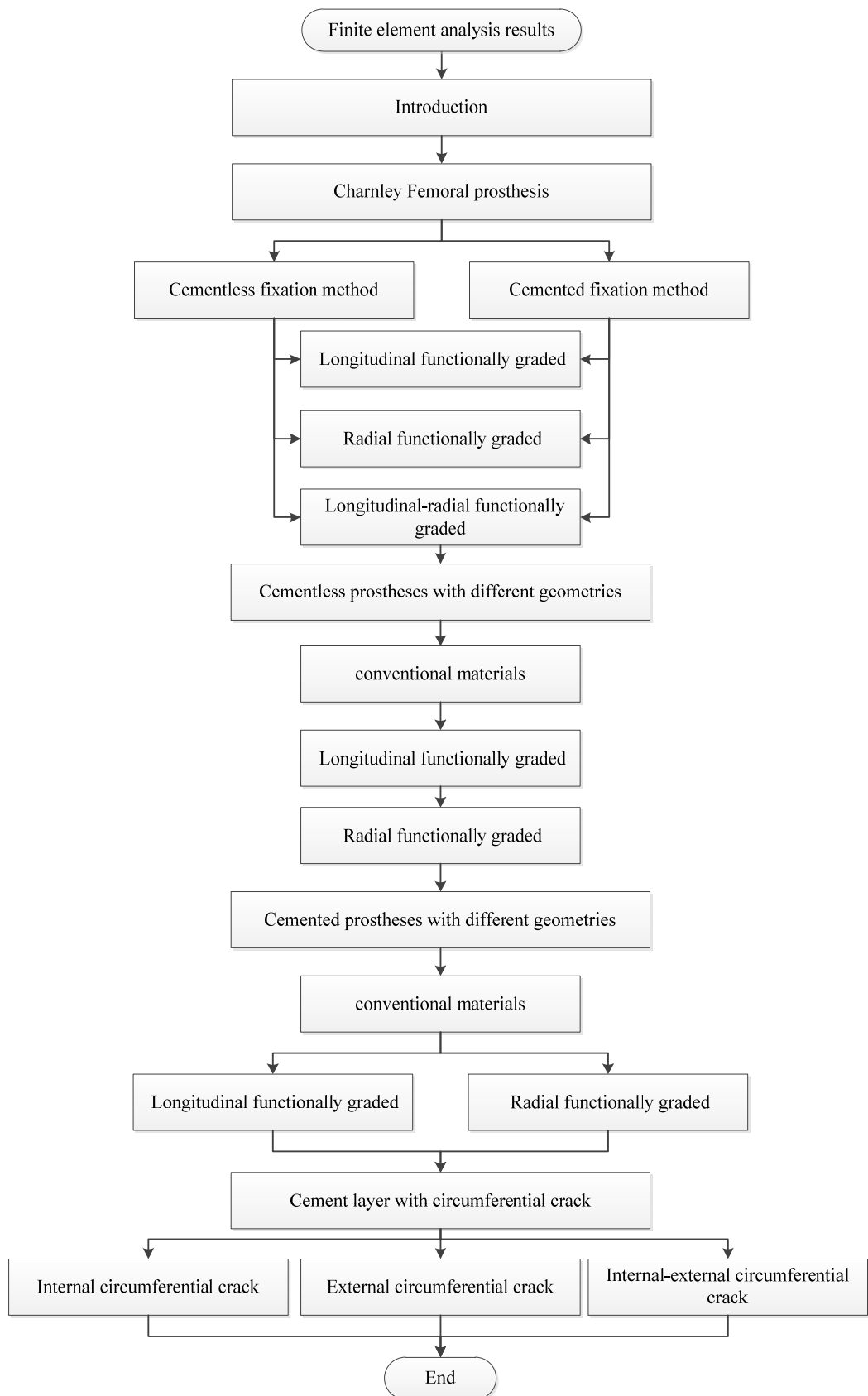


Figure 4.1: Flow chart of result presentation

#### **4.2.1 Longitudinal, radial, and longitudinal–radial FG Charnley femoral prostheses**

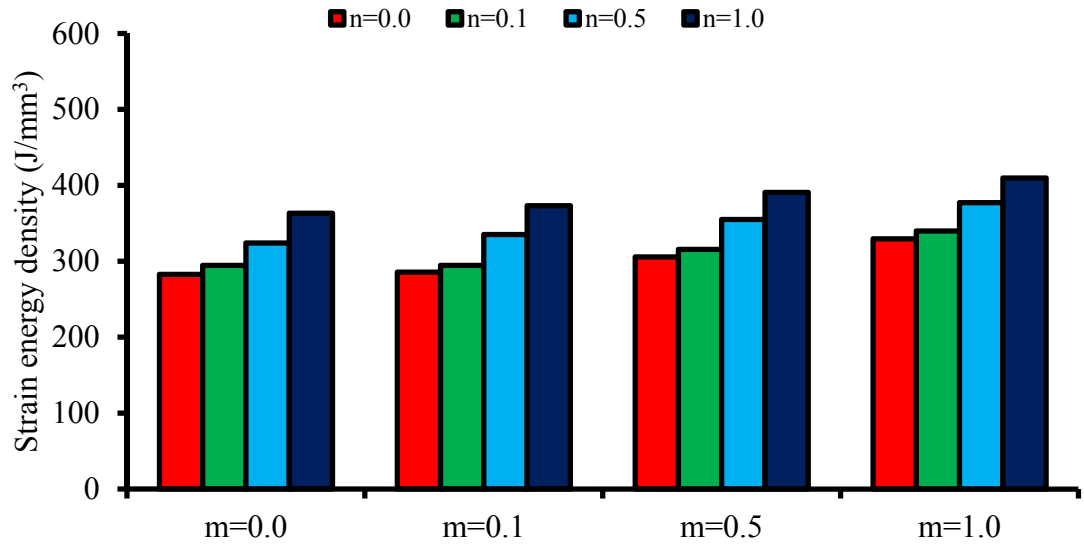
The changes in the Young's modulus of the longitudinal, radial, and longitudinal–radial Charnley femoral prostheses were investigated. In the FG longitudinal femoral prostheses (LP), the Young's modulus gradually increased from the distal to the proximal direction in the sagittal plane as shown in Figure 3.8a. Moreover, the Young's modulus of the FG radial femoral prostheses (RP) was altered in the transverse plane and gradually increased in the direction of the cortex layers to the core of the prostheses (Figure 3.8b). For the longitudinal–radial prostheses (L-RP), the Young's modulus was simultaneously altered in the sagittal and transverse planes. Thus, the stiffness of the prostheses from distal to proximal and from the cortex layer to the core simultaneously increased.

##### **4.2.1.1 Strain energy density**

Figure 4.2 shows the variation in the SED in the proximal metaphysis of the femur implanted with different FG femoral prostheses. SED is illustrated in four different bar charts according to the action models (normal walking and stair climbing) and the fixation methods of the prostheses inside the bone (cemented and non-cemented). The horizontal and vertical axes in the bar charts depict the variation in the gradient index in the longitudinal direction and SED ( $J/mm^3$ ), respectively. The legend indicates the changes in the gradient indices in the radial direction. SED exhibited an increasing trend with the longitudinal and radial gradient index, regardless of the action and fixation method. As indicated in each graph, the prostheses with longitudinal and radial gradient indices equal to 0 showed the lowest SED in the bone, whereas those equal to 1 demonstrated the highest SED. The SED minimum values of 282.8 (cemented prosthesis, normal walking), 288.0 (cementless prosthesis, normal walking), 303.1

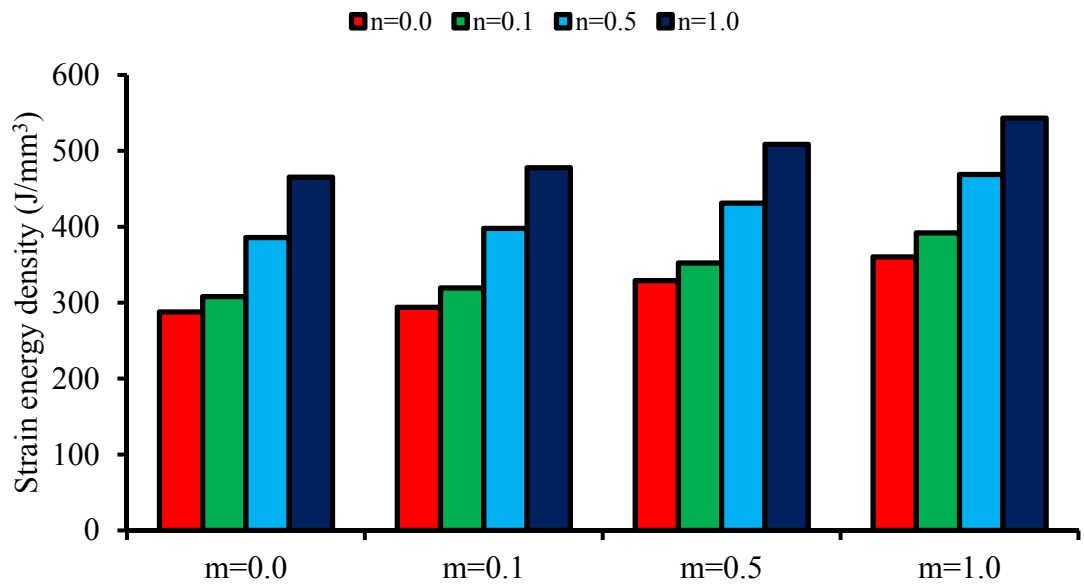
(cemented prosthesis, stair climbing), and  $304.1 \text{ J/mm}^3$  (cementless prosthesis, stair climbing) increased to the maximum values of 409.7, 543.1, 434.0, and  $545.3 \text{ J/mm}^3$ , respectively, when the gradient index increased from 0 to 1. This finding was consistent with the adverse relationship between prosthesis stiffness and induced SED to the bone. Composite beam theory and Equations (2.1) to (2.3) indicate that more loads are induced to the other components of THR when the prosthesis stiffness decreases. Thus, higher SED is developed in the bone. The effect of the increase in the radial gradient index on SED was higher than that of the longitudinal gradient index. For example, in cementless prosthesis during normal walking, when the radial gradient index ( $n$ ) was 0 and the longitudinal gradient index ( $m$ ) increased from 0 to 1, SED increased from  $288.0 \text{ J/mm}^3$  to  $360.3 \text{ J/mm}^3$ . However, when  $m = 0$  and  $n$  increased from 0 to 1, SED increased from  $288.0 \text{ J/mm}^3$  to  $465.4 \text{ J/mm}^3$ . In the cemented prosthesis, a portion of load was carried and damped by the cement. Therefore, lower loads were transferred to the bone. Thus, the cementless FG prostheses produced 11.8% higher SED than the cemented prosthesis during normal walking and stair climbing. Moreover, normal walking provided lower loads to the components of the artificial hip joints. Accordingly, the SED in the femur was lower during normal walking [ $409.7$  (cemented prosthesis) and  $543.1 \text{ J/mm}^3$  (cementless prosthesis)] than that during stair climbing [ $434.0$  (cemented prosthesis) and  $545.3 \text{ J/mm}^3$  (cementless prosthesis)].





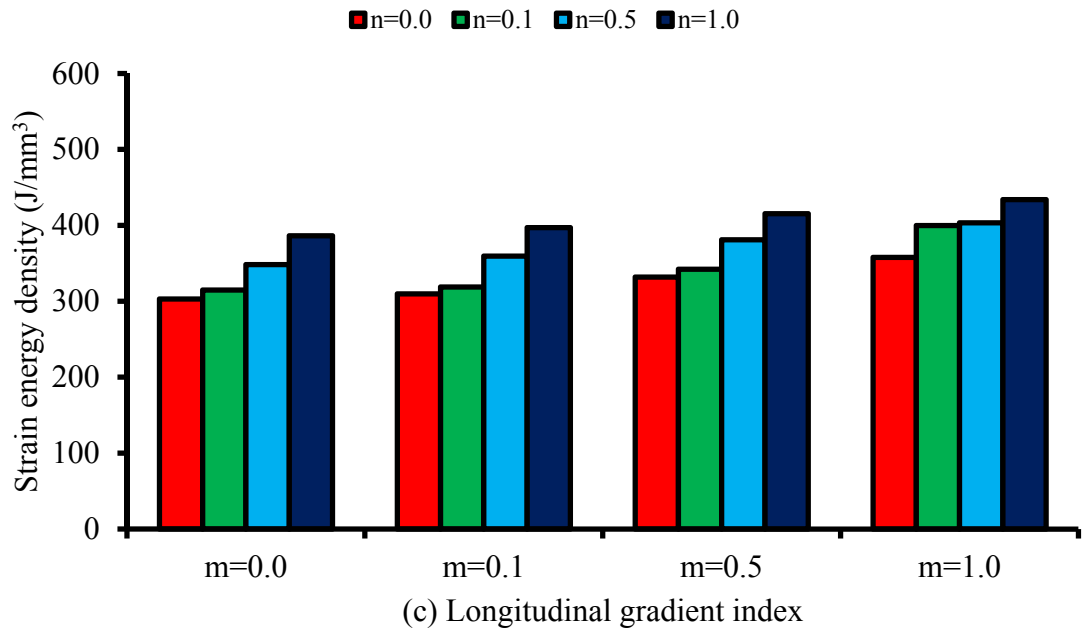
(a) Longitudinal gradient index

$n$  is the radial gradient index

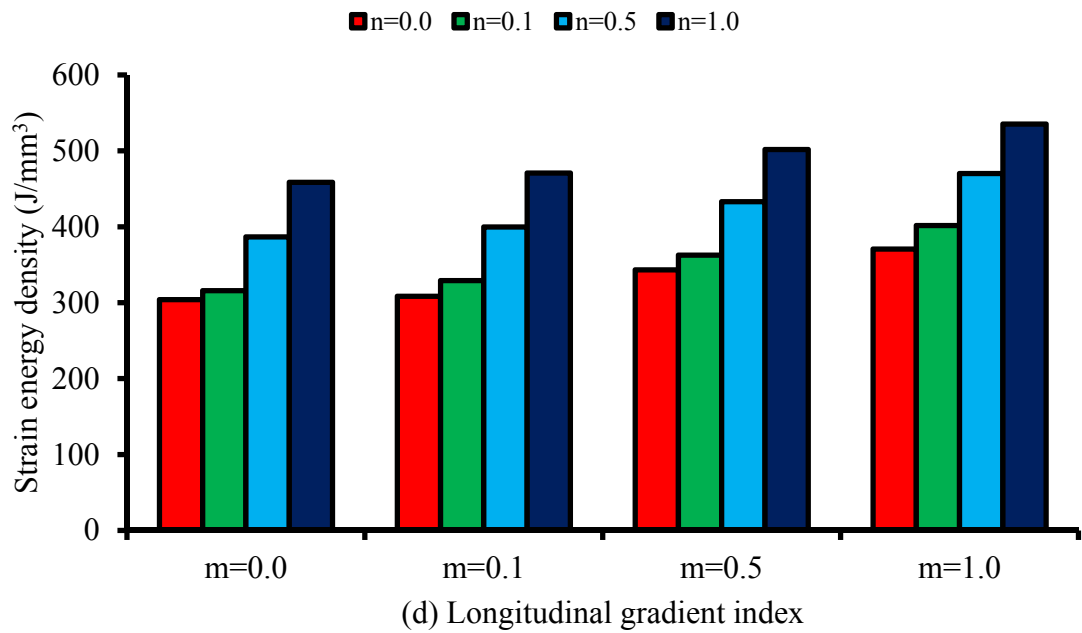


(b) Longitudinal gradient index

$n$  is the radial gradient index



$n$  is the radial gradient index

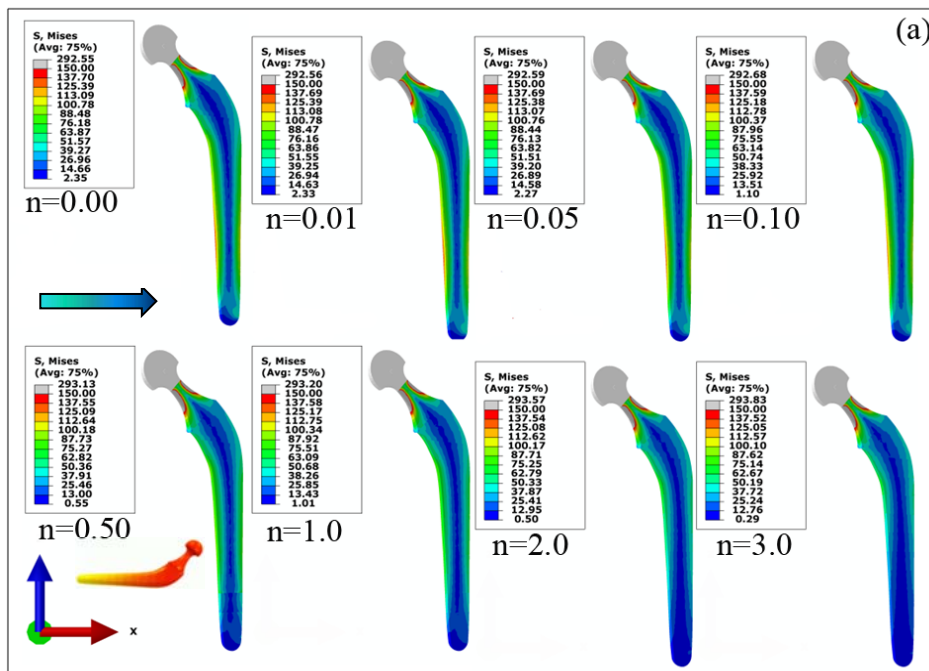


$n$  is the radial gradient index

Figure 4.2: Strain energies in the spongy portion of the proximal metaphysis of the femur caused by implantation of (a) normal walking–cemented, (b) normal walking–non-cemented, (c) stair climbing–cemented, and (d) stair climbing–non-cemented prostheses. (The legend shows the changes in the radial volume fraction gradient exponent)

### 4.2.1.2 Femoral prosthesis stress

Figure 4.3a shows the changes in the stress inside LP caused by increasing the gradient index ( $n$ ) from 0.0 to 3.0. The increase in the gradient index in LP caused the unloading of the distal portion of the prostheses and thus decreased the maximum von Mises stress in the stem. Moreover, in RP (Figure 4.3b), the stress from the cortex layer shifted to the core of the FG RP because of the increase in the gradient index. The difference in the stress distribution in the RP and LP was caused by the changes in their stiffness. Moreover, the increase in the gradient index changed the stress in the neck of LP, which was similar to that observed in RP.



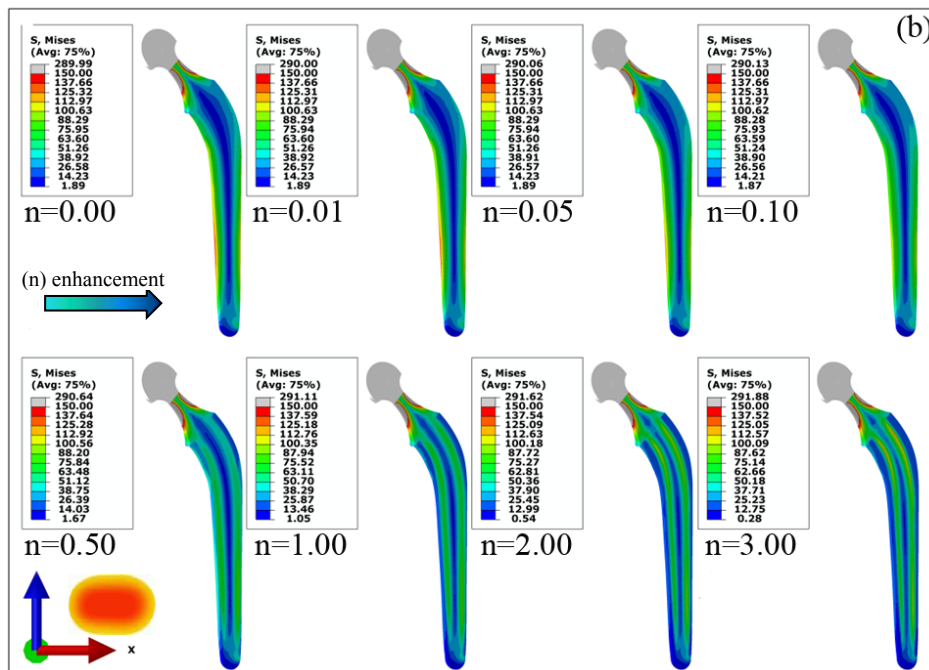


Figure 4.3: Variation in the von Mises stress in the prosthesis as a function of volume fraction gradient exponent in the non-cemented (a) longitudinal and (b) radial prostheses

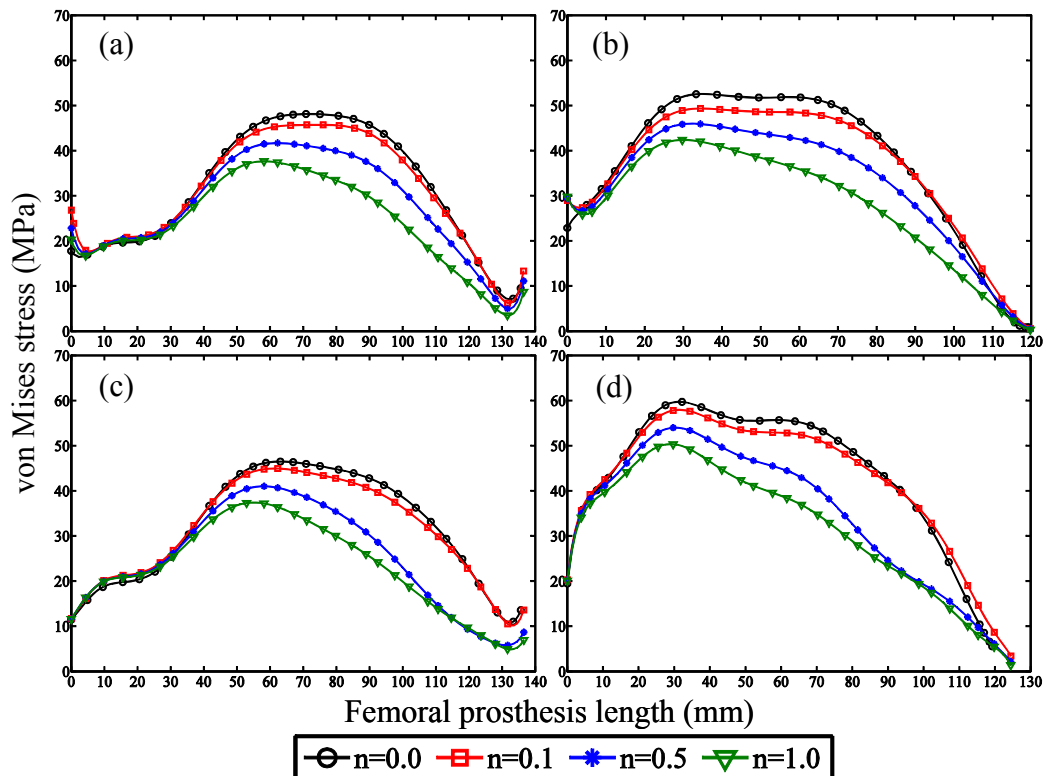


Figure 4.4: Stress variations in the longitudinal femoral prosthesis during normal walking at the (a) lateral and (b) medial sides of cemented prosthesis as well as at the (c) lateral and (d) medial sides of the cementless prosthesis

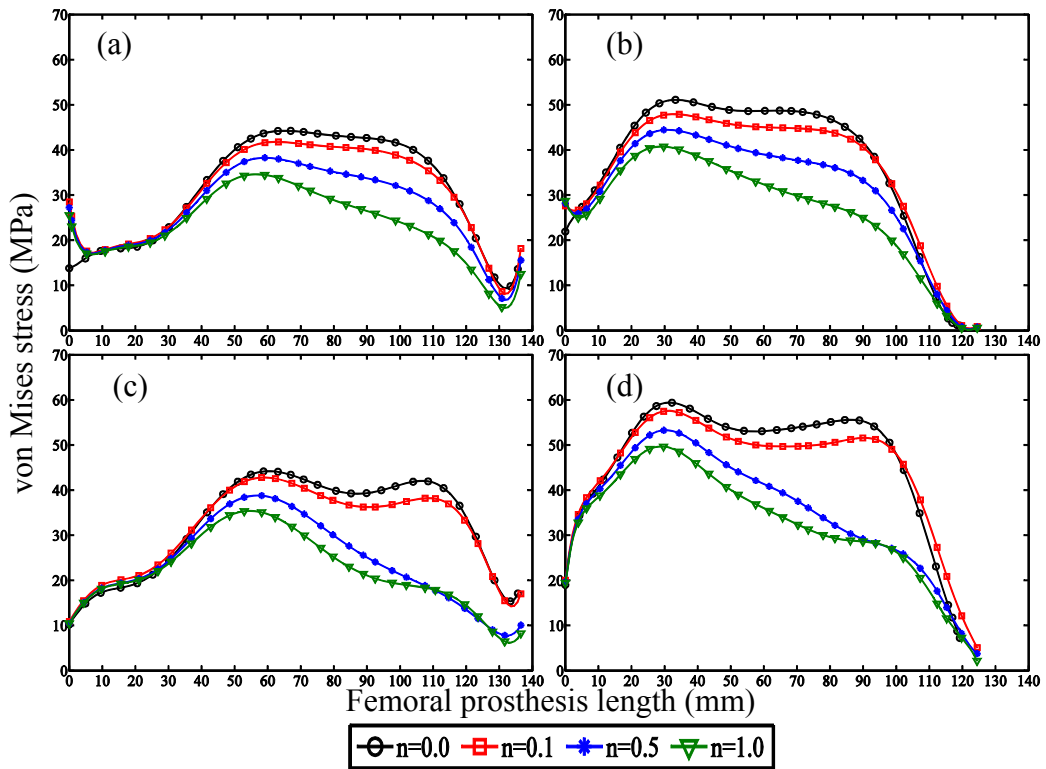


Figure 4.5: Stress variation in the longitudinal femoral prosthesis in stair climbing at the (a) lateral and (b) medial sides of the cemented prosthesis as well as at the (c) lateral and (d) medial sides of the cementless prosthesis

Figures 4.4 and 4.5 depict the stress variation at the lateral and medial sides of LP as a function of the prosthesis length. The stress variation during normal walking and stair climbing showed a similar trend with the increasing prosthesis length. Concave plots for different gradient indices were observed, whereas the peak value of the stress decreased with the increase in the gradient index. For example, in the longitudinal cemented prosthesis under normal walking, the peak stress decreased from 48.9 MPa to 39.1 MPa at the lateral side and from 53.2 MPa to 43.6 MPa at the medial side. The cementless longitudinal prosthesis also showed decreased peak stresses from 47.0 MPa to 38.6 MPa (at lateral side) and from 61.1 MPa to 52.3 MPa (at medial side). The femoral prosthesis was under bending loading, and more loads were transferred at the medial side. Therefore, the medial side of the cemented and cementless femoral prostheses exhibited about 21.4% more stress than the lateral side of the femur. The peak values of the von Mises stress on the prostheses with different material models are

presented in Table 4.1. Similar to Figures 4.4 and 4.5, the stress decreased as the gradient index increased because of the reduced stiffness of the prostheses and the higher loads shared between the prostheses and the other components of THR. Accordingly, during normal walking and stair climbing, the cemented and cementless prostheses with 0 longitudinal and radial gradient indices exhibited the highest values for stress: 53.2 (cemented prosthesis, normal walking), 76.7 (cemented prosthesis, stair climbing), 61.1 (cementless prosthesis, normal walking), and 60.6 MPa (cementless prosthesis, stair climbing). However, the prostheses with radial and longitudinal gradient indices equal to 1 demonstrated the lowest values for stress: 12.1 (cemented prosthesis, normal walking), 13.7 (cemented prosthesis, stair climbing), 16.8 (cementless prosthesis, normal walking), and 16.1 MPa (cementless prosthesis, stair climbing). The cementless prostheses tolerated about 13.8% lower stress than the cemented prostheses under normal walking and stair climbing (Table 4.1).

Table 4.1: von Mises stress on femoral prosthesis (MPa)

		Lateral				Medial				
		<sup>*n</sup>	0.0	0.1	0.5	1.0	0.0	0.1	0.5	1.0
		<sup>*m</sup>								
Cemented	Normal walking	0.0	48.9	39.9	18.6	9.6	53.2	43.7	21.9	12.6
		0.1	46.7	38.7	18.2	9.5	49.4	43.5	22.0	12.5
		0.5	42.6	35.0	16.6	9.3	46.5	39.9	21.0	12.3
		1.0	39.1	33.5	15.8	9.2	43.6	37.4	20.0	12.1
	Stair climbing	0.0	51.0	42.8	21.5	12.4	76.7	36.5	29.9	16.4
		0.1	48.2	41.6	21.6	12.3	75.4	35.1	16.3	16.0
		0.5	45.3	39.1	20.6	11.9	69.7	32.1	56.9	13.7
		1.0	42.1	38.2	19.5	11.6	62.4	33.7	15.6	13.7
cementless	Normal walking	0.0	47.0	38.4	18.2	20.6	61.1	51.6	27.5	17.6
		0.1	45.9	37.7	18.3	17.5	58.6	50.4	27.1	17.9
		0.5	42.2	35.1	17.3	16.0	55.3	47.9	26.0	17.1
		1.0	38.6	32.1	16.2	16.1	52.3	45.1	24.9	16.8
	Stair climbing	0.0	44.2	36.1	17.0	14.8	60.6	51.1	27.1	17.0
		0.1	43.8	35.3	17.8	14.7	58.5	50.3	26.8	18.5
		0.5	39.9	32.7	16.0	14.8	54.6	47.6	25.7	16.3
		1.0	36.4	29.8	15.2	14.8	51.6	44.6	24.5	16.1

<sup>\*n</sup>: radial gradient index

<sup>\*m</sup>: longitudinal gradient

#### 4.2.1.3 Developed stress in the bone

Figures 4.6a, 4.6c, 4.7a, and 4.7c represent the maximum principal stresses induced by the implanted LP at the lateral side of the femur, whereas Figures 4.6b, 4.6e, 4.7c, and 4.7b show the minimum principal stresses at the medial side. Figures 4.6 and 4.7 illustrate normal walking and stair climbing, respectively. More loads were distributed at the medial side of the femur because of the nature of hip loading. The following values represented the absolute minimum principal stresses: 23.9 (cemented prosthesis, normal walking), 47.0 (cemented prosthesis, stair climbing), 11.4

(cementless prosthesis, normal walking), and 23.3 MPa (cementless prosthesis, stair climbing) at the medial side. These values were higher than their corresponding absolute maximum principal stresses: 17.9, 20.8, 10.9, and 11.2 MPa at the lateral side of the femur. The increase in the gradient index affected the stress variation at the lateral and medial sides of the femur, whereas the stress increased because more loads were distributed as a result of the reduced stiffness.

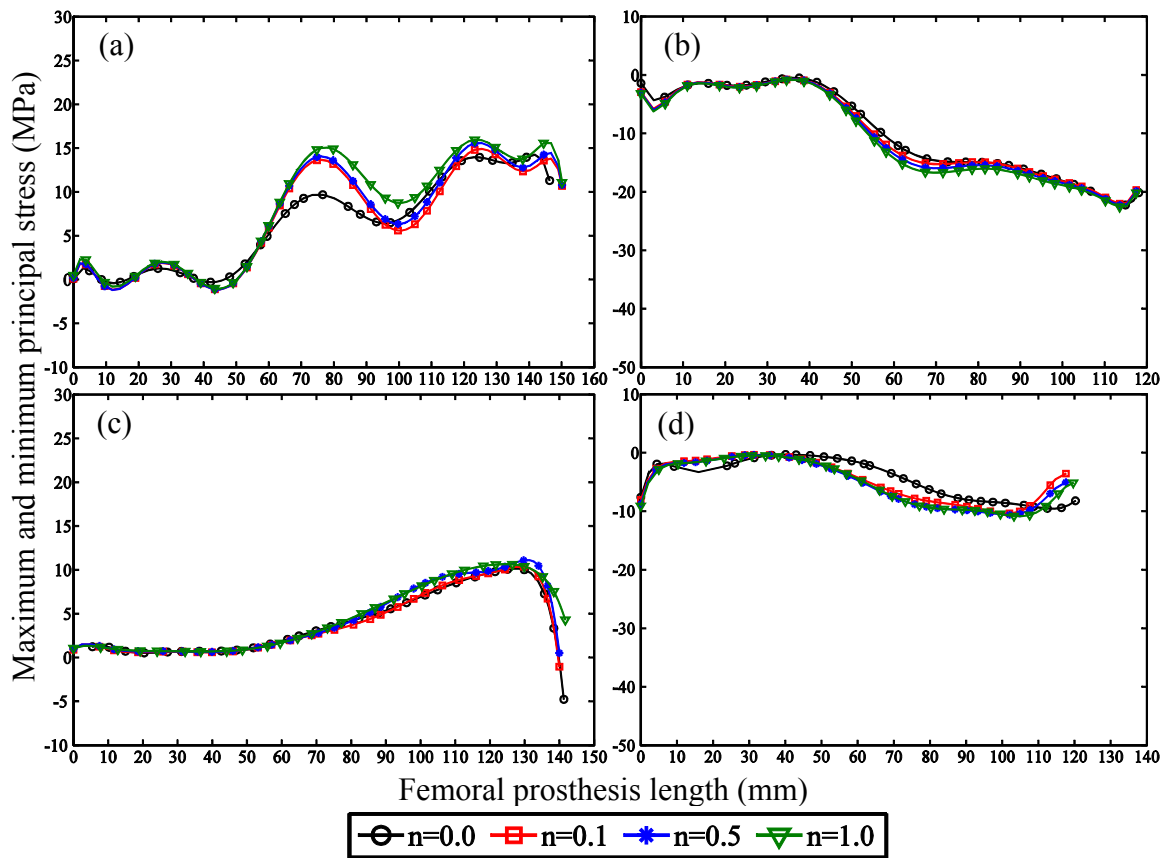


Figure 4.6: Stress variation in the femur during normal walking. (a) Maximum principal stress and cemented prosthesis, (b) minimum principal stress and cemented prosthesis, (c) maximum principal stress and cementless prosthesis, and (d) minimum principal stress and cementless prosthesis



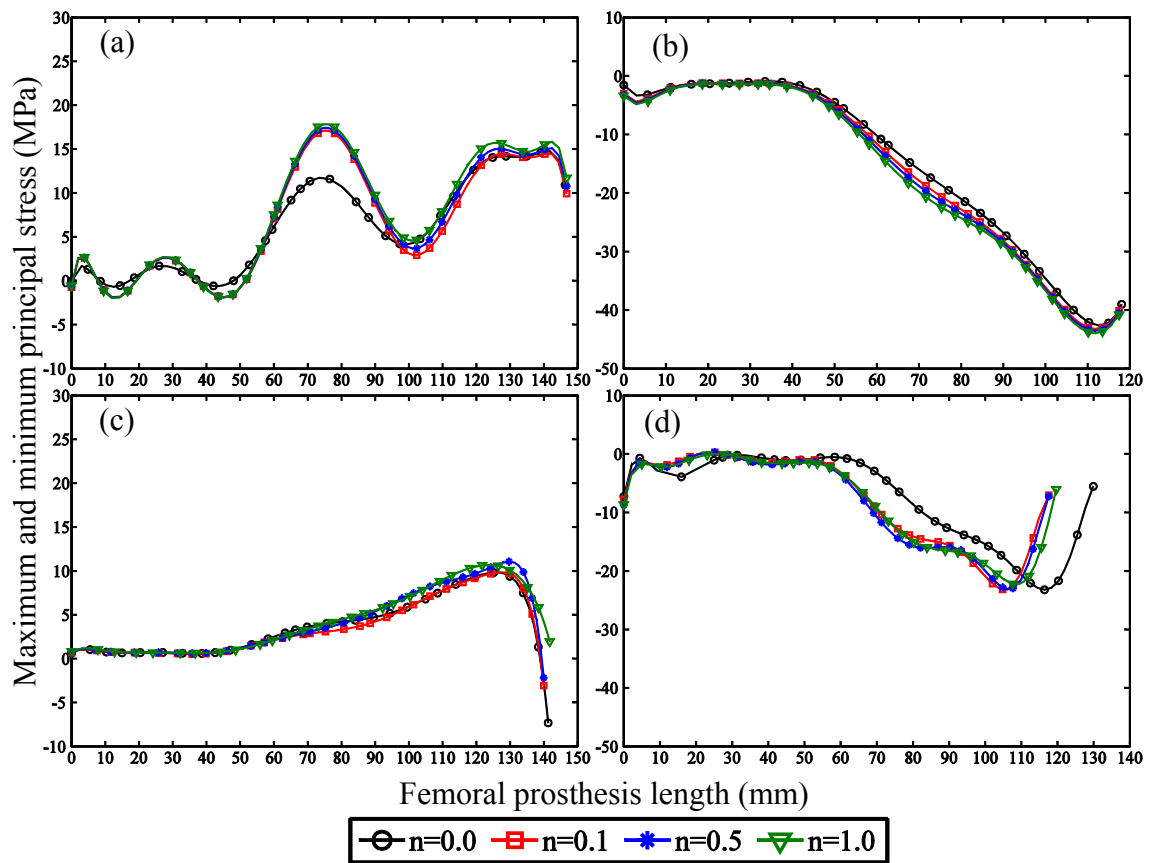


Figure 4.7: Stress variation in the femur during stair climbing. (a) Maximum principal stress and cemented prosthesis, (b) minimum principal stress and cemented prosthesis, (c) maximum principal stress and cementless prosthesis, and (d) minimum principal stress and cementless prosthesis

The peak values of the maximum and minimum principal stresses on the femur caused by the implantation of the prostheses with different material models are presented in Table 4.2. The inserted cementless FG femoral prostheses produced less stress in the femur than the cemented prostheses. The developed stress in the bone increased with the gradient index in the longitudinal, radial, and longitudinal–radial directions. The increase in the developed stress was caused by the reduced prosthesis stiffness and more equal load distribution between the bone and prosthesis. Stair climbing exhibited 36.4% more stress to the bone in the cemented and cementless implantation than normal walking. This result was attributed to the higher amount of loads distributed to the hip joint in stair climbing.

Table 4.2: Maximum and minimum principal stresses on the femur (MPa).

		Maximum principal stress				Minimum principal stress					
		Lateral				Medial					
		$*m$	$*n$	0.0	0.1	0.5	1.0	0.0	0.1	0.5	1.0
Cemented	Normal waking	0.0		16.4	16.8	18.0	18.9	23.4	24.5	24.4	24.6
		0.1		16.6	17.0	18.2	19.1	23.4	24.7	25.0	25.2
		0.5		17.2	17.5	18.7	19.5	23.6	25.0	25.2	25.4
		1.0		17.9	18.8	19.3	19.9	23.9	25.0	25.5	25.6
	Stair climbing	0.0		19.5	19.9	21.2	22.1	46.7	46.7	46.5	46.7
		0.1		19.7	20.1	21.3	22.2	46.4	47.0	47.4	47.7
		0.5		20.2	20.6	21.7	22.6	46.7	47.5	47.8	48.0
		1.0		20.8	21.3	22.2	23.0	47.0	67.5	48.1	48.2
Cementless	Normal waking	0.0		10.2	10.3	10.6	10.8	9.8	10.0	10.8	13.6
		0.1		10.4	10.4	10.5	10.6	10.9	13.9	14.5	14.9
		0.5		11.0	10.5	10.5	10.6	11.0	15.5	15.5	15.3
		1.0		10.9	10.6	10.7	10.7	11.4	15.9	15.5	15.4
	Stair climbing	0.0		10.0	10.1	10.6	10.9	25.0	25.0	25.1	25.1
		0.1		10.5	10.6	10.8	11.0	24.1	24.5	24.7	24.7
		0.5		11.5	10.9	11.0	11.0	23.8	24.1	24.4	24.6
		1.0		11.2	10.9	10.9	10.9	23.3	24.0	24.3	24.7

$*n$ : radial gradient index

$*m$ : longitudinal gradient

#### 4.2.1.4 Developed stress in the cement

The maximum principal stress variations on the internal and external surfaces of the cement layer induced by the implantation of LP during normal walking and stair climbing are presented in Figure 4.8. The peak values of stresses were observed at the distal and proximal end along the middle length of the cement layer. The peak values of the stresses on the internal and external surfaces of the cement layer increased along with gradient index during normal walking and stair climbing. The highest value of

stress in the cement layer was induced by the FG prosthesis with a gradient index of 1.0, whereas the prosthesis with gradient index of 0.0 provided the minimum stress in the cement layer.

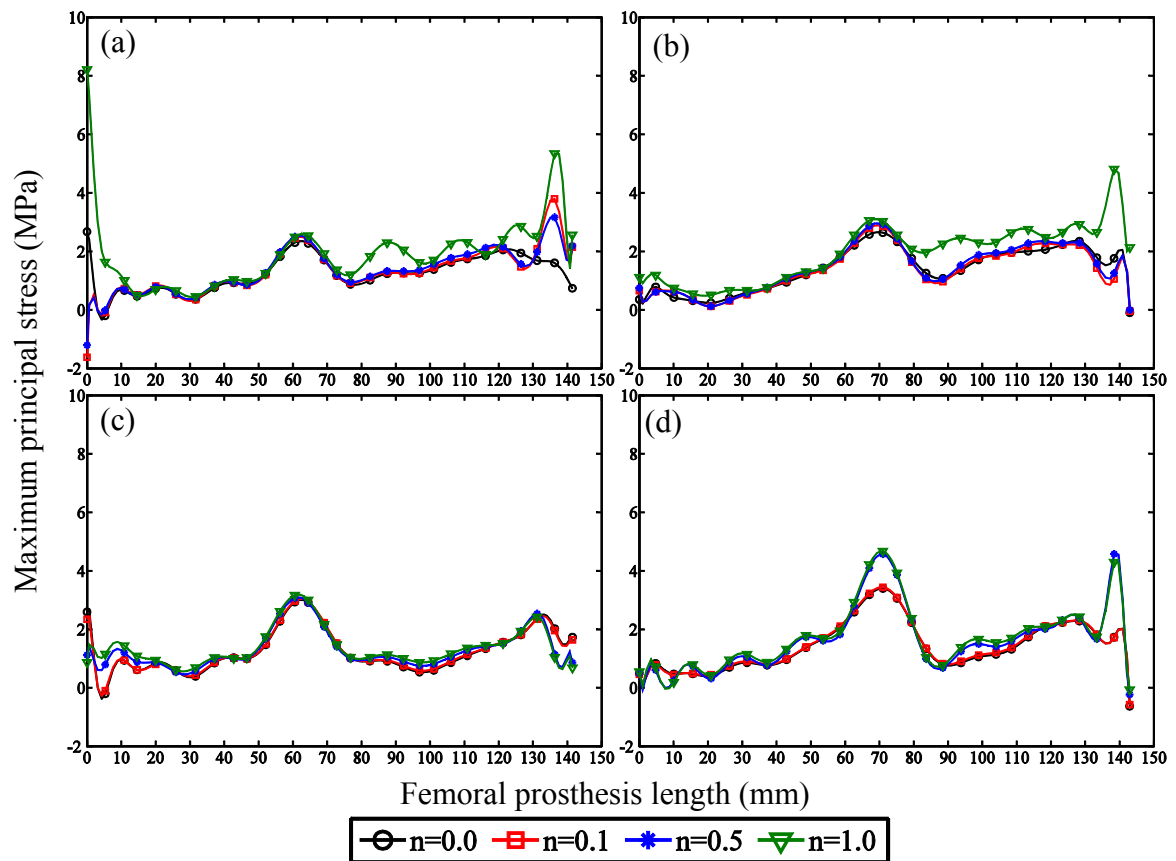


Figure 4.8: Stress variation in the cement layers during normal walking [(a) internal and (b) external layers] and stair climbing [(c) internal and (d) external layers]

Figure 4.9 displays the maximum principal stress variation on the external and the internal surfaces of the cement layer caused by implanting RP. The maximum principal stress showed similar trend along the cement length in both surfaces (internal and external surfaces) and both action models (normal walking and stair climbing). The maximum principal stress behavior in the cement was similar to the behavior induced by inserting LP.

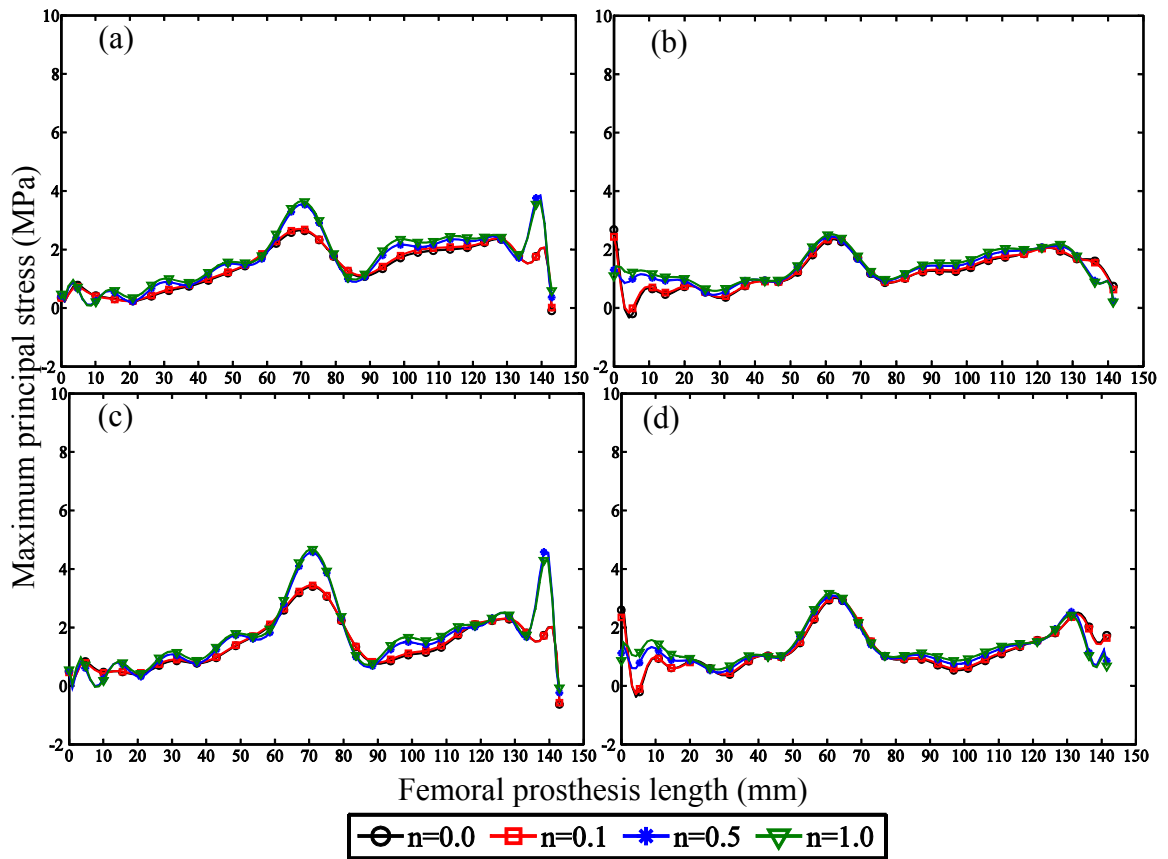


Figure 4.9: Stress variation in the cement layers during normal walking [(a) internal and external layers] and stair climbing [(c) internal and (d) external layers]

The maximum principal stresses computed on the internal and external surfaces of the cement and the peak values of the maximum principal stress calculated based on the different gradient indexes of the prostheses are presented in Table 4.3. Similar to the response of stress to the increase in the gradient index on the bone, the stress on the internal and external surfaces of the cement increased with the gradient index (Table 4.3). On the external surface of the cement layer, the stress during stair climbing was 22.3% higher than that during normal walking. However, the internal surface of the cement layer had 27.8% more stress during normal walking than that during stair climbing.

Table 4.3: Maximum principal stress on the cement (MPa)

		Internal				External			
	<sup>*n</sup>	0.0	0.1	0.5	1.0	0.0	0.1	0.5	1.0
	<sup>*m</sup>								
Normal Walking	0.0	4.5	4.6	4.8	5.0	3.6	3.7	3.8	4.0
	0.1	4.8	4.9	5.0	5.2	3.7	3.7	3.9	4.0
	0.5	4.9	5.0	5.2	5.3	3.7	3.8	3.9	4.1
	1.0	5.0	5.1	5.3	5.3	3.9	3.9	4.0	4.1
Stair Climbing	0.0	3.4	3.5	3.6	3.7	4.7	4.8	4.9	5.1
	0.1	3.5	3.5	3.6	3.7	4.7	4.8	5.0	5.1
	0.5	3.5	3.5	3.7	3.8	4.9	4.9	5.0	5.2
	1.0	3.6	3.6	3.7	3.8	5.0	5.1	5.1	5.2

<sup>\*n</sup>: radial gradient index

<sup>\*m</sup>: longitudinal gradient

#### 4.2.1.5 Interface stresses

Table 4.4 shows the interface stress levels in the implanted femur with the cemented and cementless FG femoral prostheses. In the cemented prostheses, the stresses at the prosthesis–cement and cement–bone interfaces remained constant with the increase in the gradient indices. The stress at the cement–bone interface was higher than that at the prosthesis–cement interface during normal walking and stair climbing. In the cementless FG femoral prostheses, the interface stress decreased with the increase in the gradient indices. Similar to the implanted femur with the cemented FG femoral prostheses, 26.0% higher interface stress was observed during stair climbing than that during normal walking.

Table 4.4: Interface stresses in cemented prosthesis (MPa)

	Fixation	Cemented								Cementless			
		Prosthesis–cement				Cement–bone				Bone–prosthesis			
	$*n$	0	0.1	0.5	1.0	0.0	0.1	0.5	1.0	0	0.1	0.5	1.0
Normal Walking	$*m$ 0.0	1.5	1.5	1.6	1.6	1.6	1.7	1.7	1.7	8.3	8.1	7.0	6.4
	0.1	1.5	1.5	1.6	1.6	1.6	1.7	1.7	1.7	7.1	7.1	6.1	5.6
	0.5	1.5	1.5	1.6	1.6	1.7	1.7	1.7	1.7	6.5	5.9	5.1	4.6
	1.0	1.6	1.6	1.6	1.6	1.7	1.6	1.7	1.7	5.4	4.5	4.0	3.7
Stair Climbing	0.0	1.7	1.7	1.7	1.7	2.2	2.3	2.3	2.3	10.9	10.9	10.1	9.2
	0.1	1.7	1.7	1.7	1.7	2.3	2.3	2.3	2.3	9.9	9.6	9.0	8.7
	0.5	1.7	1.7	1.7	1.7	2.3	2.2	2.3	2.3	9.5	9.2	8.0	7.0
	1.0	1.7	1.7	1.7	1.7	2.3	2.3	2.3	2.3	7.3	6.8	5.6	3.6

$*n$ : radial gradient index

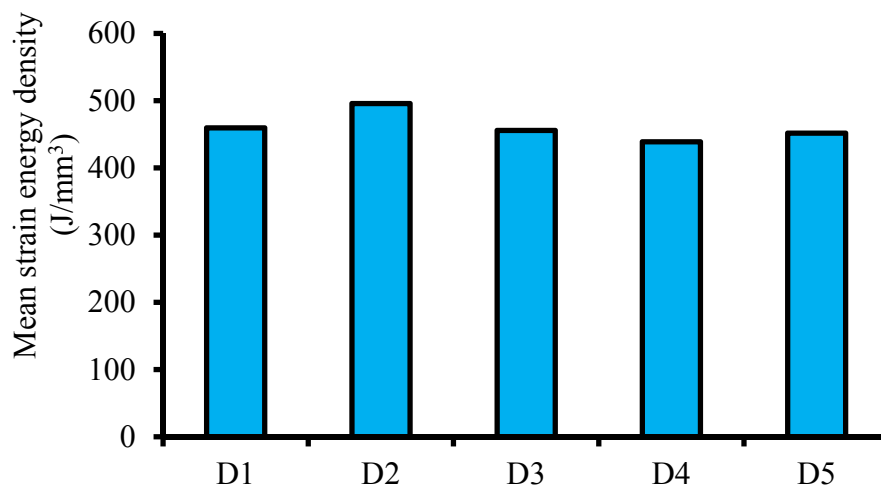
$*m$ : longitudinal gradient

## 4.2.2 Cementless prostheses with conventional materials

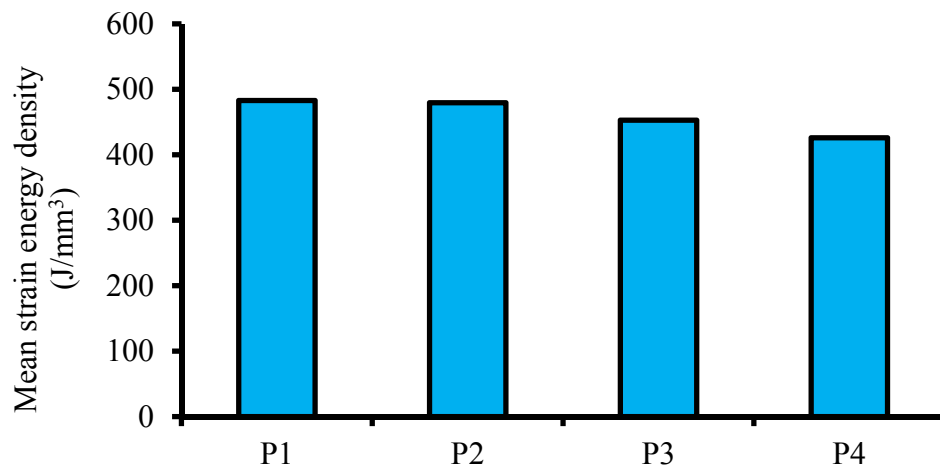
This section presents the results of FEA on the cementless prostheses composed of conventional materials (St and Ti). The simplified model of the femur was used in this study.

### 4.2.2.1 Strain energy density

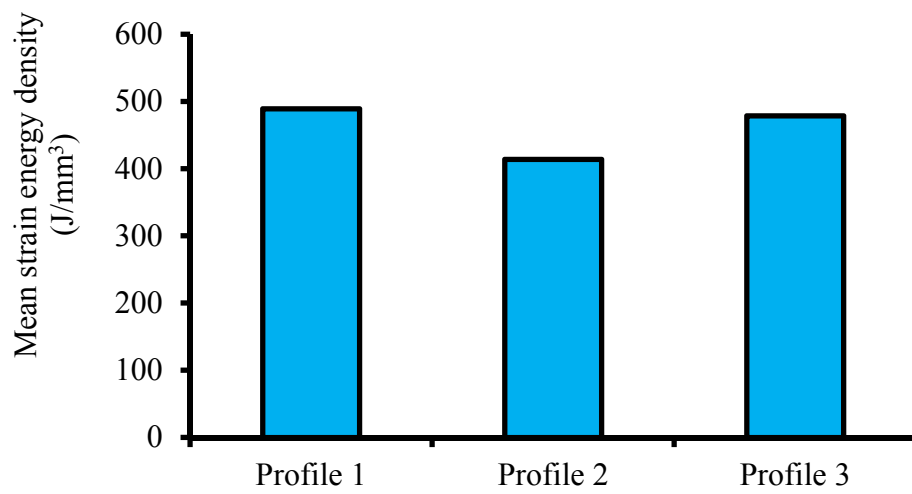
SED variation for the cementless prostheses composed of conventional materials, such as St and Ti, is presented in Figure 4.10. The rigidity of the prosthesis is a function of the prosthesis cross section and material. Thus, the SED at the proximal metaphysis of the femur depended on the geometrical parameters and the materials of prosthesis. The Ti-based prostheses (533.38 J/mm<sup>3</sup>) with geometrical specifications of D2 distal cross section (496.03 J/mm<sup>3</sup>), P1 proximal cross section (483.14 J/mm<sup>3</sup>), and Profile 1 (489.17 J/mm<sup>3</sup>) provided the highest SED in the bone. However, the minimum SED was induced to the bone by the St-based prosthesis (387.59 J/mm<sup>3</sup>) with geometrical features of D4 distal cross section (438.95 J/mm<sup>3</sup>), P4 proximal cross section (426.21 J/mm<sup>3</sup>), and Profile 2 (413.73 J/mm<sup>3</sup>).



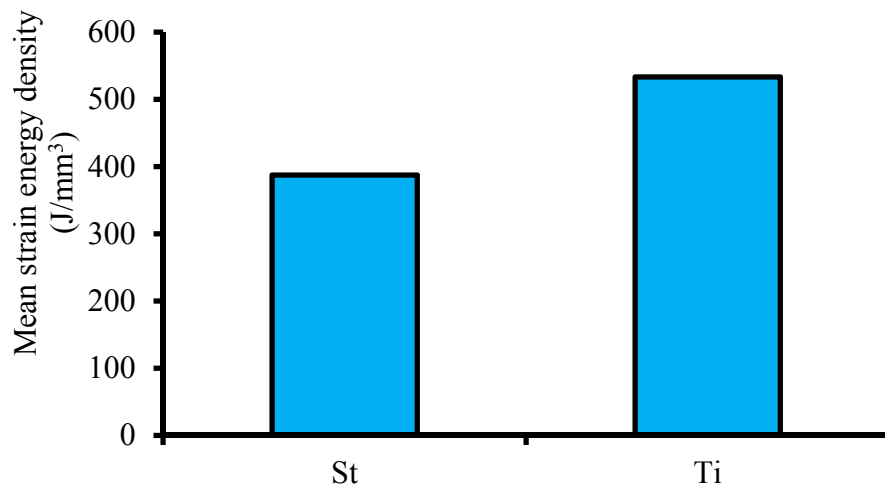
(a) Distal cross-section of prosthesis



(b) Proximal cross-section of prosthesis



(c) Profile of prosthesis



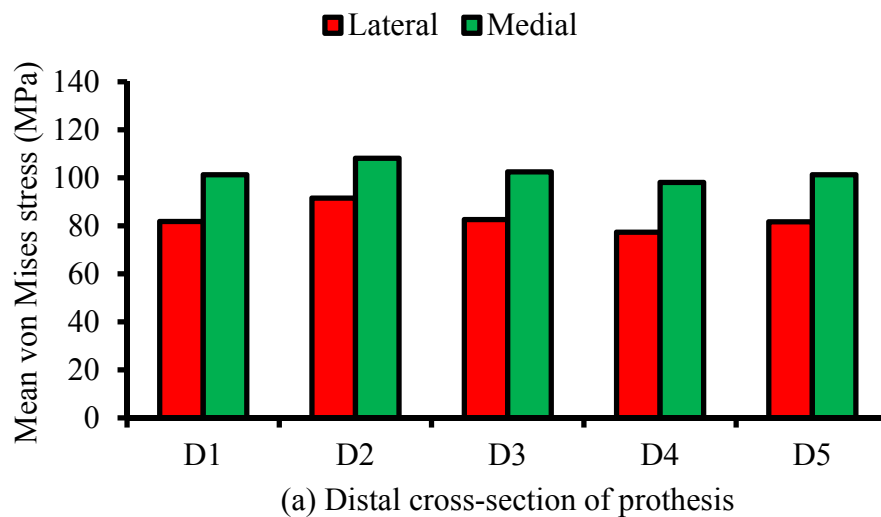
(d) Material of prosthesis

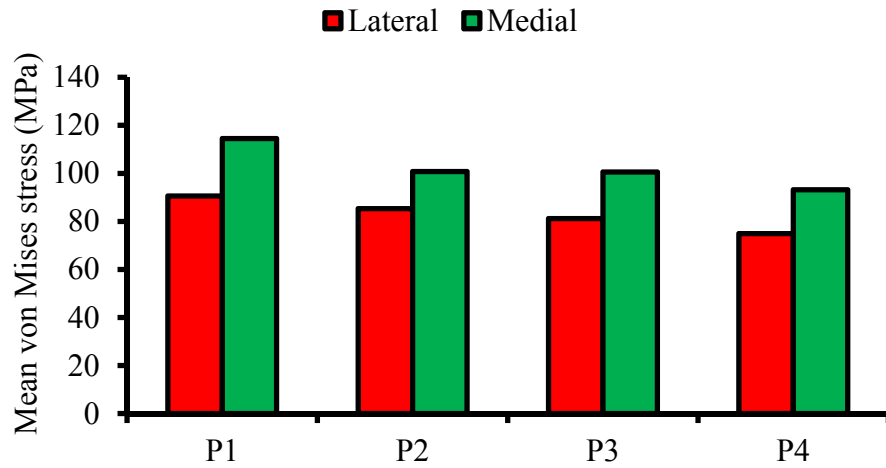
Figure 4.10: Strain energy density as a function of (a) distal cross section, (b) proximal cross section, (c) profile, and (d) material composition



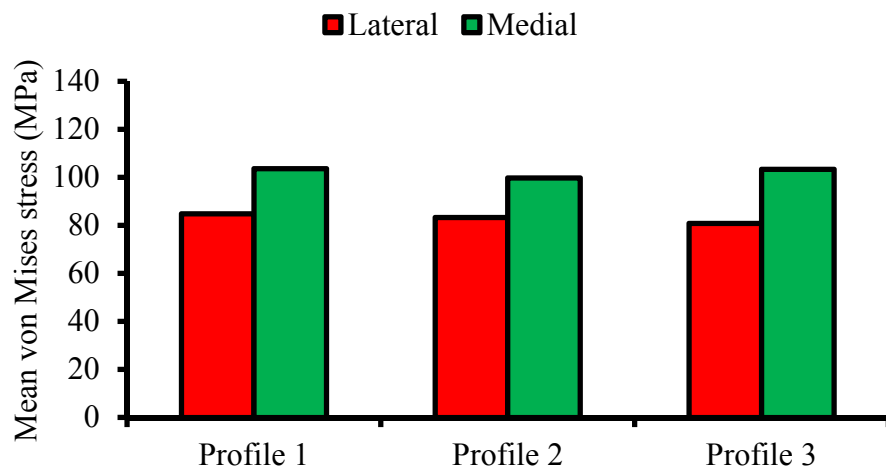
#### 4.2.2.2 Developed stress in the prostheses

Figure 4.11 represents the mean value of the maximum von Mises stress developed in the St- and Ti-based cementless prostheses. Similar to the developed stress in the Charnley femoral prostheses, higher von Mises stresses were exerted at the medial side of the prostheses than at their lateral side (Figure 4.11). Distal and proximal cross sections had 12.4% and 18.0% effect, respectively, on the developed stress in the prostheses compared with the profiles with 4.2% effect. Moreover, the Ti-based prostheses with lower stiffness carried less stress at the lateral and medial sides than St-based prostheses because more loads were shared with the femur. The mean values of the developed stress in the Ti-based prostheses were 60.71 and 79.05 MPa at the lateral and medial sides, respectively, whereas those composed of ST were 105.31 and 125.51 MPa, respectively.

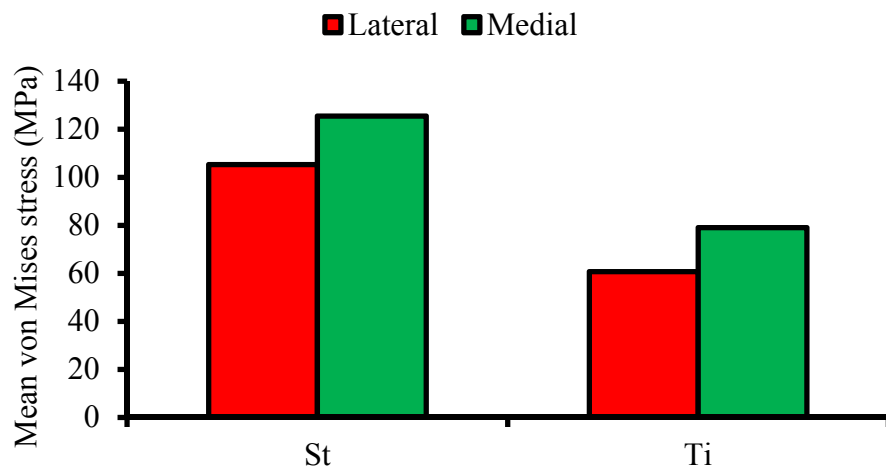




(b) Proximal cross-section of prosthesis



(c) Profile of prosthesis

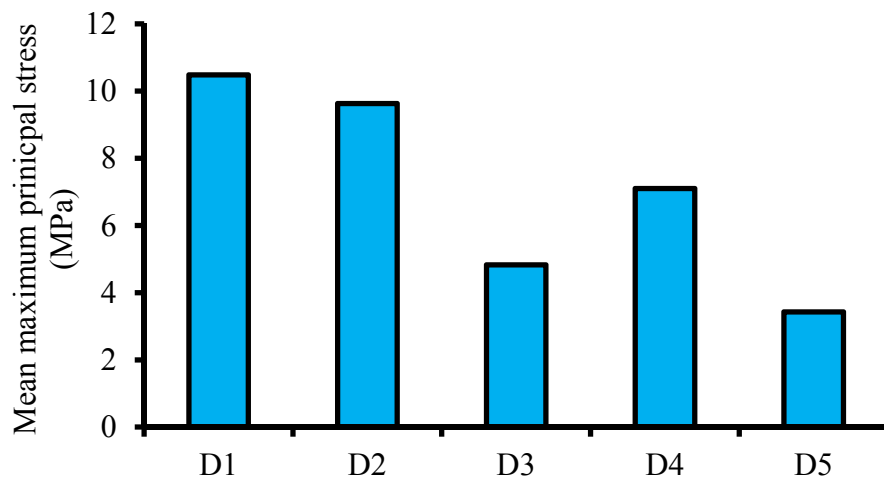


(d) Material of prosthesis

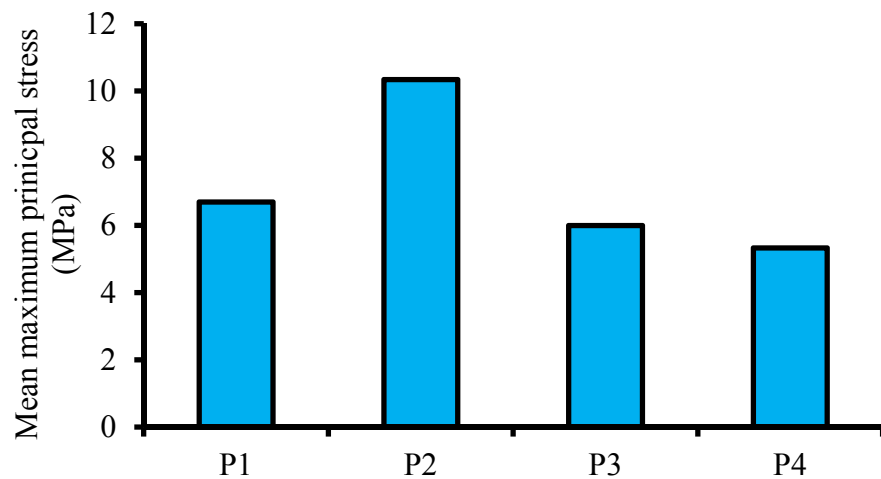
Figure 4.11: Variation in the mean von Mises stress variation as a function of (a) distal cross section, (b) proximal cross section, (c) profile, and (d) material composition

### 4.2.2.3 Developed stress to the bone

Figure 4.12 shows the mean values of the maximum principal stresses, whereas Figure 4.13 illustrates the minimum principal stresses in the simplified model of the femur. The maximum and minimum principal stresses were significantly affected by geometrical parameters and material composition. The profile and material effects on the minimum principal stress were lower than those of the other factors. The average differences between the maximum and minimum principal stresses caused by the changes in the distal cross sections, proximal cross sections, profiles, and materials were 55.9%, 50.7%, 6.0%, and 17.5%, respectively.



(a) Distal cross-section of prosthesis



(b) Proximal cross-section of prosthesis

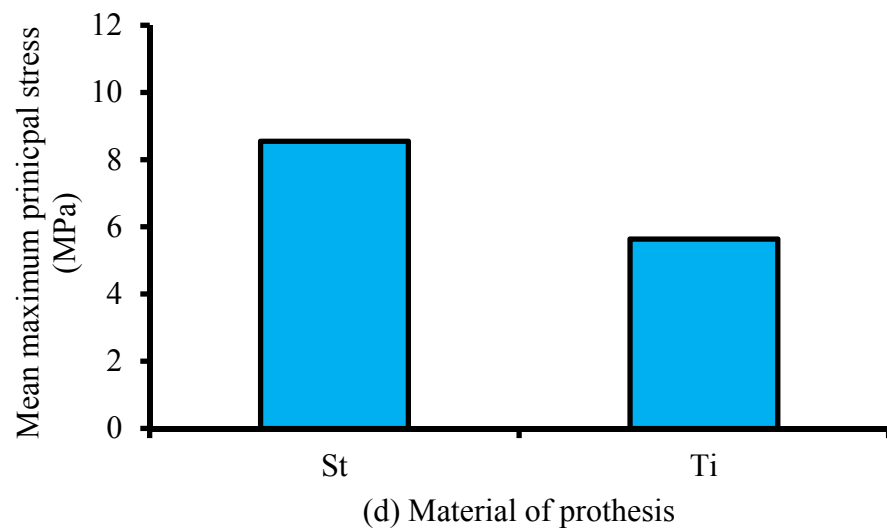
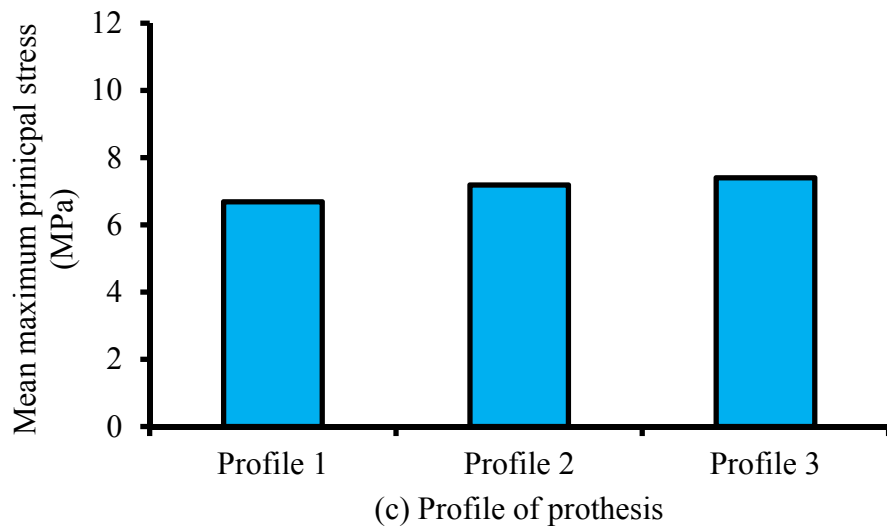
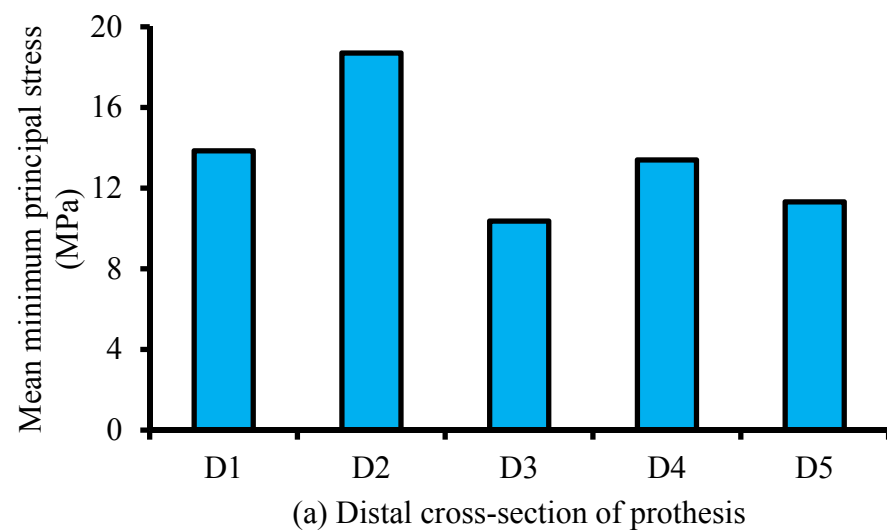
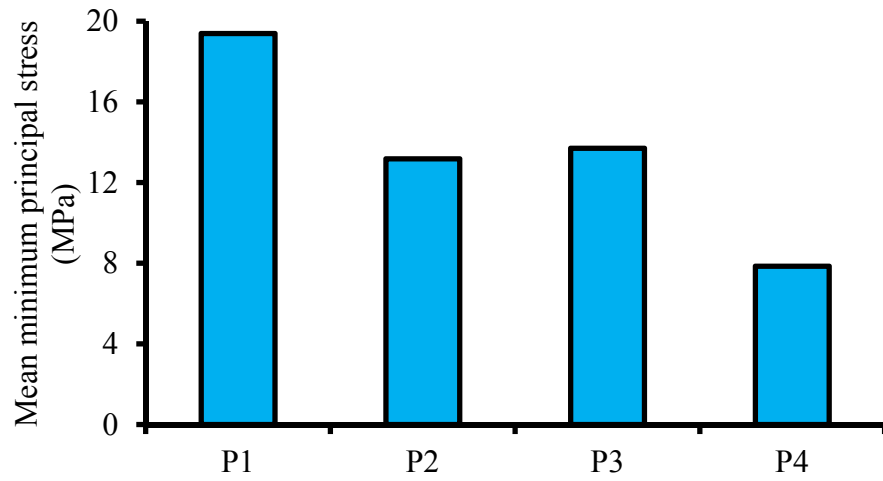
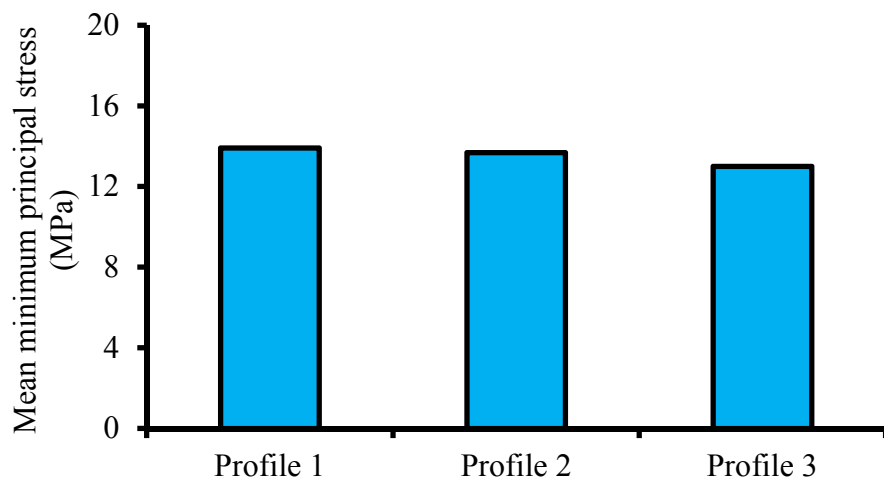


Figure 4.12: Variation in the mean maximum principal stress as a function of (a) distal cross section, (b) proximal cross section, (c) profile, and (d) material composition

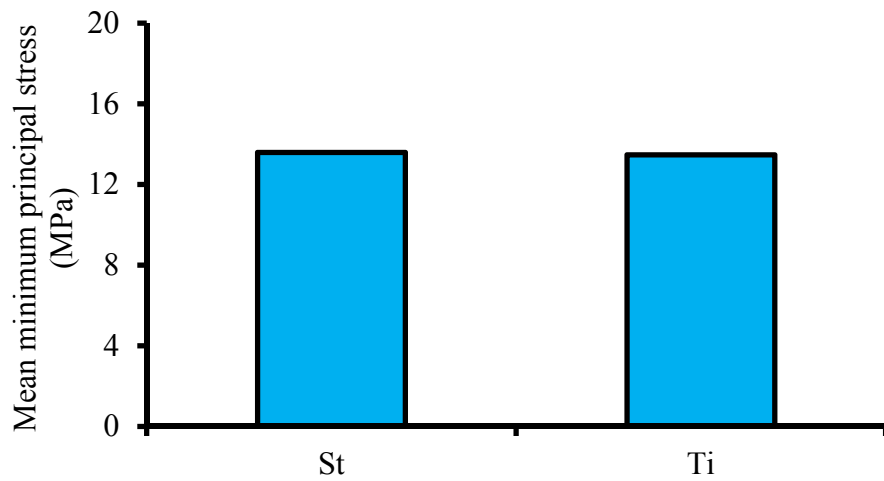




(b) Proximal cross-section of prosthesis



(c) Profile of prosthesis



(d) Material of prosthesis

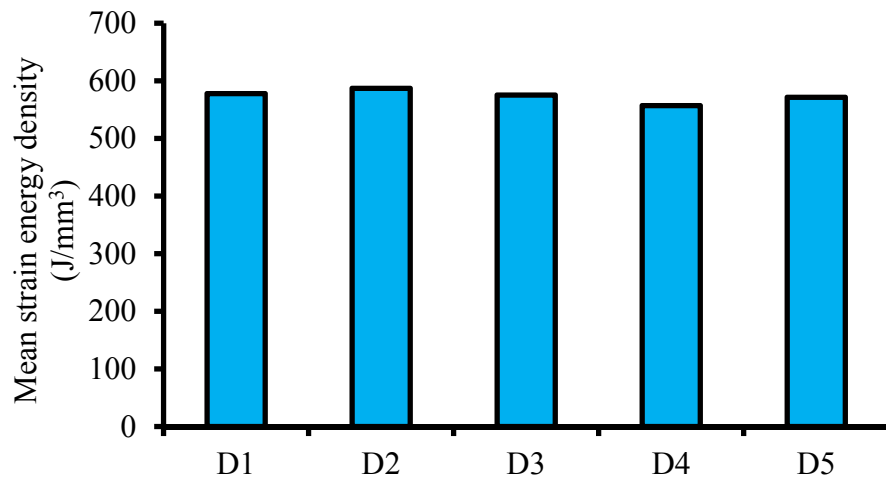
Figure 4.13: Variation in the mean minimum principal stress variation as a function of (a) distal cross section, (b) proximal cross section, (c) profile, and (d) material composition

### **4.2.3 Cementless longitudinal functionally graded femoral prosthesis with different geometries**

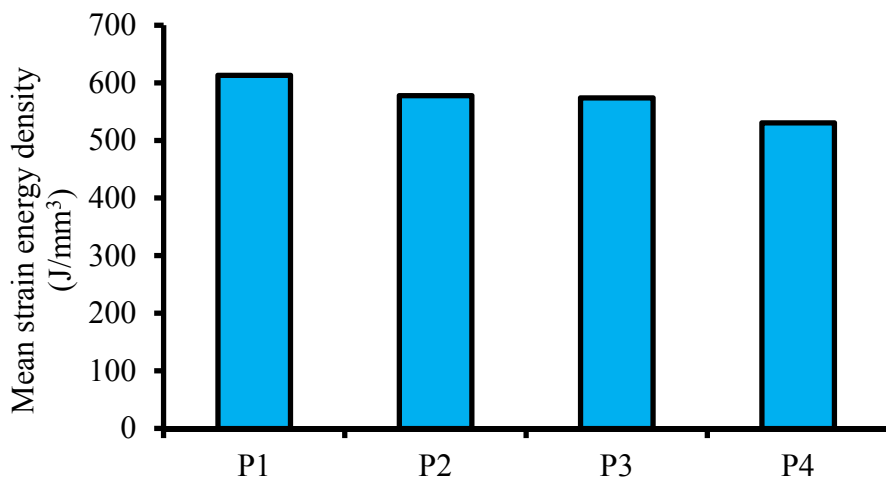
The results of applying FGMs in the femoral prostheses with different geometries are presented in the following sections. The Young's modulus changes in the sagittal plane, and the prostheses geometry is composed of five different distal cross sections, four different proximal cross sections, and three different profiles. The simplified model of the femur was used in this FEA.

#### **4.2.3.1 Strain energy density**

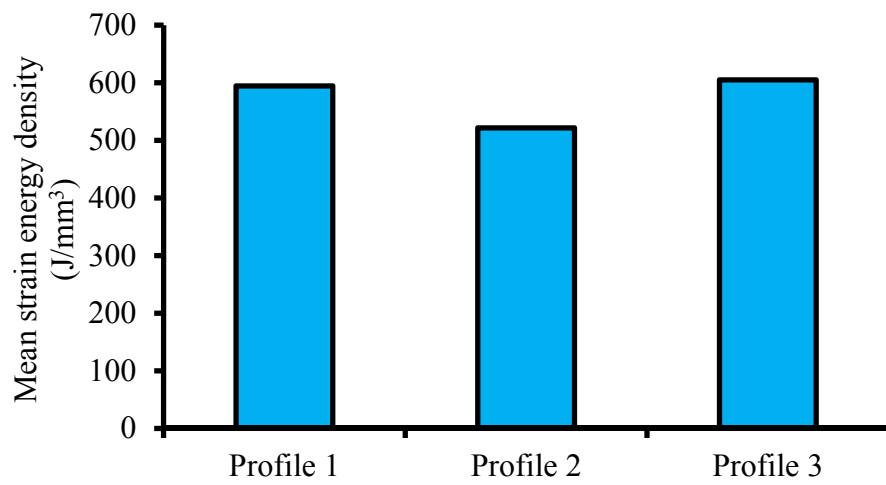
Figure 4.14 illustrates the SED variation at the proximal metaphysis of the femur for five distal cross-sections, four proximal cross-sections, three profiles, two implant–bone interface conditions, and four gradient indices. The distal cross-sections showed minor effect of 5.2% on SED variation (Figure 4.14a). The prostheses with proximal cross-sections of P1 and P4 produced maximum ( $612.96 \text{ J/mm}^3$ ) and minimum ( $530.69 \text{ J/mm}^3$ ) amount of SED, respectively, on the proximal metaphysis of femur (Figure 4.14b). The prostheses with proximal cross-sections of P2 and P3 induced almost the same SEDs of approximately  $575.84 \text{ J/mm}^3$  in the bone, which was at the mid-range of the SED generated by the prostheses with P1 and P4 proximal cross-sections (Figure 4.14b). The prostheses developed from Profiles 1 and 3 provoked almost the same SEDs of about  $599.82 \text{ J/mm}^3$ , which was 13.0% more than the SED induced by the prostheses with Profile 2 ( $521.87 \text{ J/mm}^3$ ) (Figure 4.14c). The implant–bone surface property showed insignificant effect of 0.6% on the SED variation (Figure 4.14d). The SED increased by approximately 20.2% with the increase in gradient index from 0 to 1 (Figure 4.14e).



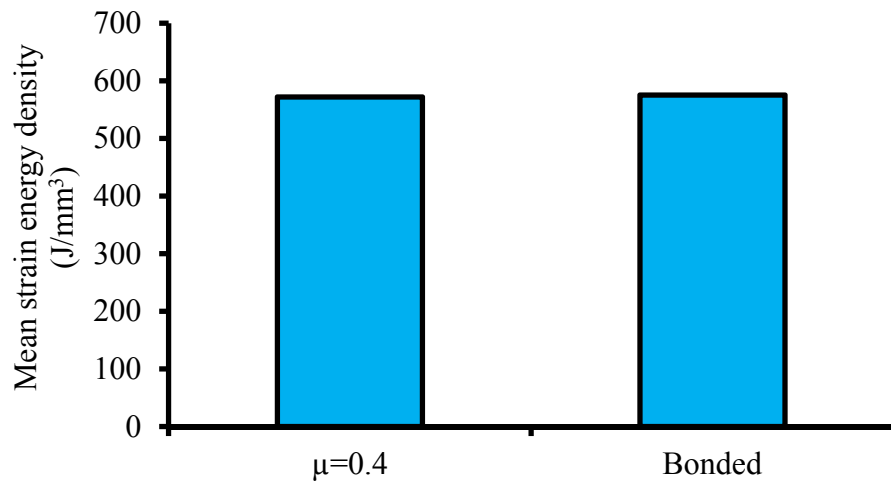
(a) Distal cross-section of prosthesis



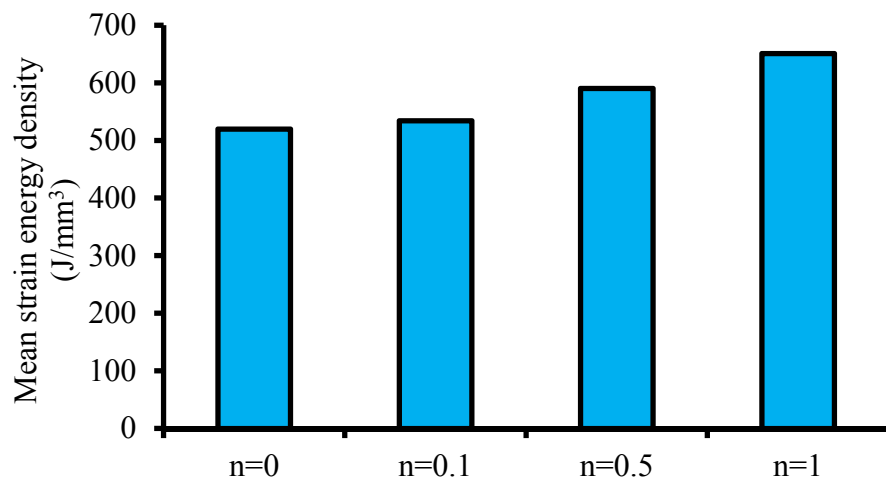
(b) Proximal cross-section of prosthesis



(c) Profile of prosthesis



(d) Interface property



(e) Gradient index

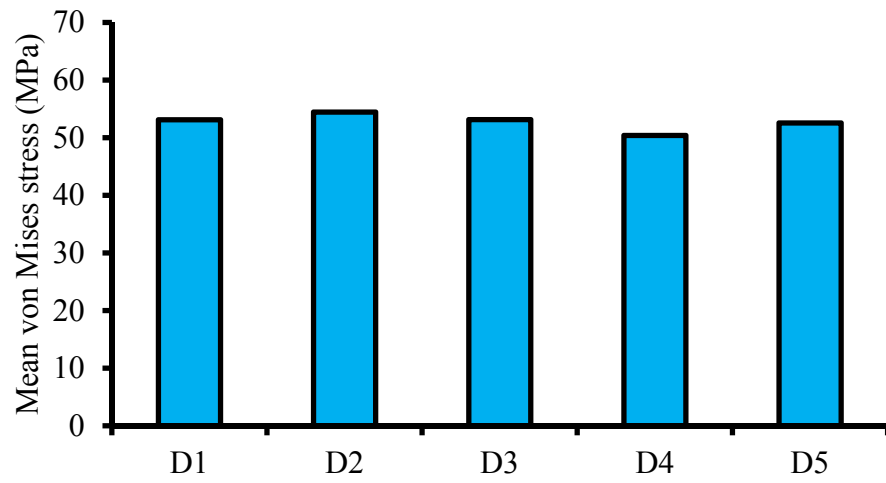
Figure 4.14: Variation in the mean strain energy variation for the different (a) distal cross-sections, (b) proximal cross-sections, (c) profiles, (d) interface properties, and (e) gradient indices

#### 4.2.3.2 Prostheses stress

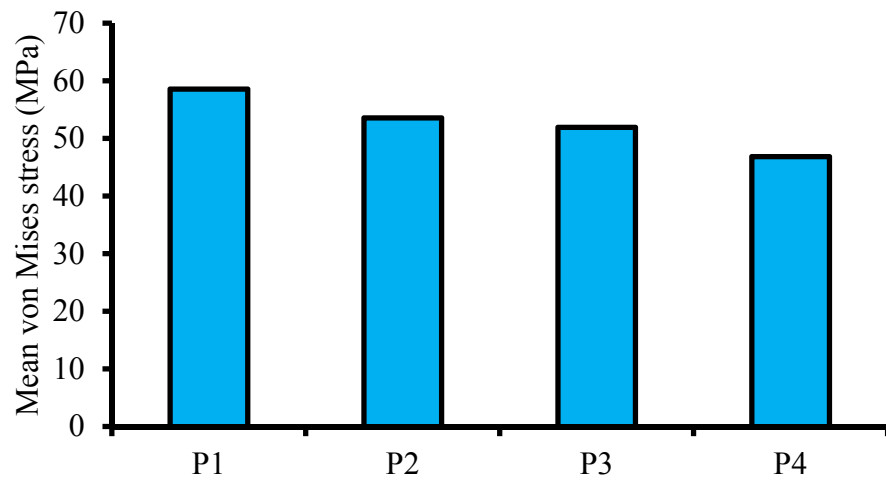
The developed stress in the femoral prostheses is presented in Figure 4.15. The von Mises stress behavior was similar to the SED variation with respect to the distal and proximal cross-sections (Figures 4.15a and 4.15b). The effect of profiles on the stress distribution in the prostheses was insignificant (0.6%). The prostheses with non-bonded implant–bone surface condition carried 8.3% more stress than the prostheses with



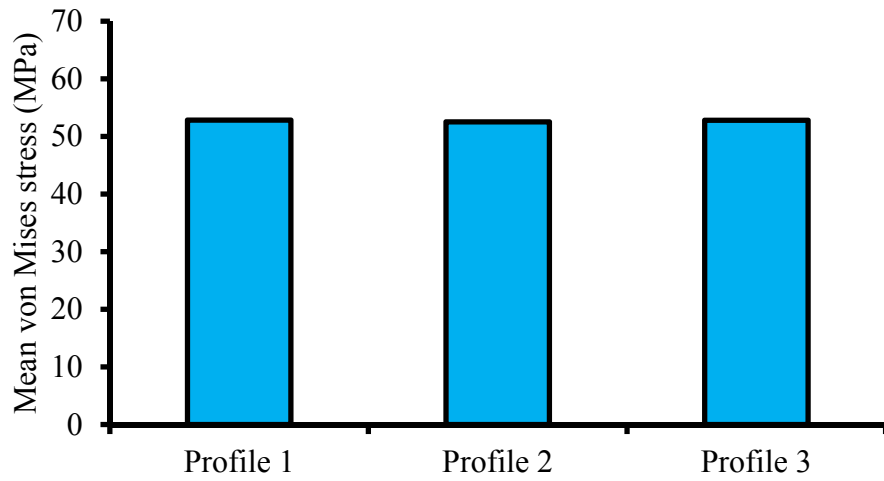
bonded implant–bone surface condition. Stress decreased by 31.9% with the increase in gradient index from 0 to 1.



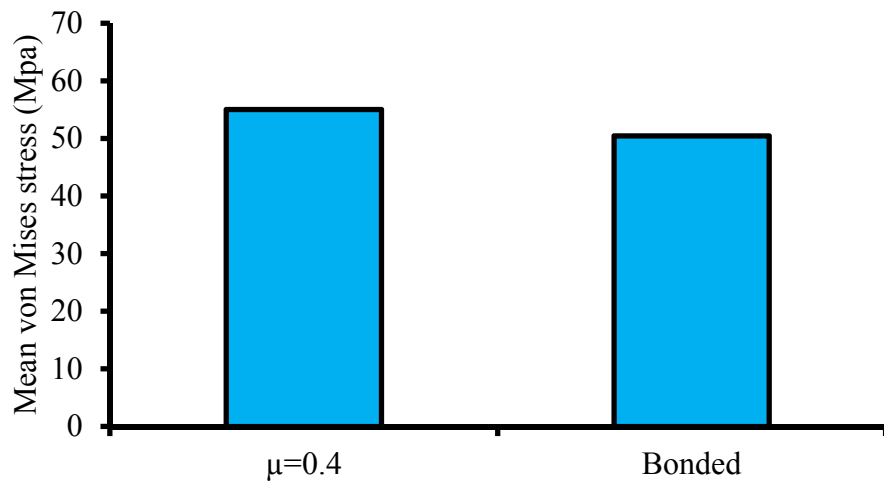
(a) Distal cross-section of prosthesis



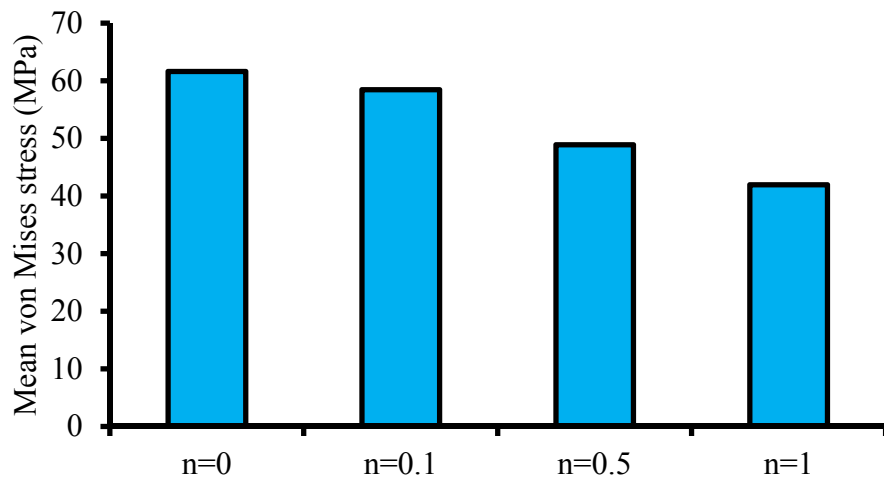
(b) Proximal cross-section of prosthesis



(c) Profile of prosthesis



(d) Interface property

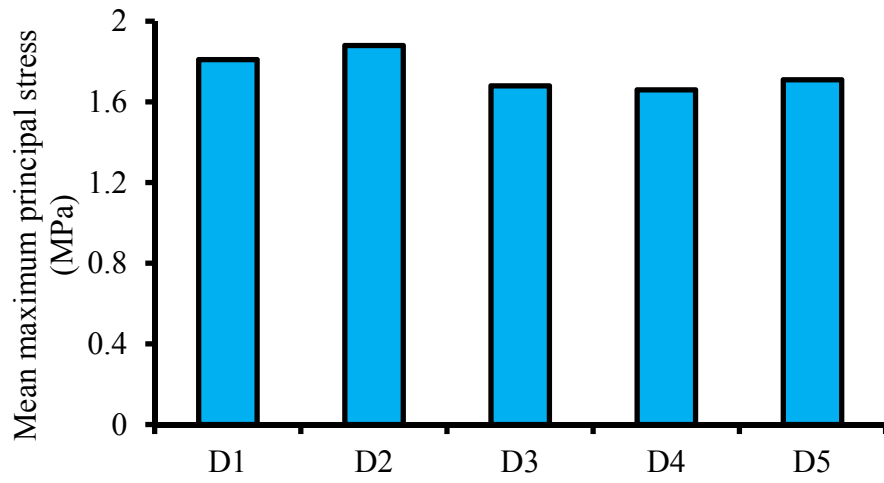


(e) Gradient index

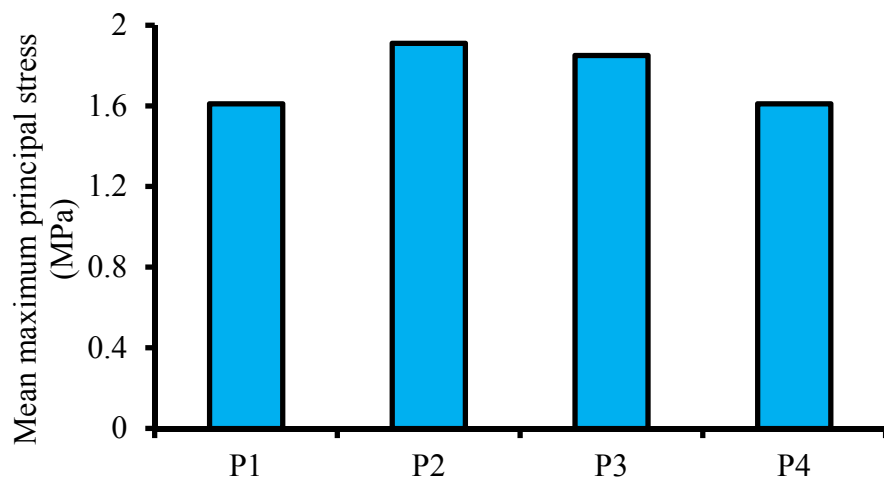
Figure 4.15: Variation in the mean von Mises for the different (a) distal cross-sections, (b) proximal cross-sections, (c) profiles, (d) interface properties, and (e) gradient indices

### 4.2.3.3 Bone Stress

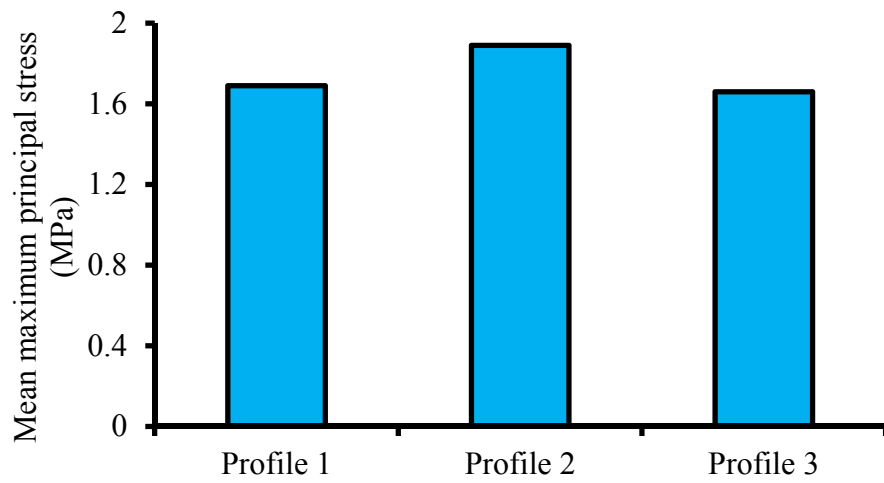
The maximum and minimum principal stress variations in the bone are presented in Figures 4.16 and 4.17. The comparison of the mean values of the principal stress showed higher values of the minimum principal stress. The prostheses with distal cross-sections of D1 and D2 produced almost the same maximum principal stresses in the bone, which were greater than those of the prostheses with D3, D4, and D5. Meanwhile, the prostheses with proximal cross-sections of P1 and P2 caused more maximum principal stress in the bone compared with the prostheses made of proximal cross-sections of P3 and P4. The prostheses with proximal cross-sections of P1 and P4 stimulated the highest (19.14 MPa) and the lowest (6.64 MPa) minimum principal stresses in the femur, respectively. The effect of profiles and interface conditions on maximum principal stress was contrary to their effects on minimum principal stress. In other words, the prostheses with Profile 2 and non-bonded interface provoked high maximum principal stress on the lateral side of the femur, but less minimum principal stress on the medial side of the bone. The maximum and minimum principal stresses showed increasing trend with the increase in gradient index. The maximum and minimum principal stresses increased by 5.0% and 13.4%, respectively, with the increase in gradient index from 0 to 1.



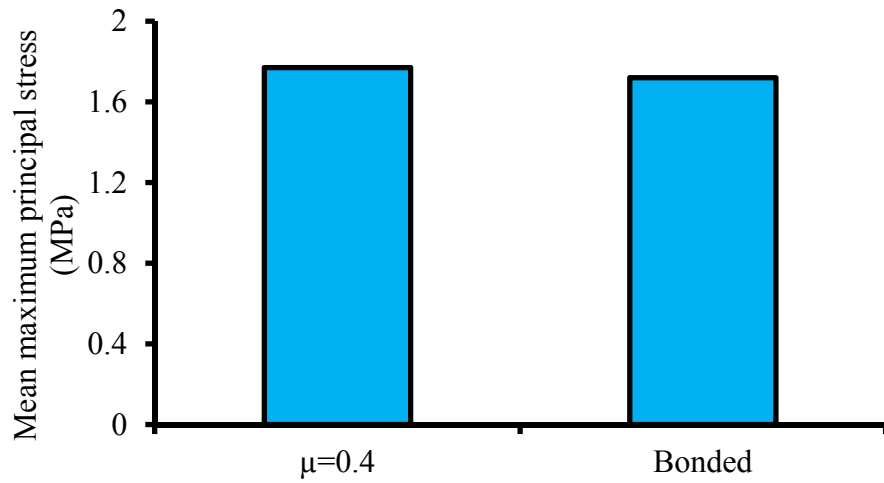
(a) Distal cross-section of prosthesis



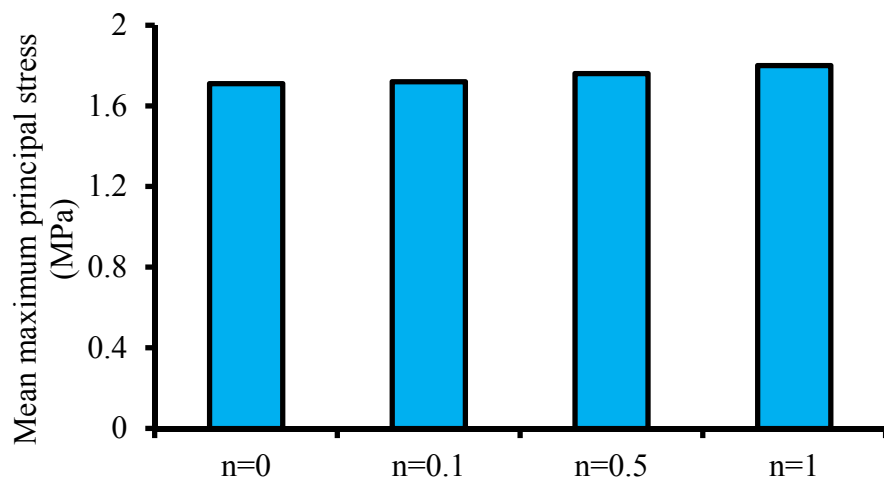
(b) Proximal cross-section of prosthesis



(c) Profile of prosthesis

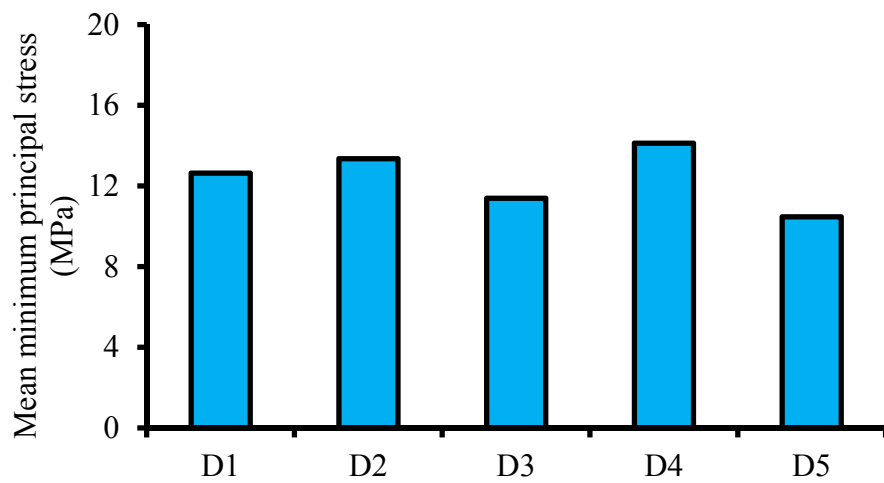


(d) Interface property

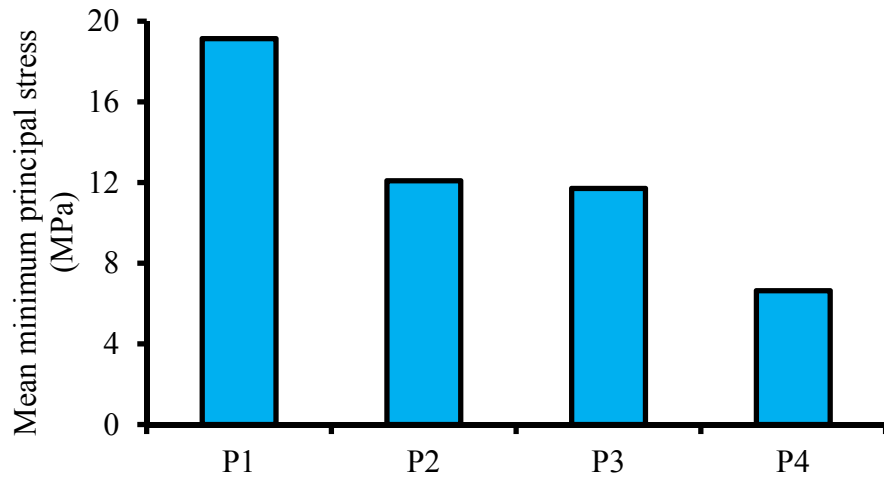


(e) Gradient index

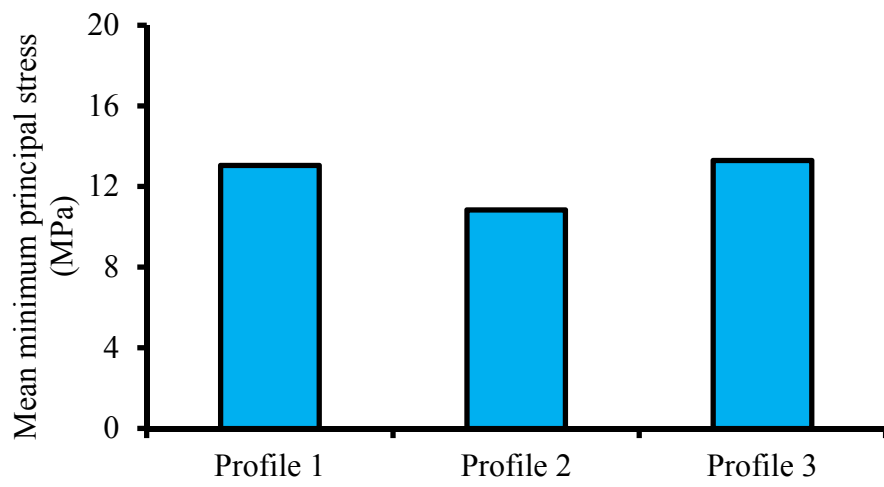
Figure 4.16: Variation in the mean maximum principal stress for the different (a) distal cross-sections, (b) proximal cross-sections, (c) profiles, (d) interface properties, and (e) gradient indices



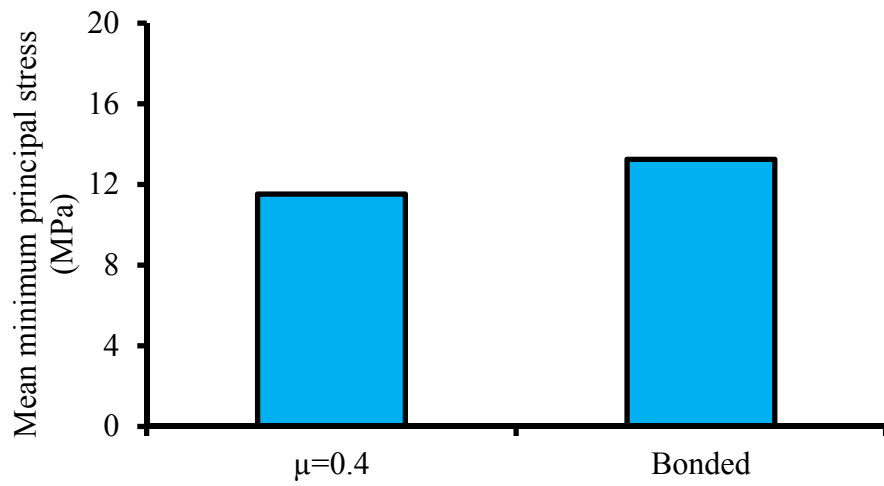
(a) Distal cross-section of prosthesis



(b) Proximal cross-section of prosthesis



(c) Profile of prosthesis



(d) Interface property

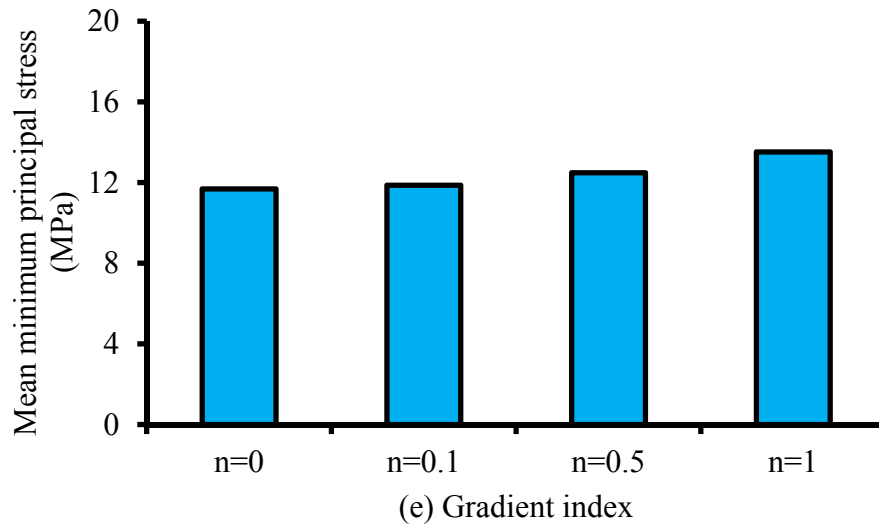
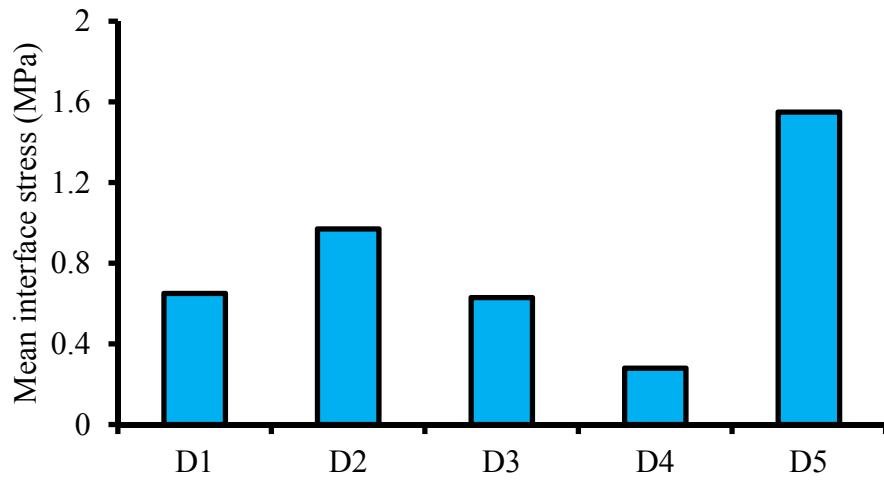


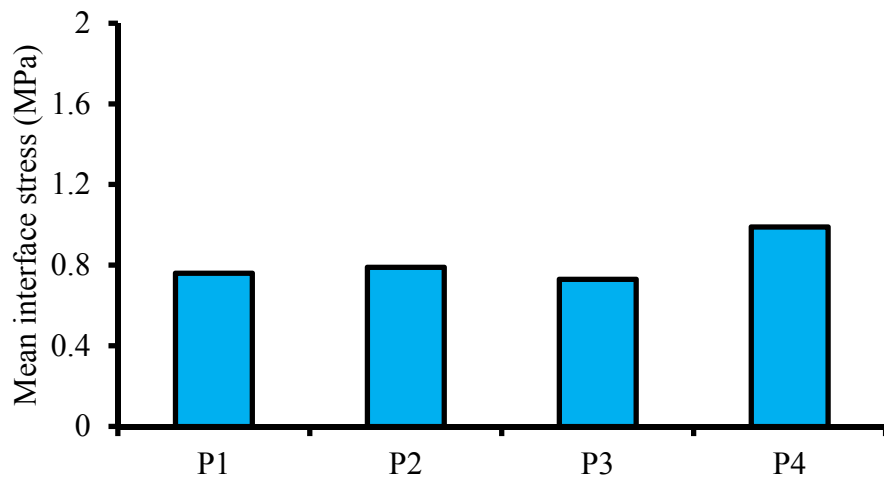
Figure 4.17: Variation in the mean minimum principal stress for the different (a) distal cross-sections, (b) proximal cross-sections, (c) profiles, (d) interface properties, and (e) gradient indices

#### 4.2.3.4 Interface stress

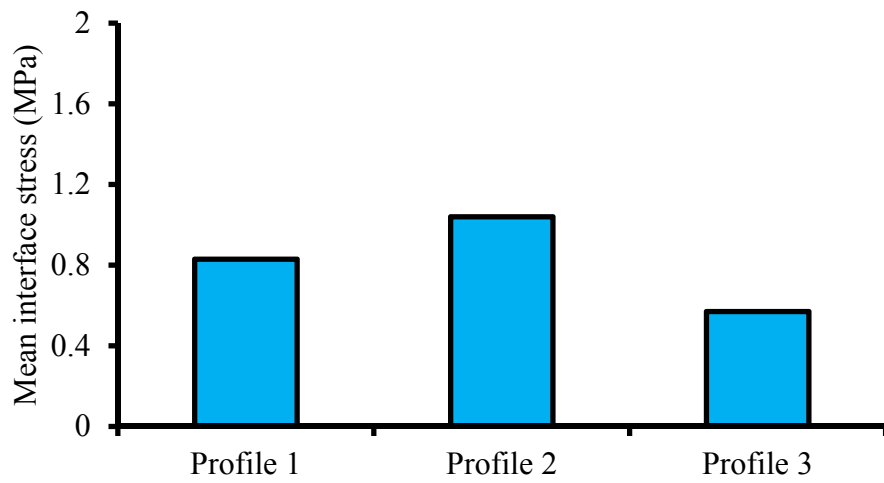
The interface stress behavior at the implant–bone surface is illustrated in Figure 4.18 for the non-bonded implant–bone surface. The highest and lowest values of the interface stresses were obtained from the implant–bone surface of the implanted prostheses with distal cross-sections of D5 (1.55 MPa) and D4 (0.28MPa), respectively. The interface stresses caused by the prostheses with distal cross-sections of D1 and D3 were almost the same at approximately 0.64 MPa and were more than the interface stress for the prosthesis with D4. On the contrary, the stresses for these two distal cross-sections were less than the stresses induced by the prosthesis with D2 (0.97 MPa). The implant–bone surface stresses caused by the implantation of the prostheses with proximal cross-sections of P4 (0.99 MPa), P2 (0.79 MPa), P1 (0.76 MPa), and P3 (0.73 MPa) exhibited the highest to the lowest value of interface stresses. The interface stress followed a decreasing trend at the implant–bone interface with the increase in gradient index. The gradient index growth led to 21.7% reduction in the interface stresses.



(a) Distal cross-section of prosthesis



(b) Proximal cross-section of prosthesis



(c) Profile of prosthesis



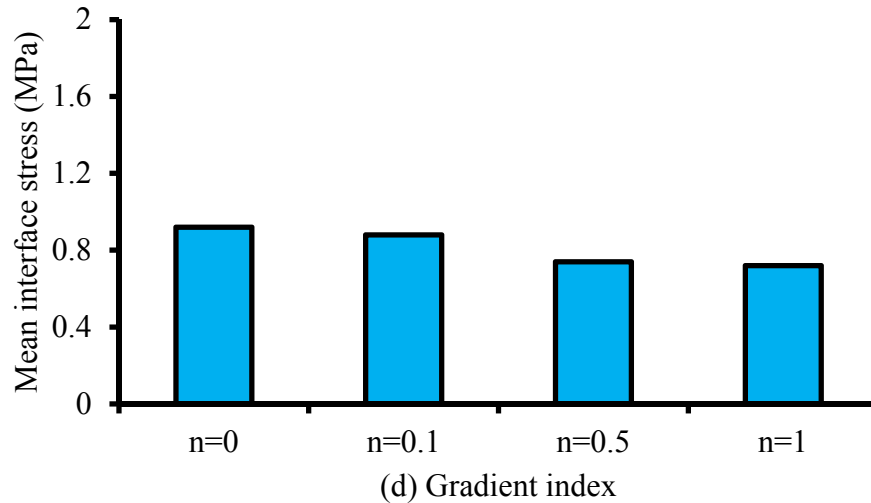


Figure 4.18: Variation in the mean interface stress for the different (a) distal cross-sections, (b) proximal cross-sections, (c) profiles, and (d) gradient indices

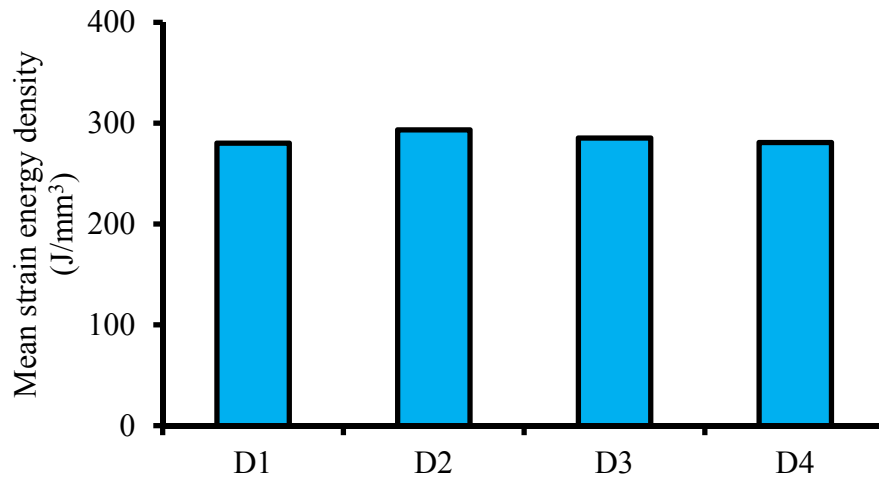
#### 4.2.4 Cementless radial functionally graded femoral prosthesis with different geometries

This section presents the results of inserting an implant with variable Young's modulus in the transverse plane in the anatomical bone. The Young's modulus of the prostheses increased from the cortex layer to the core of the prostheses.

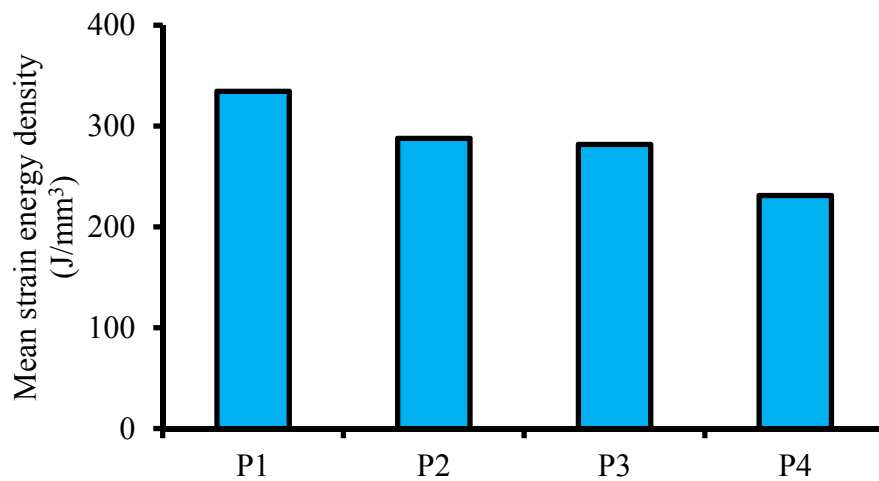
##### 4.2.4.1 Strain energy density

Figures 4.19a to 4.19d present the mean values of the SED as a function of distal cross-section, proximal cross-section, profiles, and gradient index. The prostheses change in the distal cross-section showed a negligible effect of 4.48% on the change in SED. Prostheses with P1 proximal cross-section caused the maximum SED in the bone, whereas the prostheses with P4 proximal cross-section induced the minimum SED in the bone (Figure 4.19b). The effect of P1 on SED was 30.85% more than that of P4. The prostheses with proximal cross-section of P2 and P3 produced almost similar SEDs in the bone, with values between those of the prostheses with P1 and P4 proximal cross-sections (Figure 4.19b). Profiles 1 and 3 stimulated almost the same SEDs in the bone,

which was approximately 21.52% more than that of Profile 2 (Figure 4.19c). The increase in gradient index showed a positive impact on the change in SED (Figure 4.19d). Consequently, the prostheses with gradient indices of 1 and 0 showed the maximum (352.2 J/mm<sup>3</sup>) and minimum (237.5 J/mm<sup>3</sup>) values of SED, respectively (Figure 4.19d), with an approximate difference of 32.56%.



(a) Distal cross-section of prosthesis



(b) Proximal cross-section of prosthesis

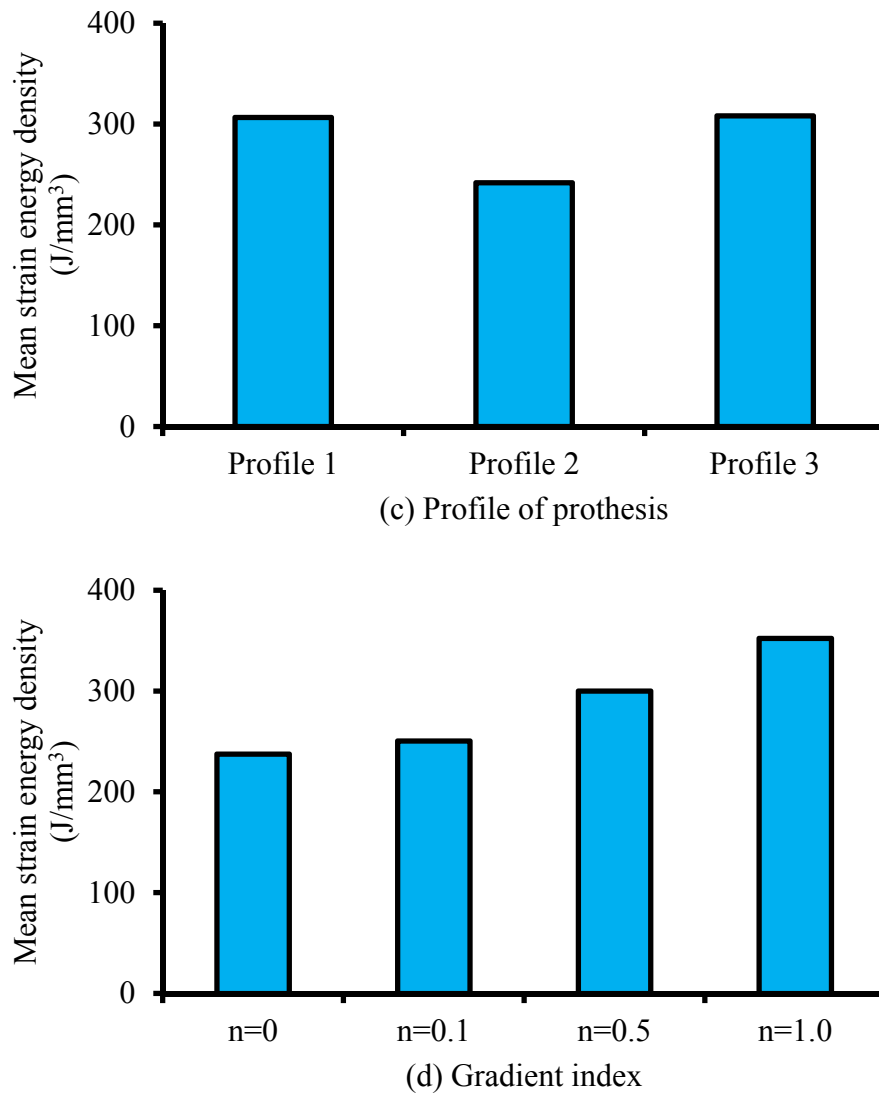
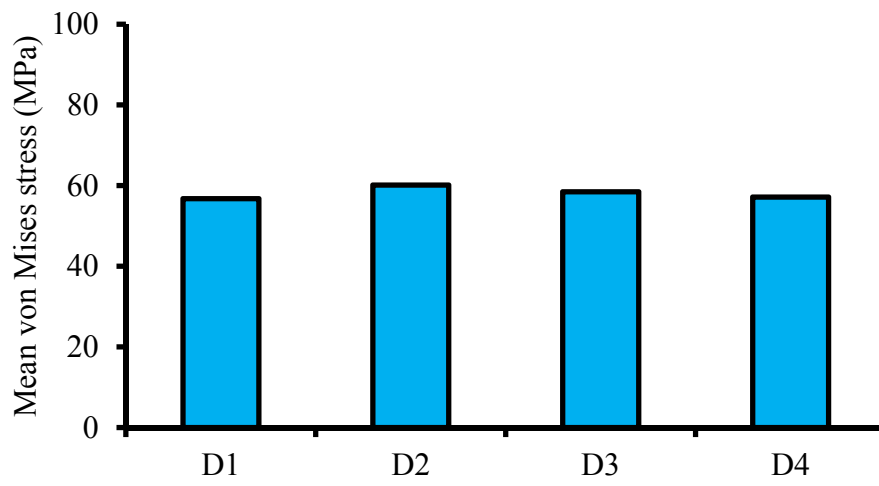


Figure 4.19: Variation in the strain energy density a function of (a) distal cross-section, (b) proximal cross-section, (c) profile, and (d) gradient index

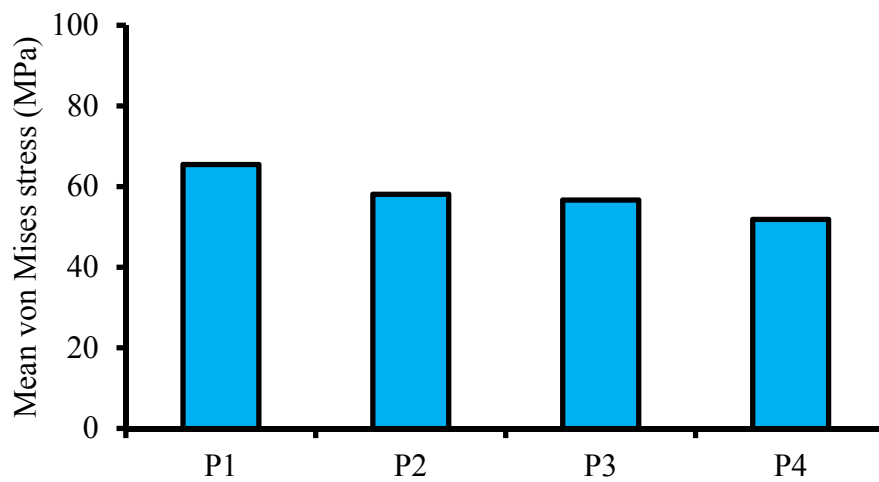
#### 4.2.4.2 Developed stress in prostheses

The changes in the mean values of von Mises stress on the femoral prostheses are illustrated in Figures 4.20a to 4.20d. The prosthesis profile, proximal cross-section, and distal cross-section effects on von Mises stress were similar to that on the SED. The increase in gradient index showed a negative impact on the developed stress over the femoral prostheses, which was contrary to its effect on the SED. In other words, von

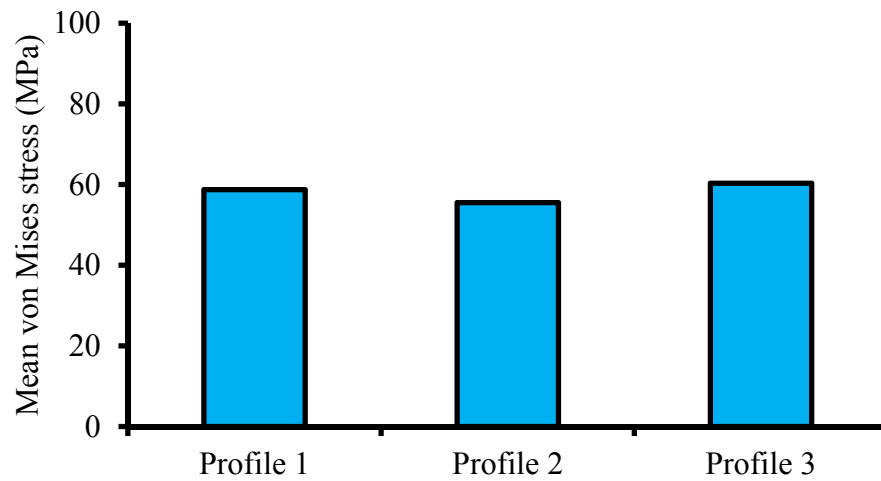
Mises stress on femoral prostheses declined with the increase in gradient index (Figure 4.20d). Consequently, prostheses with gradient indices of 1 and 0 induced the minimum and maximum von Mises stresses, respectively. The gradient index, profile, proximal cross-section, and distal cross-section caused corresponding differences of 79.06%, 7.97%, 20.82%, and 5.60% between the maximum and minimum mean von Mises stresses at the prostheses.



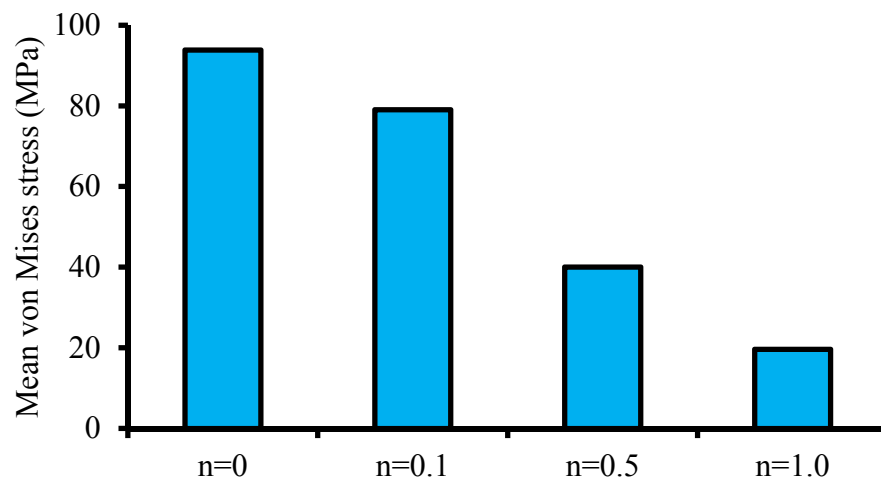
(a) Distal cross-section of prosthesis



(b) Proximal cross-section of prosthesis



(c) Profile of prosthesis



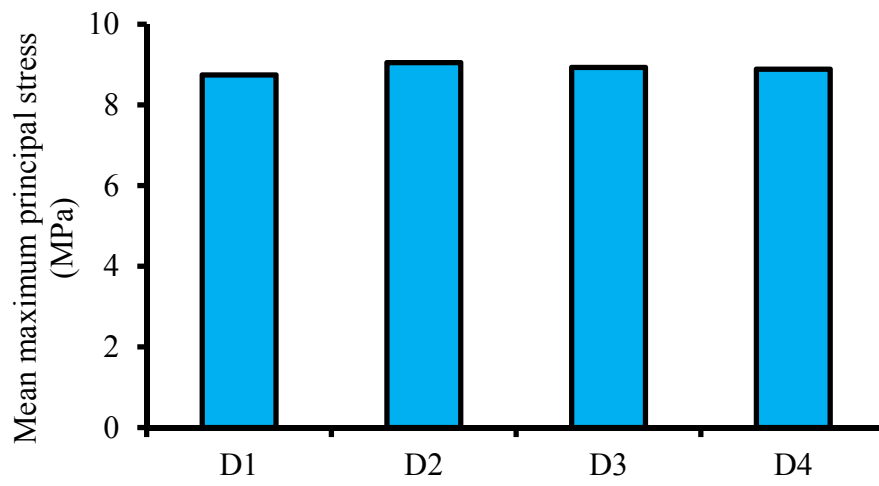
(d) Gradient index

Figure 4.20: Variation in the von Mises stress as a function of (a) distal cross-section, (b) proximal cross-section, (c) profile, and (d) gradient index

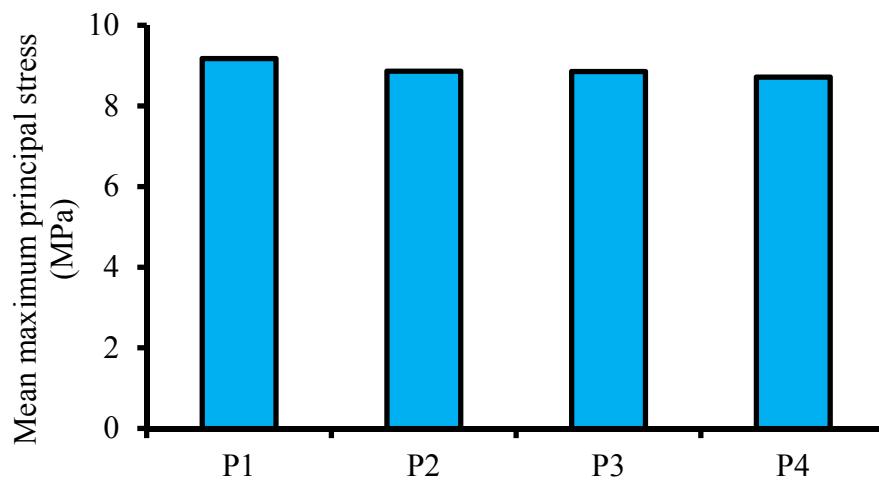
#### 4.2.4.3 Developed stress in the bone

The variations in the mean values of the developed maximum and minimum principal stresses in the bone as functions of distal cross-section, proximal cross-section, profile, and gradient index are presented in Figures 4.21a to 4.22d. A negligible effect was observed in the maximum principal stress caused by the change in all considered parameters (Figures 4.21a to 4.21d). The maximum and minimum principal stresses increased with gradient index (Figures 4.21d and 4.22d). The developed maximum principal stress in the bone attributed to the implantation of the prostheses with Profile 2

was approximately 2.0% more than that attributed to the implantation of the prostheses with Profiles 1 and 3. The effects of both proximal and distal cross-sections on the maximum and minimum principal stresses were insignificant. The average effect of the distal and proximal cross-sections on the maximum and minimum principal stresses was 5.4%, whereas the average effect of the gradient index growth on the maximum and minimum principal stresses was 13.6%.



(a) Distal cross-section of prosthesis



(b) Proximal cross-section of prosthesis

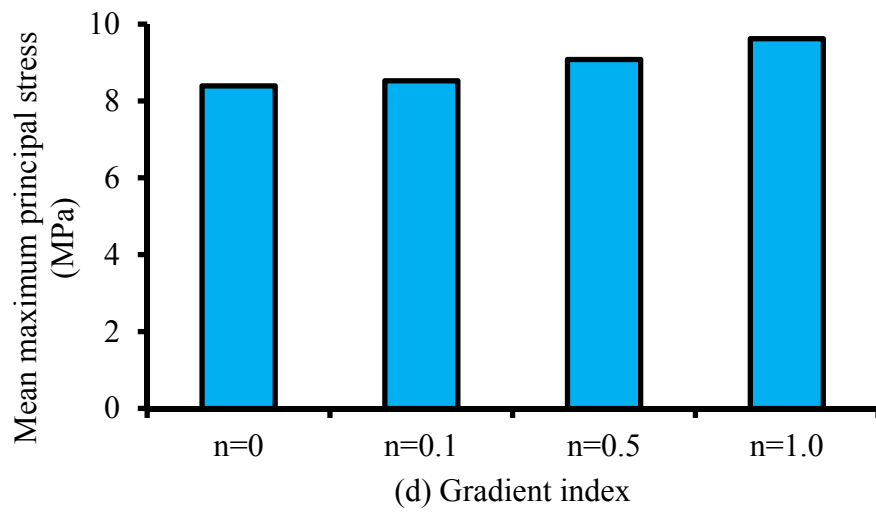
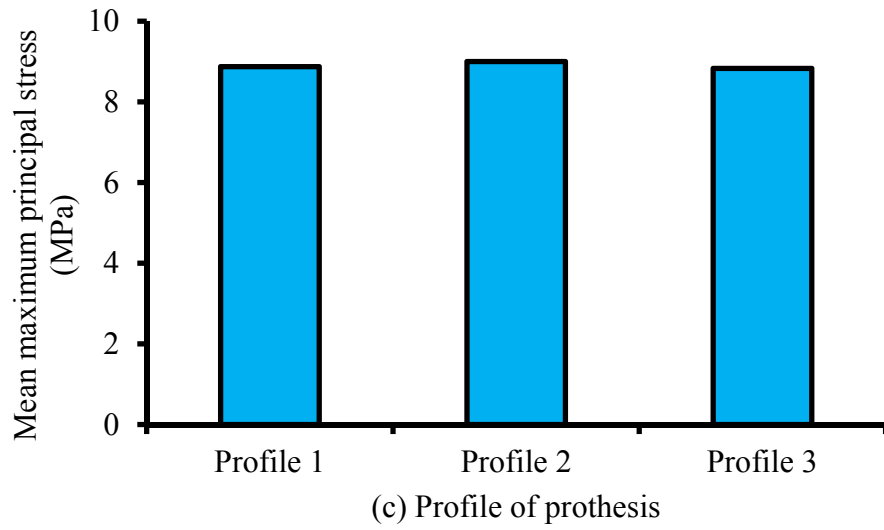
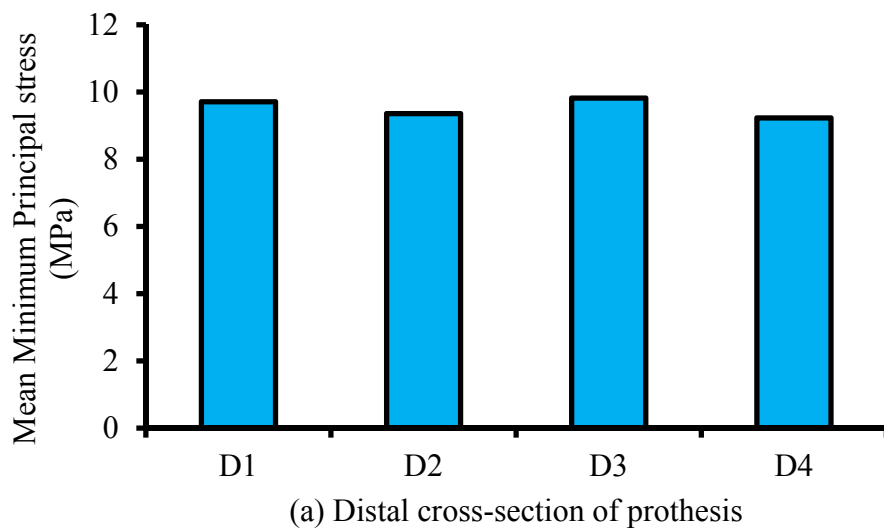
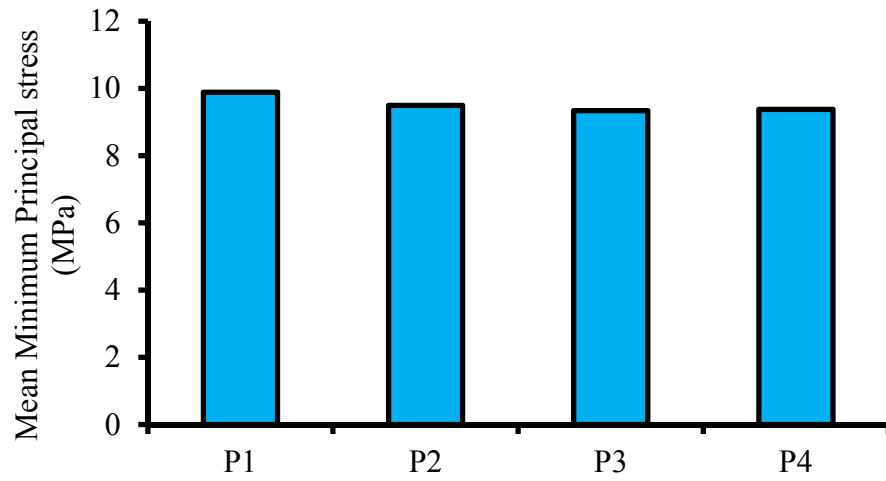
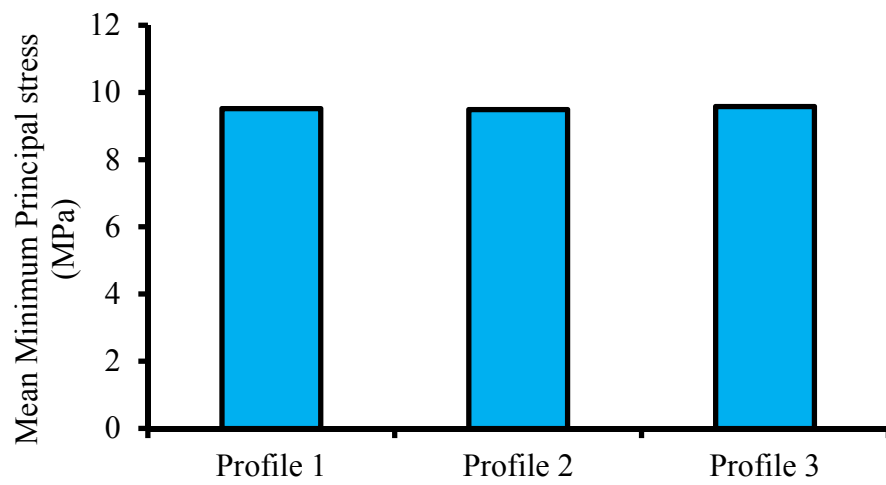


Figure 4.21: Variation in the maximum principal stress as a function of (a) distal cross-section, (b) proximal cross-section, (c) profile, and (d) gradient index

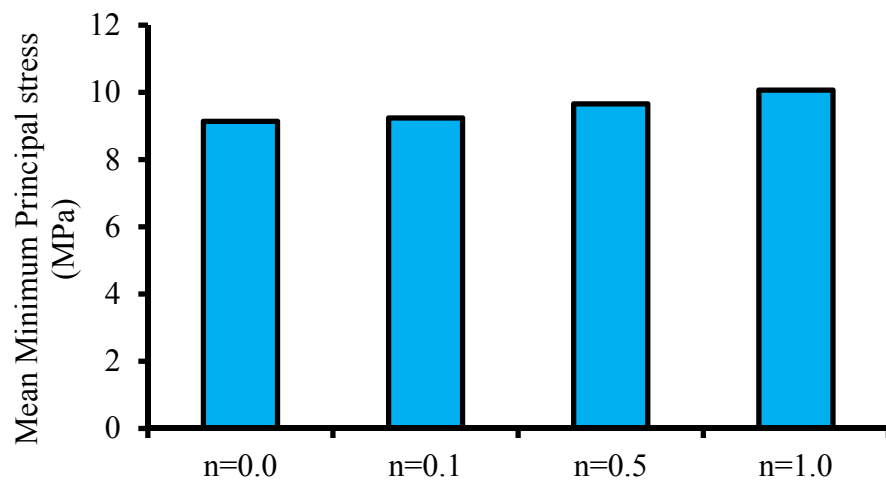




(b) Proximal cross-section of prosthesis



(c) Profile of prosthesis



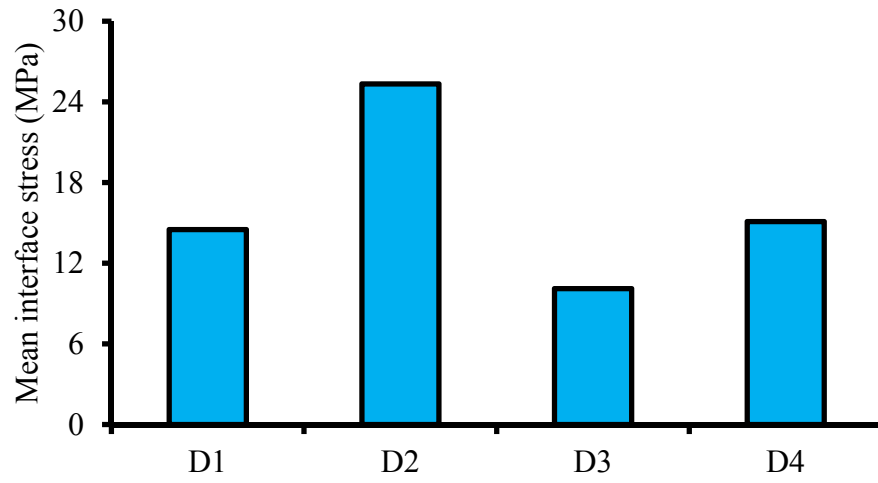
(d) Gradient index

Figure 4.22: Variation in the minimum principal stress as a function of (a) distal cross-section, (b) proximal cross-section, (c) profile, and (d) gradient index

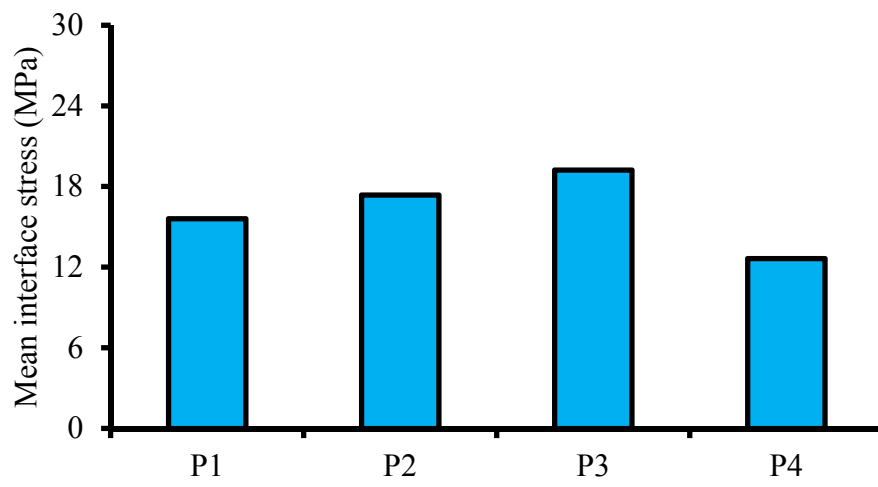


#### 4.2.4.4 Interface Stress

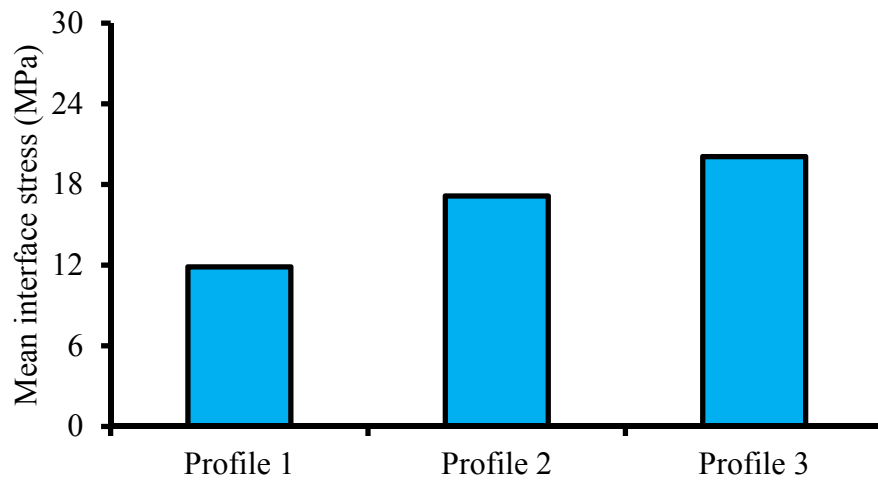
The interface stress variations at the implant–bone interface are illustrated in Figures 4.23a to 4.23d. The maximum and minimum interface stresses were observed with the implantation of the prostheses with D2 and D3 distal cross-sections, respectively. The D1 and D4 distal cross-sections showed a similar effect on the interface stresses. The distal cross-sections caused a 60.09% difference between the maximum and minimum mean interface stresses. As shown in Figure 4.23b, the prostheses with the maximum to minimum interface stresses are those with proximal cross-sections of P3, P2, P1, and P4, and a 34.23% difference was observed between the minimum and maximum mean interface stresses. The interface stresses displayed an increasing trend with the change from Profiles 1 to 3 (Figure 4.23c). The difference between the change in the maximum and minimum interface stress that was attributed to the profiles was 40.90%. The interface stresses decreased with the gradient index (Figure 4.23d). The maximum interface stress emerged in the implant–bone interface because of the prostheses with gradient index of 0, and the minimum interface stress resulted from the prostheses with gradient index of 1 (Figure 4.23d). The mean interface stress reduction was 62.44% caused by the increase in gradient index from 0 to 1.



(a) Distal cross-section of prosthesis



(b) Proximal cross-section of prosthesis



(c) Profile of prosthesis

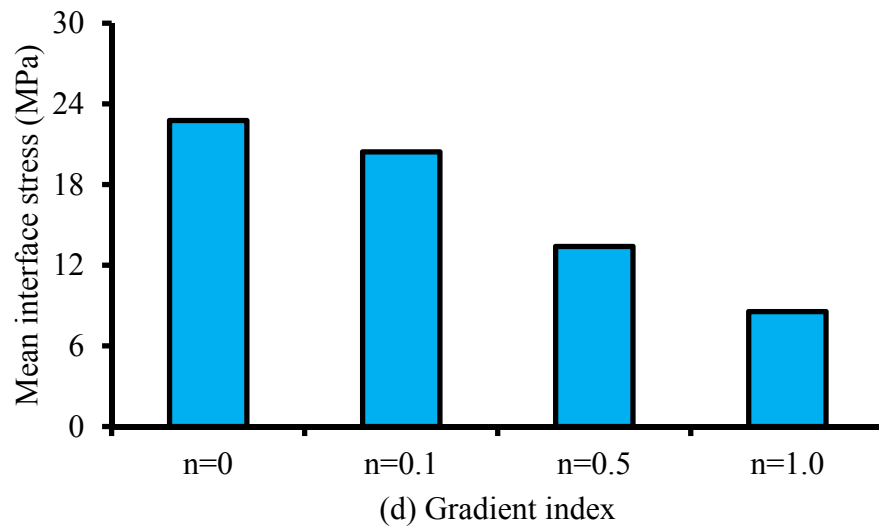


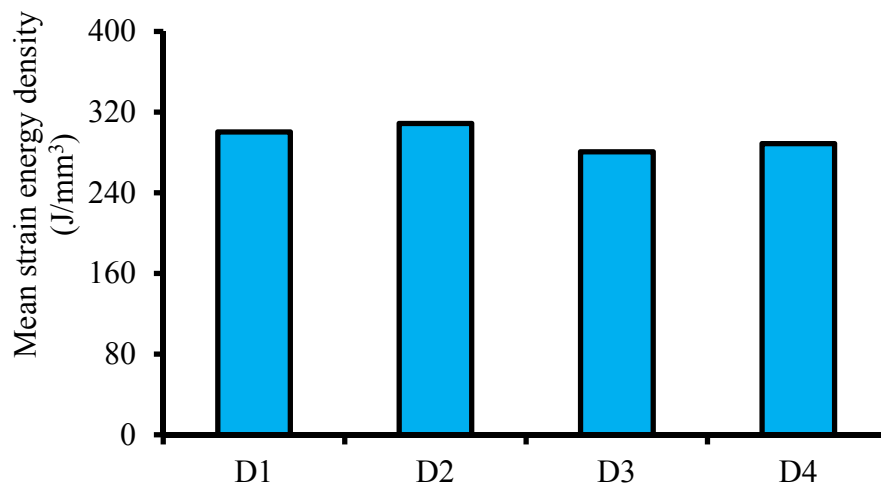
Figure 4.23: Variation in the interface stress as a function of (a) distal cross-section, (b) proximal cross-section, (c) profile, and (d) gradient index

## 4.2.5 Cemented prostheses with conventional materials

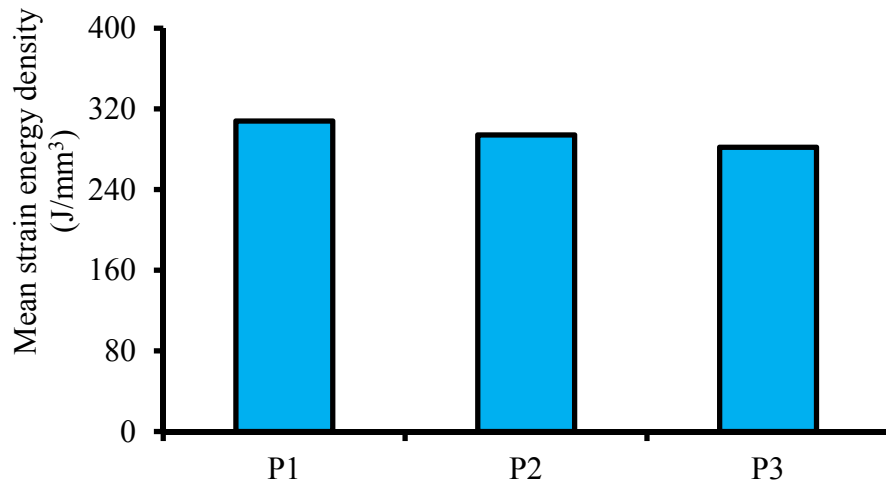
This section presents the FEA results of the anatomical femur implanted with different cemented prostheses composed of conventional materials of St and Ti.

### 4.2.5.1 Strain energy density

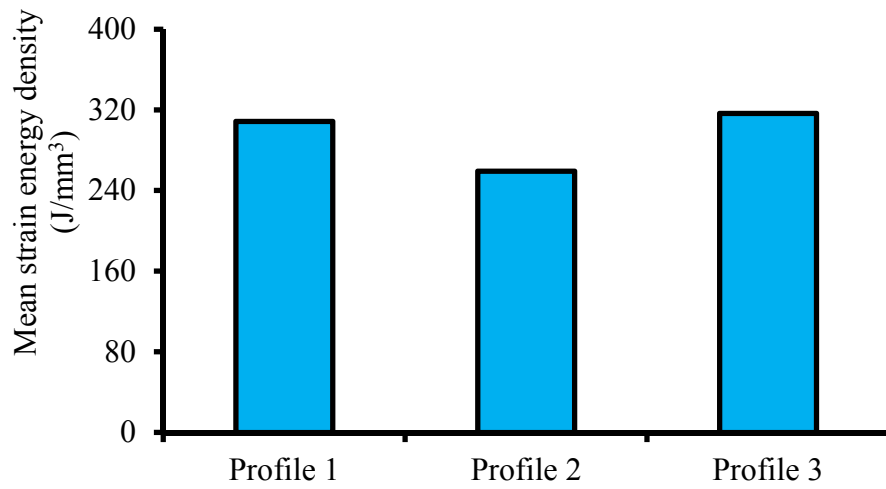
Figures 4.24a to 4.24d illustrate the variation in the SED in the proximal metaphysis of femur as a function of distal cross-section, proximal cross-section, profile, and material. Among the prostheses with different distal cross-sections, the prostheses with distal cross-sections of D1 and D4 provoked about 7.8% more SED in the bone. The prostheses with distal cross-section of D3 produced the minimum SED of  $280.84 \text{ J/mm}^3$  in the bone. The prostheses with P1 proximal cross-section induced 4.5% and 8.4% more SED than the prostheses with P2 and P3 proximal cross-sections, respectively. The prostheses with Profiles 3, 1, and 2 caused the highest SED to the lowest SEDs of  $316.53$ ,  $308.58$ , and  $259.13 \text{ J/mm}^3$  in the bone, respectively. Meanwhile, the Ti-based prostheses stimulated 31.0% more SED in the bone than the St-based prostheses.



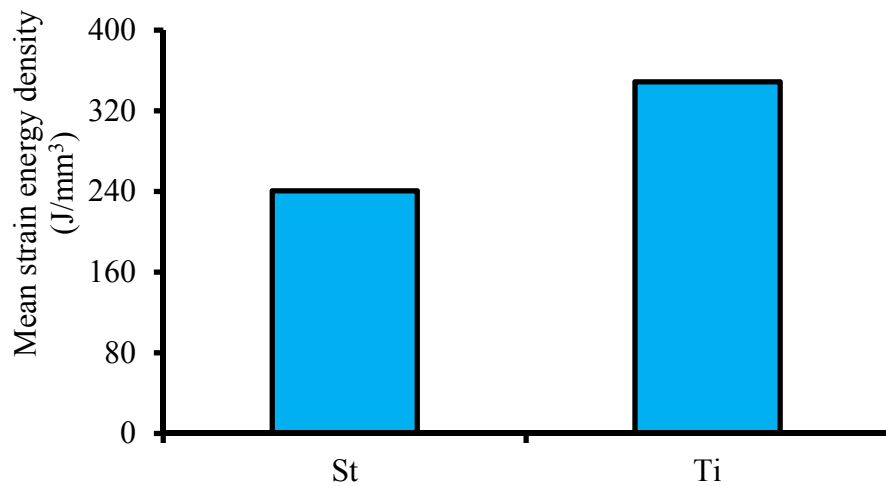
(a) Distal cross-section of prosthesis



(b) Proximal cross-section of prosthesis



(c) Profile of prosthesis

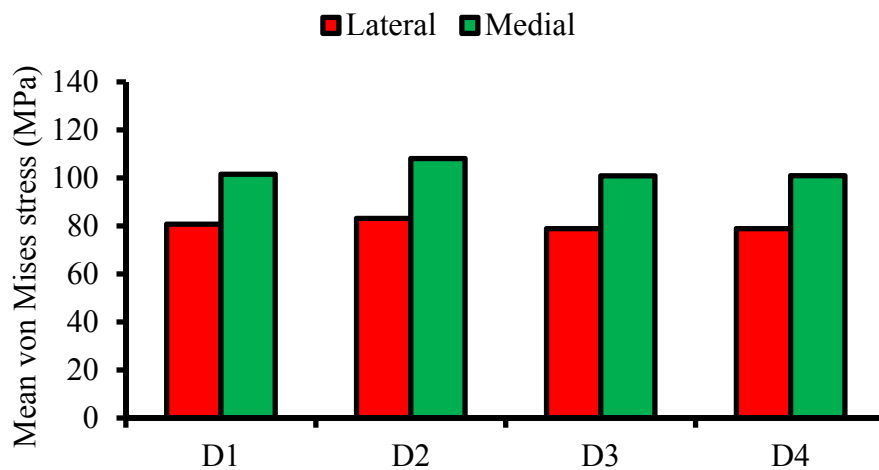


(d) Material of prosthesis

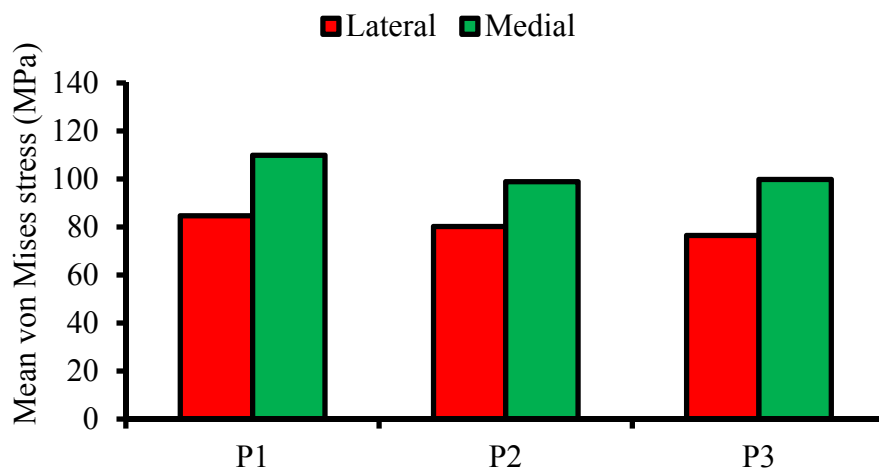
Figure 4.24: Strain energy density as a function of the (a) distal cross-section, (b) proximal cross-section, (c) profile, and (d) material of the prostheses

#### 4.2.5.2 Developed stress in the prostheses

The von Mises stress variations at the lateral and medial sides of prostheses composed of conventional materials as functions of distal cross-section, proximal cross-section, profile, and material are illustrated in Figure 4.25. As shown in Figure 4.25, the medial side of prostheses exhibited 21.8% more stress compared with the lateral side. Geometrical parameters showed minor effect of 7.8% on the prostheses stress variation (Figures 4.25a to 4.25c). On the contrary, the material of the prostheses demonstrated more effect on stress, and the St-based prostheses tolerated 30.9% more stress than the Ti-based prostheses (Figure 4.25d).



(a) Distal cross-section of prosthesis



(b) Proximal cross-section of prosthesis

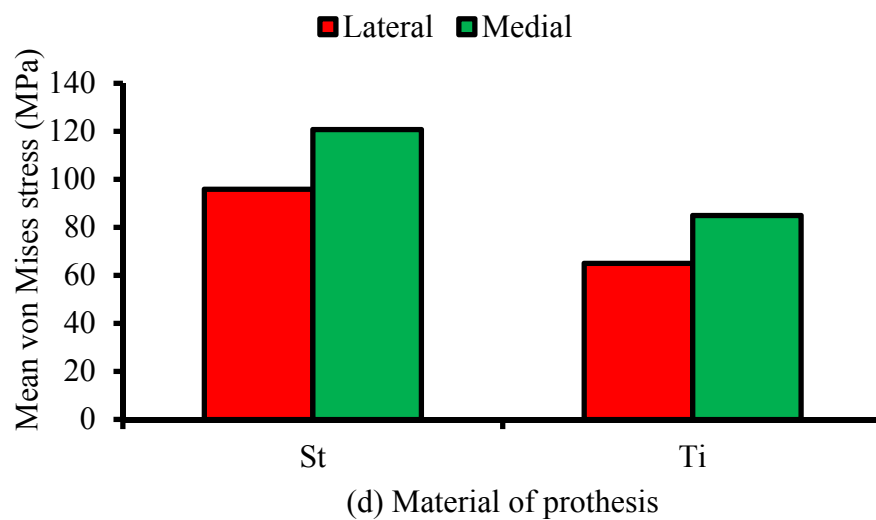
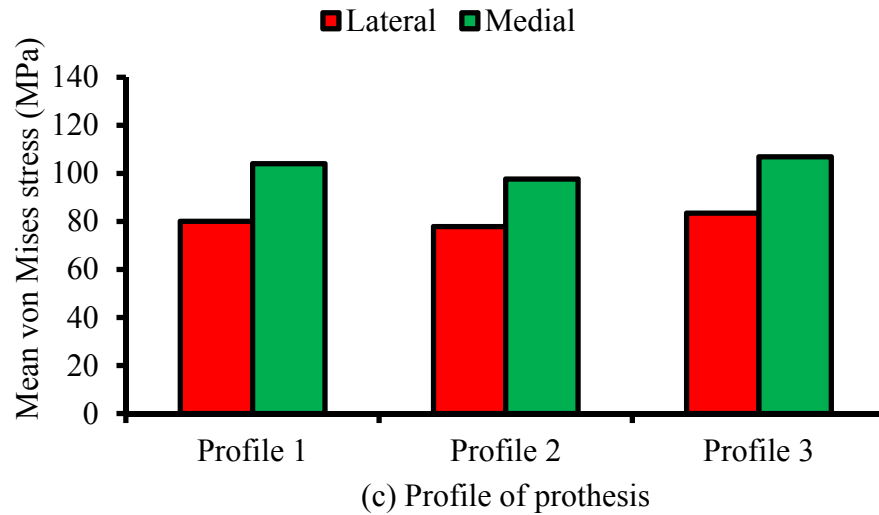
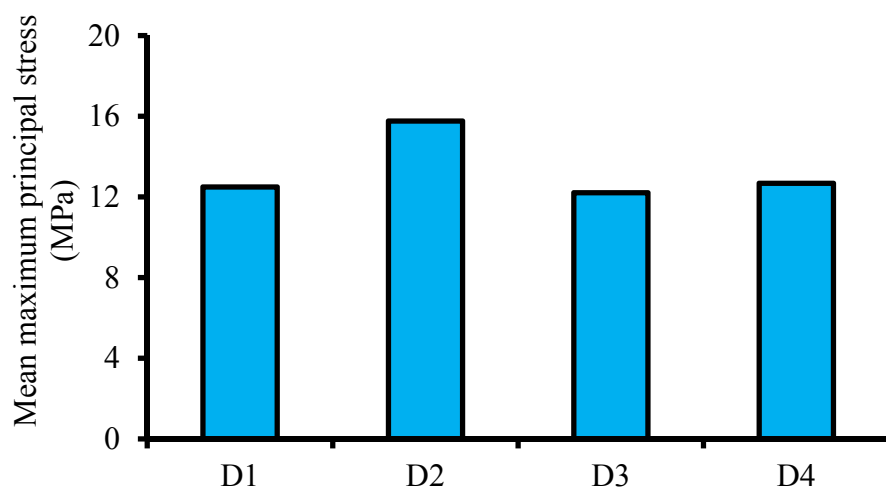


Figure 4.25: Variation in the mean von Mises stress as a function of the (a) distal cross-section, (b) proximal cross-section, (c) profile, and (d) material of the prostheses

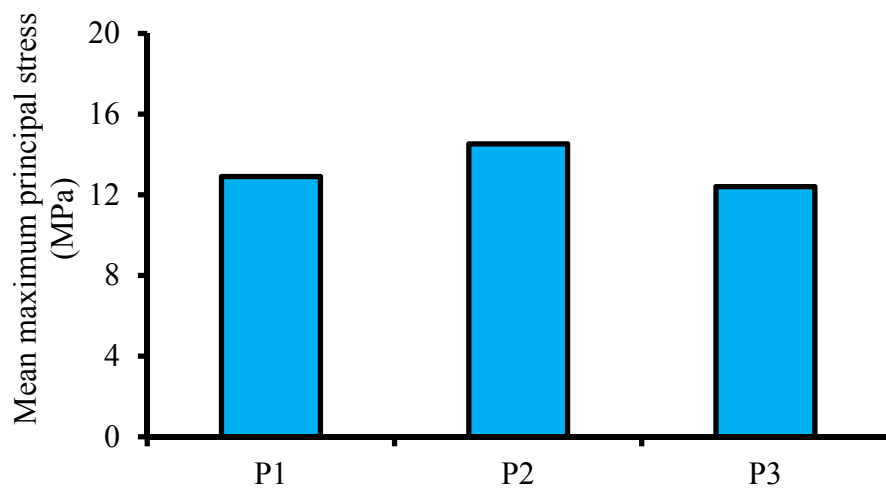
#### 4.2.5.3 Developed stress in the bone

The variation in the maximum and minimum principal stresses on the lateral and medial sides of the bone are shown in Figures 4.26 and 4.27, respectively. The maximum and minimum principal stresses express the crucial tensile stress and the compressive stress in the bone, respectively. A comparison between Figures 4.26 and 4.27 revealed that the femur showed 23.4% more minimum principal stress on the medial side than maximum principal stress on the lateral side after prostheses implantation. Geometrical parameters and material influenced the stress. Prostheses

with distal cross-section of D2, proximal cross-section of P2, and Profile 2 provoked more maximum principal stress in the bone, whereas prostheses composed of D4 distal cross-section, P3 proximal cross-section, and Profile 2 caused more minimum principal stress in the bone. The profile effect on the minimum principal stress was negligible (2.7%). Meanwhile, the Ti-based prostheses induced 10.5% more maximum principal stress and 1.8% more minimum principal stress in the bone than the St-based prostheses (Figures 4.26d and 4.27d).

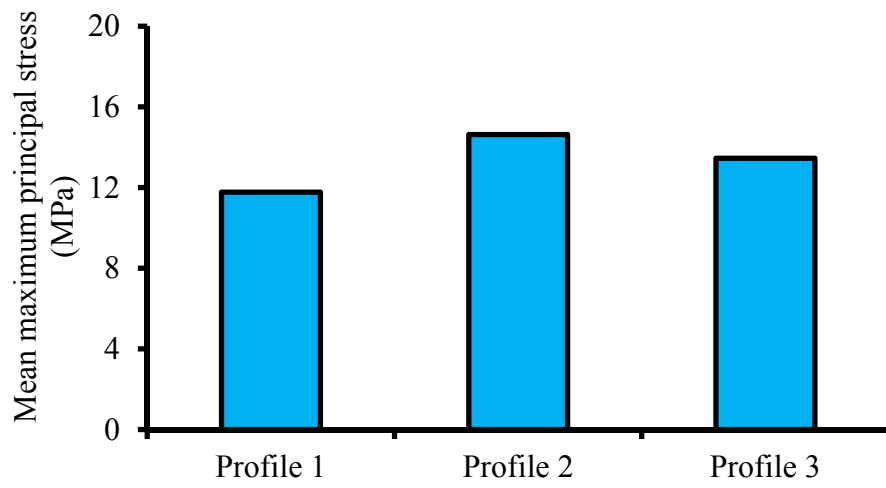


(a) Distal cross-section of prosthesis

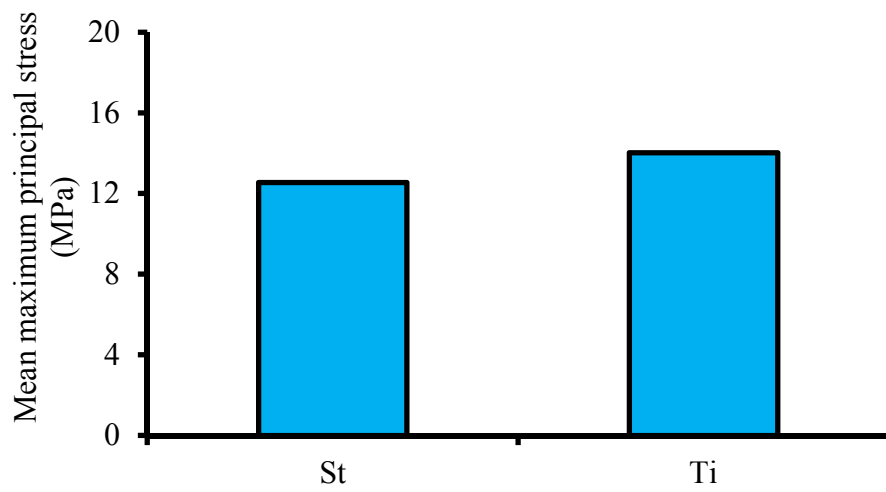


(b) Proximal cross-section of prosthesis



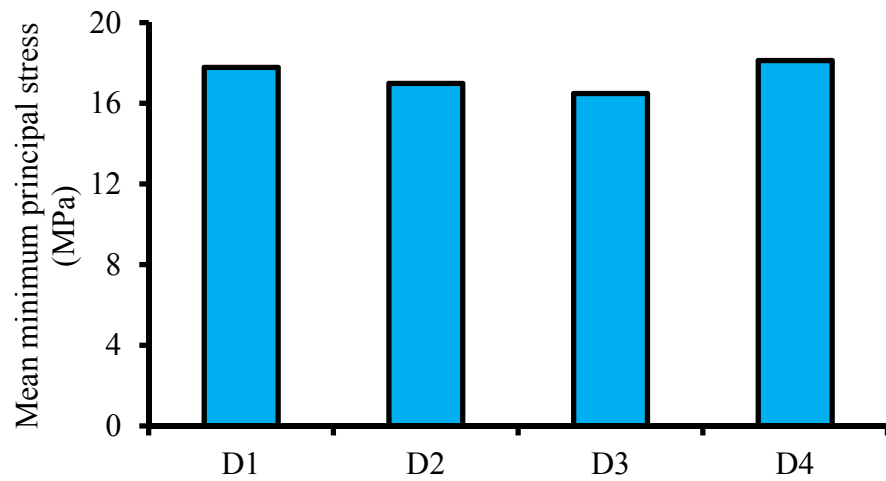


(c) Profile of prosthesis

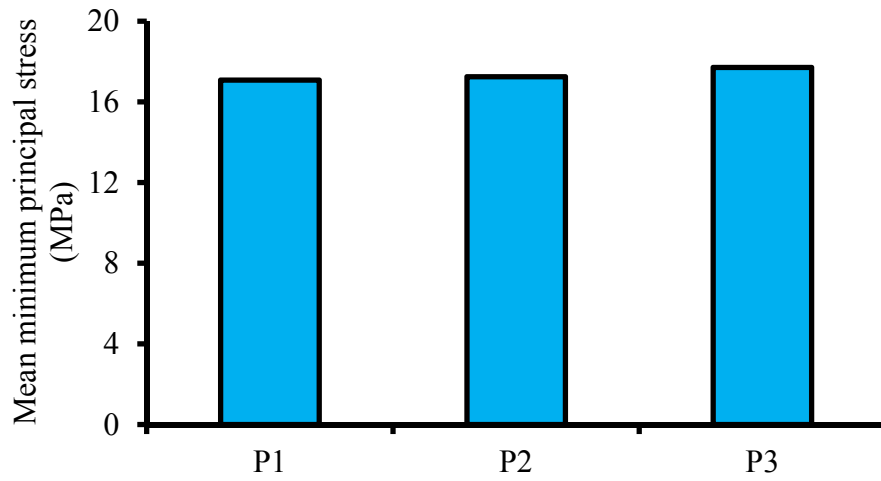


(d) Material of prosthesis

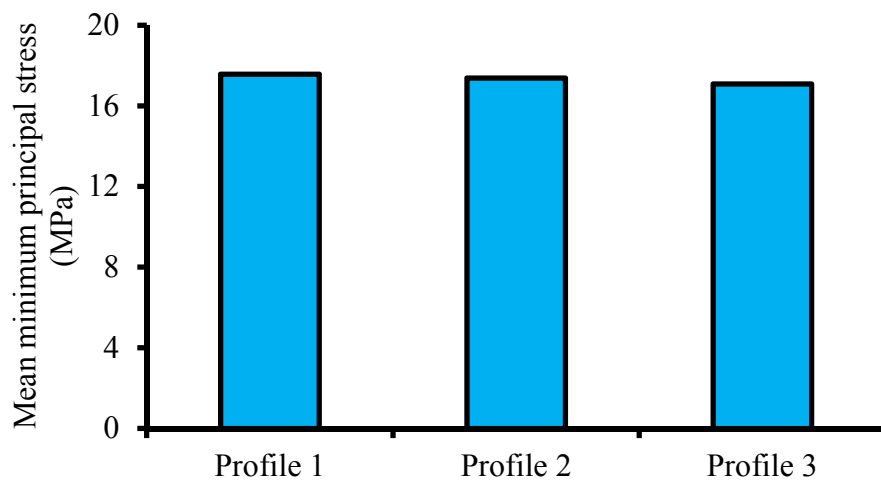
Figure 4.26: Variation in the mean maximum principal stress as a function of the (a) distal cross-section, (b) proximal cross-section, (c) profile, and (d) material of the prostheses



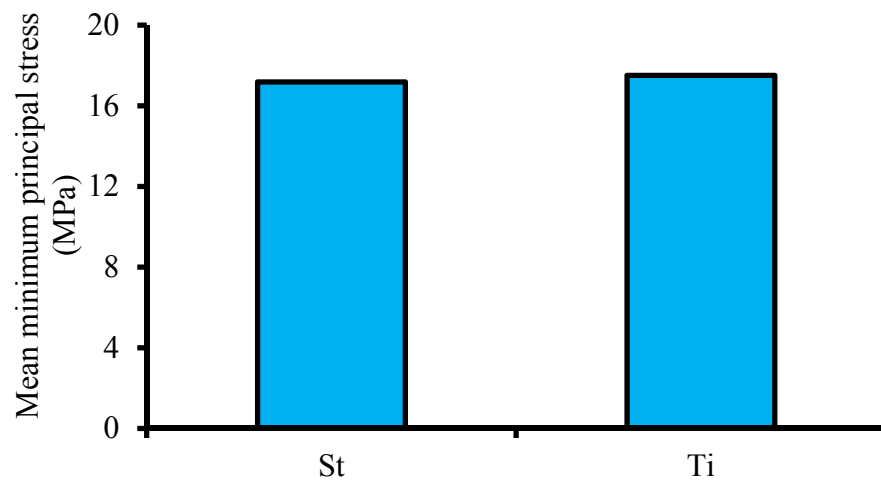
(a) Distal cross-section of prosthesis



(b) Proximal cross-section of prosthesis



(c) Profile of prosthesis

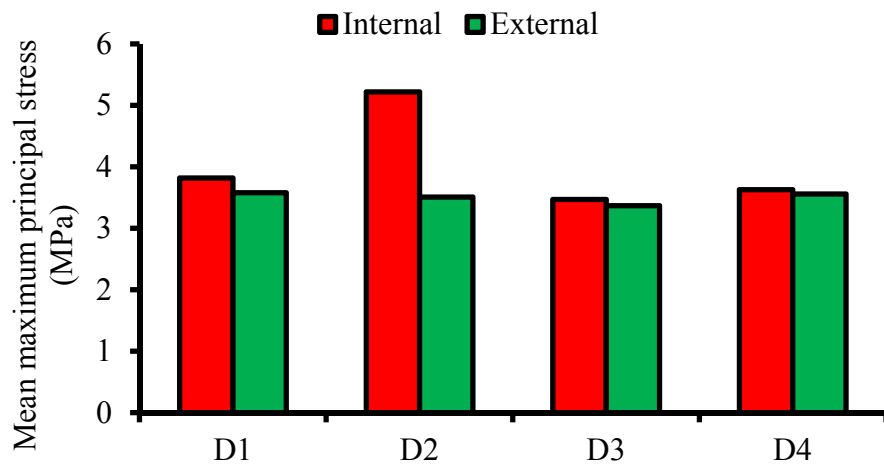


(d) Material of prosthesis

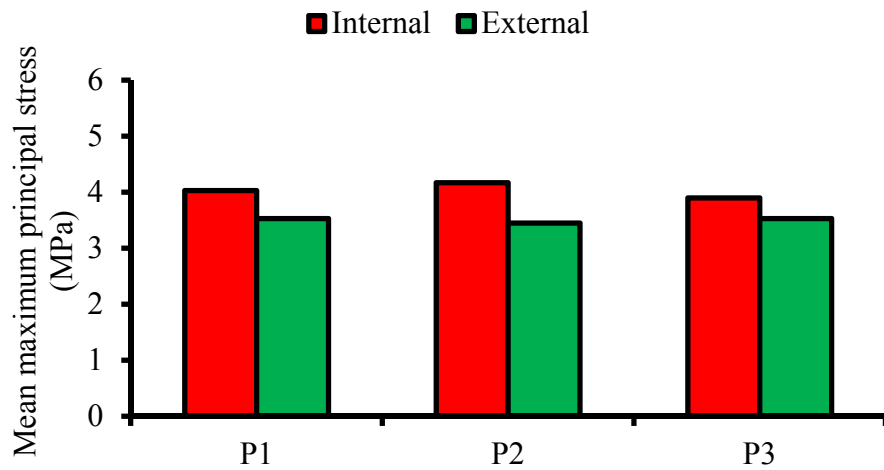
Figure 4.27: Variation in the mean minimum principal stress as a function of the (a) distal cross-section, (b) proximal cross-section, (c) profile, and (d) material of the prostheses

#### **4.2.5.4 Developed stresses in the cement layer**

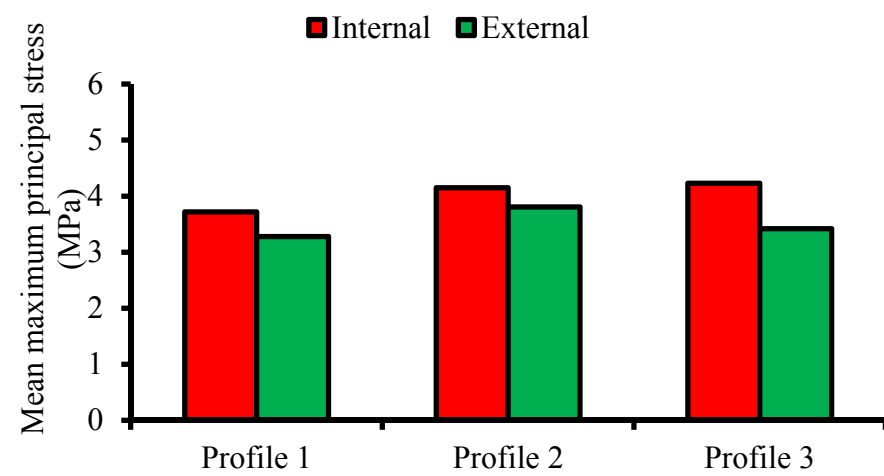
The stress variations on the internal and external surfaces of the cement layer are illustrated in Figures 4.28 and 4.29, which show the maximum and the minimum principal stresses developed in the cement, respectively. The minimum and maximum principal stresses on the internal surface of the cement layer were 68.8% and 13.2% more than those on the external surface, respectively. The developed stresses in the cement were significantly influenced by the geometry and material of the prostheses. The peak (5.2 MPa) and nadir (3.4 MPa) values of the maximum principal stress were induced to the cement by the prostheses with D2 and D3 distal cross-sections on the internal and external surfaces of the cement layer. On the contrary, the peak (21.3 MPa) and nadir (5.0 MPa) values of the minimum principal stress were developed to the cement by the prostheses with D1 and D3 distal cross-sections on the internal and external surfaces of the cement layer. The average proximal cross-section effects on the maximum and minimum principal stresses were 4.3% and 18.3%, respectively. Meanwhile, the profile change influenced the maximum principal stress at the lateral side by 13.0% and the minimum principal stress at the medial side by 24.7%. The change in material showed an average effect of 12.9% and 21.6% on the maximum principal stress at the lateral and the minimum principal stress at the medial of the cement layer, respectively.



(a) Distal cross-section of prosthesis



(b) Proximal cross-section of prosthesis



(c) Profile of prosthesis

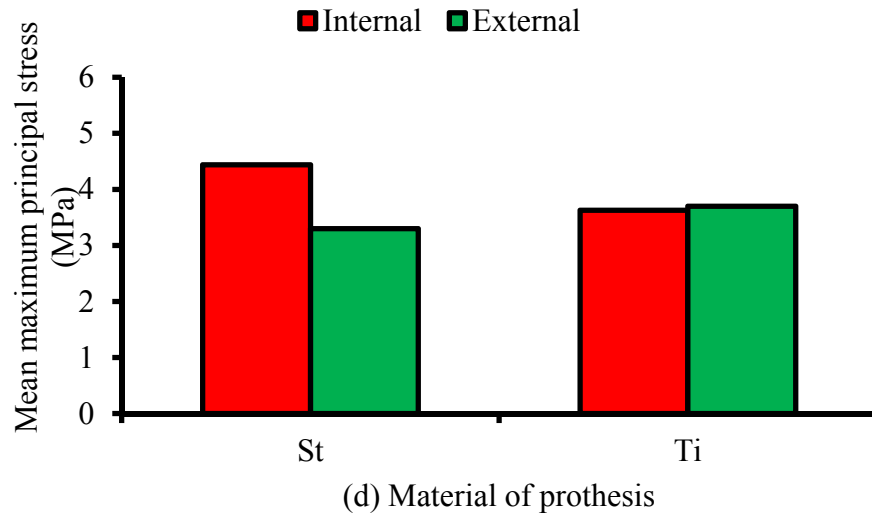
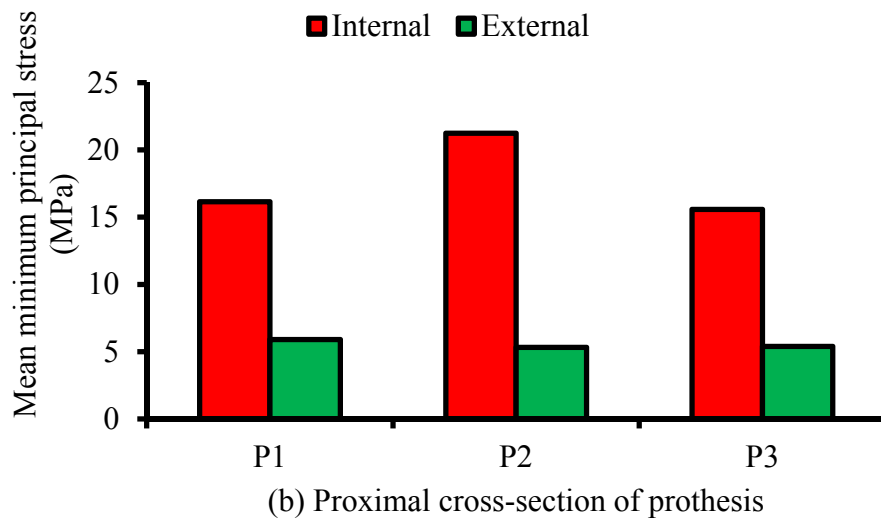
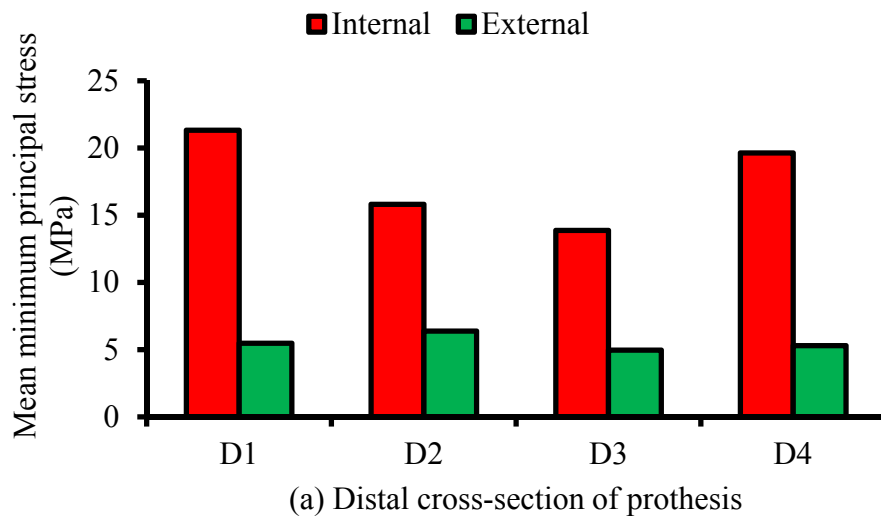


Figure 4.28: Variation in the mean maximum principal stress as a function of the (a) distal cross-section, (b) proximal cross-section, (c) profile, and (d) material of the prostheses



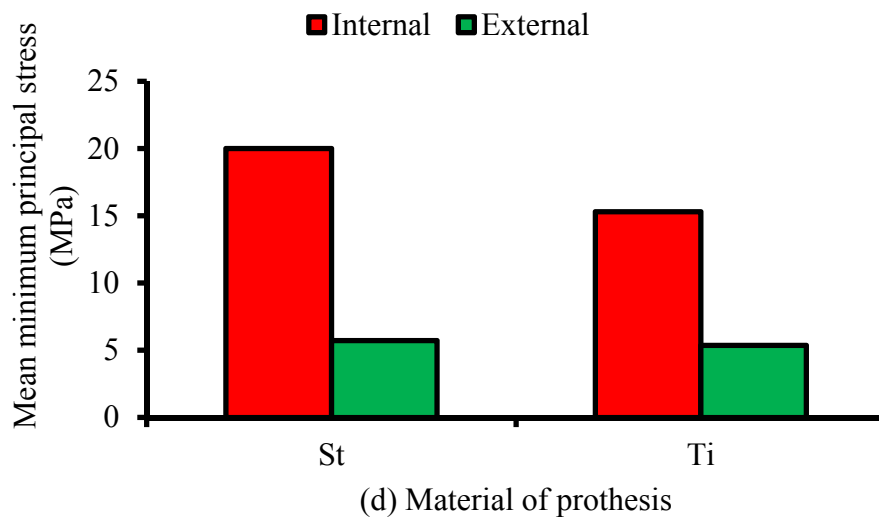
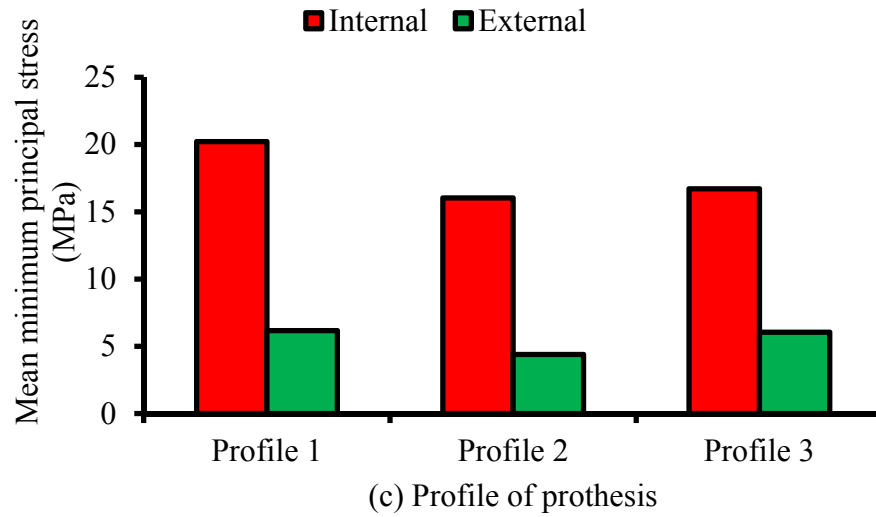


Figure 4.29: Variation in the mean minimum principal stress as a function of the (a) distal cross-section, (b) proximal cross-section, (c) profile, and (d) material of the prostheses

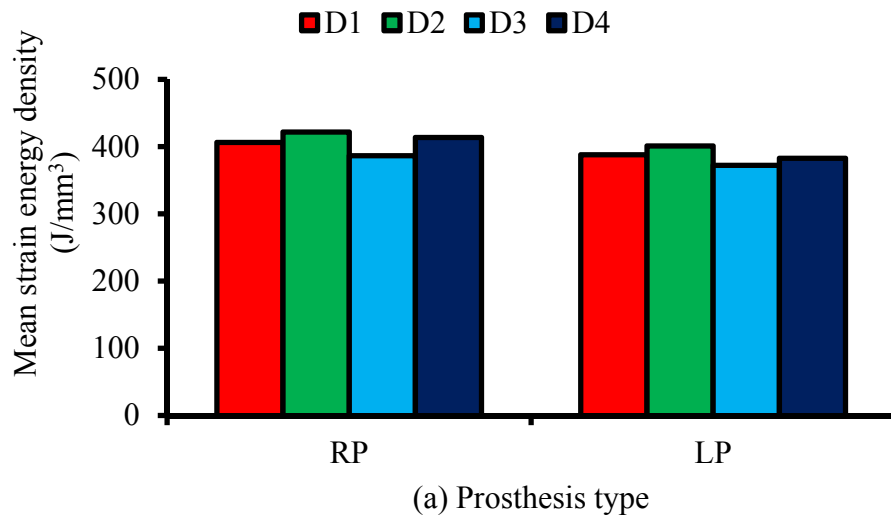
#### 4.2.6 Radial and longitudinal cemented functionally graded prostheses

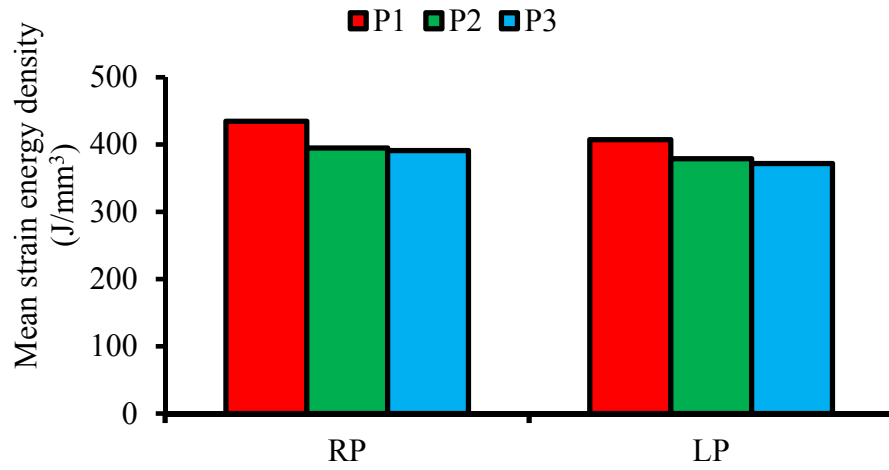
The results of FEA on cemented FG RPs and LPs are presented in the following section.

##### 4.2.6.1 Strain energy density

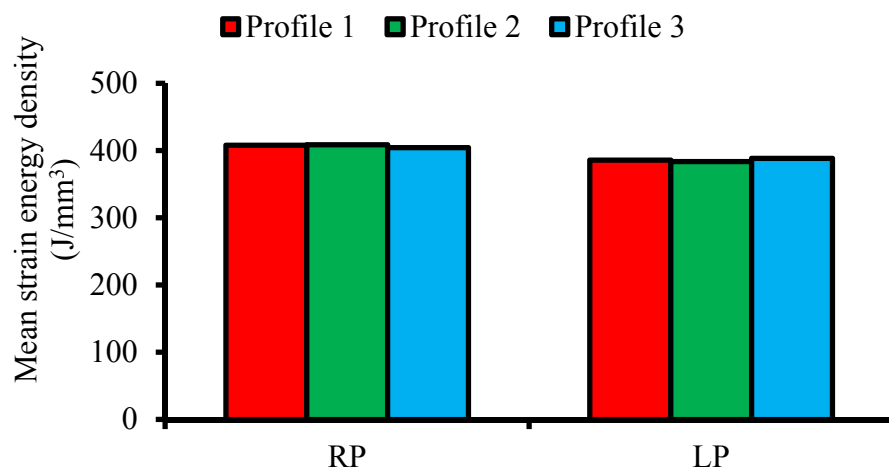
The SED values were derived from FEA results and plotted as bar charts in the two groups on the basis of the implanted RP and LP. Figure 4.30 shows the variation in

the SED for different distal cross-sections. The prostheses with distal cross-section of D2 exhibited 7.8% more SED than the other prostheses in both group of FG RPs and LPs, whereas the prostheses with distal cross-section of D3 produced minimum SED ( $386.61 \text{ J/mm}^3$  for RP and  $372.19 \text{ J/mm}^3$  for LP) in the proximal metaphysis of femur in both groups. The prostheses with proximal cross-sections of P1 and P3 caused maximum SEDs of  $434.80$  (RP) and  $407.26 \text{ J/mm}^3$  (LP) and minimum SEDs of  $391.27$  (RP) and  $371.80 \text{ J/mm}^3$  (LP) in the bone. The prostheses with Profile 2 induced maximum SED of  $408.68 \text{ J/mm}^3$  in the proximal metaphysis of femur in RP, whereas the prostheses with Profile 2 provoked minimum SED of  $383.60 \text{ J/mm}^3$  in the bone by LPs. The SED increased by approximately 24.6% with the increase in gradient index in both groups similar to cementless prostheses. The RPs provoked 8.3% more SED in the bone compared with the LPs.

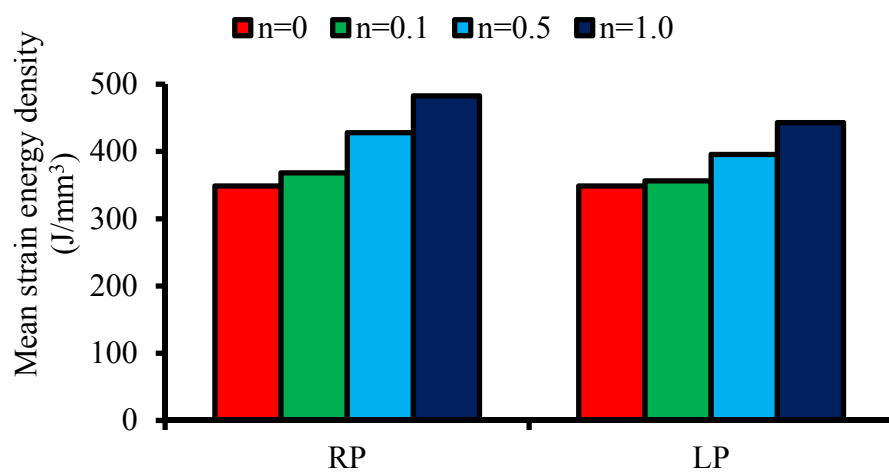




(b) Prosthesis type



(c) Prosthesis type



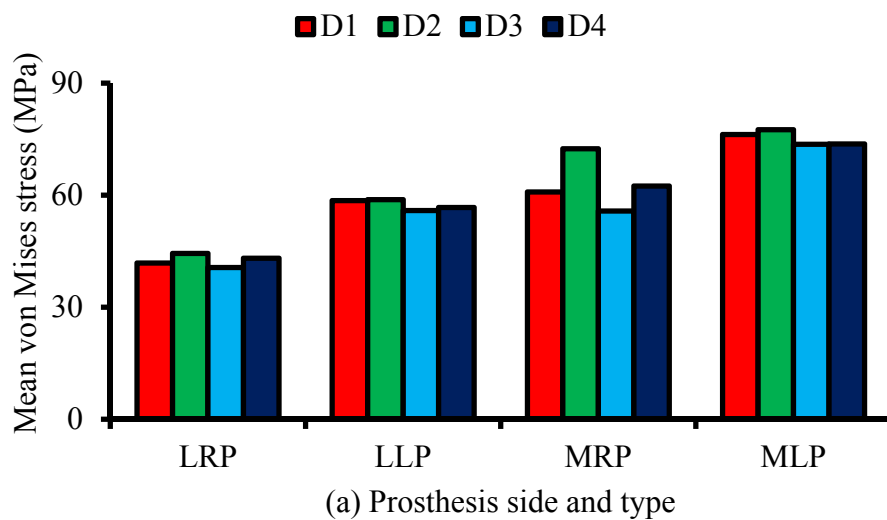
(d) Prosthesis type

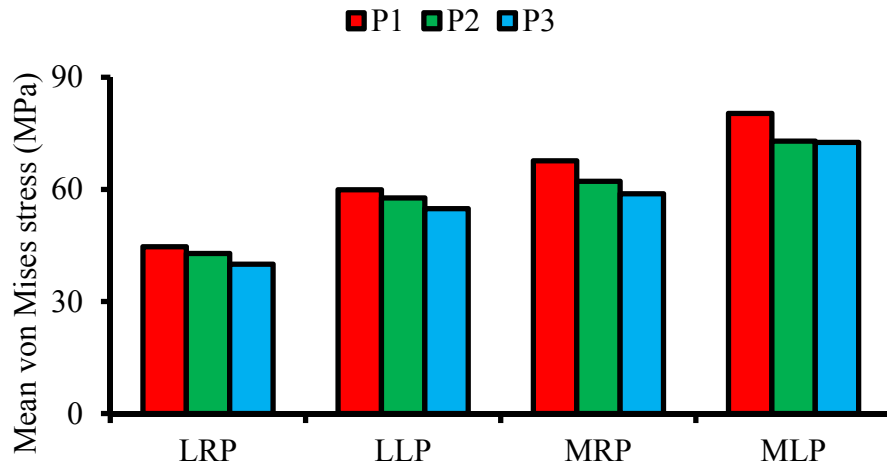
Figure 4.30: Variation in the strain energy density at the different (a) distal cross-sections, (b) proximal cross-sections, (c) profiles, and (d) gradient indices



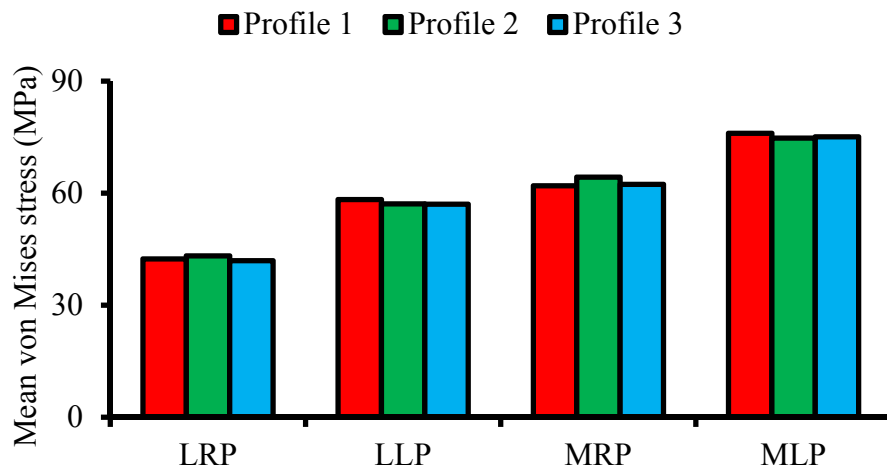
#### 4.2.6.2 Developed stress in the prostheses

The developed von Mises stress on the lateral and medial sides of the femoral prostheses are presented in Figure 4.31. The developed stress presented in bar charts are divided into four groups, namely, the lateral side of radial femoral prostheses (LRP), lateral side of longitudinal prostheses (LLP), medial side of radial prostheses (MRP), and medial side of longitudinal prostheses (MLP). The medial side of prostheses in both groups of cemented prostheses endured approximately 28.0% more stress. The prostheses with D2 and D3 distal cross-sections exhibited the maximum and minimum von Mises stresses, respectively. The von Mises stress declined with the increase in gradient index from 0 to 1 at the LRP, LLP, MRP, and MLP by approximately 71.4%, 27.0%, 54.2%, and 26.0%, respectively.

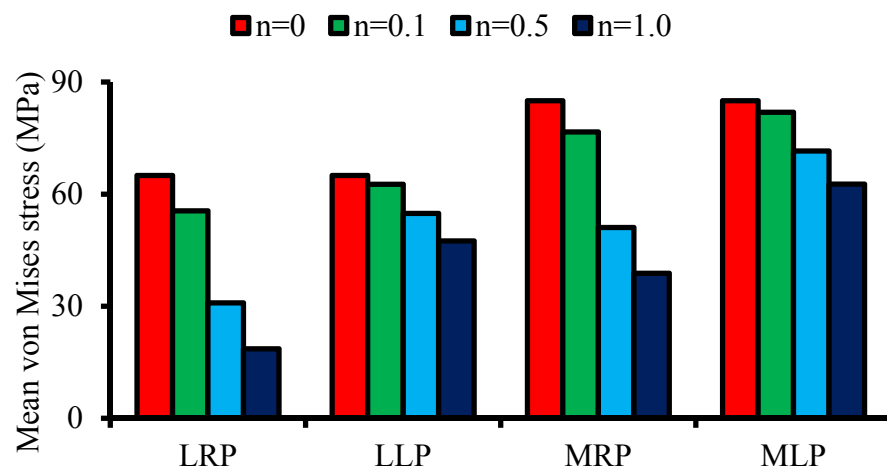




(b) Prosthesis side and type



(c) Prosthesis side and type

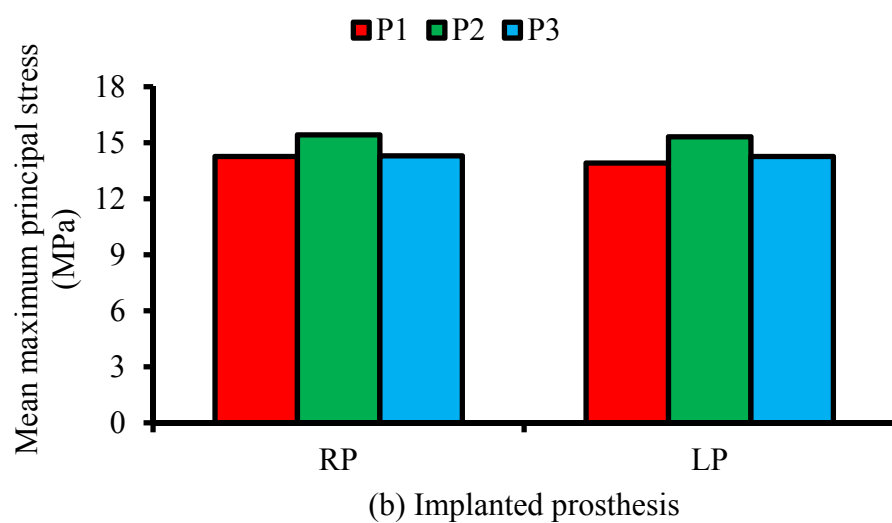
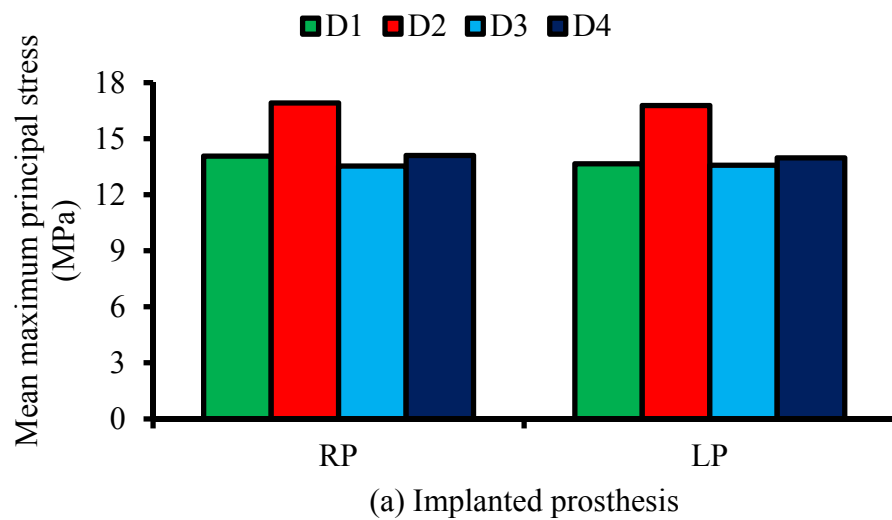


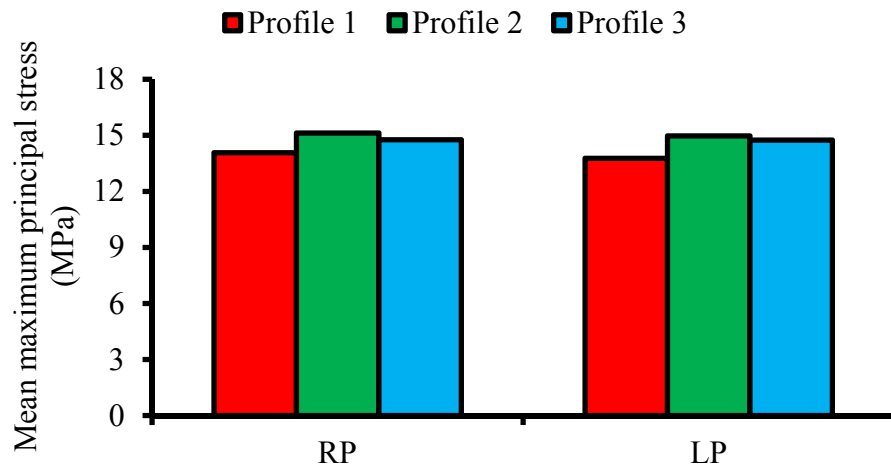
(d) Prosthesis side and type

Figure 4.31: Variation in the von Mises stress in various femoral prosthesis type and side at the different (a) distal cross-sections, (b) proximal cross-sections, (c) profiles, and (d) gradient indices

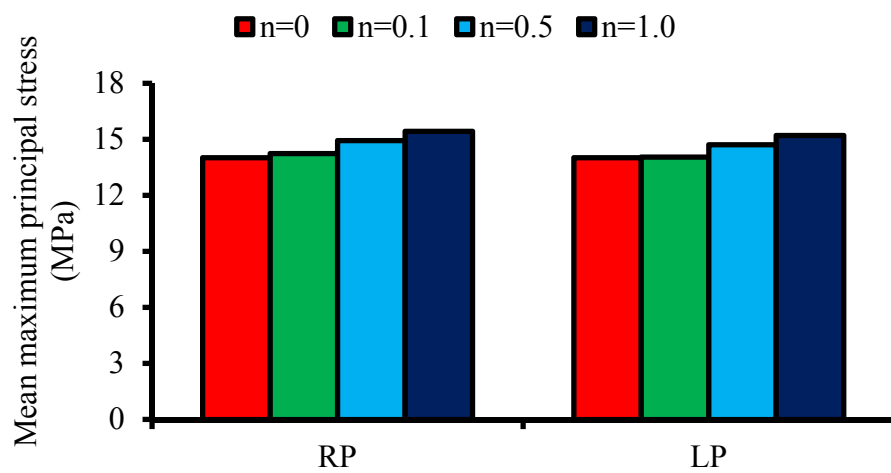
### 4.2.6.3 Developed stress in the bone

The mean values of the maximum principal stress at the lateral side and the minimum principal stress at the medial side of the femur are presented in Figures 4.32 and 4.33, respectively. The femur carried more maximum principal stress by the implantation of prostheses with D2 distal cross-section, P2 proximal cross-section, and Profile 2 regardless of radial or longitudinal change in Young's modulus. The stress also showed an increasing trend with the increase in gradient index.





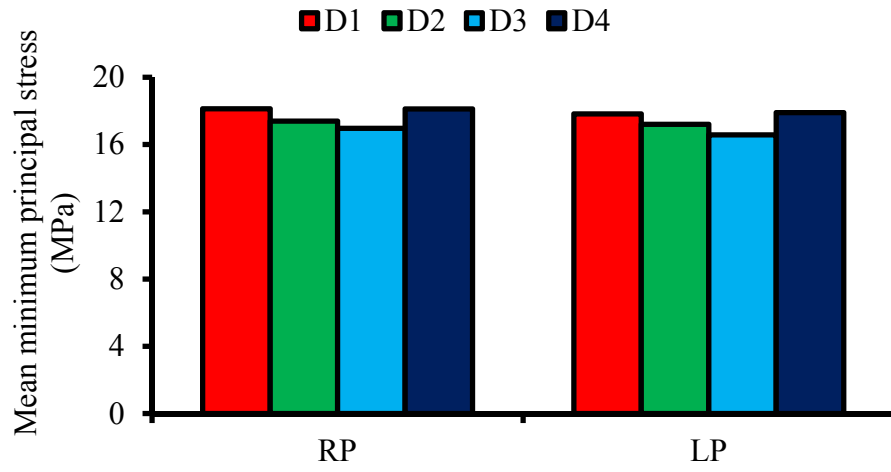
(c) Implanted prosthesis



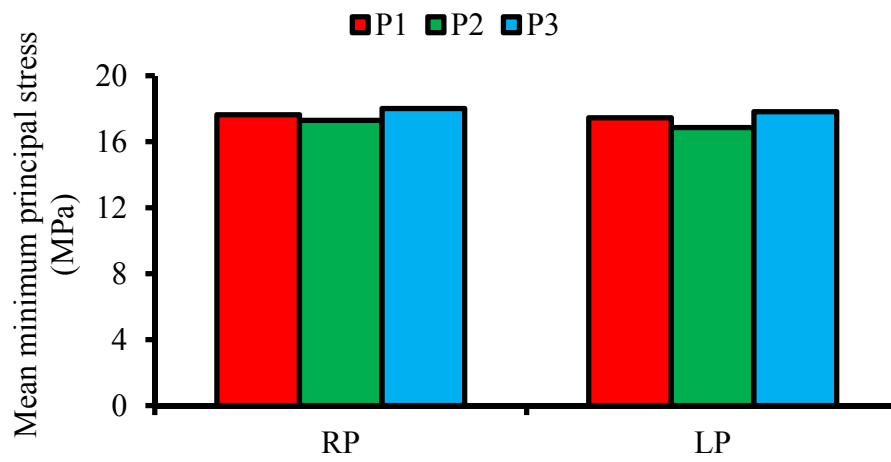
(d) Implanted prosthesis

Figure 4.32: Variation in the maximum principal stress at the lateral side of femur at the different (a) distal cross-sections, (b) proximal cross-sections, (c) profiles, and (d) gradient indices

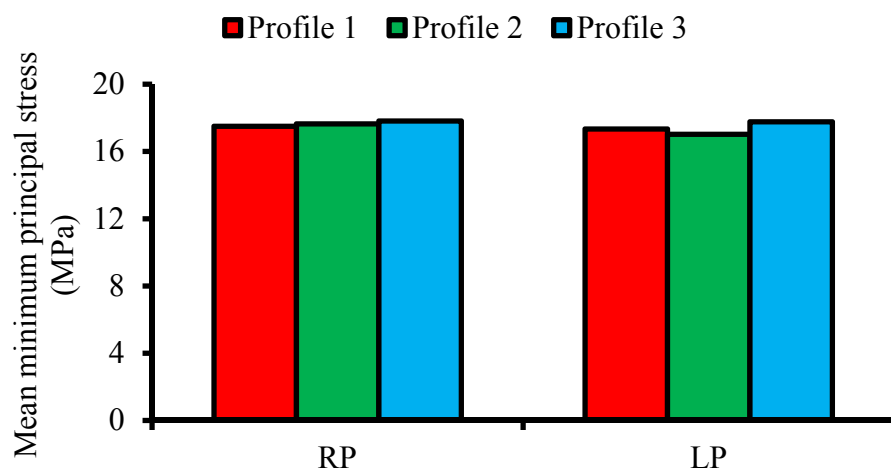
As shown in Figure 4.33, the prostheses with D2 and D4 distal cross-sections induced more minimum principal stress in the bone. By contrast, with the maximum principal stress, the prostheses with P2 proximal cross-section and Profile 2 caused less minimum principal stress in the bone. The minimum principal stress increased with the increase in gradient index. However, the minimum principal stress growth caused by the gradient index increase for the implantation of LP was less than that of RP.



(a) Implanted prosthesis



(b) Implanted prosthesis



(c) Implanted prosthesis

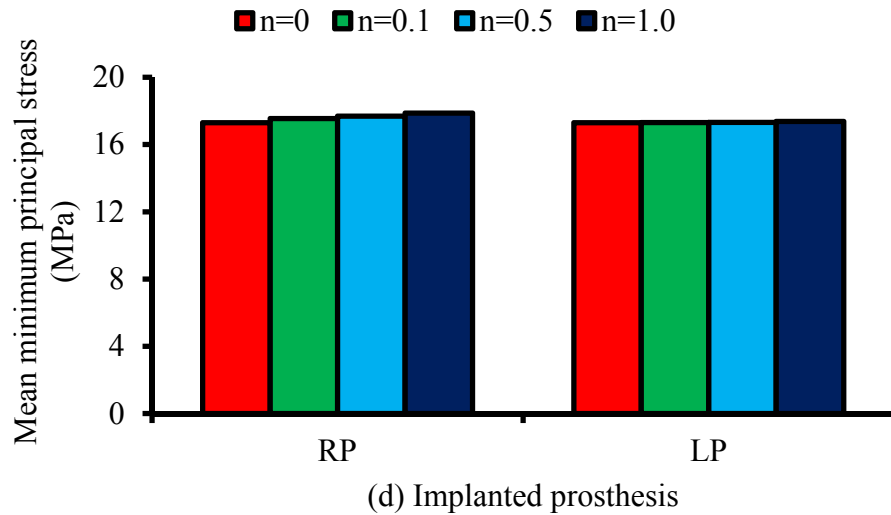
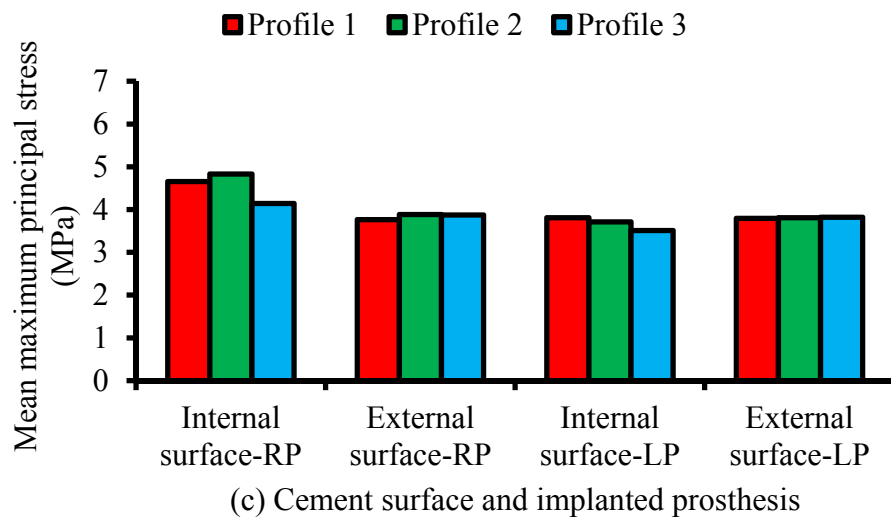
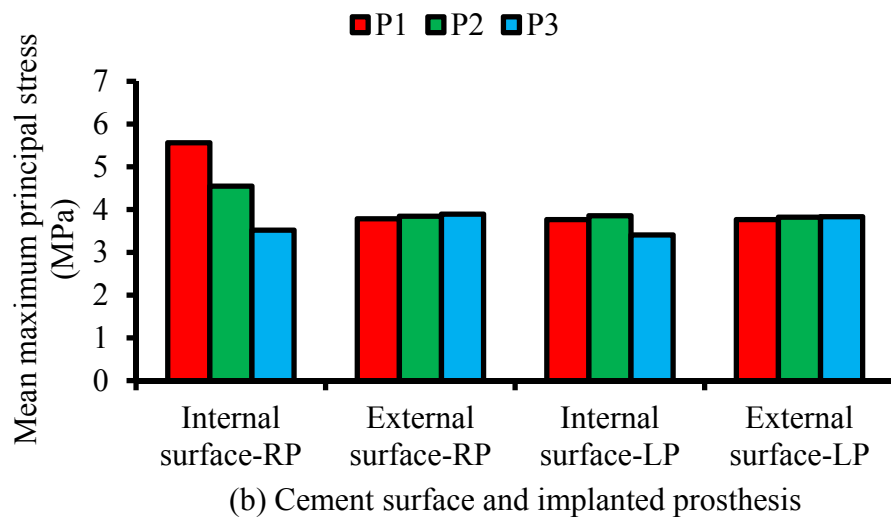
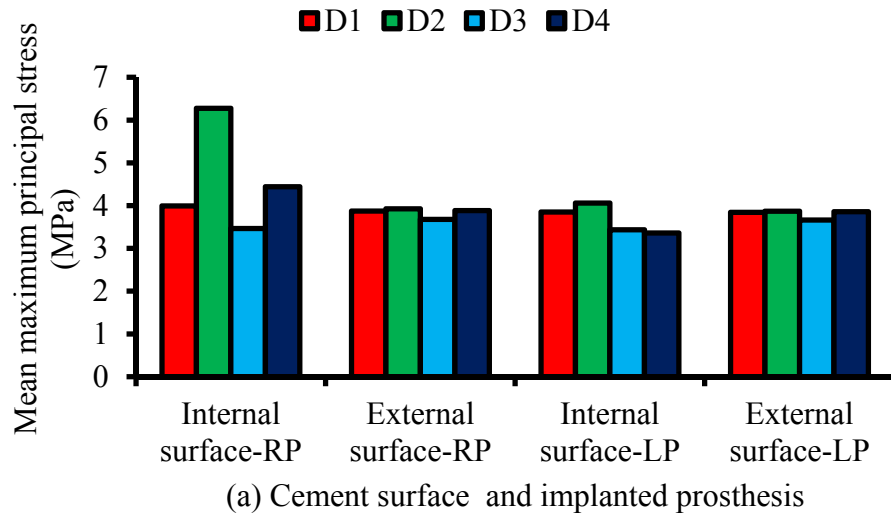


Figure 4.33: Variation in the minimum principal stress at the lateral side of the femur at the different (a) distal cross-sections, (b) proximal cross-sections, (c) profiles, and (d) gradient indices

#### 4.2.7 Developed stress in the cement

The maximum principal stresses developed at the lateral side on the internal and external surface of the cement because of the implantation of FG LP and RP are illustrated in Figure 4.34. RP induced approximately 10.7% more maximum principal stress in the cement than LP. The internal surface of the cement layer in RP carried 15.5% more maximum principal stress than the external surface, whereas the external surface in LP tolerated 3.5% more maximum principal stress than the internal surface. The prostheses with D2 cross-section stimulated higher stress in the cement than the prostheses with other distal cross-sections. RP with Profile 2 produced more maximum principal stress, whereas LP with Profile 1 induced less maximum principal stress in cement. The increase in gradient index led to the increase in the maximum principal stress in LP and RP by approximately 17.5% and 6.2%, respectively.



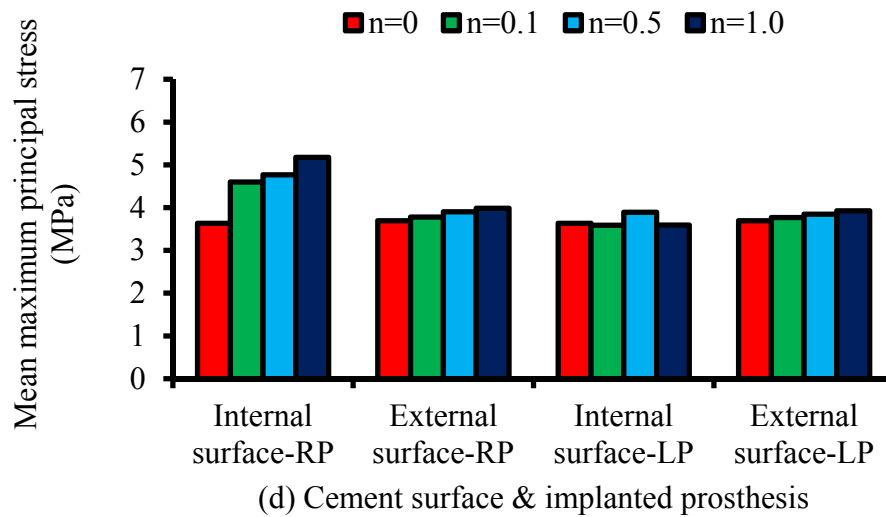
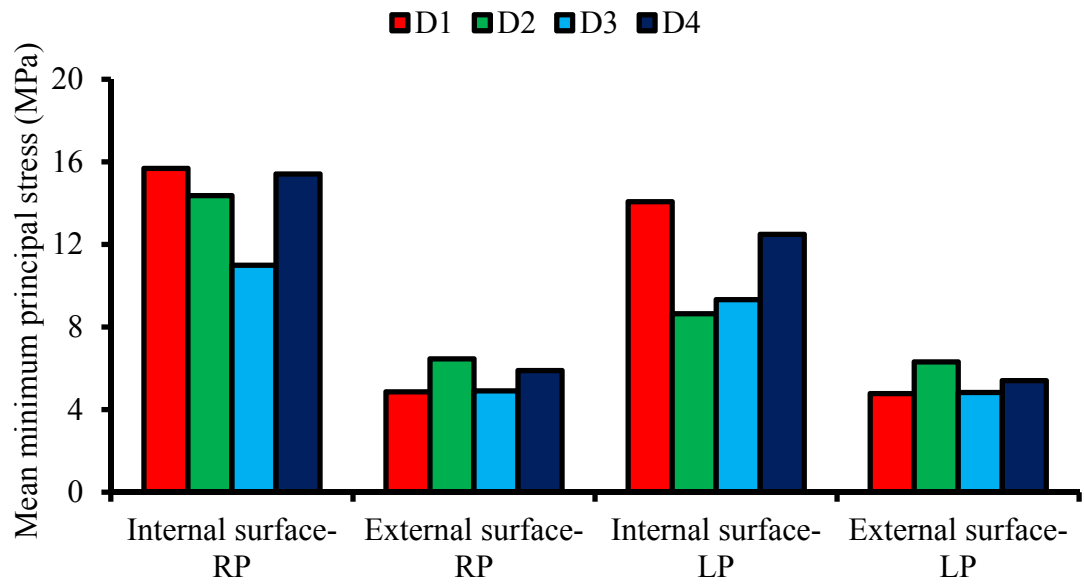


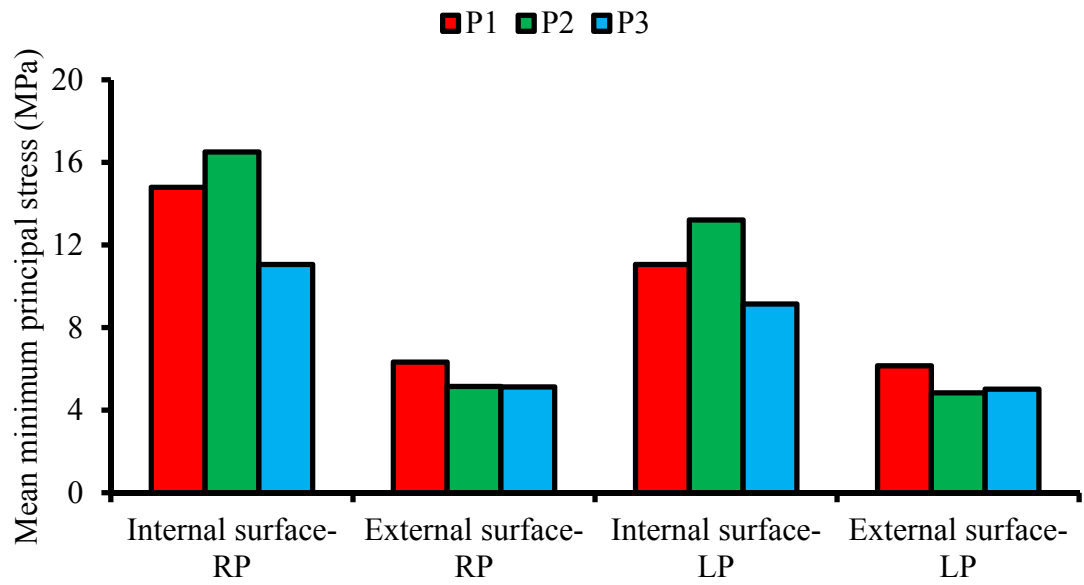
Figure 4.34: Variation in the maximum principal stress at the different (a) distal cross-sections, (b) proximal cross-sections, (c) profiles, and (d) gradient indices

The minimum principal stresses developed in the cement are shown in Figure 4.35. The internal surface of the cement layer showed approximately 56.4% more minimum principal stress compared with the external surface of the femur. The prostheses with distal cross-sections of D1 and D4 caused more stress in the cement. The prostheses with proximal cross-sections of P2 and P1 stimulated more stress at the internal and external surfaces, respectively. The minimum principal stress declined with increase in gradient index at the interface surface of the cement layer. The minimum principal stresses decreased with the increase in gradient index by 14.0% in LP and 27.9% in the RP.

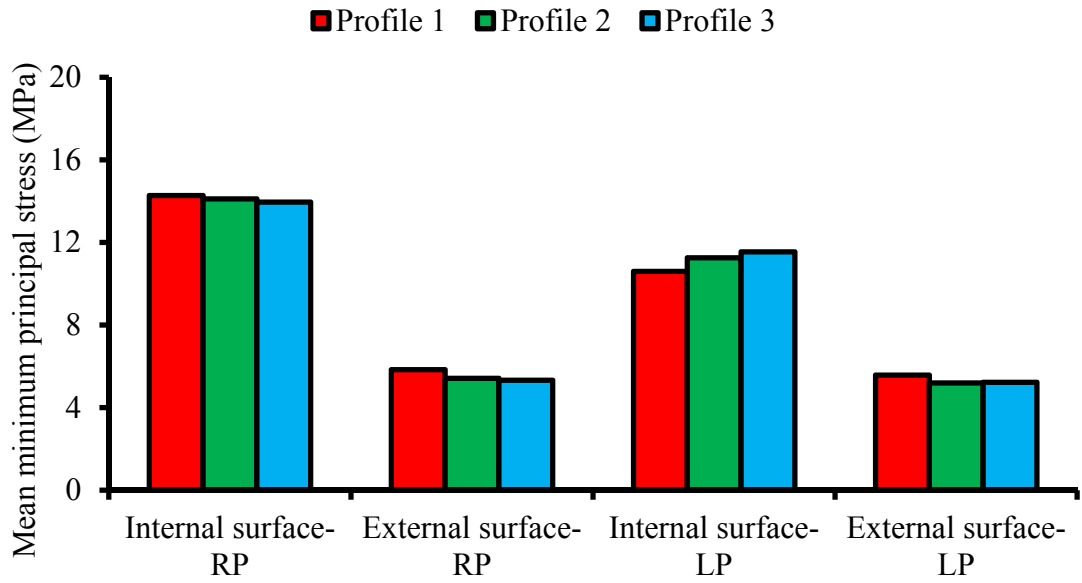




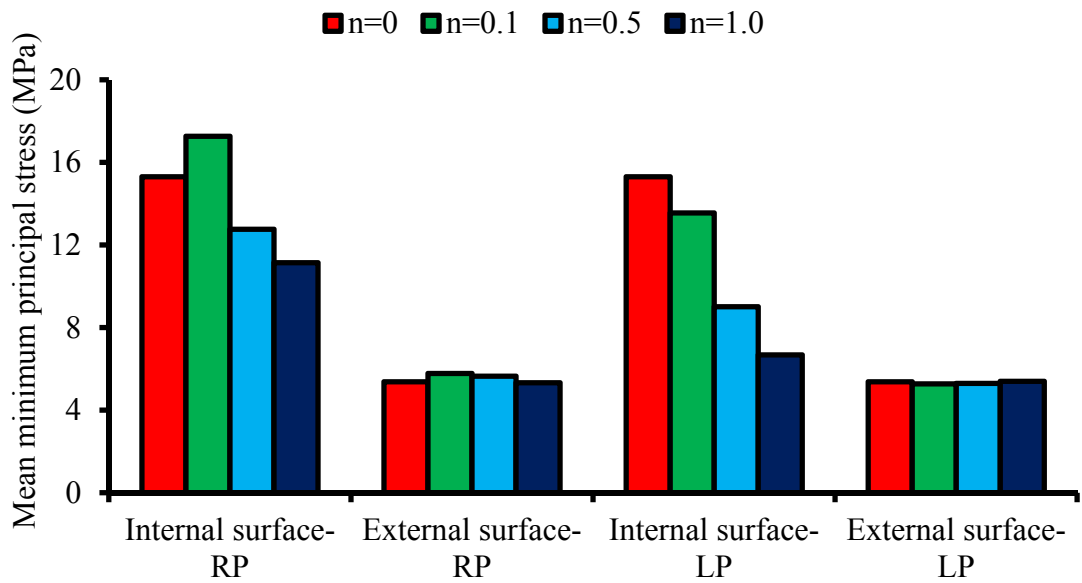
(a) Cement surface and implanted prosthesis



(b) Cement surface and implanted prosthesis



(c) Cement surface and implanted prosthesis



(d) Cement surface and implanted prosthesis

Figure 4.35: Variation in the minimum principal stress at the different (a) distal cross-sections, (b) proximal cross-sections, (c) profiles, and (d) gradient indices

## **4.2.8 Circumferential cracks in cement**

Cracks at the cement–femoral prosthesis interface or cement–bone interface endanger the femoral prosthesis stability, which can ultimately cause the THR to collapse. Therefore, circumferential cracks were examined for the cemented implanted femur, and the SIFs were measured along the crack front in the cement layer. The findings are presented in this section. SIFs are plotted as a function of crack front length in a counterclockwise path, with start point at the corner of the lateral posterior in the five main phases of gait: heel strike, single-leg stance, push off, toe off, and swing phase commencement. The presented results were divided into the SIFs for internal, external, and internal–external cracks.

### **4.2.8.1 Internal circumferential crack**

#### **4.2.8.1.1 $K_I$ behavior**

Figure 4.36 shows the variation in  $K_I$  along the crack front in different gait phases.  $K_I$  manifested the same trend in all gait phases regardless of the crack location.  $K_I$  in all sections (25, 50, 75, and 100 mm) and in three gait stages (single-leg stance, toe off, and push off) commenced and finalized at the maximum values, with minimum SIFs at the middle of the crack front length. In addition, the heel strike and swing phases demonstrated an almost sinusoidal behavior with opposite trends. The maximum absolute values of  $K_I$  for all crack models occurred in the single-leg stance and push off phases. However, the minimum absolute  $K_I$  value was recorded during the swing phase.

The absolute minimum and maximum values of the  $K_I$  steadily declined along the length of the cement mantle ( $z$  direction) except for  $K_{I,C100}$ , which presented an

unexpected positive trend compared with  $K_{I,C75}$  because of the increase in the induced stress to the cement at the beneath of the prosthesis neck.  $K_I$  decreased during the heel strike (89.5%), single-leg stance (91.2%), push off (87.6%), toe off (86.8%), and swing (88.6%) phases at the lateral side of the cement layer. Moreover, the absolute values of  $K_I$  in the medial side of the cement layer in the heel strike, single-leg stance, push off, and toe off declined by approximately 69.4%, 51.4%, 47.3%, and 61.5%, respectively.

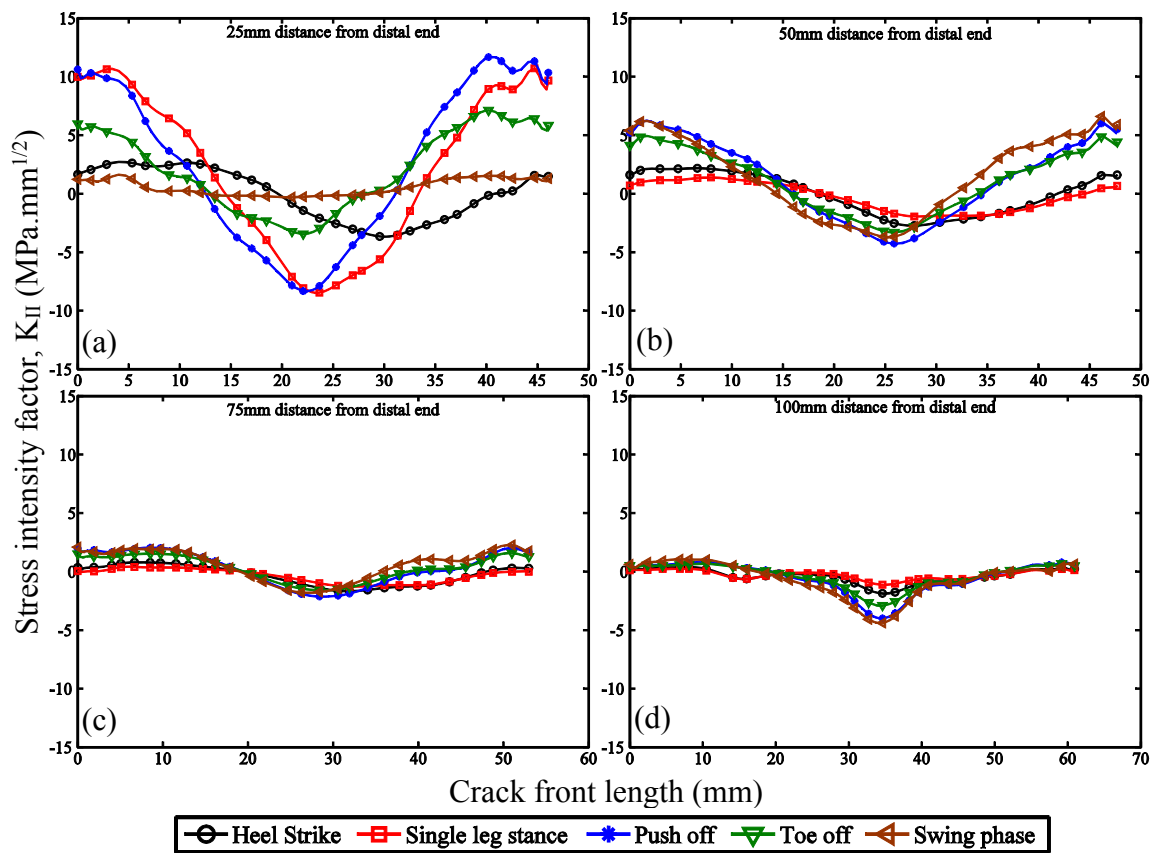


Figure 4.36:  $K_I$  variation along the crack front length at different crack locations: (a) 25, (b) 50, (c) 75, and (d) 100 mm

#### 4.2.8.1.2 $K_{II}$ behavior

Figure 4.37 shows the  $K_{II}$  variations versus the crack front length.  $K_{II}$  evidently fluctuated along the crack front length with the highest peak at the middle of the graph. Meanwhile, the peak amplitude of the graphs slightly increased with movement toward the distal end.

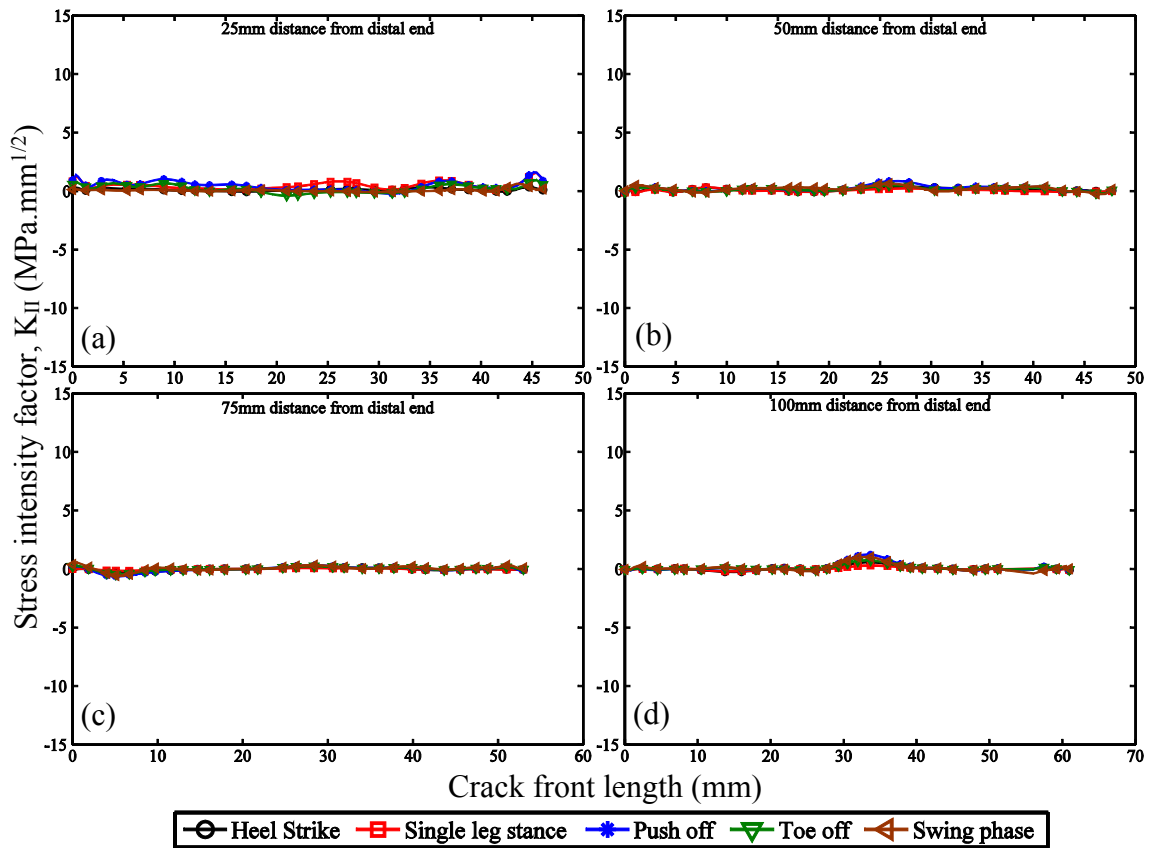


Figure 4.37:  $K_{II}$  variations along the crack front length at different crack locations: (a) 25, (b) 50, (c) 75, and (d) 100 mm

#### 4.2.8.1.3 $K_{III}$ behavior

Figure 4.38 illustrates the  $K_{III}$  behavior along the crack front. It shows a similar sinusoidal graph in different gait phases at four various levels. The three gait phases (push off, single-leg stance, and toe off) presented descending amplitudes in the  $z$  direction. The SIFs in the swing phase graph fluctuated with nearly the same trends in

all sections. However, the heel strike phase exhibited a sinusoidal behavior with a length lag from the starting points and a decreasing amplitude along the  $z$  direction.

Based on the graph, the values of  $K_{III}$  decreased during gait, along with the increasing distance from the distal end at the anterior during the heel strike (73.1%), single-leg stance (80.0%), push off (73.0%), toe off (75.0%), and swing (28.6%) phases. Similarly, at the posterior side of the cement layer, the absolute values of  $K_{III}$  declined by 68.4%, 70.0%, 67.6%, 76.2%, and 0.0% during the heel strike, single-leg stance, push off, toe off, and swing phases, respectively.

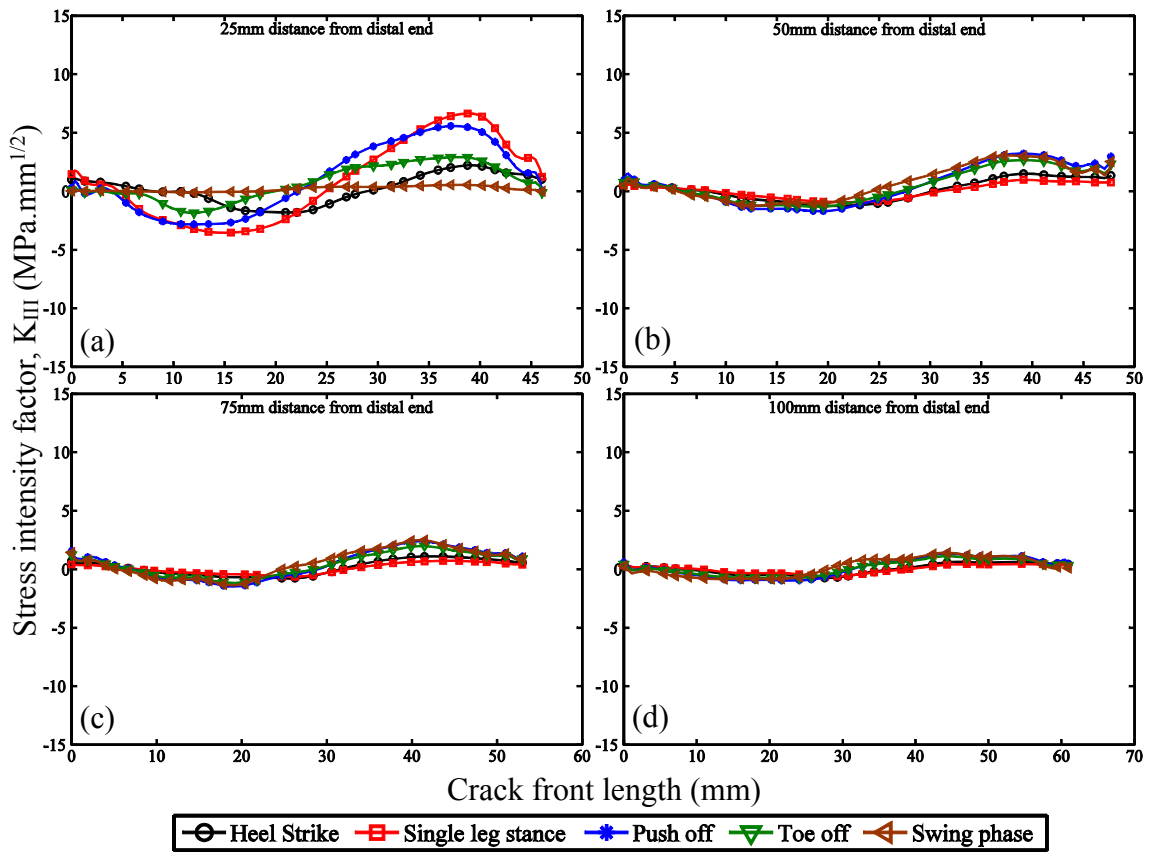


Figure 4.38:  $K_{III}$  variation along the crack front length at different crack locations: (a) 25, (b) 50, (c) 75, and (d) 100 mm

## 4.2.8.2 External circumferential crack

### 4.2.8.2.1 $K_I$ Behavior

Figure 4.39 presents the  $K_I$  variations for the external circumferential crack as a function of crack front length. The trend of SIFs for the external crack along the crack front was similar to the SIF behavior at the crack front in the internal circumferential cracks. The highest values of SIFs were observed in the distal part, and SIFs decreased toward the proximal portion of the cement layer.

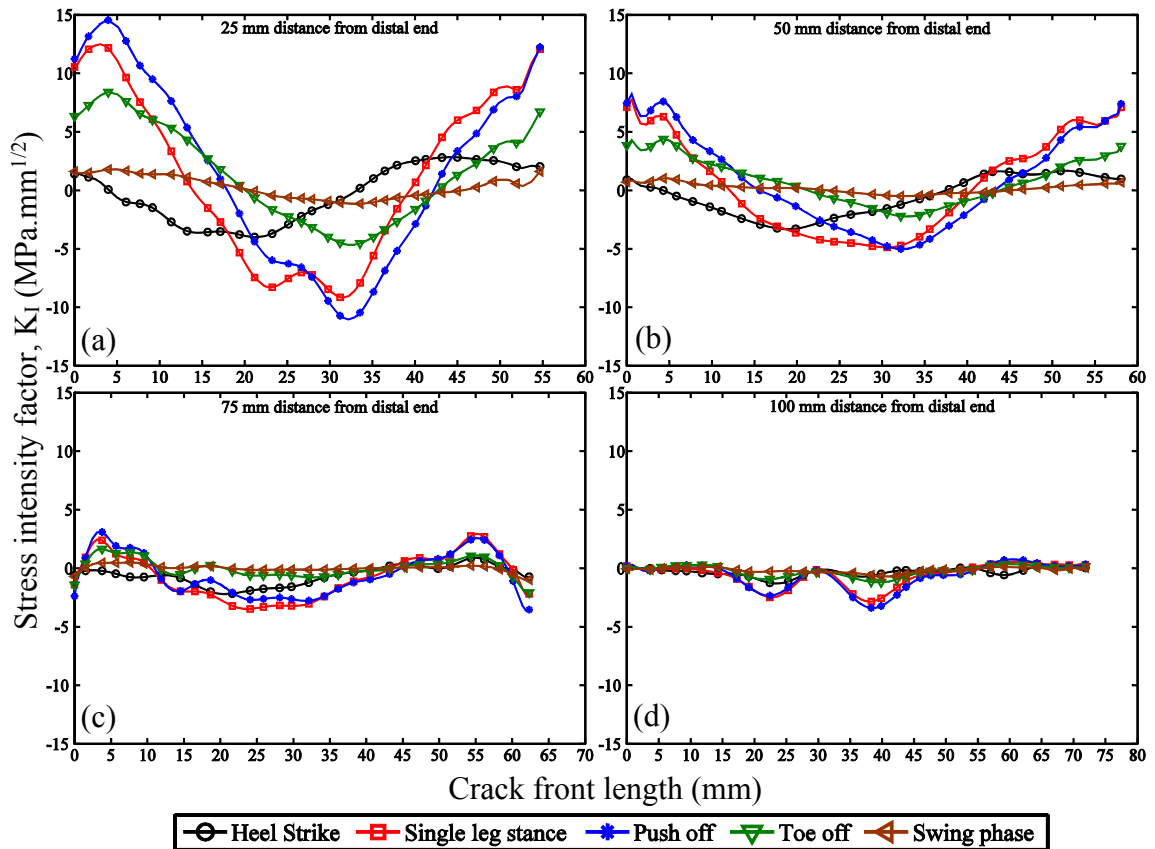


Figure 4.39:  $K_I$  variation along the crack front length at different crack locations: (a) 25, (b) 50, (c) 75, and (d) 100 mm

#### 4.2.8.2.2 $K_{II}$ behavior

$K_{II}$  trend as a function of crack front length is portrayed in Figure 4.40. Compared with the  $K_I$  values, the  $K_{II}$  values were small and close to zero, similar to the  $K_{II}$  in internal circumferential cracks. The  $K_{II}$  close to the distal and proximal ends showed peaks in single-leg stance and push off phases.

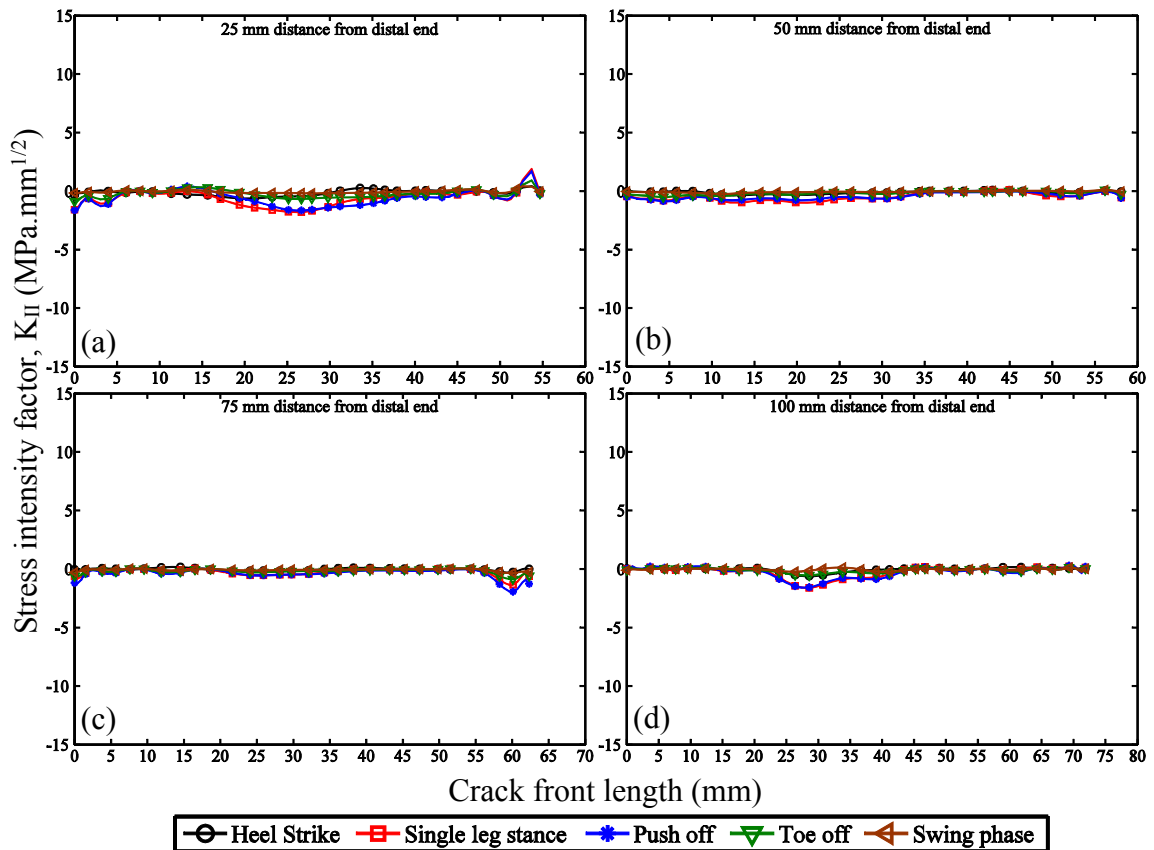


Figure 4.40:  $K_{II}$  variation along the crack front length at different crack locations (a) 25, (b) 50, (c) 75, and (d) 100 mm

#### 4.2.8.2.3 $K_{III}$ behavior

The  $K_{III}$  variations along the crack front length were plotted and presented in Figure 4.41.  $K_{III}$  for external crack showed a trend similar to that of  $K_{III}$  at the internal surface of the cement layer. Similar to  $K_I$ ,  $K_{III}$  had maximum values in the distal portion



of the cement layer, and it showed a descending trend from the distal to the proximal portion.

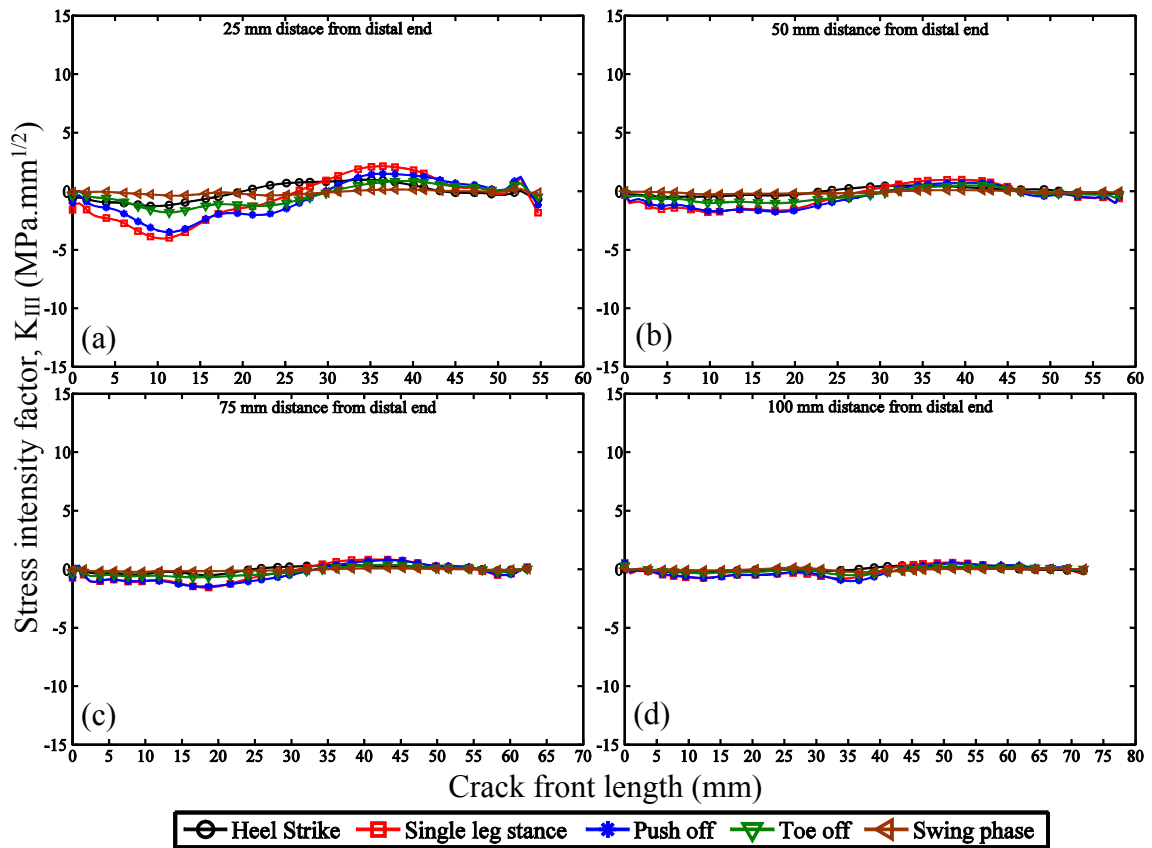


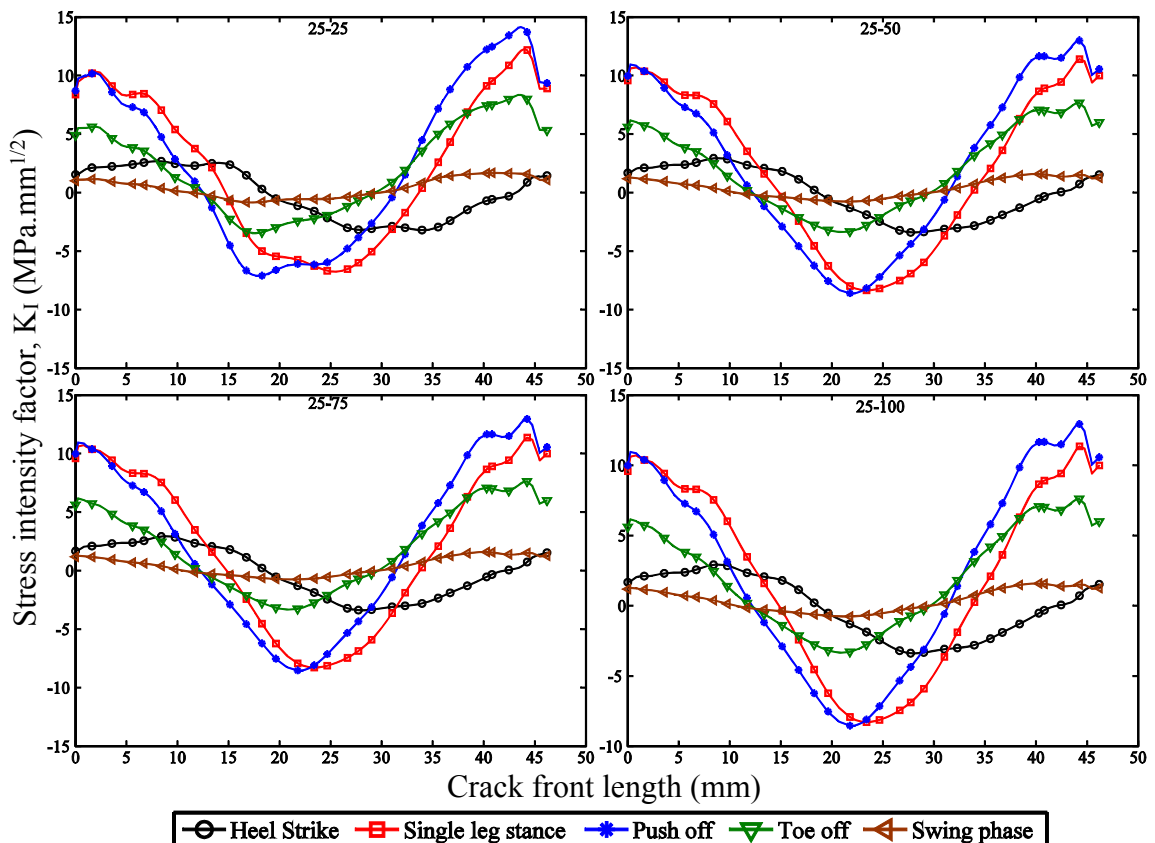
Figure 4.41:  $K_{III}$  variations along the crack front length at different crack locations: (a) 25, (b) 50, (c) 75, and (d) 100 mm

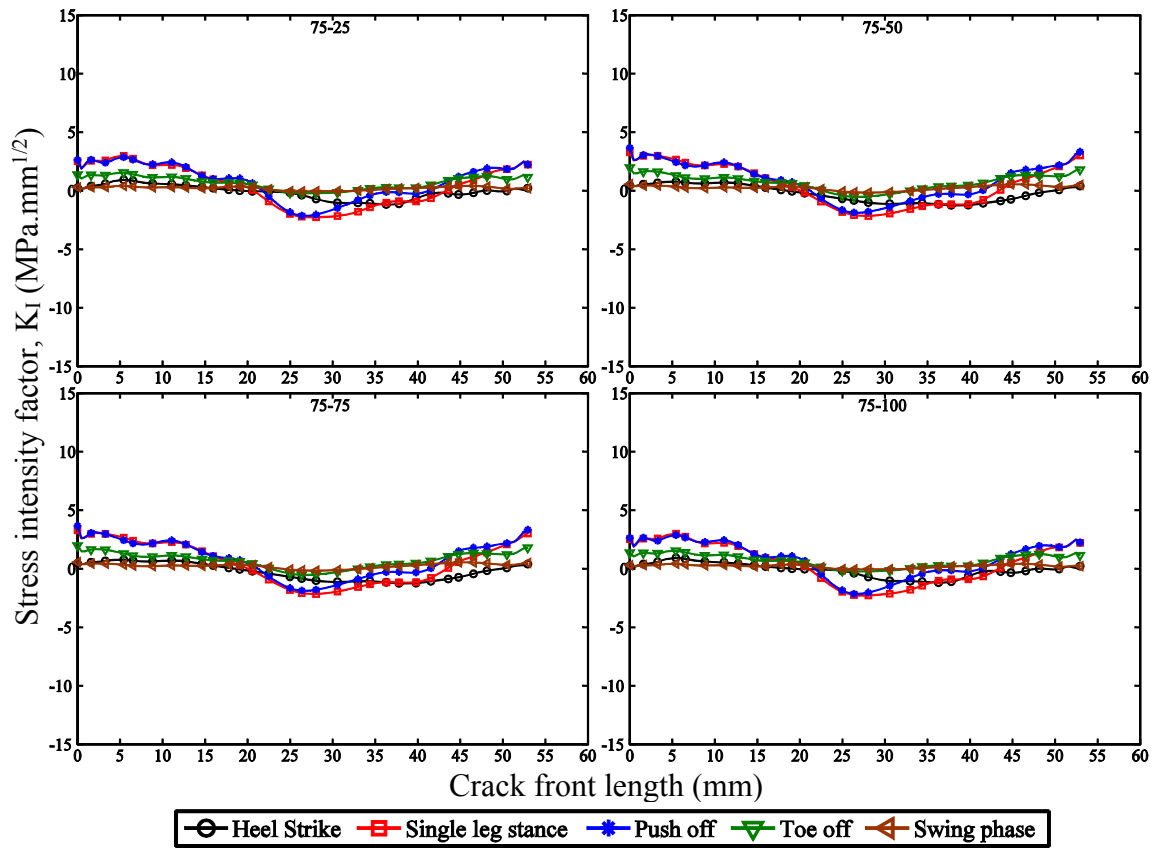
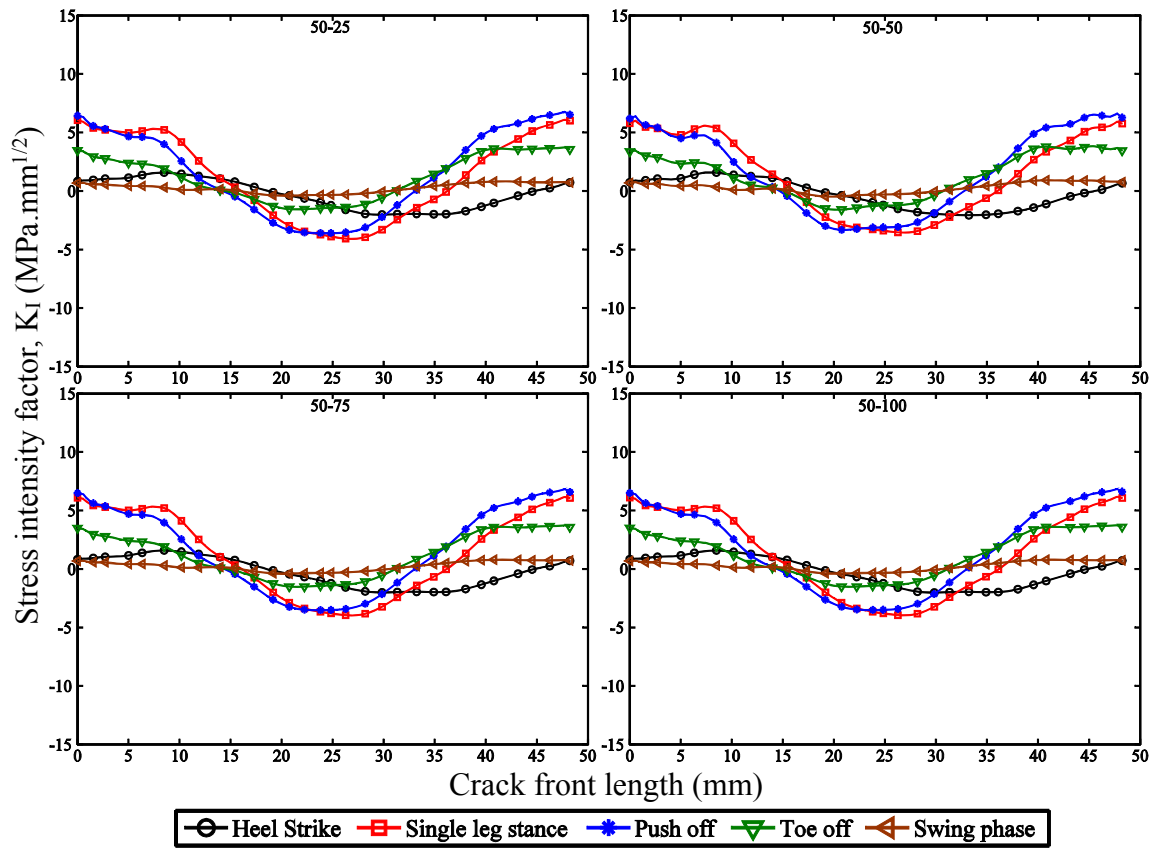
#### 4.2.8.3 Internal–external circumferential crack

In this section, circumferential crack interactions were examined by placing cracks on the external and internal surfaces of the cement layer. The results of SIFs were taken at modes I and III. Given that the SIFs at mode II were very small compared with those at modes I and III, mode II values were not considered.

#### 4.2.8.3.1 $K_I$ behavior at the internal and external surfaces

The SIF behavior at the crack front for the interaction of the internal and external cracks is illustrated in Figures 4.42 and 4.43. In the figure title, the first number signifies the crack position at the internal surface, and the second number shows the location of the crack on the external surface of the cement layer. The  $K_I$  for the cracks at different positions, regardless of internal or external location, started from a maximum value and gradually decreased to a minimum value. Afterward, the  $K_I$  trend increased to the end of the crack front. The  $K_I$  variations along the crack front created concave plots except at the heel strike phase. The  $K_I$  behavior plot along the crack front in the heel strike phase at the internal surface comprised convex and concave plots. The  $K_I$  behavior in the heel strike phase on the external surface created concave and convex plots. The single-leg stance and push off phases had the maximum absolute values of  $K_I$  among the different phases of gait cycles. In addition, the absolute value of  $K_I$  decreased by attaining distance from the distal end.





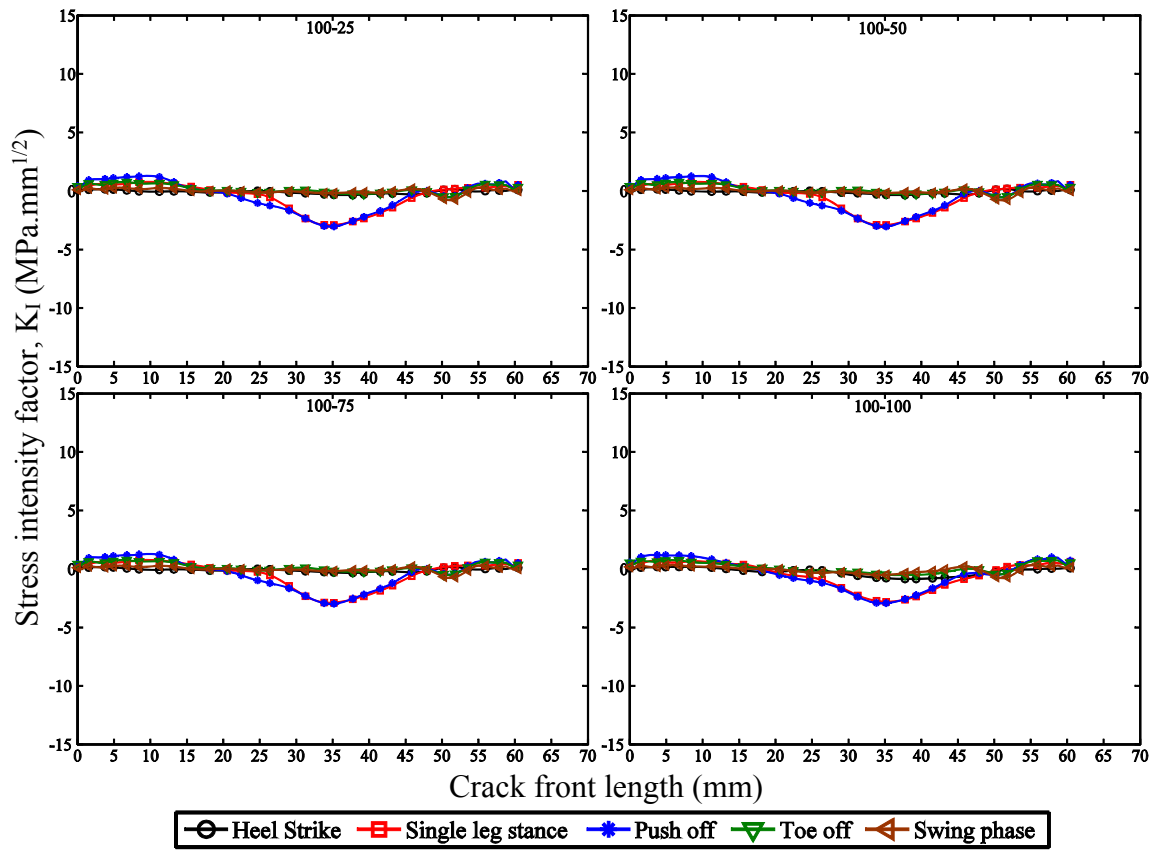
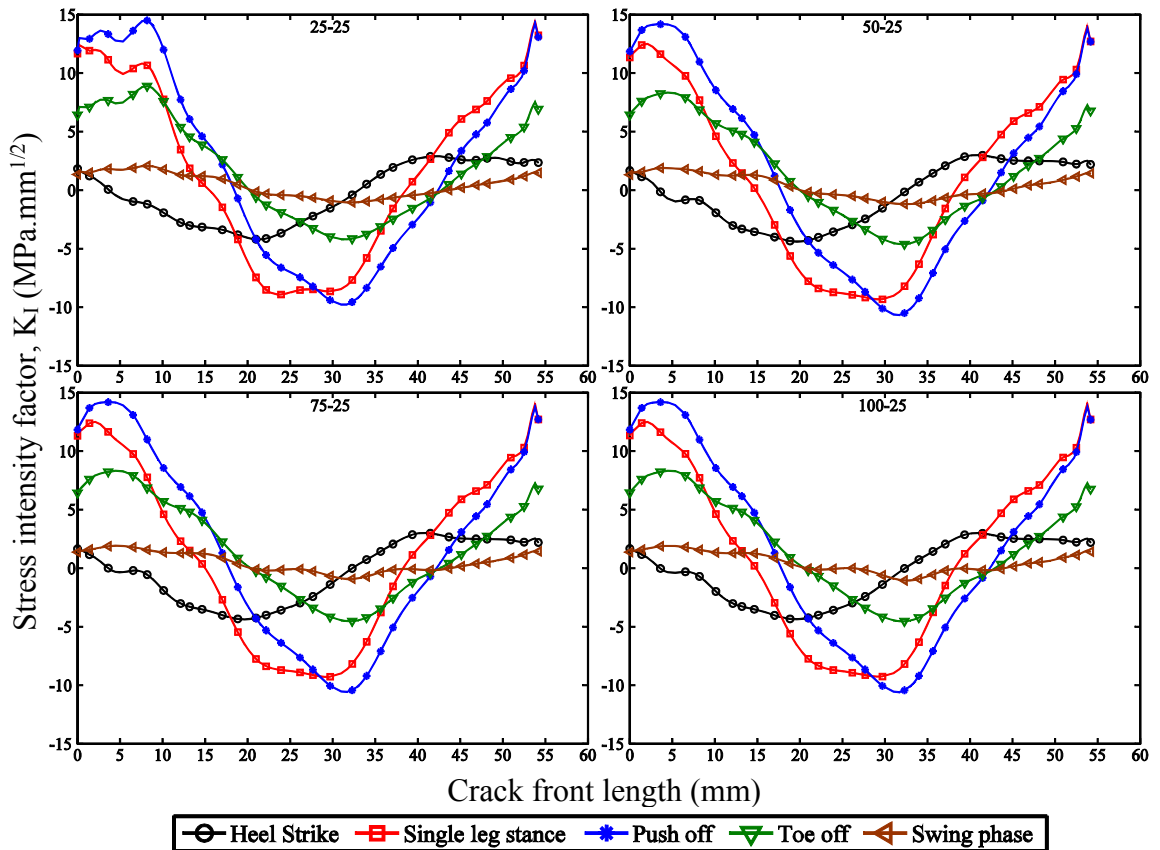
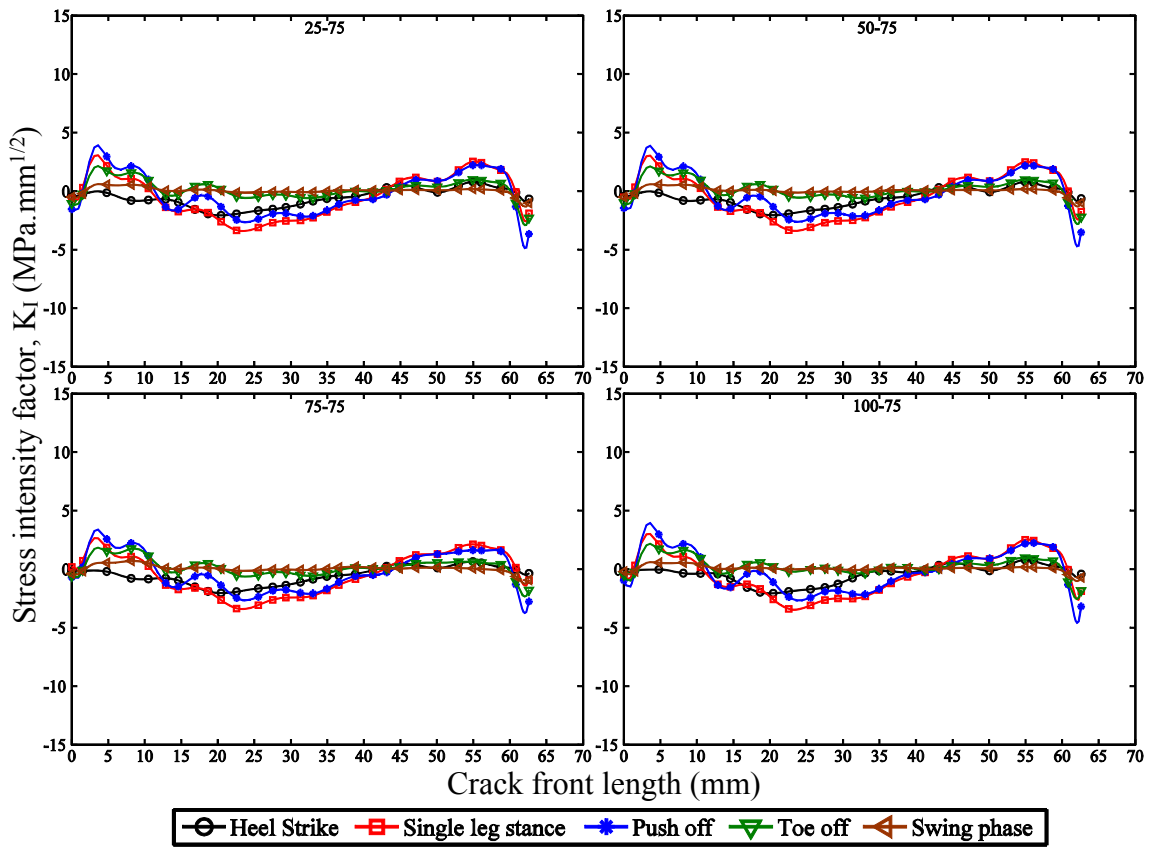
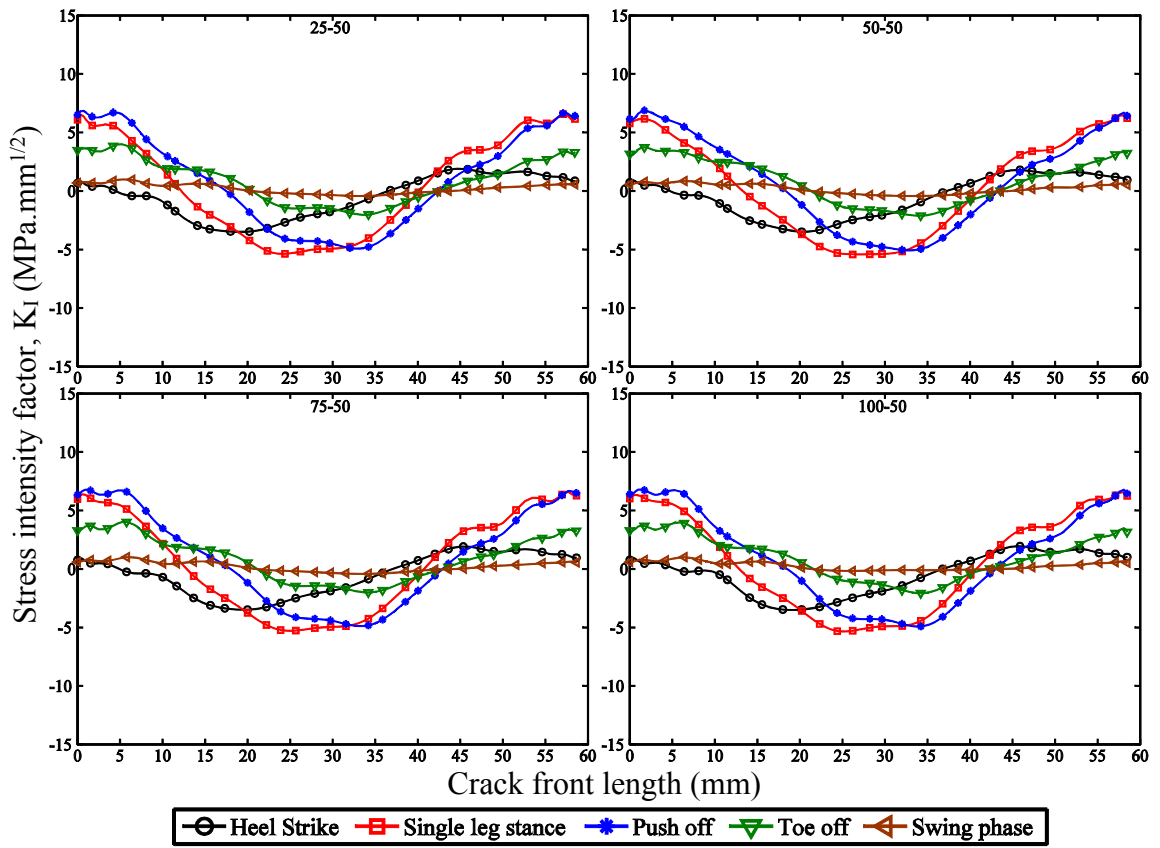


Figure 4.42:  $K_I$  variation along the crack front on the internal surface: (a)  $I_{25}$ , (b)  $I_{50}$ , (c)  $I_{75}$ , and (d)  $I_{100}$  interactions with  $E_{25}$ ,  $E_{50}$ ,  $E_{75}$ , and  $E_{100}$





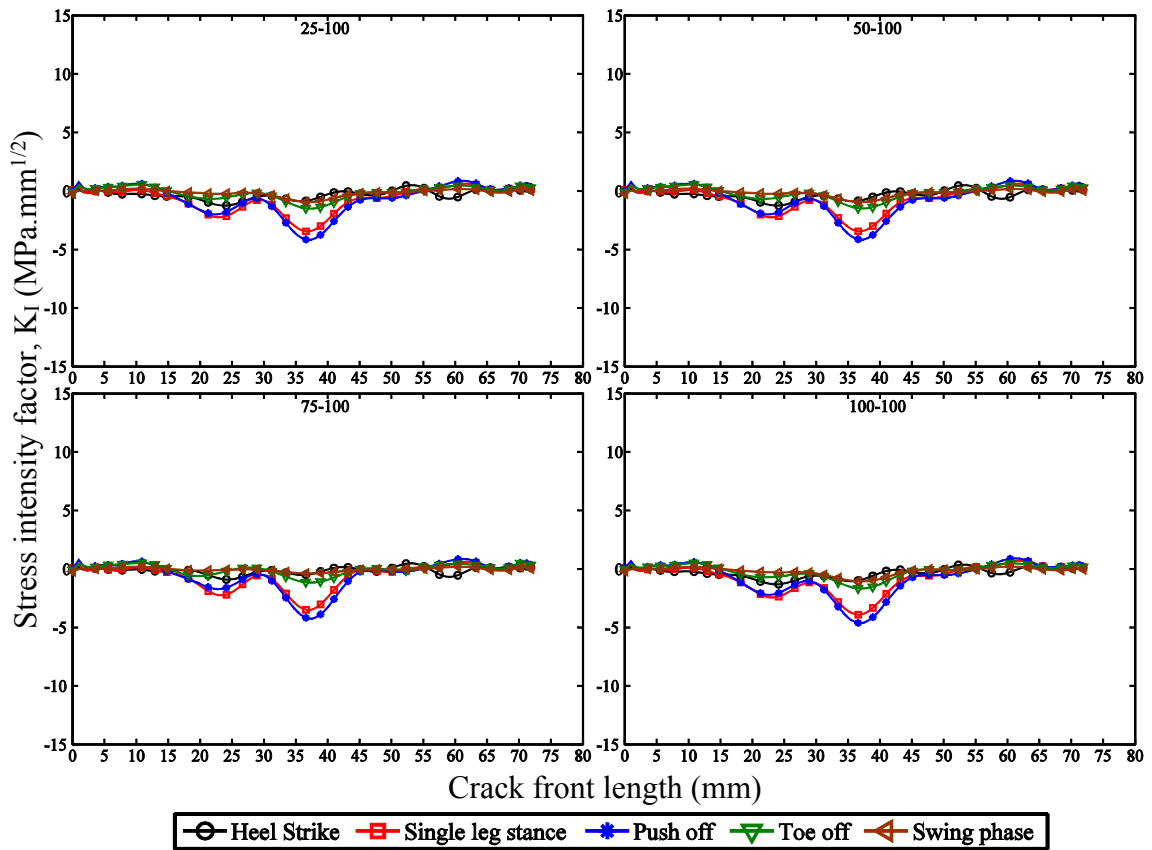
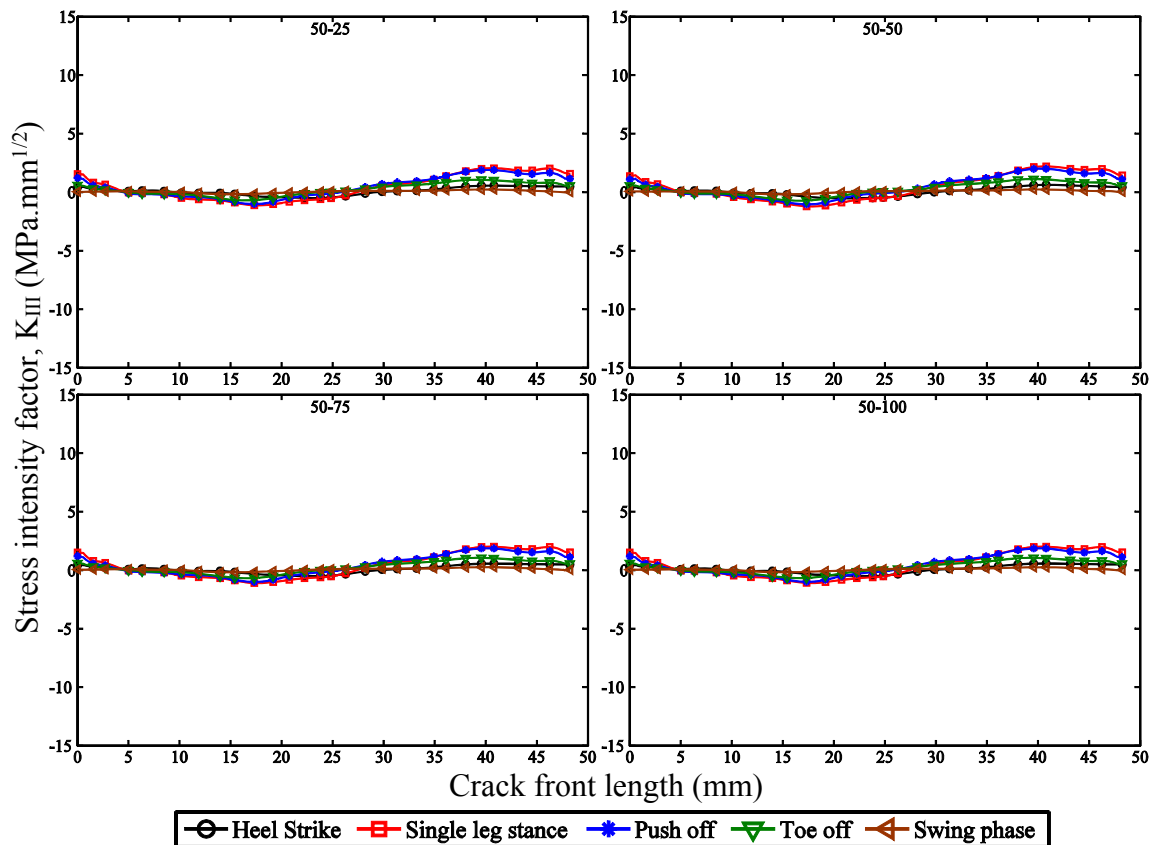
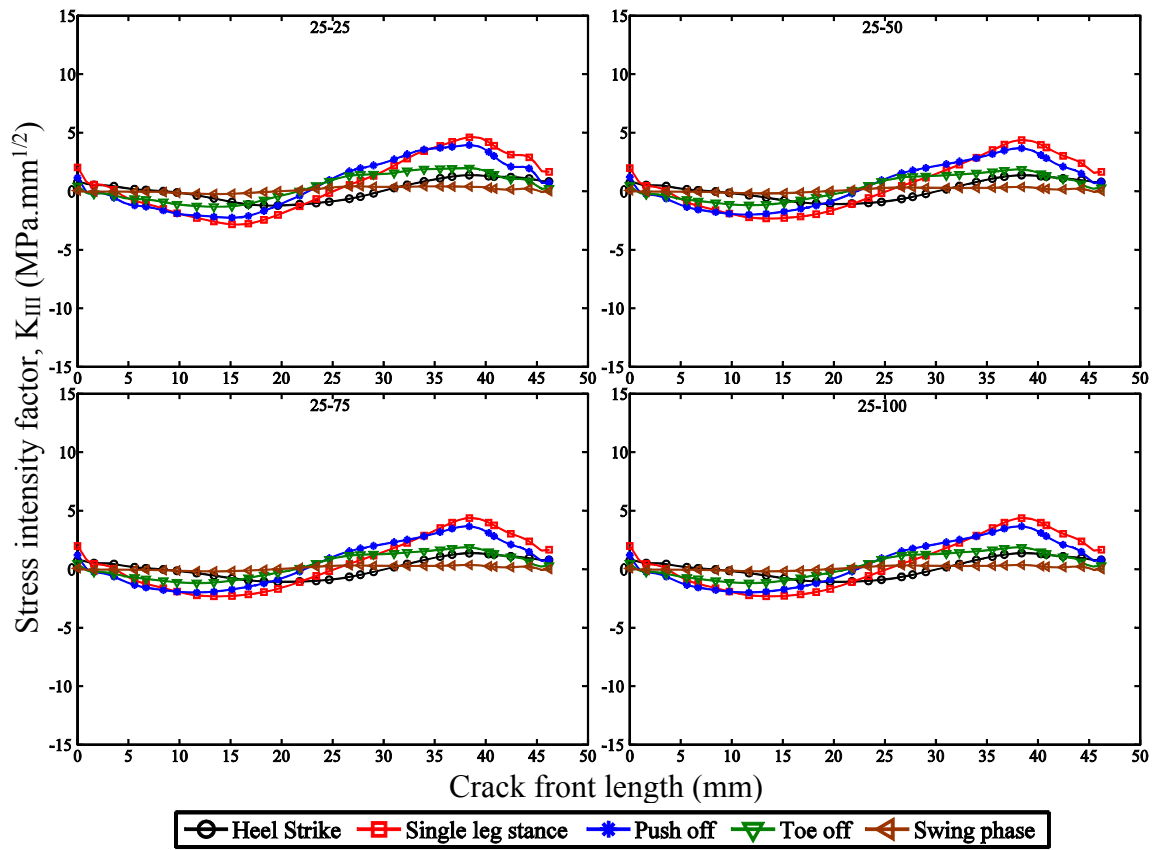


Figure 4.43:  $K_I$  variation along the crack front on the internal surface: (a)  $E_{25}$ , (b)  $E_{50}$ , (c)  $E_{75}$ , and (d)  $E_{100}$  interactions with  $I_{25}$ ,  $I_{50}$ ,  $I_{75}$ , and  $I_{100}$

#### 4.2.8.3.2 $K_{III}$ behavior at the internal and external surfaces

The  $K_{III}$  trend at the internal surface in its interaction with the external cracks is shown in Figures 4.44a to 4.44d. Figures 45a to 45d illustrate the interaction of the  $K_{III}$  external surfaces of the cement layer with the internal cracks. The figure title represents the location of the crack on the internal and external surfaces of the cement layer, similar to Figures 4.42 and 4.43. Initially, the  $K_{III}$  variation along the crack front commenced in a decreasing manner, and subsequently increased at the crack front. After reaching the peak point, the  $K_{III}$  followed a downward trend to the end of the crack front. Consequently, the  $K_{III}$  behavior plot along the crack front at the internal and external surfaces of the cement layer comprised concave and convex plots. Similar to  $K_I$  behavior,  $K_{III}$  showed a maximum value at the distal part, and it decreased with

increasing distance from the distal end. The single-leg stance and push off phases showed maximum absolute values of SIFs at mode III.



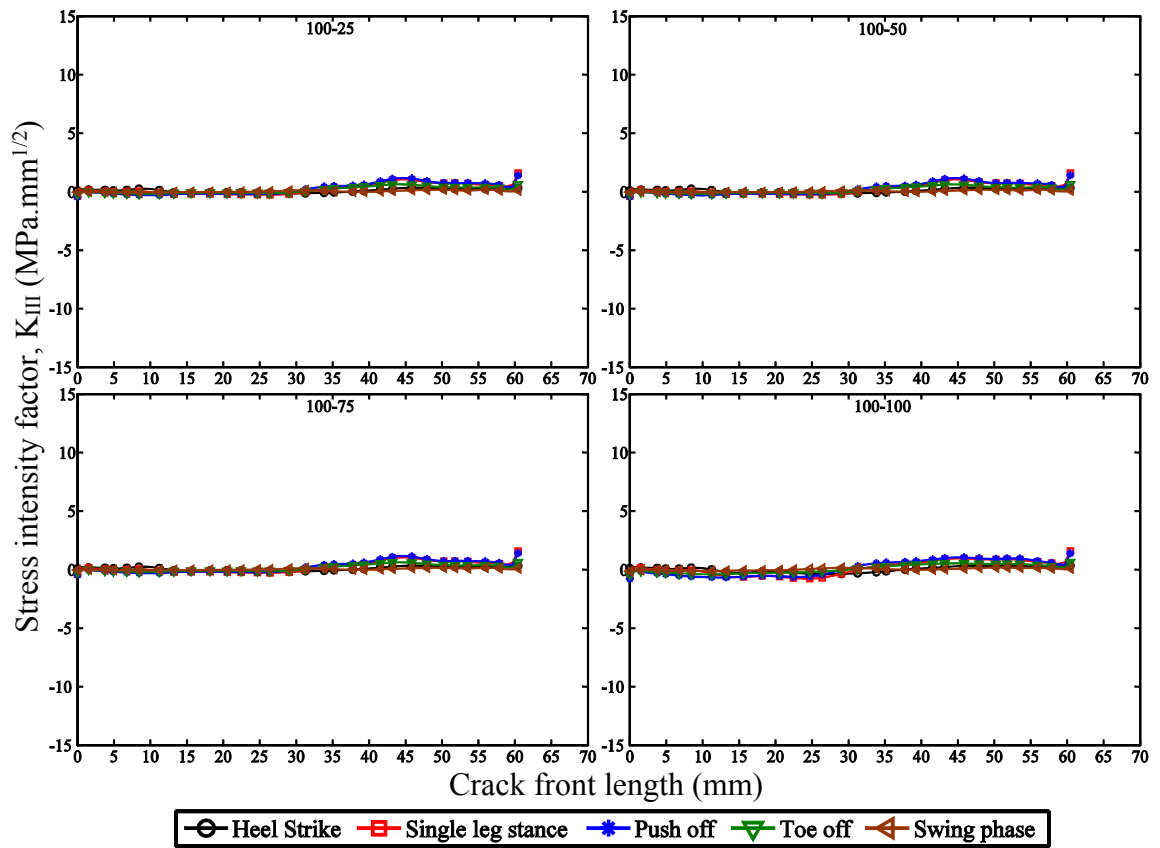
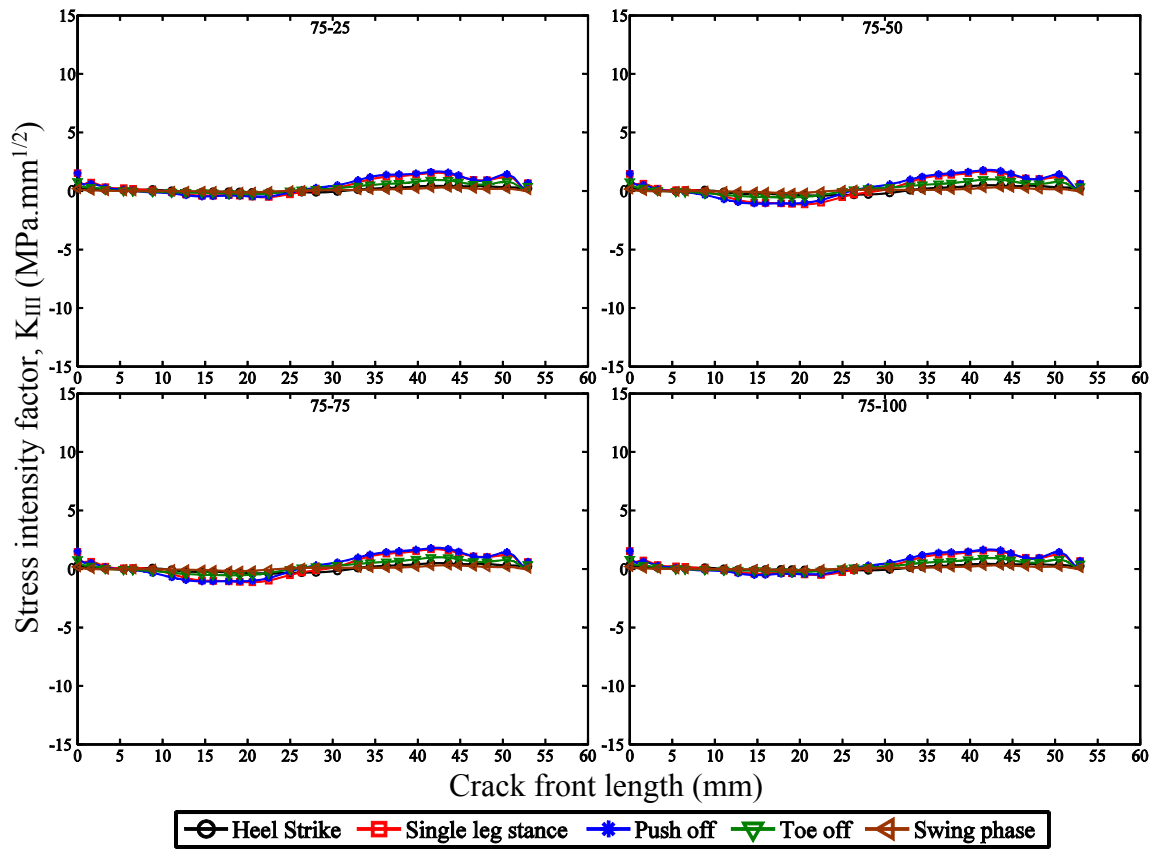
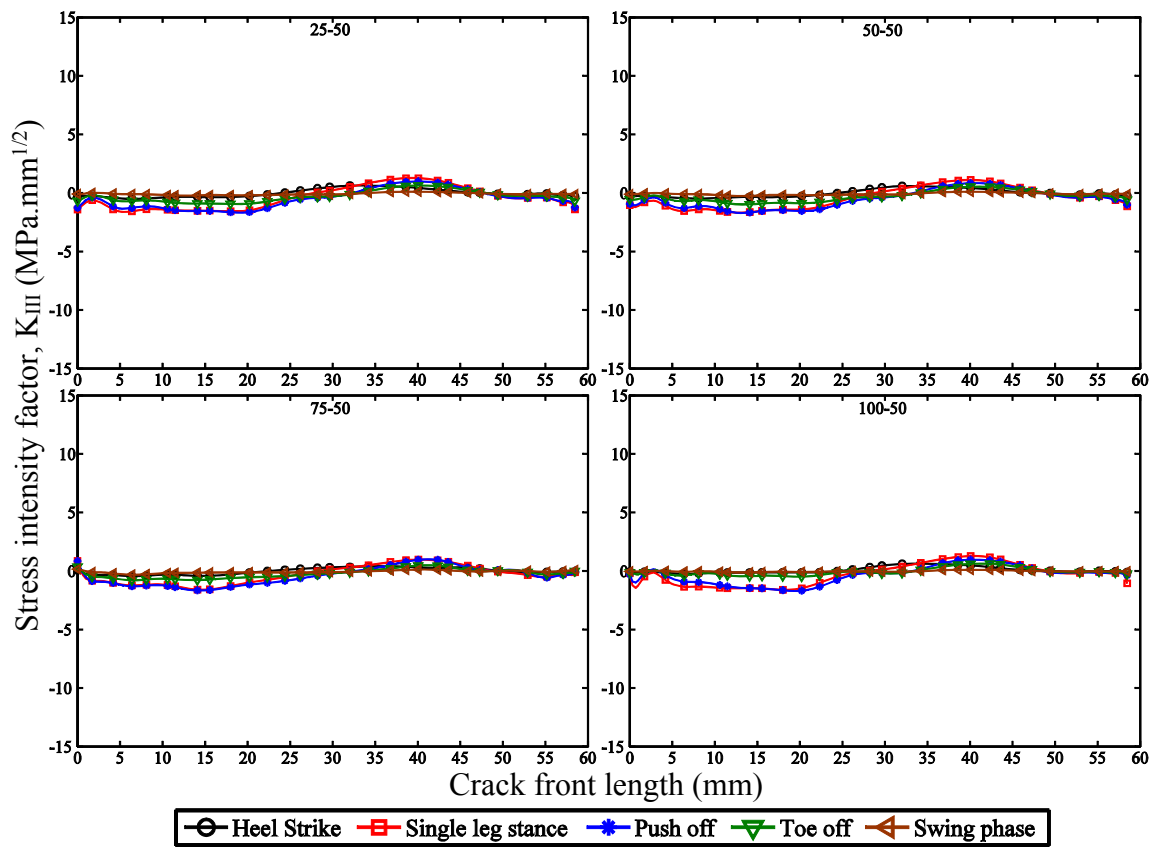
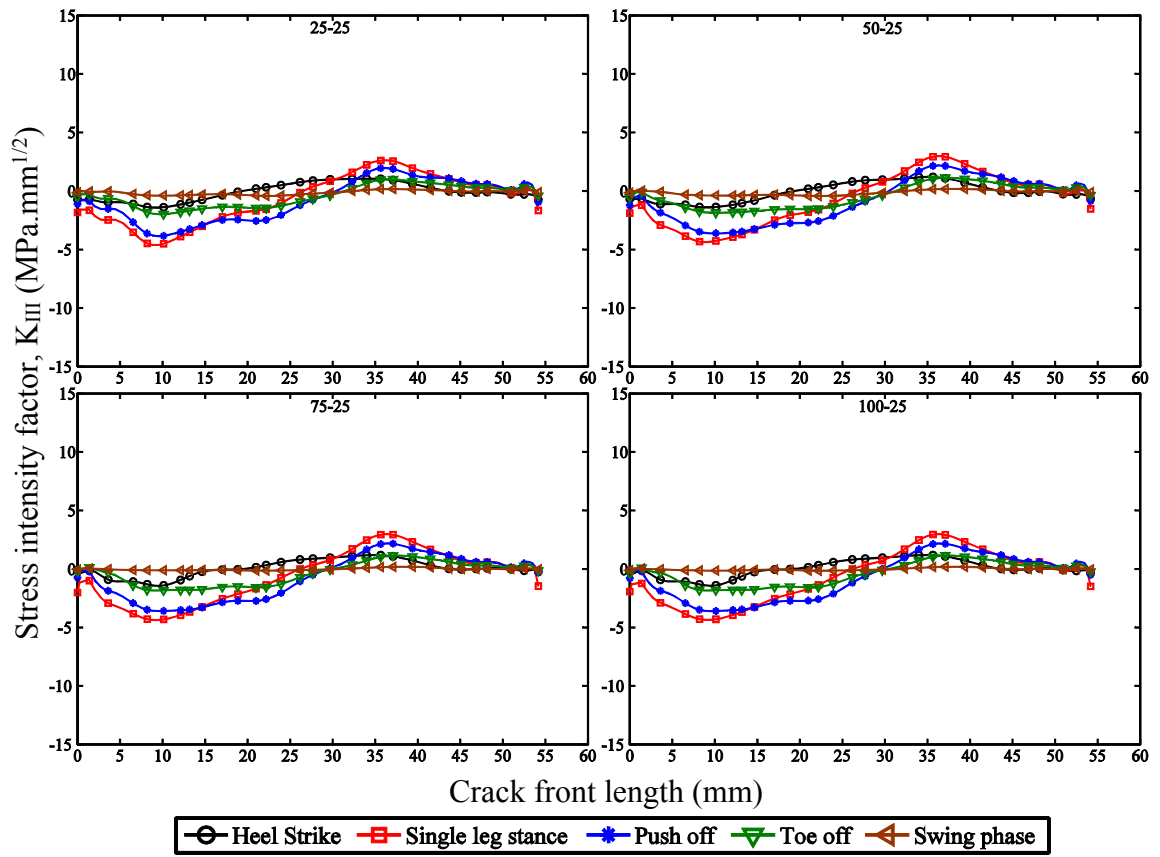


Figure 4.44:  $K_{III}$  variation along the crack front on the internal surface: (a)  $I_{25}$ , (b)  $I_{50}$ , (c)  $I_{75}$ , and (d)  $I_{100}$  interactions with  $E_{25}$ ,  $E_{50}$ ,  $E_{75}$ , and  $E_{100}$





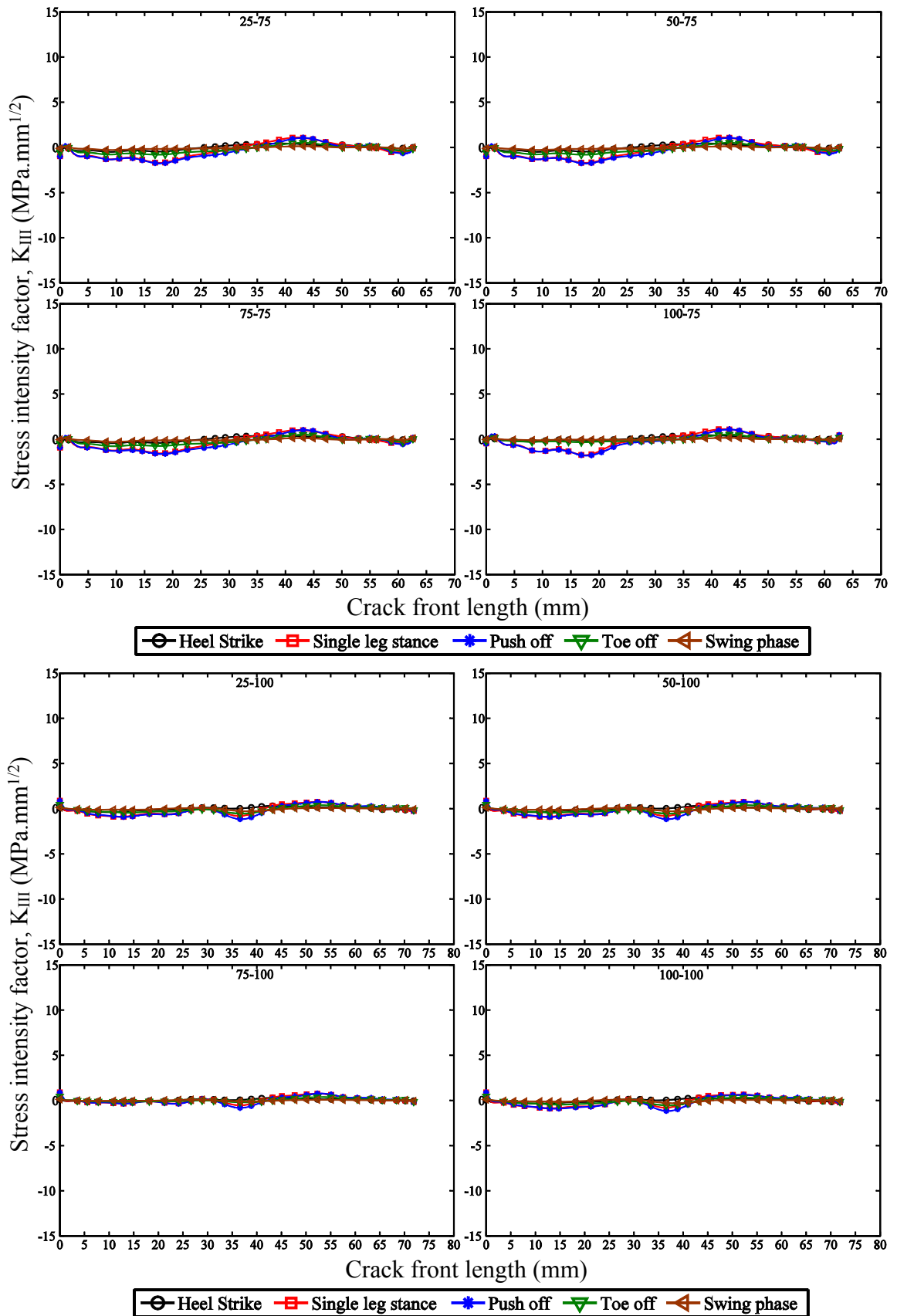


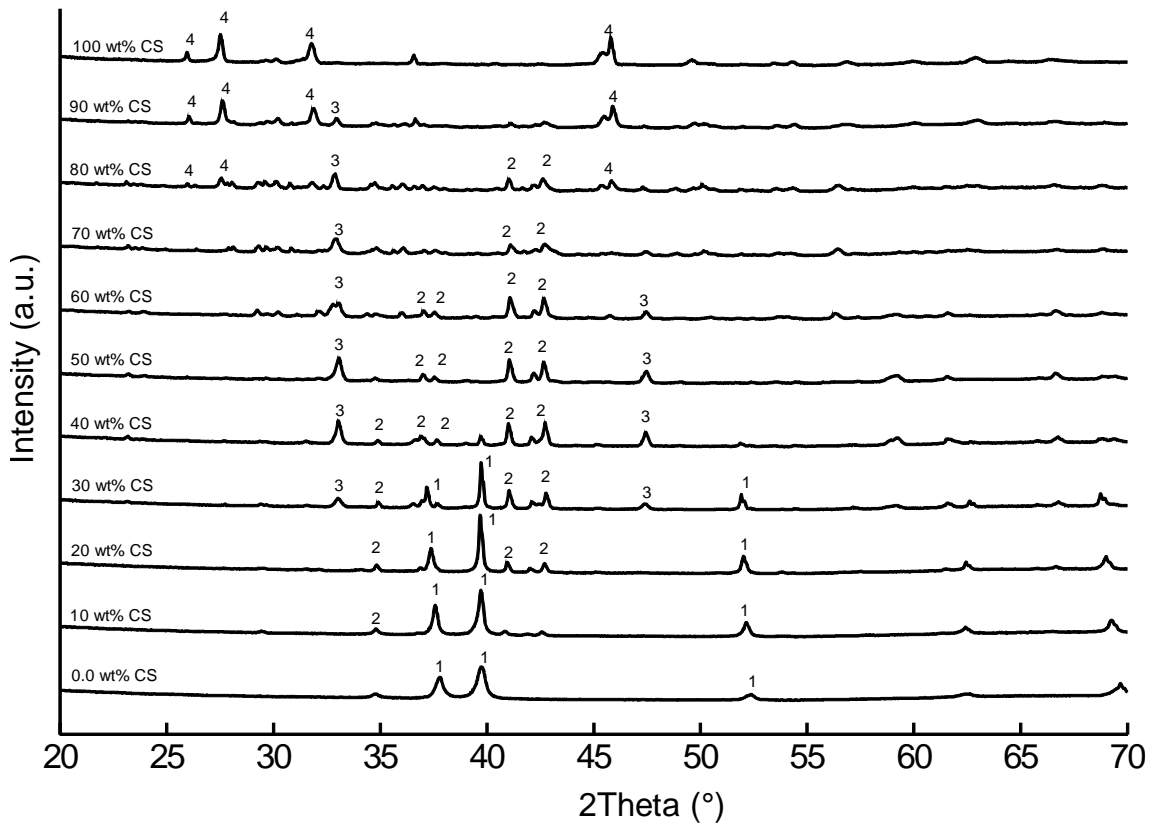
Figure 4.45:  $K_{III}$  variation along the crack front on the internal surface: (a)  $E_{25}$ , (b)  $E_{50}$ , (c)  $E_{75}$ , and (d)  $E_{100}$  interactions with  $I_{25}$ ,  $I_{50}$ ,  $I_{75}$ , and  $I_{100}$

## **4.3 Experimental results**

### **4.3.1 Composite of calcium silicate and hydroxyapatite with metal phases**

#### **4.3.1.1 Structure characterization**

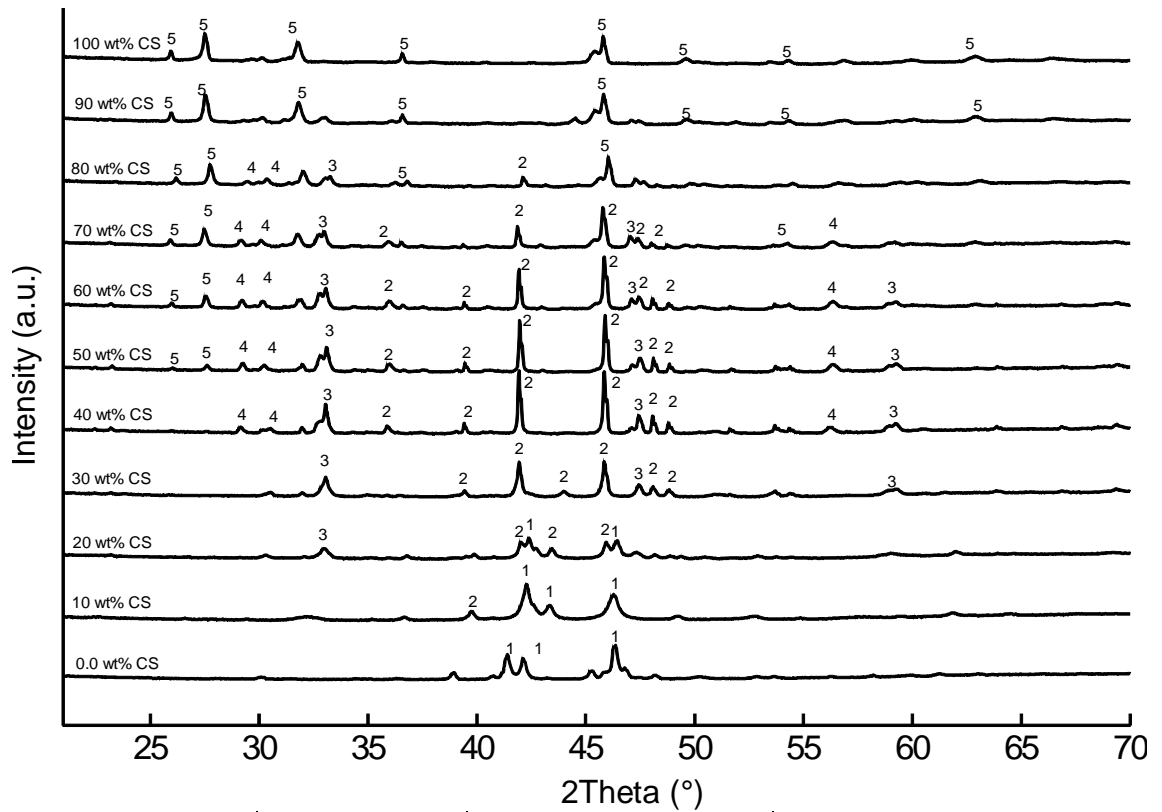
Figures 4.46 to 4.52 illustrate the XRD patterns of different composites of Ti-CS, Ti-55Ni-CS, Ti-6Al-4V-CS, SS-316L-CS, Ti-HA, Ti-6Al-4V-HA, and SS-316L-HA after sintering at 1200 °C. Figure 4.46 presents the XRD patterns of the Ti-CS composite groups based on CS weight percentage. Two new phases of  $Ti_5Si_3$  and  $CaTiO_3$  emerged in Ti-CS composites during sintering.  $Ti_5Si_3$  was mainly in the composites with dominant Ti metal phase, and the  $CaTiO_3$  peaks became more obvious with the increase in CS weight percentage.



Symbol	Reference code	ICSD name	Chemical formula
1	00-001-1197	Titanium	Ti
2	00-008-0041	Titanium silicon	Ti <sub>5</sub> Si <sub>3</sub>
3	01-076-2400	Calcium titanium oxide	CaTiO <sub>3</sub>
4	00-001-0720	Calcium silicate	CaSiO <sub>3</sub>

Figure 4.46: X-ray diffraction patterns of the CaSiO<sub>3</sub>-Ti sintered composites

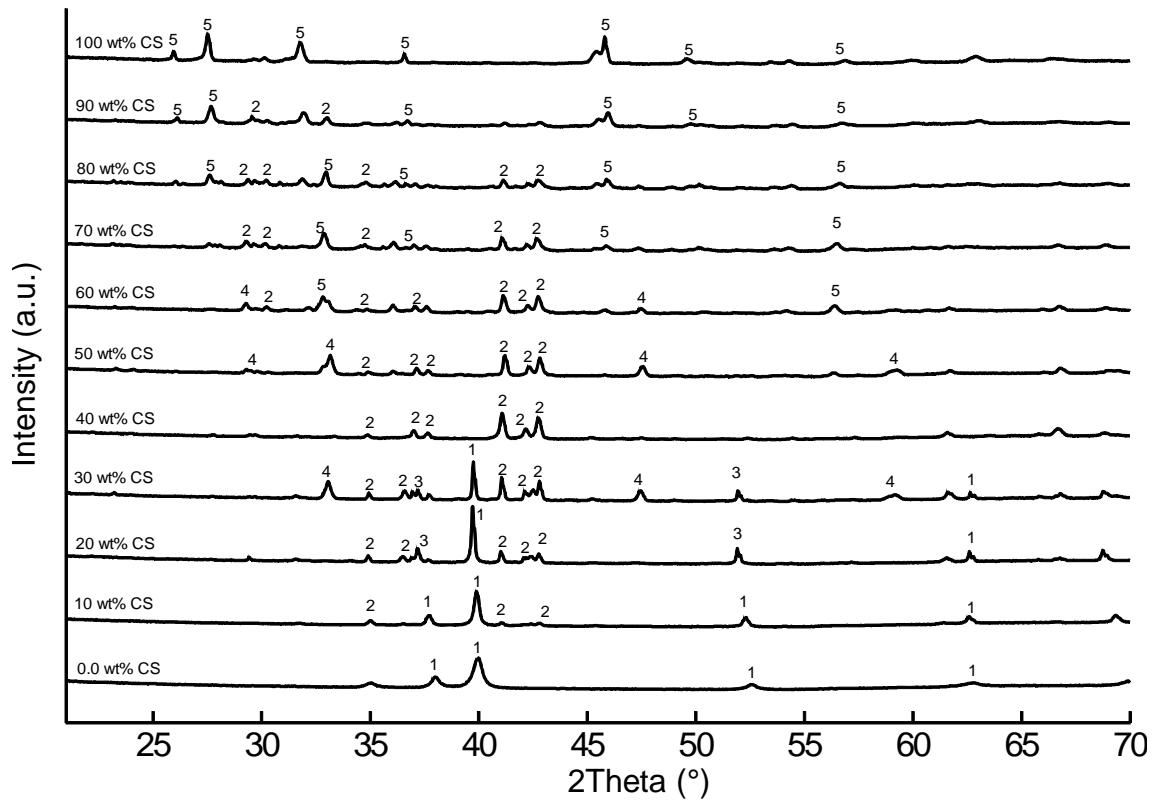
In the sintering process, three new phases of Ni<sub>16</sub>Ti<sub>6</sub>Si<sub>7</sub>, CaTiO<sub>3</sub>, and Ni<sub>31</sub>Si<sub>12</sub> appeared in the XRD patterns of Ti-55Ni-CS composites (Figure 4.47). These phases resulted from the reaction between the compounds of Ti-55Ni and CS. The volume fraction of the new phases in the sintered composites was a function of CS weight percentage. Peaks of Ni<sub>16</sub>Ti<sub>6</sub>Si<sub>7</sub>, CaTiO<sub>3</sub>, and Ni<sub>31</sub>Si<sub>12</sub> emerged in the XRD diagrams of the composites with 10 wt% to 80 wt%, 20wt% to 80 wt%, and 40 wt% to 80 wt% of CS, respectively.



Symbol	Reference code	ICSD name	Chemical formula
1	00-051-1169	Nickel titanium	Ni <sub>3</sub> Ti
2	00-011-0541	Nickel silicon titanium	Ni <sub>16</sub> Ti <sub>6</sub> Si <sub>7</sub>
3	01-076-2400	Calcium titanium oxide	CaTiO <sub>3</sub>
4	00-024-0524	Nickel silicon	Ni <sub>31</sub> Si <sub>12</sub>
5	00-001-0720	Calcium silicate	CaSiO <sub>3</sub>

Figure 4.47: X-ray diffraction patterns of CaSiO<sub>3</sub>-Ti-55Ni sintered composites

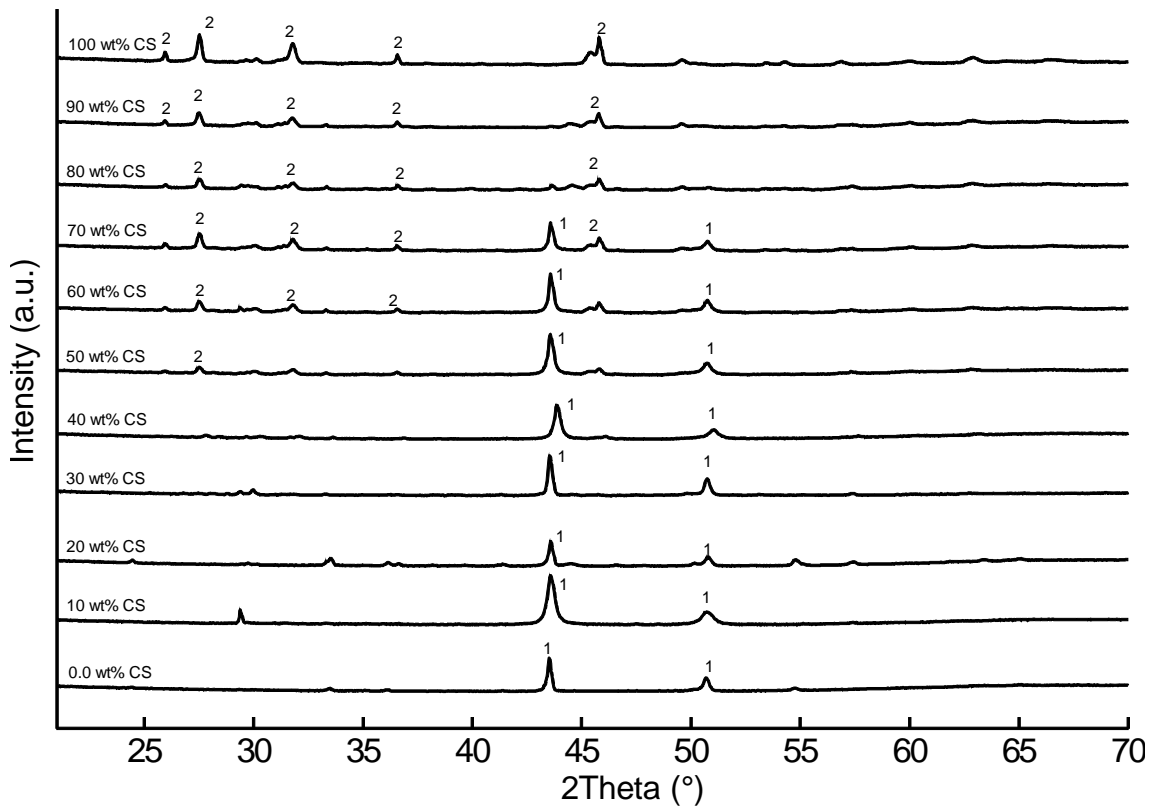
Similar to the Ti-55Ni-CS composites, three new phases of Ti<sub>5</sub>Si<sub>3</sub>, Ti<sub>2</sub>O, and TiCaO<sub>3</sub> appeared in the final sintered composites of Ti-6Al-4V and CS (Figure 4.48). Ti<sub>5</sub>Si<sub>3</sub> was found in all composite groups of Ti-6Al-4V with 10 wt% to 90 wt% CS. CaTiO<sub>3</sub> was found in the sintered composites with more than 30 wt% CS except in the group with 40 wt% CS, in which only Ti<sub>5</sub>Si<sub>3</sub> was found. On the contrary, only Ti<sub>2</sub>O was found in the groups with 10 wt% and 20 wt% CS.



Symbol	Reference code	ICSD name	Chemical formula
1	00-043-1159	Aluminum titanium vanadium	$Al_3V_{0.333}Ti_{0.666}$
2	00-008-0041	Titanium silicon	$Ti_5Si_3$
3	01-072-1805	Titanium oxide	$Ti_2O$
4	01-076-2400	Calcium titanium oxide	$CaTiO_3$
5	00-001-0720	Calcium silicate	$CaSiO_3$

Figure 4.48: X-ray diffraction patterns of  $CaSiO_3$ -Ti-6Al-4V sintered composites

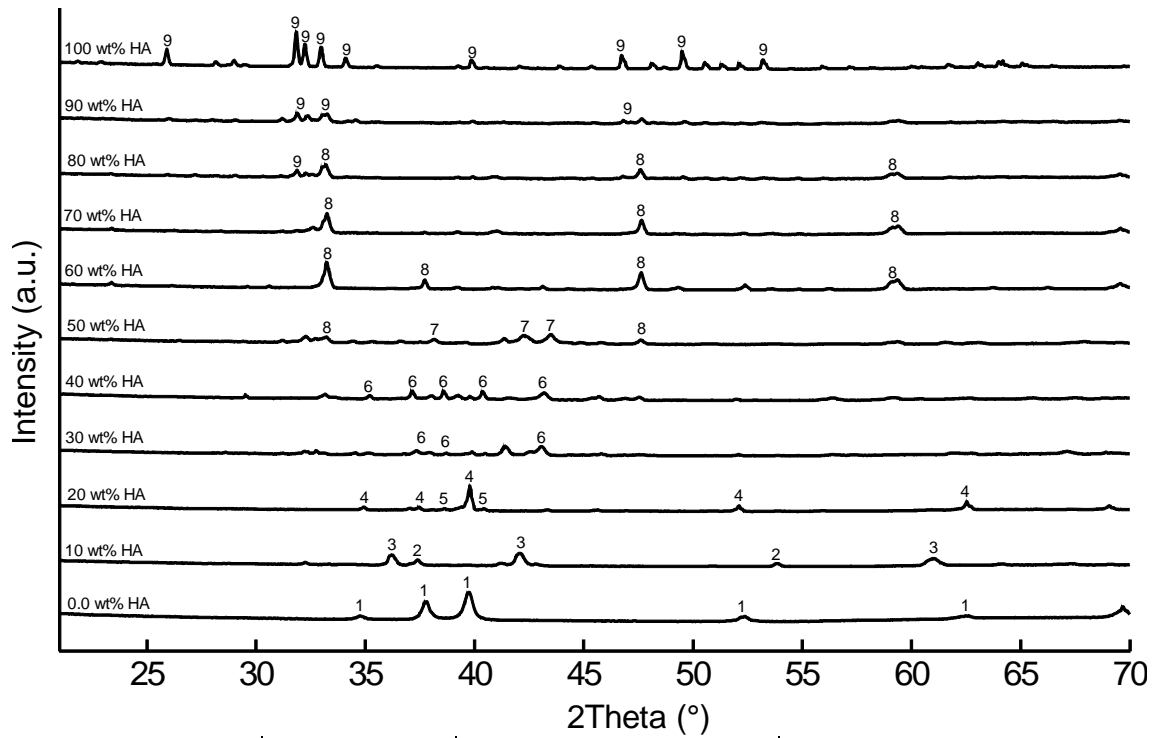
The XRD diagrams of the SS-316L-CS composites are presented in Figure 4.49. In this group of composites, the XRD patterns only showed peaks of the SS-316L and CS, unlike the Ti and Ti alloy composites with CS.



Symbol	Reference code	ICSD name	Chemical formula
1	00-033-0397	304-stainless steel	$\text{Cr}_{0.19}\text{Fe}_{0.7}\text{Ni}_{0.11}$
2	00-001-0720	Calcium silicate	$\text{CaSiO}_3$

Figure 4.49: X-ray diffraction patterns of  $\text{CaSiO}_3$ –SS–316L sintered composites

Figure 4.50 shows the appearance of the new phases in the composites of Ti with HA. When Ti and HA reacted together, seven new phases appeared in the final product. TiO and CaO appeared in the composite Ti–HA with 10 wt% HA. In the composite group with 20 wt% HA,  $\text{Ti}_2\text{O}$  and  $\text{Ti}_3\text{PO}_{0.58}$  emerged. Titanium phosphorus oxide was found singly in the composites of Ti–HA with 30 wt% and 40 wt% HA. In the composites with 50 wt% HA, titanium phosphorus oxide was replaced with titanium phosphide and calcium titanium oxide. Calcium titanium oxide was the main phase in the sintered composites with 70 wt% and 80 wt% HA. The HA peaks appeared in the composites with 90 wt% HA.

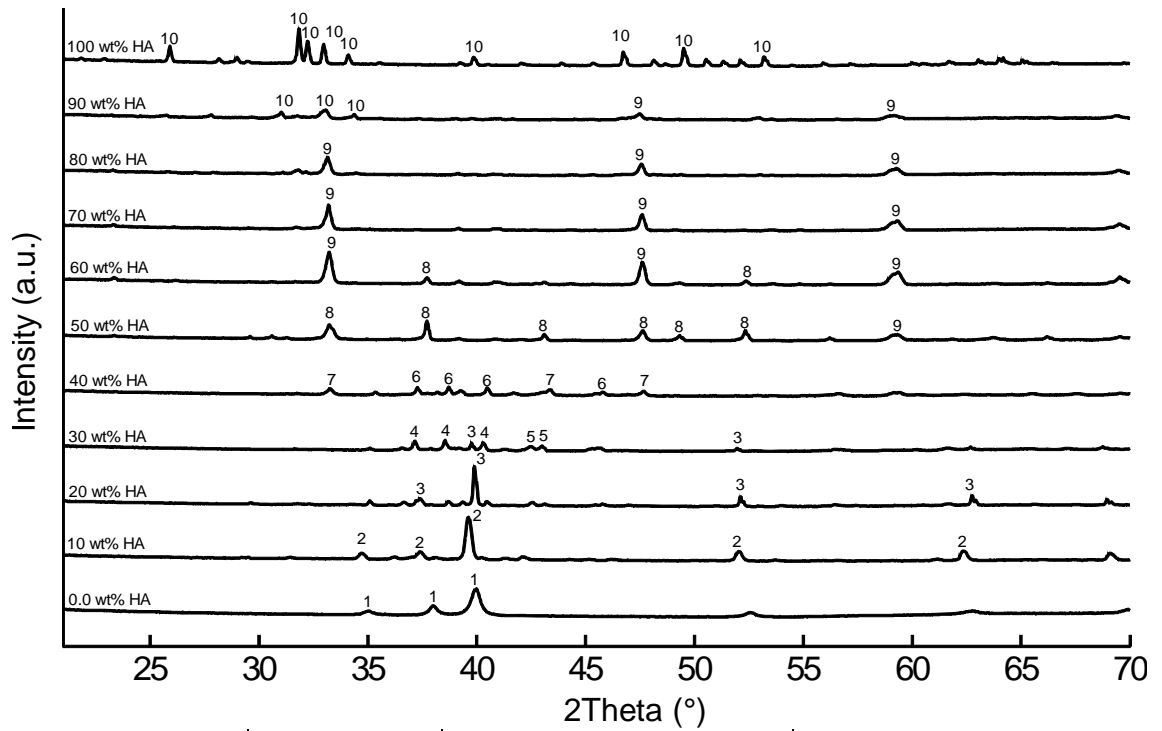


Symbol	Reference code	ICSD name	Chemical formula
1	00-001-1197	Titanium	Ti
2	00-043-1001	Calcium oxide	CaO
3	01-086-2352	Titanium oxide	TiO
4	01-072-1805	Titanium oxide	Ti <sub>2</sub> O
5	00-050-0247	Titanium phosphate	Ti <sub>3</sub> PO <sub>0.58</sub>
6	01-087-2178	Titanium phosphorus oxide	Ti <sub>3</sub> PO <sub>0.58</sub>
7	01-073-1816	Titanium phosphide	Ti <sub>3</sub> P <sub>3.16</sub>
8	00-042-0423	Calcium titanium oxide	CaTiO <sub>3</sub>
9	00-001-1008	Hydroxyapatite	Ca <sub>10</sub> (OH) <sub>2</sub> (PO <sub>4</sub> ) <sub>6</sub>

Figure 4.50: X-ray diffraction patterns of Ca<sub>10</sub>(OH)<sub>2</sub>(PO<sub>4</sub>)<sub>6</sub>-Ti sintered composites

The XRD patterns of the composites of Ti-6Al-4V-HA are shown in Figure 4.51. Titanium oxide, titanium phosphorus oxide, titanium phosphide, titanium phosphate, calcium titanium oxide, titanium phosphide, and calcium titanium oxide were the new phases that appeared during the sintering of the composites of Ti-6Al-4V with HA. Similar to the Ti-HA composites, the Ti oxides emerged in the Ti-rich composites, and calcium titanium oxide appeared in the HA-rich composites. Titanium phosphorus oxide, titanium phosphate, and titanium phosphide appeared in the composites with 40wt%-60wt% HA.

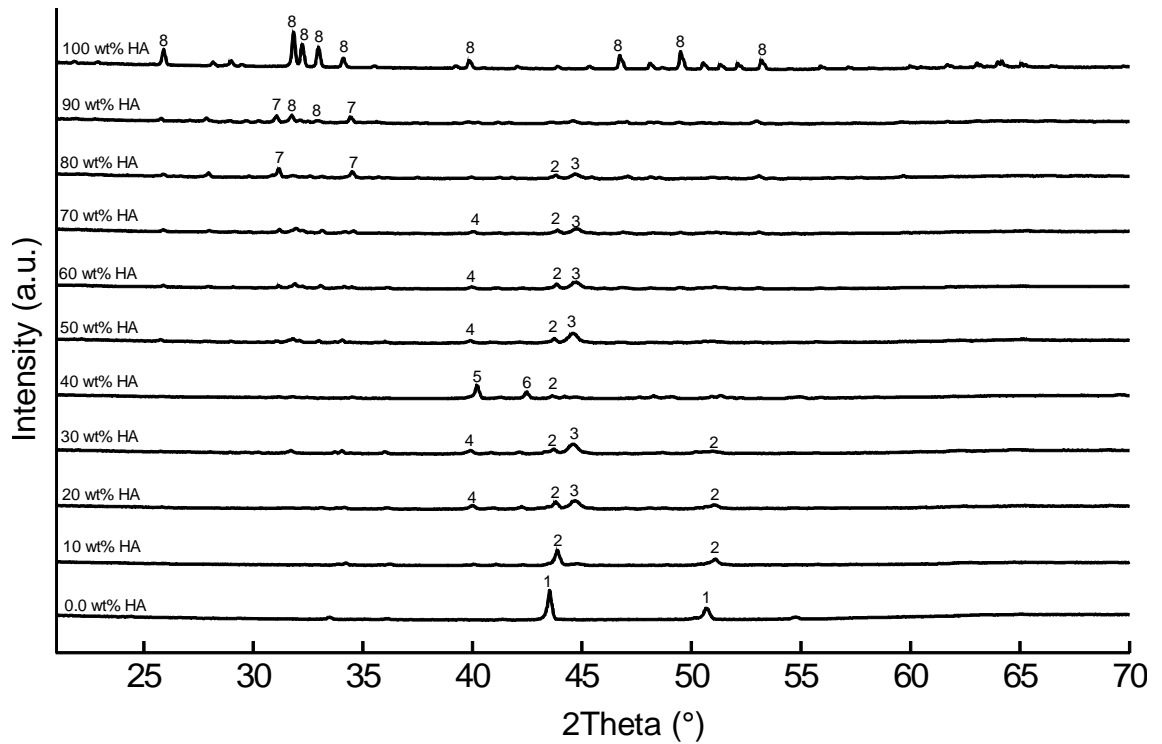




Symbol	Reference code	ICSD name	Chemical formula
1	00-043-1159	Aluminum titanium vanadium	$\text{Al}_3\text{V}_{0.333}\text{Ti}_{0.666}$
2	01-073-1581	Titanium oxide	$\text{TiO}_{325}$
3	01-073-1116	Titanium oxide	$\text{Ti}_2\text{O}$
4	01-087-2178	Titanium phosphorus oxide	$\text{Ti}_3\text{PO}_{0.58}$
5	01-073-1816	Titanium phosphide	$\text{Ti}_3\text{P}_{3.16}$
6	00-050-0247	Titanium phosphate	$\text{Ti}_3\text{PO}_{0.58}$
7	00-009-0365	Calcium titanium oxide	$\text{CaTiO}_3$
8	01-073-1821	Titanium phosphide	$\text{TiP}$
9	01-078-1013	Calcium titanium oxide	$\text{CaTiO}_3$
10	00-001-1008	Hydroxyapatite	$\text{Ca}_{10}(\text{OH})_2(\text{PO}_4)_6$

Figure 4.51: X-ray diffraction patterns of  $\text{Ca}_{10}(\text{OH})_2(\text{PO}_4)_6$ -Ti-6Al-4V sintered composites

Figure 4.52 illustrates the XRD results of the composites of SS-316-HA. SS-316 reacted with the HA in the composites of SS-316L-HA during the sintering process, and about four new phases appeared. The result was contrary to the behavior of the composites of SS-316L-CS during sintering.



Symbol	Reference code	ICSD name	Chemical formula
1	00-033-0397	304-stainless steel	$\text{Cr}_{0.19}\text{Fe}_{0.7}\text{Ni}_{0.11}$
2	00-050-1292	Chromium iron molybdenum nickel silicon	$\text{Cr}_2\text{Fe}_{6.7}\text{Mo}_{0.1}\text{Ni}_{1.3}\text{Si}_{0.3}$
3	00-033-0945	Nickel chromium iron	$\text{Ni}_{2.9}\text{Cr}_{0.7}\text{Fe}_{0.36}$
4	01-083-1903	Calcium iron oxide	$\text{Ca}_2\text{Fe}_7\text{O}_{11}$
5	00-051-0943	Iron phosphide	$\text{Fe}_2\text{P}$
6	01-071-0399	Iron zinc	$\text{Fe}_3\text{Zn}_{10}$
7	00-049-1223	Calcium iron phosphate	$\text{Ca}_{19}\text{Fe}_2(\text{PO}_4)_{14}$
8	00-001-1008	Hydroxyapatite	$\text{Ca}_{10}(\text{OH})_2(\text{PO}_4)_6$

Figure 4.52: XRD patterns of  $\text{Ca}_{10}(\text{OH})_2(\text{PO}_4)_6$ -SS-316L sintered composites

#### 4.3.1.2 Physical properties

Figure 4.53 presents the shrinkage in the composites of Ti, Ti-55Ni, Ti-6Al-4V, and SS-316L with CS and HA during sintering. The shrinkage of the composites as a function of the weight percentages of CS and HA produced convex plots. The plots declined in all groups of composites with the increase in ceramic phase content of up to 50 wt%, and then gradually increased. The Ti-6Al-4V-CS group showed less shrinkage than the Ti-CS, Ti-55Ni-CS, and SS-316L-CS groups. On the contrary, SS-316L-CS composites revealed maximum shrinkage in metallic composites with CS. The composites of the SS-316L with more than 70 wt% CS showed more shrinkage than the pure ceramic phase of CS (Figure 4.53). The composites of the metallic phases

with more than 30 wt% and less than 70 wt% HA revealed expansion during the sintering process, which presented as negative shrinkage in Figure 4.53.

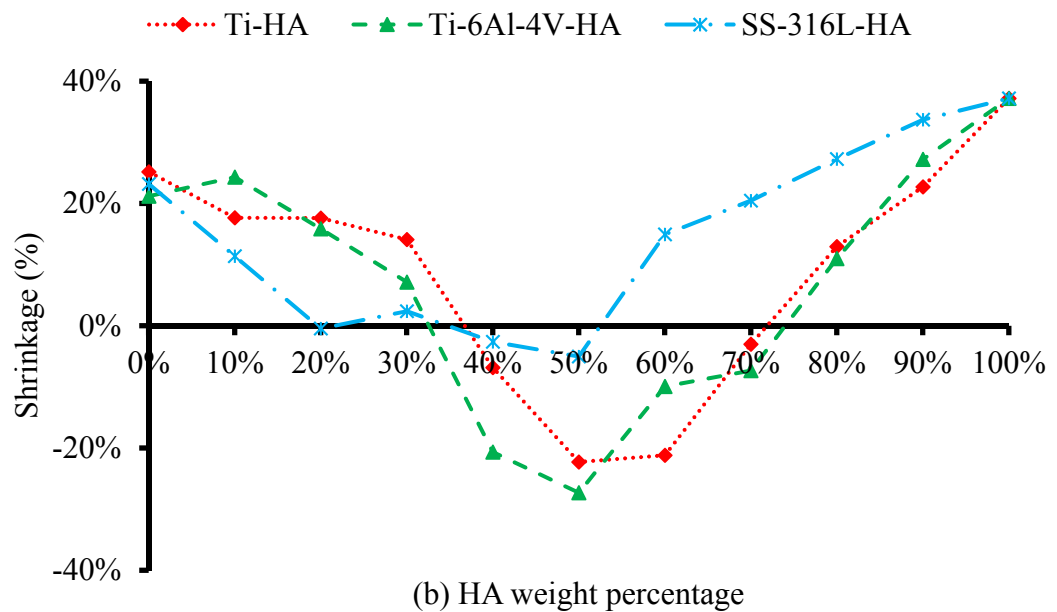
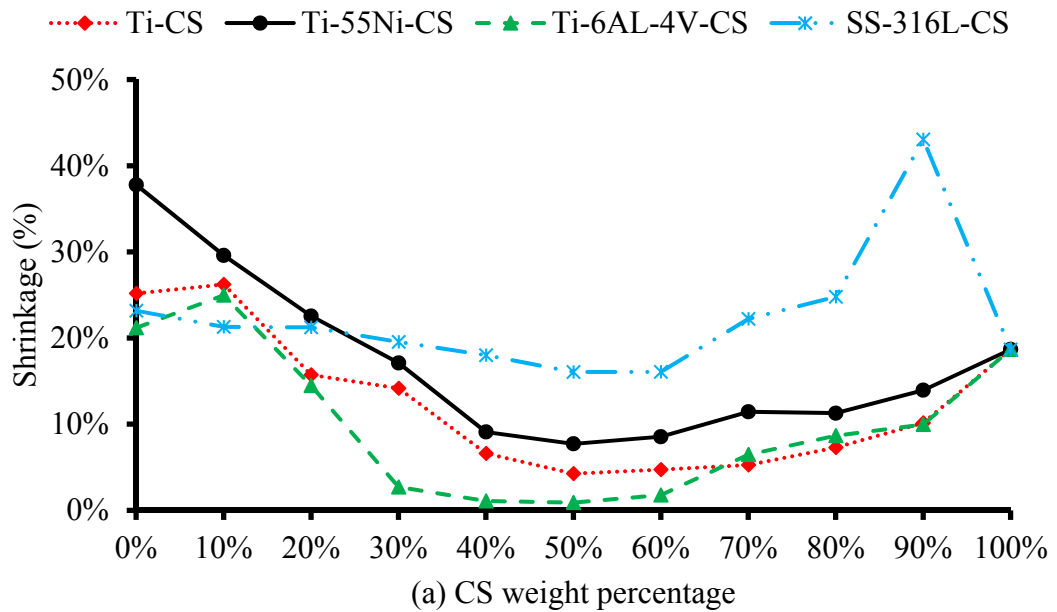


Figure 4.53: Variation in shrinkage as a function of weight percentages of (a) calcium silicate and (b) hydroxyapatite

The variations in the density of the cermetes of HA and CS with Ti, Ti-55Ni, Ti-6Al-4V, and SS-316L are presented in Figure 4.54. The density of the CS composites with metallic phases showed a decreasing trend with the increase in CS weight

percentage. Accordingly, the pure metallic phases had maximum density, and the pure ceramic phases showed minimum density. On the contrary, the composites of HA and metallic phases produced convex plots with the peak density in the pure phase of metals and HA, and the groups with expansion showed minimum densities because of the increase in their volume during sintering.

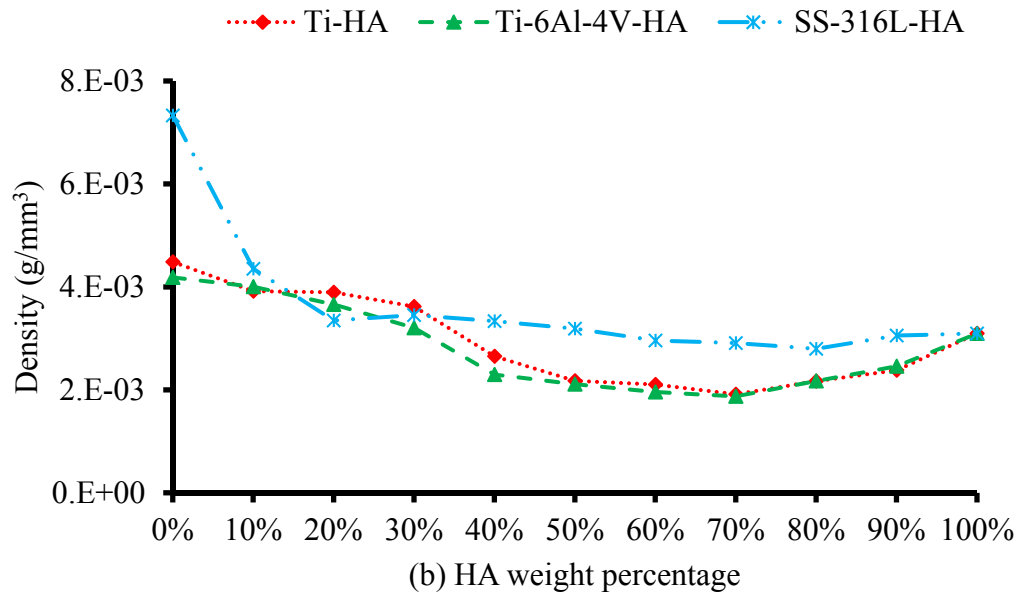
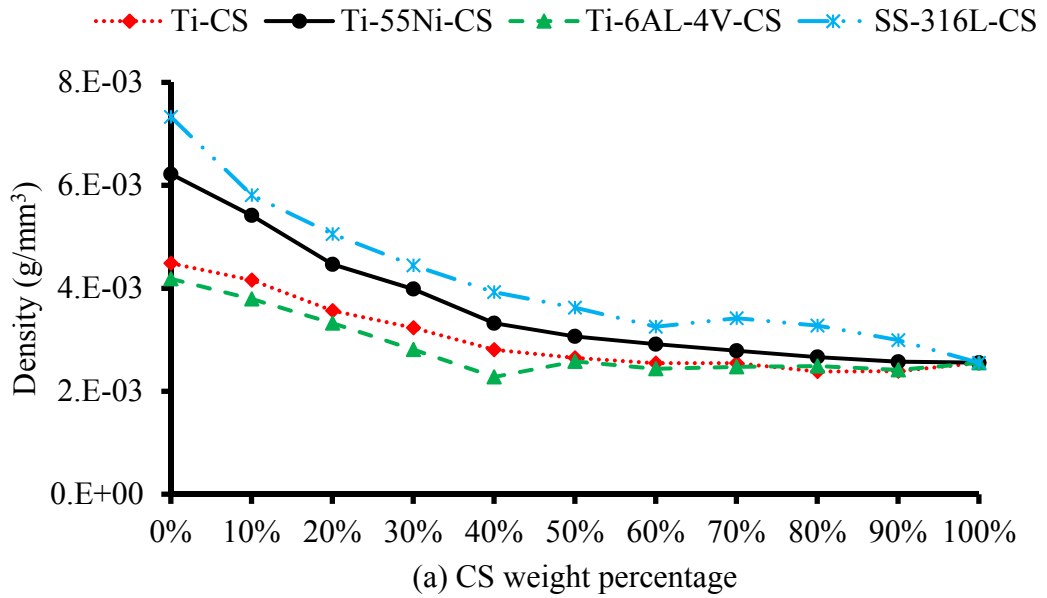
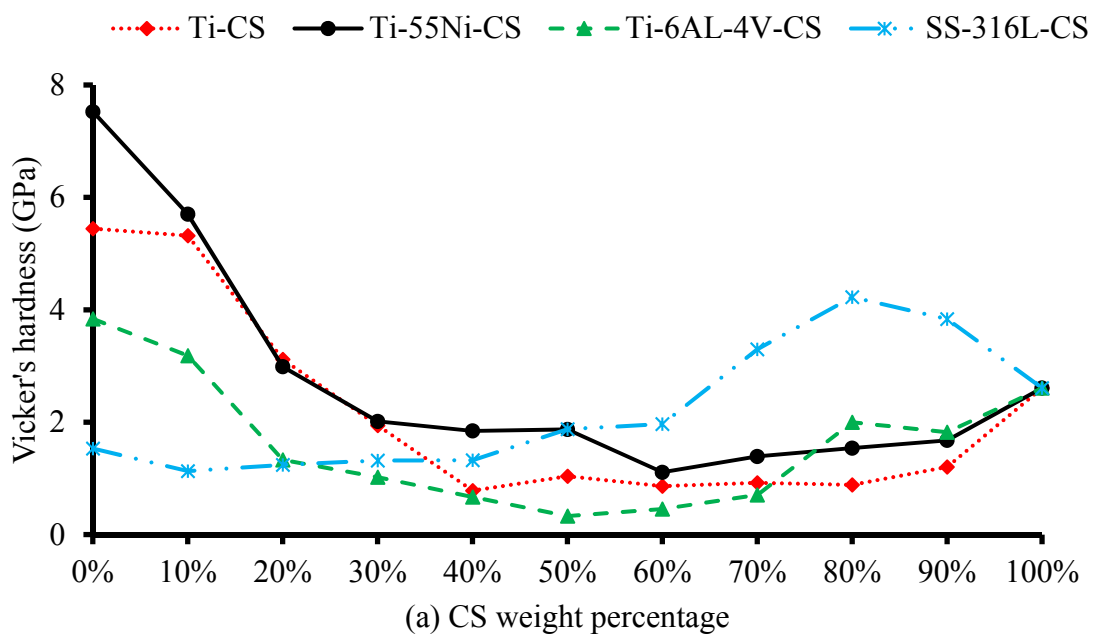


Figure 4.54: Variation in density as a function of the weight percentages of (a) calcium silicate and (b) hydroxyapatite

Figure 4.55a presents the Vickers hardness variation as a function of CS weight percentage in the composites of CS with metallic phases. The hardness of the CS composites with Ti alloys exhibited a decreasing trend with the increase in CS content up to 50wt%, and then their hardness increased gradually at 100wt% CS. On the contrary, the hardness of the composites of CS with SS-316L enhanced gradually with the increase in CS content. The composite of SS-316L with 90 wt% CS showed more hardness than pure CS. Figure 4.55b illustrates the trend of the Vickers hardness variation as a function of HA weight percentage in the composite metals with HA. The hardness of Ti alloys with HA decreased with the increase in HA weight percentages up to 40wt%, and then showed a flat trend between 40wt% and 70 wt% HA. Afterwards, the hardness enhanced with the increase in HA weight percentage. In SS-316L composites with HA, the hardness decreased with the increase in HA content up to 40wt%, similar to the Ti alloy composites, and then increased with the increase in HA weight percentage up to 100%.



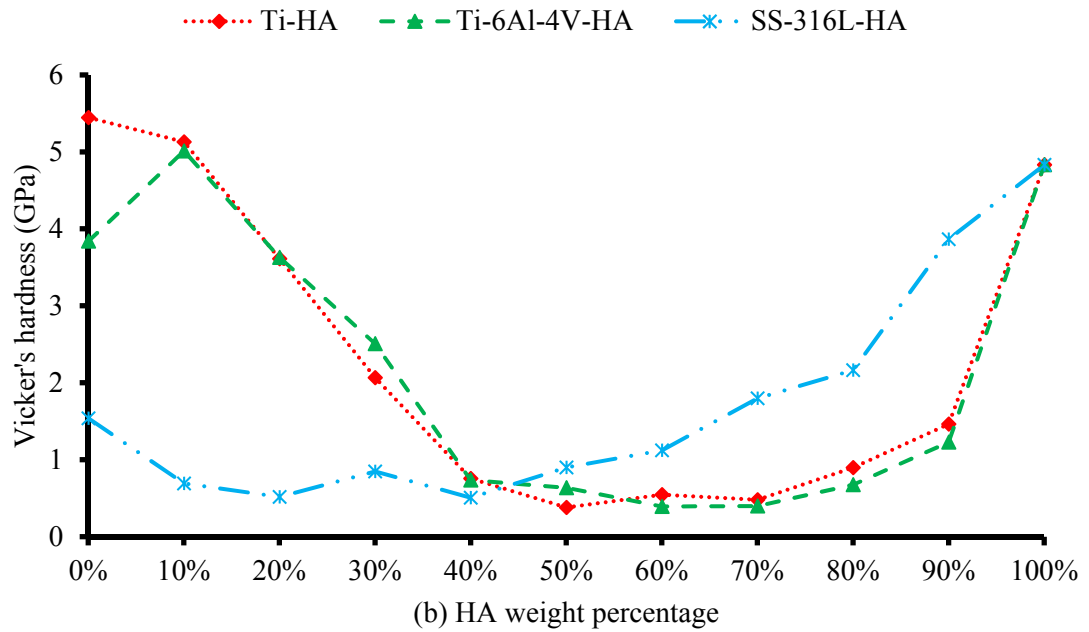


Figure 4.55: Vickers hardness variation as a function of weight percentages of (a) calcium silicate and (b) hydroxyapatite

#### 4.3.1.3 Mechanical properties of the composites

The compressive Young's modulus of the different composites as a function of the weight percentages CS and HA are tabulated in Tables 4.5 and 4.6, respectively. The compressive Young's modulus decreased with the increase in ceramic phases up to around 50wt%. Afterward, the Young's modulus gradually increased with the ceramic phase content. The CS composite groups showed higher values of Young's modulus than the HA composite groups.

Table 4.5: Variation in Young's modulus as a function of calcium silicate weight percentage

Material CS (wt.%)	E (GPa) ± STD (GPa)							
	Ti		Ti-55Ni		Ti-6Al-4V		SS-316L	
	E	STD	E	STD	E	STD	E	STD
0	120.4	3.9	112.1	27.7	131.7	6.0	213.8	13.3
10	88.3	5.9	103.9	17.4	84.2	6.0	127.0	2.3
20	72.3	9.6	85.9	8.0	84.5	8.4	121.7	12.8
30	89.7	13.4	81.2	9.0	62.4	1.5	85.4	2.2
40	63.5	4.7	77.3	8.8	39.6	7.2	81.5	10.0
50	64.1	4.3	82.7	26.5	59.7	4.2	78.6	21.4
60	80.3	4.9	88.9	10.0	70.2	3.2	90.6	4.2
70	87.3	11.9	107.9	63.3	78.1	6.2	99.7	4.6
80	97.4	2.6	106.7	6.2	89.2	7.1	115.0	17.0
90	102.1	8.7	108.2	9.6	95.7	2.0	119.4	12.5
100	106.9	24.8	106.9	24.8	106.9	24.8	106.9	24.8

Table 4.6: Young's modulus variation as a function of hydroxyapatite weight percentage

Material HA (wt.%)	E (GPa) ± STD (GPa)					
	Ti		Ti-6Al-4V		SS-316L	
	E	STD	E	STD	E	STD
0	120.4	3.9	131.7	6.0	213.8	13.3
10	117.3	1.6	108.8	5.7	132.3	15.9
20	108.1	3.5	107.1	10.6	41.9	4.5
30	95.7	7.0	98.6	3.5	58.6	5.9
40	35.0	1.4	39.6	2.8	51.2	3.3
50	56.2	4.5	27.3	4.4	82.0	2.8
60	24.4	6.7	24.1	2.1	118.2	8.0
70	13.3	5.5	10.9	5.5	128.4	3.2
80	17.3	3.1	28.1	2.1	128.4	7.9
90	73.6	4.6	83.4	1.5	89.2	19.1
100	56.3	6.1	56.3	6.1	56.3	6.1

The ultimate compressive strengths of the composite metallic phases with different CS and HA contents are presented in Tables 4.7 and 4.8, respectively. Similar to the Young's modulus, the ultimate compressive strength of the composites declined with the increase in the contents of ceramic phases up to 50wt%. Afterward, the ultimate compressive strength of the composites increased along with the ceramic phase contents. The CS composites with SS-316L showed better performance than the composites of Ti alloys with CS. On the contrary, in the HA composite groups, the composites of the Ti alloys with HA showed better performance compared with the composites of the SS-316L with HA.

Table 4.7: Ultimate compressive strength as a function of calcium silicate weight percentage

$\sigma_{UCS}$ (MPa) $\pm$ STD (MPa)								
Material	Ti		Ti-55Ni		Ti-6Al-4V		SS-316L	
CS (wt%)	$\sigma_{UCS}$	STD	$\sigma_{UCS}$	STD	$\sigma_{UCS}$	STD	$\sigma_{UCS}$	STD
0	669.4	40.3	730.7	64.1	562.1	42.2	753.7	25.0
10	485.6	74.8	590.3	85.8	397.5	26.0	630.4	53.2
20	350.7	14.5	413.5	33.4	243.5	12.2	515.2	15.9
30	284.0	28.9	439.8	75.8	76.0	14.2	282.7	74.6
40	107.5	10.6	148.1	19.1	34.6	1.5	246.8	9.6
50	75.5	6.3	130.3	26.6	55.4	12.1	280.3	51.0
60	103.5	4.2	131.8	21.6	87.8	6.4	235.4	14.2
70	105.6	5.1	106.5	29.2	88.5	4.7	357.7	18.5
80	128.4	8.0	177.3	24.4	145.0	11.1	397.5	46.9
90	118.3	54.7	155.6	24.7	174.4	20.4	324.6	54.5
100	184.8	19.4	184.8	19.4	184.8	19.4	184.8	19.4

Table 4.8: Ultimate compressive strength as a function of hydroxyapatite weight percentage

$\sigma_{UCS}$ (MPa) $\pm$ STD (MPa)						
Material	Ti		Ti-6Al-4V		SS-316L	
HA (wt%)	$\sigma_{UCS}$	STD	$\sigma_{UCS}$	STD	$\sigma_{UCS}$	STD
0	669.4	40.3	562.1	59.7	753.7	25.0
10	436.5	28.5	378.0	22.8	244.6	32.5
20	413.4	81.7	367.0	53.0	45.5	2.3
30	270.5	34.9	172.6	28.7	74.8	10.4
40	60.0	2.7	39.0	6.1	59.5	2.1
50	18.9	10.7	21.0	1.5	103.3	4.1
60	17.8	0.9	9.9	3.8	150.1	35.7
70	5.2	1.3	10.8	2.0	149.9	26.2
80	17.0	3.8	39.2	5.0	192.7	38.0
90	67.9	27.5	99.6	39.9	126.4	21.4
100	64.4	24.3	64.4	24.3	64.4	24.3

The strain percentages at the maximum load for the composites of CS and HA are presented in Tables 4.9 and 4.10, respectively. The trend of strain percentage at the maximum load was similar to that of the ultimate compressive strength as the ceramic phases were enhanced except for the composites of SS-316L with CS. The strain percentage at the maximum load decreased in the composites of SS-316L with the increase in CS content. All composites of SS-316L with CS showed more strain percentage at the maximum load than pure CS. The strain percentage at the maximum load for the composites of SS-316L with HA showed a decreasing trend with the



increase in HA content up to 50 wt% HA, and then gradually increased with the increase in HA wt%.

Table 4.9: Strain percentage at maximum load as a function of calcium silicate weight percentage

Material	$\epsilon$ (%) $\pm$ STD (%)							
	Ti		Ti-55Ni		Ti-6Al-4V		SS-316L	
CS (wt%)	$\epsilon$	STD	$\epsilon$	STD	$\epsilon$	STD	$\epsilon$	STD
0	3.9	0.6	4.4	0.5	5.0	0.4	14.8	0.4
10	3.1	0.3	4.5	0.5	3.9	2.0	14.0	0.2
20	2.8	0.3	3.9	0.7	2.7	0.1	11.7	0.9
30	2.2	0.2	3.1	0.6	2.9	0.4	4.5	0.6
40	2.2	0.7	1.7	0.1	1.3	0.0	3.5	0.3
50	2.3	0.2	1.5	0.2	1.6	0.6	3.6	0.2
60	1.8	0.4	1.6	0.0	1.5	0.0	3.0	0.8
70	1.4	0.3	1.3	0.4	1.6	0.2	3.0	0.5
80	1.7	0.2	2.1	0.3	2.2	0.8	2.4	0.3
90	1.7	0.2	1.4	0.2	2.4	0.1	2.2	1.1
100	1.8	0.7	1.8	0.7	1.8	0.7	1.8	0.7

Table 4.10: Strain percentage at maximum load as a function of hydroxyapatite weight percentage

Material	$\epsilon$ (%) $\pm$ STD (%)					
	Ti		Ti-6Al-4V		SS-316L	
HA (wt%)	$\epsilon$	STD	$\epsilon$ %	STD	$\epsilon$	STD
0	3.9	0.6	5.0	0.4	14.8	0.4
10	3.3	0.5	4.3	0.2	11.7	1.4
20	3.0	0.6	3.6	0.4	3.3	0.2
30	2.8	0.4	3.4	0.4	2.1	0.6
40	2.4	0.4	2.2	0.1	1.7	0.2
50	0.7	0.6	1.4	0.3	1.8	0.3
60	1.4	0.2	1.5	1.1	1.9	0.5
70	1.1	0.7	2.2	0.8	1.5	0.4
80	1.7	0.5	2.7	0.4	2.4	0.8
90	2.1	1.1	3.4	0.9	2.5	0.8
100	3.7	0.9	3.7	0.9	3.7	0.9

## 4.3.2 Functionally graded materials

### 4.3.2.1 Physical properties

The physical properties [shrinkage ( $\epsilon$ %) and density ( $\rho$ )] of the FGMs composed of CS and HA with Ti, Ti-6Al-4V, Ti-55Ni, and SS-316L are presented in Tables 4.11 to 4.12. The FGMs were sintered at 1000 °C, 1100 °C, and 1200 °C. The

FGMs showed increasing shrinkage and density as the temperature increased. The FGMs composed of CS showed more shrinkage than the FGMs composed of HA. The minimum shrinkage was shown by the FGMs composed of SS-316L and HA.

Table 4.11: Variation in shrinkage as a function of weight percentages of calcium silicate and hydroxyapatite

		$\epsilon$ (%) $\pm$ STD (%)							
	Metal	Ti		Ti-6AL-4V		Ti-55Ni		SS-316L	
Ceramic	Temperature	$\epsilon$	STD	$\epsilon$	STD	$\epsilon$	STD	$\epsilon$	STD
CS	1000	12.4	1.2	14.9	0.8	13.2	0.8	6.4	0.6
	1100	12.6	0.6	14.9	1.1	20.2	0.5	11.1	0.4
	1200	17.3	0.7	19.5	1.1	27.4	1.7	17.1	2.8
HA	1000	15.7	1.1	16.0	0.8	7.3	0.7	0.9	0.5
	1100	15.4	1.0	17.2	1.7	13.8	0.6	3.2	1.1
	1200	16.1	2.6	18.3	6.3	17.0	4.7	4.8	1.4

Table 4.12: Variation in density as a function of weight percentages of calcium silicate and hydroxyapatite

		$\rho \times 10^{-3}$ (g/mm <sup>3</sup> ) $\pm$ STD $\times 10^{-5}$ (g/mm <sup>3</sup> )							
	Metal	Ti		Ti-6AL-4V		Ti-55Ni		SS-316L	
Ceramic	Temperature	$\rho$	STD	$\rho$	STD	$\rho$	STD	$\rho$	STD
CS	1000	3.7	4.4	3.4	2.5	4.4	4.3	4.7	9.1
	1100	3.7	1.1	3.5	2.7	4.8	1.1	5.0	4.7
	1200	3.7	1.8	3.5	2.8	5.0	6.6	5.1	1.3
HA	1000	3.7	1.7	3.8	3.6	4.2	4.0	4.7	10.1
	1100	3.7	4.2	3.8	6.8	4.6	4.1	4.6	8.2
	1200	3.8	5.1	3.9	2.7	4.5	8.9	4.4	3.0

#### 4.3.2.2 Mechanical properties

The mechanical properties of the FGMs are shown in Tables 4.13 to 4.15. Young's modulus and the ultimate compressive strength of the FGMs, except for the FGM composed of HA and SS-316L, were enhanced with increase in temperature. In other words, the Young's modulus and ultimate compressive strength of the FGM composed of HA and SS-316L decreased with increase in temperature. The Ti alloy-based FGMs showed better performance in terms of strain percentage at maximum load at 1100 °C. Meanwhile, the FGMs composed of SS-316L and CS showed maximum and minimum strain percentages at maximum load at 1000 °C and 1200 °C,

respectively. On the contrary, the strain percentage at maximum load decreased in the FGMs composed of SS-316L and HA with the increase in temperature.

Table 4.13: Compressive Young's modulus as a function of weight percentages of calcium silicate and hydroxyapatite

		E (GPa) $\pm$ STD (GPa)									
		Metal		Ti		Ti-6AL-4V		Ti-55Ni		SS-316L	
Ceramic	Temperature	E	STD	E	STD	E	STD	E	STD	E	STD
CS	1000	106.9	37.7	67.7	12.8	108.7	17.33	110.8	7.4		
	1100	119.3	15.3	61.8	5.6	110.9	10.60	143.4	18.0		
	1200	144.4	28.8	103.0	12.1	143.3	20.92	187.4	35.0		
HA	1000	104.4	15.3	94.2	18.0	118.1	8.58	94.3	6.7		
	1100	114.2	8.4	102.5	45.2	137.9	3.37	85.4	16.3		
	1200	129.9	45.0	113.8	7.4	139.4	14.37	74.7	8.2		

Table 4.14: Ultimate compressive strength as a function of weight percentages of calcium silicate and hydroxyapatite

		$\sigma_{UCS}$ (MPa) $\pm$ STD (MPa)									
		Metal		Ti		Ti-6AL-4V		Ti-55Ni		SS-316L	
Ceramic	Temperature	$\sigma_{UCS}$	STD	$\sigma_{UCS}$	STD	$\sigma_{UCS}$	STD	$\sigma_{UCS}$	STD	$\sigma_{UCS}$	STD
CS	1000	130.3	10.7	69.7	9.6	187.4	16.6	175.8	46.3		
	1100	134.4	9.1	59.0	2.9	190.7	8.6	206.4	28.8		
	1200	170.9	78.2	86.9	12.0	349.6	22.1	347.3	20.6		
HA	1000	96.6	14.0	165.4	33.9	169.2	21.9	168.4	29.6		
	1100	101.9	11.4	125.5	7.2	183.2	20.6	76.9	20.6		
	1200	178.3	45.8	145.9	24.3	228.3	50.6	75.3	3.1		

Table 4.15: Compressive strain percentage at maximum load as a function of weight percentages of calcium silicate and hydroxyapatite

		$\epsilon$ (%) $\pm$ STD (%)									
		Metal		Ti		Ti-6AL-4V		Ti-55Ni		SS-316L	
Ceramic	Temperature	$\epsilon$	STD	$\epsilon$	STD	$\epsilon$	STD	$\epsilon$	STD	$\epsilon$	STD
CS	1000	4.1	0.5	3.3	0.4	3.6	0.9	4.8	1.4		
	1100	4.7	1.0	3.5	0.0	3.2	0.4	5.6	2.1		
	1200	3.3	0.6	2.6	1.0	5.9	1.0	6.1	1.5		
HA	1000	3.1	1.2	3.4	0.7	3.4	0.1	5.6	0.5		
	1100	4.8	1.5	3.7	0.2	3.7	0.4	3.2	0.9		
	1200	3.3	0.5	5.4	0.1	3.3	0.8	3.4	0.4		

## **CHAPTER 5**

### **DISCUSSION**

#### **5.1 Introduction**

This chapter discusses the inferences from FEA and experimental results presented in the previous chapter. It is commenced with the discussion on the FEA results on the utilization of FGMs in prostheses. The presence of circumferential cracks in the cement layer is then discussed. Finally, the chapter is ended by a discussion about the experimental results.

#### **5.2 Finite element analysis on the utilization of functionally graded material in femoral prosthesis design**

The selection of materials for use in prosthesis is complex because the introduction of any implant to the aggressive physiological environment of the human body results in various biological and mechanical stresses (Enab & Bondok, 2013). The implant material must be biocompatible and resistant to corrosion and wear (Janssen et al., 2008). Moreover, the Young's modulus of prosthesis material directly affects prosthesis stiffness, stress shielding, and interface stresses. The Young's modulus of the most conventional materials (Ti alloy, Cr–Co, and St alloy) applied in femoral prosthesis is higher than that of the cortical bone, which leads to a risk of THR failure because of stress shielding. Therefore, the ability to design and manufacture a prosthesis that can incorporate bespoke and adjustable stiffness is one of the main objectives in prosthesis design (Taylor et al., 2013). This feature allows prosthetists to match the prosthesis and bone stiffness. Changes in the designs and materials used in the construction of the prostheses present the two possible methods to achieve this goal.

In the FGM-based prostheses, the increase in gradient index dictates an increase in the volume fraction of the phase with low Young's modulus. Consequently, the Young's modulus of FG prosthesis decreases in the gradient direction in both sagittal and transverse planes with gradient index growth. This condition leads to the reduction in the stiffness of prostheses regardless of gradient direction. Therefore, more SED are induced to the bone because of the adverse relationship between the stiffness of prosthesis and the stimulated SED to the proximal metaphysis of femur. This incident is also reported by Yildiz et al. (1998), and they showed more SED in the bone for Ti-based prosthesis than St-based prosthesis. In the present study, the Ti-based prostheses caused 31.0% and 27.3% more SED in the bone than the St-based prostheses in the cemented and cementless prostheses, respectively. The FG prostheses with gradient index of 1 produced more SED regardless of prostheses type (RP or LP) and geometry. Meanwhile, Simões and Marques (2005) showed an increase in the SED for LP prosthesis composed of carbon fiber with a metal core. Their finding was generally consistent with the findings in the current study. The SED increased by approximately 20.2% in cementless LP, 32.6% in cementless RP, 21.3% in cemented LP, and 27.8% in cemented RP for the increase in gradient index from 0 to 1. The SED also showed dependence on prostheses geometry because the rigidity of prosthesis is also a function of the prosthesis cross-section geometry. The distal cross-sections showed less effect on the SED variation compared with the proximal cross-sections based on the measurement of SED at the proximal and spongy portion of the femur. The average difference in the SED caused by the implantation of the prostheses with different distal cross-sections was about 6.3%, whereas proximal cross-sections provoked a difference of about 9.4% and 21.4% for cemented and cementless prostheses, respectively. Altering the profiles of the prostheses changed the SED by approximately 1.3% and 17.6% in the cemented

and cementless prostheses, respectively. The effect of the interface property on SED for cementless LP was negligible at about 0.6%.

The increase in gradient index as previously mentioned leads to the reduction in prosthesis stiffness and the mismatch between bone and prostheses stiffness. Therefore, loads distribute more equally between the constituents of the THR. Prostheses with lower stiffness carry less stress than stiffer prostheses. This phenomenon was demonstrated by El-Sheikh et al. (2002) and is also compatible with the findings of the present work for St and Ti. In FG prostheses, the developed stress in the cementless RP showed maximum reduction of 79.1% when gradient index increased from 0 to 1, and the minimum decrease in the developed stress to the prostheses was revealed in the cemented LP prostheses at about 26.3%. The stresses in the cementless LP and cemented RP declined by about 31.9% and 54.3%, respectively. This reduction in the stress in the femoral prostheses for FG prostheses was in agreement with the findings of Simões and Marques (2005) for LP. The developed stress in the implant is also a function of prostheses geometry specifications. Among the prostheses specifications, the profile exhibited minor effect on stress variation, but the proximal cross-section showed maximum influence on stress distribution. The average variations in stress caused by the change in the distal cross-sections, proximal cross-sections, and profiles were 10.3%, 15.9%, and 3.4%, respectively.

Loads transfer to the bone mainly from the proximal portion of the prosthesis in low-stiffness prostheses, nearly the whole length of prosthesis in moderate-stiffness prostheses, and distal part of prosthesis in highly stiff prosthesis (Pyburn & Goswami, 2004). Meanwhile, bone is a live tissue that adapts to its biological and mechanical environment. The alteration in load transfer and removal of a portion of the load caused by inserting an implant lead to changes in bone structures and strength. Therefore, an

implant should as much as possible mimic the natural loading condition of the hip joint without exposing the bone to too much stress. In addition, the maximum stress criterion can predict bone failure showing <30% error (Doblaré et al., 2004). The increase in gradient index as previously noted reduces the mismatch between prosthesis and bone, and more loads transfer to the bone. Consequently, both maximum and minimum principal stresses increases with the gradient index. This observation indicates that more load transfer to the proximal portion of the femur and subsequently leads to less stress shielding in the bone, whereas the developed stresses to the bone caused by the increase in loads are much less than the ultimate tensile strength (121 MPa) and ultimate compressive strength (167 MPa) of the bone. The gradient index contributes more to the change in the developed stress in the bone in the cementless prostheses than in the cemented prostheses. In addition, the stress distribution in the bone is also a function of prosthesis geometry. The geometry of prosthesis was more influential on the developed stress in the bone in the cemented prostheses than the cementless prostheses. The distal cross-sections showed greater contribution in the change in stresses than the proximal cross-section and profile, the effects of which on the developed stress in the bone were almost similar.

Load transfer to the bone in the cemented fixation method occurs through the cement layer, which also provides stability and fixation of the cemented prostheses within the host bone. Therefore, overstressing the cement layer leads to the failure of the cement layer, loosening of the stem, and ultimately THR failure. Mechanical failure is the main reason for cement failure (James et al., 1992). Given that orthopedic cement is a brittle material, it is weaker under tensile loads than at compressive loads. Loads transfer through the prosthesis to the cement and then to the bone. Therefore, the main portion of the loads are applied to the internal surface of the cement, and then moved to the external surface. Hence, the internal surface of the cement layer carried more

maximum and minimum principal stresses in both LP and RP. The maximum principal stress at the lateral side and the minimum principal stress at the medial side of the cement layer showed two different trends with the increase in gradient index. In other words, the maximum principal stress increased with the increase in gradient index, contrary to the decreasing trend of the minimum principal stress under the same condition. The developed stresses in the cement layer showed sensitivity to the geometry of prostheses, which is consistent with the findings of Ramos et al. (2012). The prostheses with D3 distal cross-section and P3 proximal cross-section induced the lowest values of the maximum and minimum principal stress.

The interface stresses have a significant role on the initial stability of the prostheses and the long term survival of THR, especially for cementless prostheses. The geometry and gradient index high influence the interface stresses. The interface stresses at the implant–bone interface decreased with the increase in gradient index, which is not consistent with those in prostheses composed of conventional materials. In other words, the interface stresses at the implant–bone interface declined with the increasing Young's modulus of the conventional materials applied in the prosthesis, whereas their stress shielding effect increased (Simões & Marques, 2005). The results in the present study are supported by the findings of Hedia et al. (2004; 2006). The effect of geometrical specification on the interface stresses is consistent with the statements of Pal et al. (2013) with regard to the effect of geometric features on the stability of hip stem. Meanwhile, in RP, the prosthesis with D3 distal cross-section, P4 proximal cross-section, and Profile 1 induced minimum interface stresses, whereas in LP, the minimum interface stress was provoked by the prosthesis with D4 distal cross-section, P3 proximal cross-section, and Profile 3.



### 5.3 Existence of circumferential crack in the cement layer

Orthopedic cement is categorized as a brittle material (Culleton et al., 1993; McCormack et al., 1999; Topoleski et al., 1998), and SIFs are valid and applicable for the analysis of the crack behavior inside the cement. Accordingly, by understanding the SIFs during the different stages of walking, the lifespan of the cement layer and the crack growth rate in a gait cycle can be predicted using crack propagation laws such as Paris' law. Crack initiation and propagation at the cement–prosthesis or cement–bone interfaces present a contradictory discussion. Several researchers believe that cracks initiate and propagate from the cement–prosthesis interface, while other researchers noted that crack initiation and propagation occur in the cement–bone interface (Moreo et al., 2006; Ramos & Simões, 2009). However, any improvement in the bonding properties of the cement–bone interface increases the stresses in the interface (Achour et al., 2010), which explains the high SIFs at the cement–bone interface.

Internal and external cracks do not indicate significant interaction. The numerical study on the circumferential crack behavior revealed that  $K_{II}$  is smaller than  $K_I$  and  $K_{III}$ . This behavior is in agreement with the crack geometry effect on the SIFs explored by Shahani and Habibi (2007). In addition, higher SIF values were obtained at the distal part compared with the proximal part of the cement layer because post-THR loads transfer via shear forces across the material interfaces at the proximal to the distal ends of the stem (Gross & Abel, 2001). Thus, excessive loads were transferred from the distal area of the prosthesis to the bone through the cement (Ramos et al., 2012) because of the mismatch between the stiffness of THR components (prosthesis, cement, and bone). The results of the current study are also supported by the findings of Afsharpoya et al. (2009) about Charnley prosthesis, in which the peak stresses were concentrated at the distal end of the prosthesis–cement interface. Such transfer causes extreme stresses

at the distal end of the cement layer, thereby enhancing the  $K_I$ ,  $K_{II}$ , and  $K_{III}$  values. This behavior has been proven by Flitti et al. (2010) and Jeffers et al. (2007). The results of the present study also indicated that SIFs vary along the crack front in the hoop direction, which correspond to the stress variations in the hoop path reported by McCormack and Prendergast (1999).

Furthermore,  $K_I$  and  $K_{III}$  displayed opposite trends in the hoop direction.  $K_I$  declined along the lateral and medial to the anterior and posterior directions, whereas  $K_{III}$  decreased along the anterior and posterior to the lateral and medial directions. Accordingly, at the crack front, the absolute maximum and minimum values of  $K_I$  coincided with the absolute minimum and maximum values of  $K_{III}$ . The crack propagation was mostly subjected to the combination of both opening and tearing except at areas with maximum  $K_I$  or  $K_{III}$  values. The cement corners were under the highest SIFs on the lateral and medial sides. Subsequently, the risk of crack initiation and propagation increased at the distal corners of the cement layer, which is consistent with results from previous studies (Jasty et al., 1991; Verdonschot & Huiskes, 1997).

Finally, the cement layer must withstand the cyclic load during walking. In the gait cycle, the SIFs attained maximum values in the single-leg stance and push off phases and then declined to the minimum values during the swing phase. Accordingly, the cement layer suffered a fatigue load because of the SIF fluctuations, resulting in crack propagation and cement failure in THR for an extended period (Hung et al., 2004). Given that the lateral side has to endure regular tensile stress, the risk of a fatigue crack propagation in this side is greater than that in the medial side. This result corresponds with the finding of Jeffers et al. (2007). However, both normal and tear fatigue cracks may occur at the anterior and posterior sides of the cement layer.

## 5.4 Composites and functionally graded materials

Different composites of CS and HA with Ti, Ti-6Al-4V, Ti-55Ni, and SS-316L were produced and then physically and mechanically tested. Sintering at high temperature led to the appearance of new phases of materials. The weight ratio of the raw powders in the mixture showed high impact on the emergence of the new phases. The appearance of the new phases of the materials demonstrated by (Arifin et al., 2014) are consistent with findings of the present work. These phases significantly affect the physical and mechanical properties of the sintered composite materials. Metal or ceramic-rich composites showed better mechanical performance and hardness than the composites with 40wt% to 60 wt% metal or ceramic. The trend of hardness in the present study for the composites of Ti-HA and SS-316L-HA was in agreement with the demonstrated results in the studies of Chenglin (1999) and Younesi and Bahrololoom (2010), respectively. Meanwhile, the metal-rich composites carried more load than the ceramic-rich composites. The composites of CS with SS-316L showed better mechanical performance compared with the CS composites with Ti and Ti alloys. The CS composites with SS-316L exhibited more plastic deformation than pure CS by showing more strain percentage at the maximum load. Meanwhile, the increased hardness of these composites could help them to resist wear compared with pure SS-316L (Younesi & Bahrololoom, 2010). On the contrary, the composites of SS-316L with HA in the metal-rich group showed weak mechanical properties, whereas the ceramic-rich group exhibited good mechanical performance. The Ti and Ti alloy composites with HA and CS had almost similar mechanical performance.

FGMs were developed from metal-rich composites because these composites showed better mechanical performance. Therefore, the FGM layer was composed of pure metal and the composite with 90 wt%, 80wt%, and 70wt% metal phases and

sintered at 1000 °C, 1100 °C, and 1200 °C. The increase in temperature positively affected the mechanical performance of the FGMs, except for the FGMs composed of SS-316L and HA, because of the increase in the rate of reaction between SS-316L and HA. The FGMs showed better properties for hard tissue substitution compared with the pure materials and single-layer composites. The Young's modulus of the FGMs was less than that of pure metals, and their ultimate compressive strength was more than those of the single-layer composites with CS or HA content  $\geq 30$  wt%. Meanwhile, the FGMs showed more strain at the maximum load and more plasticity and less brittle properties compared with the single layer of the composites, except for SS-316L composites with contents of HA or CS and SS-316L  $\geq 20$ wt%.

## CHAPTER 6

### CONCLUSION AND RECOMMENDATIONS

#### 6.1 Conclusions

The material and the gradient index are the most influential factors that control SED in LP and RP. The increase in gradient index resulted in increased SED to the bone. The geometrical parameters were more influential in the cementless prostheses than in the cemented prostheses. The cementless RP provoked more SED in the bone compared with the LP.

The gradient index and geometry are the key factors in changing the developed stress in the prostheses. However, the influence of the material and gradient index were greater than that of the geometry of prostheses on the developed stress in the prostheses. The induced stress to the prostheses decreased with the increase in gradient index. Profiles showed less effect on the induced stress to the prostheses compared with the proximal and distal cross-sections. Meanwhile, the cementless prostheses carried less stress than the cemented prostheses.

The gradient index and geometric parameters are important factors in controlling and adjusting the developed stress in the bone. The effect of gradient index was more significant in the cementless prostheses, and the geometric factors were more influential in the cemented prostheses.

The increase in gradient index showed bilateral effect on the developed stress in the cement layer. The maximum and minimum principal stresses showed increasing and

decreasing trends with the increase in gradient index, respectively. The prostheses made of distal cross-section D3 and proximal cross-section P3 developed minimum stress in the cement layer. The effect of the profile depended on the prosthesis type.

The gradient index and geometry highly affected the interface stresses. The utilization of FGMs and the increasing gradient index led to the decrease in the interface stress. The geometry should be designed based on prostheses type (RP or LP) to achieve minimum interface stresses. The RP with distal cross-section D3, proximal cross-section P4, and Profile 1 induced minimum interface stress, whereas the LP with distal cross-section D4, proximal cross-section P3, and Profile 3 provoked the minimum interface stress.

The SIFs were enhanced along the cement from the proximal to the distal end. In a certain cross section, the SIFs attained a maximum value in the push off and single-leg stance phases, whereas minimum SIF values were attained in the swing phase of a gait.  $K_I$  and  $K_{III}$  were the most superior SIF modes in the cement layer with internal circumferential cracks. By contrast,  $K_{II}$  was approximately a tenth of  $K_I$ . The  $K_I$  domain was at the lateral and medial sides of the cement layer, whereas the  $K_{III}$  domain was at the anterior and posterior sides. Consequently, the circumferential cracks endured a normal fatigue at the lateral and medial sides of the cement layer, whereas the anterior and posterior sides of the cement layer were subjected to a torsional fatigue. Moreover, the circumferential cracks were propelled by a mixed mode of opening and tearing loads at a large portion of the crack front. Cracks at the internal and external surfaces of the cement layer did not show any significant interaction.

The FGMs could be utilized in implants as a proper substitute to conventional materials because of their unique properties. The FGMs composed of CS and HA with

Ti, Ti-6Al-4V, Ti-55Ni, and SS-316L showed lower Young's moduli than the pure metals and higher ultimate compressive strength compared with the pure ceramic and composites with 30 wt% ceramic. In addition, the FGMs showed more plasticity by exhibiting higher strain percentage at the maximum load compared with the pure ceramic and composites with more than 30 wt% ceramic.

## **6.2 Recommendations**

The following studies are recommended to improve the performance of the FG prostheses and prolong the lifespan of the THR, understand the crack behavior and crack propagation in the cement layer of THR during daily activities, and develop an MCC, CMC, or FGM with the best performance for the FG prostheses.

The geometry of the prosthesis should be optimized based on a defined gradient direction (radial or longitudinal). Failure criteria should be embedded to a 3D FEA, and the risk of failure in the components of the THR with an FG prosthesis should be assessed. Meanwhile, the adaptation of the bone caused by the impact of the FGMs in prosthesis should be also examined.

Different cracks should be inserted into the cement layer and evaluated during main daily activities such as normal walking and stair climbing. In addition, the fatigue crack propagation should also be considered in the studies to assess the crack propagation mechanism during different activities.

The composite of metal and ceramic should be optimized in terms of the material, volume fraction of each phase, sintering temperature, and sintering process to achieve a composite or FGM with the best mechanical properties for prosthesis.

Finally, a prototype of the prosthesis composed of the optimized geometry and material should be prepared for final assessment and in vitro test.



## References

- Abdul-Kadir, M. R., Hansen, U., Klabunde, R., Lucas, D., & Amis, A. (2008). Finite element modelling of primary hip stem stability: The effect of interference fit. *Journal of Biomechanics*, 41(3), 587-594.
- Achour, T., Tabeti, M. S. H., Bouziane, M. M., Benbarek, S., Bachir Bouiadjra, B., & Mankour, A. (2010). Finite element analysis of interfacial crack behaviour in cemented total hip arthroplasty. *Computational Materials Science*, 47(3), 672-677.
- Afsharpoya, B., Barton, D., Fisher, J., Purbach, B., Wroblewski, M., & Stewart, T. (2009). Cement mantle stress under retroversion torque at heel-strike. *Medical engineering & physics*, 31(10), 1323-1330.
- Akay, M., & Aslan, N. (1996). Numerical and experimental stress analysis of a polymeric composite hip joint prosthesis. *Journal of biomedical materials research*, 31(2), 167-182.
- Al-Hajjar, M., Jennings, L. M., Begand, S., Oberbach, T., Delfosse, D., & Fisher, J. (2013). Wear of novel ceramic-on-ceramic bearings under adverse and clinically relevant hip simulator conditions. *Journal of Biomedical Materials Research Part B: Applied Biomaterials*.
- Aminzare, M., Eskandari, A., Baroonian, M., Berenov, A., Razavi Hesabi, Z., Taheri, M., & Sadrnezhaad, S. (2012). Hydroxyapatite nanocomposites: Synthesis, sintering and mechanical properties. *Ceramics International*.
- Arifin, A., Sulong, A. B., Muhamad, N., Syarif, J., & Ramli, M. I. (2014). Material processing of hydroxyapatite and titanium alloy (HA/Ti) composite as implant materials using powder metallurgy: A review. *Materials & Design*, 55, 165-175.
- Asgari, S. A., Hamouda, A., Mansor, S., Singh, H., Mahdi, E., Wirza, R., & Prakash, B. (2004). Finite element modeling of a generic stemless hip implant design in comparison with conventional hip implants. *Finite elements in analysis and design*, 40(15), 2027-2047.
- Asthana, R., Kumar, A., & Dahotre, N. B. (2006). 3 - Powder Metallurgy and Ceramic Forming *Materials Processing and Manufacturing Science* (pp. 167-245). Burlington: Academic Press.
- Behrens, B., Wirth, C., Windhagen, H., Nolte, I., Meyer-Lindenberg, A., & Bouguecha, A. (2008). Numerical investigations of stress shielding in total hip prostheses. *Proceedings of the Institution of Mechanical Engineers, Part H: Journal of Engineering in Medicine*, 222(5), 593-600.
- Beldame, J., Carreras, F., Oger, P., & Beaufils, P. (2009). Cementless cups do not increase osteolysis risk in metal-on-metal total hip arthroplasty. *Orthopaedics & Traumatology: Surgery & Research*, 95(7), 478-490.

- Bennett, D., & Goswami, T. (2008). Finite element analysis of hip stem designs. *Materials & design*, 29(1), 45-60.
- Borrmann, T., Edgar, K., McFarlane, A., Spencer, J., & Johnston, J. (2004). Calcium silicate-carbon nanotube composites. *Current Applied Physics*, 4(2), 359-361.
- Bougherara, H., Zdero, R., Dubov, A., Shah, S., Khurshid, S., & Schemitsch, E. H. (2011). A preliminary biomechanical study of a novel carbon-fibre hip implant versus standard metallic hip implants. *Medical engineering & physics*, 33(1), 121-128.
- Bourghli, A., Fabre, T., Tramond, P., & Durandean, A. (2010). Total Hip Replacement pseudotumoral osteolysis. *Orthopaedics & Traumatology: Surgery & Research*, 96(3), 319-322.
- Bowman Jr, K. F., Fox, J., & Sekiya, J. K. (2010). A clinically relevant review of hip biomechanics. *Arthroscopy - Journal of Arthroscopic and Related Surgery*, 26(8), 1118-1129+e1133.
- Boyle, C., & Kim, I. Y. (2011). Comparison of different hip prosthesis shapes considering micro-level bone remodeling and stress-shielding criteria using three-dimensional design space topology optimization. *Journal of Biomechanics*, 44(9), 1722-1728.
- Brown, B. S., & Huo, M. H. (2002). Revision total hip replacement for osteolysis. *Current Opinion in Orthopaedics*, 13(1), 48-52.
- Caeiro, J., Riba, J., & Gomar, F. (2011). Incidence and risk factors of dislocation after total hip replacement with a ceramic acetabular system. *Revista Española de Cirugía Ortopédica y Traumatología (English Edition)*, 55(6), 437-445.
- Canales, V., Panisello, J. J., Herrera, A., Sola, A., Mateo, J. J., & Caballero, M. J. (2010). Extensive Osteolysis Caused By Polyethylene Particle Migration in an Anatomical Hydroxyapatite-Coated Hip Prosthesis: 10 Years' Follow-Up. *The Journal of Arthroplasty*, 25(7), 1115-1124.e1111.
- Catelas, I., Wimmer, M. A., & Utschneider, S. (2011). Polyethylene and metal wear particles: characteristics and biological effects. *Proceedings of Seminars in immunopathology* (pp. 257-271).
- Chenglin, C., Jingchuan, Z., Zhongda, Y., & Shidong, W. (1999). Hydroxyapatite-Ti functionally graded biomaterial fabricated by powder metallurgy. *Materials Science and Engineering: A*, 271(1), 95-100.
- Chevalier, J. (2006). What future for zirconia as a biomaterial? *Biomaterials*, 27(4), 535-543.
- Cristofolini, L., Varini, E., Pelgreffi, I., Cappello, A., & Toni, A. (2006). Device to measure intra-operatively the primary stability of cementless hip stems. *Medical Engineering & Physics*, 28(5), 475-482.

- Crowninshield, R. (2001). Femoral hip implant fixation within bone cement. *Operative Techniques in Orthopaedics*, 11(4), 296-299.
- Culleton, T., Prendergast, P., & Taylor, D. (1993). Fatigue failure in the cement mantle of an artificial hip joint. *Clinical Materials*, 12(2), 95-102.
- De Oliveira Simoes, J., & Marques, A. (2001). Determination of stiffness properties of braided composites for the design of a hip prosthesis. *Composites Part A: Applied Science and Manufacturing*, 32(5), 655-662.
- De Santis, R., Ambrosio, L., & Nicolais, L. (2000). Polymer-based composite hip prostheses. *Journal of Inorganic Biochemistry*, 79(1-4), 97-102.
- Doblaré, M., García, J. M., & Gómez, M. J. (2004). Modelling bone tissue fracture and healing: a review. *Engineering Fracture Mechanics*, 71(13-14), 1809-1840.
- Dunne, N., & Ormsby, R. W. (2011). MWCNT Used in Orthopaedic Bone Cements.
- El-Sheikh, H., MacDonald, B., & Hashmi, M. (2002). Material selection in the design of the femoral component of cemented total hip replacement. *Journal of materials processing technology*, 122(2), 309-317.
- Enab, T. A., & Bondok, N. E. (2013). Material selection in the design of the tibia tray component of cemented artificial knee using finite element method. *Materials & Design*, 44(0), 454-460.
- Evans, S., & Gregson, P. (1998). Composite technology in load-bearing orthopaedic implants. *Biomaterials*, 19(15), 1329-1342.
- Fabbri, N., Rustemi, E., Masetti, C., Kreshak, J., Gambarotti, M., Vanel, D., Toni, A., & Mercuri, M. (2011). Severe osteolysis and soft tissue mass around total hip arthroplasty: Description of four cases and review of the literature with respect to clinico-radiographic and pathologic differential diagnosis. *European Journal of Radiology*, 77(1), 43-50.
- Flitti, A., Ouinas, D., Bouiadjra, B. B., & Benderdouche, N. (2010). Effect of the crack position in the cement mantle on the fracture behavior of the total hip prosthesis. *Computational Materials Science*, 49(3), 598-602.
- Gross, S., & Abel, E. W. (2001). A finite element analysis of hollow stemmed hip prostheses as a means of reducing stress shielding of the femur. *Journal of Biomechanics*, 34(8), 995-1003.
- Hannouche, D., Hamadouche, M., Nizard, R., Bizot, P., Meunier, A., & Sedel, L. (2005). Ceramics in Total Hip Replacement. *Clinical Orthopaedics and Related Research*, 430, 62-71.
- Hao, S., Taylor, J. T., Bowen, C. R., Gheduzzi, S., & Miles, A. W. (2010). Sensing methodology for in vivo stability evaluation of total hip and knee arthroplasty. *Sensors and Actuators A: Physical*, 157(1), 150-160.

- Havlik, R. J. (2002). Hydroxyapatite. *Plastic and Reconstructive Surgery*, 110(4), 1176-1179.
- Hedia, H., Shabara, M., El-Midany, T., & Fouda, N. (2004). A method of material optimization of cementless stem through functionally graded material. *International Journal of Mechanics and Materials in Design*, 1(4), 329-346.
- Hedia, H., Shabara, M., El-Midany, T., & Fouda, N. (2006). Improved design of cementless hip stems using two-dimensional functionally graded materials. *Journal of Biomedical Materials Research Part B: Applied Biomaterials*, 79(1), 42-49.
- Heimann, R. B. (2010). *Classic and advanced ceramics: from fundamentals to applications*: John Wiley & Sons.
- Huiskes, R. (1988). Stress patterns, failure modes, and bone remodeling. *Non-Cemented Hip Arthroplasty*, Raven Press, New York, 283-302.
- Hung, J.-P., Chen, J.-H., Chiang, H.-L., & Shih-Shyn Wu, J. (2004). Computer simulation on fatigue behavior of cemented hip prostheses: a physiological model. *Computer methods and programs in biomedicine*, 76(2), 103-113.
- Ilesanmi, O. O. (2010). Pathological basis of symptoms and crises in sickle cell disorder: implications for counseling and psychotherapy. *Hematology reports*, 2(1).
- Izzo, G. M. (2012). Support for total hip replacement surgery: Structures modeling, Gait Data Analysis and Report system. *European Journal of Translational Myology*, 22(1-2), 69-121.
- Jamali, A. A., Lozynsky, A. J., & Harris, W. H. (2006). The effect of surface finish and of vertical ribs on the stability of a cemented femoral stem: an in vitro stair climbing test. *The Journal of arthroplasty*, 21(1), 122-128.
- James, S. P., Jasty, M., Davies, J., Piehler, H., & Harris, W. H. (1992). A fractographic investigation of PMMA bone cement focusing on the relationship between porosity reduction and increased fatigue life. *Journal of biomedical materials research*, 26(5), 651-662.
- Janssen, D., Mann, K. A., & Verdonschot, N. (2008). Micro-mechanical modeling of the cement–bone interface: The effect of friction, morphology and material properties on the micromechanical response. *Journal of Biomechanics*, 41(15), 3158-3163.
- Jasty, M., Maloney, W., Bragdon, C., O'connor, D., Haire, T., & Harris, W. (1991). The initiation of failure in cemented femoral components of hip arthroplasties. *Journal of Bone & Joint Surgery, British Volume*, 73(4), 551-558.
- Jeffers, J. R., Browne, M., Lennon, A. B., Prendergast, P. J., & Taylor, M. (2007). Cement mantle fatigue failure in total hip replacement: experimental and computational testing. *Journal of biomechanics*, 40(7), 1525-1533.

- Jenabzadeh, A.-R., Pearce, S. J., & Walter, W. L. (2012). Total Hip Replacement: Ceramic-on-Ceramic. *Seminars in Arthroplasty*, 23(4), 232-240.
- Joshi, M. G., Advani, S. G., Miller, F., & Santare, M. H. (2000). Analysis of a femoral hip prosthesis designed to reduce stress shielding. *Journal of Biomechanics*, 33(12), 1655-1662.
- Juillard, F. (2011). Effects of Tissue-Level Ductility on Trabecular Bone Strength.
- Jun, Y., & Choi, K. (2010). Design of patient-specific hip implants based on the 3D geometry of the human femur. *Advances in Engineering Software*, 41(4), 537-547.
- Kaddick, C., Stur, S., & Hipp, E. (1997). Mechanical simulation of composite hip stems. *Medical Engineering and Physics*, 19(5), 431-439.
- Katoozian, H., Davy, D. T., Arshi, A., & Saadati, U. (2001). Material optimization of femoral component of total hip prosthesis using fiber reinforced polymeric composites. *Medical Engineering & Physics*, 23(7), 505-511.
- Khanuja, H. S., Vakil, J. J., Goddard, M. S., & Mont, M. A. (2011). Cementless Femoral Fixation in Total Hip Arthroplasty. *The Journal of Bone & Joint Surgery*, 93(5), 500-509.
- Kleemann, R. U., Heller, M. O., Stoeckle, U., Taylor, W. R., & Duda, G. N. (2003). THA loading arising from increased femoral anteversion and offset may lead to critical cement stresses. *Journal of Orthopaedic Research*, 21(5), 767-774.
- Kosmač, T., Oblak, C., Jevnikar, P., Funduk, N., & Marion, L. (1999). The effect of surface grinding and sandblasting on flexural strength and reliability of Y-TZP zirconia ceramic. *Dental Materials*, 15(6), 426-433.
- Kuiper, J., & Huiskes, R. (1997). Mathematical optimization of elastic properties: Application to cementless hip stem design. *Transactions-American Society of Mechanical Engineers Journal of Biomechanical Engineering*, 119, 166-174.
- Lai, Y. S., Wei, H. W., Chang, T. K., & Cheng, C. K. (2009). The effects of femoral canal geometries, stem shapes, cement thickness, and stem materials on the choice of femoral implant in cemented total hip replacement. *Journal of the Chinese Institute of Engineers*, 32(3), 333-341.
- Lewis, G. (1997). Properties of acrylic bone cement: State of the art review. *Journal of Biomedical Materials Research*, 38(2), 155-182.
- Li, Y., Yang, C., Zhao, H., Qu, S., Li, X., & Li, Y. (2014). New Developments of Ti-Based Alloys for Biomedical Applications. *Materials*, 7(3), 1709-1800.
- Long, M., & Rack, H. J. (1998). Titanium alloys in total joint replacement—a materials science perspective. *Biomaterials*, 19(18), 1621-1639.

- Löser, E., & Stropp, G. (1999). Chapter 38 - Polymers. In: M. Hans, G. S. Siegfried, M. Roger, S. G. S. R. M. Frank WelschA2 - Hans Marquardt & W. Frank (Eds.), *Toxicology* (pp. 919-936). San Diego: Academic Press.
- Luthardt, R., Holzhüter, M., Sandkuhl, O., Herold, V., Schnapp, J., Kuhlisch, E., & Walter, M. (2002). Reliability and properties of ground Y-TZP-zirconia ceramics. *Journal of dental research*, 81(7), 487-491.
- Mackenzie, J. D. (1969). Ceramics in ocean engineering. *Ocean Engineering*, 1(5), 555-571.
- Manicone, P. F., Rossi Iommetti, P., & Raffaelli, L. (2007). An overview of zirconia ceramics: Basic properties and clinical applications. *Journal of Dentistry*, 35(11), 819-826.
- Mattern, A., Huchler, B., Staudenecker, D., Oberacker, R., Nagel, A., & Hoffmann, M. (2004). Preparation of interpenetrating ceramic-metal composites. *Journal of the European ceramic Society*, 24(12), 3399-3408.
- McCormack, B., Prendergast, P., & O'Dwyer, B. (1999). Fatigue of cemented hip replacements under torsional loads. *Fatigue & Fracture of Engineering Materials & Structures*, 22(1), 33-40.
- Mehrali, M., Moghaddam, E., Shirazi, S. F. S., Baradaran, S., Mehrali, M., Latibari, S. T., Metselaar, H. S. C., Kadri, N. A., Zandi, K., & Osman, N. A. A. (2014). Synthesis, Mechanical Properties, and in Vitro Biocompatibility with Osteoblasts of Calcium Silicate-Reduced Graphene Oxide Composites. *ACS applied materials & interfaces*, 6(6), 3947-3962.
- Miao, X., & Sun, D. (2009). Graded/gradient porous biomaterials. *Materials*, 3(1), 26-47.
- Mishina, H., Inumaru, Y., & Kaitoku, K. (2008). Fabrication of ZrO<sub>2</sub>/AISI316L functionally graded materials for joint prostheses. *Materials Science and Engineering: A*, 475(1), 141-147.
- Molli, R. G., Lombardi, A. V., Berend, K. R., Adams, J. B., & Sneller, M. A. (2011). Metal-on-metal vs metal-on-improved polyethylene bearings in total hip arthroplasty. *The Journal of arthroplasty*, 26(6), 8-13.
- Moreo, P., Perez, M., García-Aznar, J., & Doblare, M. (2006). Modelling the mixed-mode failure of cement-bone interfaces. *Engineering Fracture Mechanics*, 73(10), 1379-1395.
- Musolino, M., Pettit, F., Burleigh, T., Rubash, H., & Shanbhag, A. (1996). Analysis of corrosion in stainless steel total hip prostheses. Proceedings of Biomedical Engineering Conference, 1996., Proceedings of the 1996 Fifteenth Southern (pp. 5-6).
- Naudie, D., Roeder, C. P., Parvizi, J., Berry, D. J., Egli, S., & Busato, A. (2004). Metal-on-metal versus metal-on-polyethylene bearings in total hip arthroplasty: a matched case-control study. *The Journal of arthroplasty*, 19(7), 35-41.

- Nie, G., & Batra, R. (2010). Material tailoring and analysis of functionally graded isotropic and incompressible linear elastic hollow cylinders. *Composite Structures*, 92(2), 265-274.
- Ohgaki, M., & Yamashita, K. (2003). Preparation of Polymethylmethacrylate-Reinforced Functionally Graded Hydroxyapatite Composites. *Journal of the American Ceramic Society*, 86(8), 1440-1442.
- Pal, B., Puthumanapully, P. K., & Amis, A. A. (2013). (ii) Biomechanics of implant fixation. *Orthopaedics and Trauma*, 27(2), 76-84.
- Pérez, M. A., García, J. M., & Doblaré, M. (2005). Analysis of the debonding of the stem–cement interface in intramedullary fixation using a non-linear fracture mechanics approach. *Engineering Fracture Mechanics*, 72(8), 1125-1147.
- Piconi, C., & Maccauro, G. (1999). Zirconia as a ceramic biomaterial. *Biomaterials*, 20(1), 1-25.
- Polkowski, G. G., & Clohisy, J. C. (2010). Hip biomechanics. *Sports Medicine and Arthroscopy Review*, 18(2), 56-62.
- Pompe, W., Worch, H., Epple, M., Friess, W., Gelinsky, M., Greil, P., Hempel, U., Scharnweber, D., & Schulte, K. (2003). Functionally graded materials for biomedical applications. *Materials Science and Engineering: A*, 362(1), 40-60.
- Pramanik, S., Hanif, A. S. M., Pinguan-Murphy, B., & Abu Osman, N. A. (2012). Morphological change of heat treated bovine bone: a comparative study. *Materials*, 6(1), 65-75.
- Pramanik, S., & Kar, K. (2013). Nanohydroxyapatite synthesized from calcium oxide and its characterization. *The International Journal of Advanced Manufacturing Technology*, 66(5-8), 1181-1189.
- Pyburn, E., & Goswami, T. (2004). Finite element analysis of femoral components paper III–hip joints. *Materials & design*, 25(8), 705-713.
- Ramos, A., Completo, A., Relvas, C., & Simões, J. A. (2012). Design process of a novel cemented hip femoral stem concept. *Materials & Design*, 33(0), 313-321.
- Ramos, A., & Simoes, J. (2006). Tetrahedral versus hexahedral finite elements in numerical modelling of the proximal femur. *Medical engineering & physics*, 28(9), 916-924.
- Ramos, A., & Simões, J. (2009). The influence of cement mantle thickness and stem geometry on fatigue damage in two different cemented hip femoral prostheses. *Journal of biomechanics*, 42(15), 2602-2610.
- Rodriguez-Suarez, T., Bartolomé, J., & Moya, J. (2012). Mechanical and tribological properties of ceramic/metal composites: A review of phenomena spanning from the nanometer to the micrometer length scale. *Journal of the European Ceramic Society*.

- Ruben, R., Folgado, J., & Fernandes, P. (2007). Three-dimensional shape optimization of hip prostheses using a multicriteria formulation. *Structural and Multidisciplinary Optimization*, 34(3), 261-275.
- Sabatini, A. L., & Goswami, T. (2008). Hip implants VII: finite element analysis and optimization of cross-sections. *Materials & Design*, 29(7), 1438-1446.
- Sahin, Y. (2005). The effects of various multilayer ceramic coatings on the wear of carbide cutting tools when machining metal matrix composites. *Surface and Coatings Technology*, 199(1), 112-117.
- Saithna, A. (2010). The influence of hydroxyapatite coating of external fixator pins on pin loosening and pin track infection: a systematic review. *Injury*, 41(2), 128-132.
- Scheerlinck, T., & Casteleyn, P.-P. (2006). The design features of cemented femoral hip implants. *Journal of Bone & Joint Surgery, British Volume*, 88(11), 1409-1418.
- Scholz, M.-S., Blanchfield, J., Bloom, L., Coburn, B., Elkington, M., Fuller, J., Gilbert, M., Muflahi, S., Pernice, M., & Rae, S. (2011). The use of composite materials in modern orthopaedic medicine and prosthetic devices: A review. *Composites Science and Technology*, 71(16), 1791-1803.
- Shahani, A., & Habibi, S. (2007). Stress intensity factors in a hollow cylinder containing a circumferential semi-elliptical crack subjected to combined loading. *International journal of fatigue*, 29(1), 128-140.
- Shikha, D., Jha, U., Sinha, S., Barhai, P., Nair, K., Dash, S., Tyagi, A., Kalavathy, S., & Kothari, D. (2009). Microstructure and biocompatibility investigation of biomaterial alumina after 30 keV and 60 keV nitrogen ion implantation. *Surface and Coatings Technology*, 203(17), 2541-2545.
- Shirazi, F., Mehrali, M., Oshkour, A., Metselaar, H., Kadri, N., & Abu Osman, N. (2014). Mechanical and physical properties of calcium silicate/alumina composite for biomedical engineering applications. *Journal of the mechanical behavior of biomedical materials*, 30, 168-175.
- Simões, J., & Marques, A. (2005). Design of a composite hip femoral prosthesis. *Materials & design*, 26(5), 391-401.
- Simpson, D. J., Little, J. P., Gray, H., Murray, D. W., & Gill, H. S. (2009). Effect of modular neck variation on bone and cement mantle mechanics around a total hip arthroplasty stem. *Clinical Biomechanics*, 24(3), 274-285.
- Singh, S., Trikha, S., & Edge, A. (2004). Hydroxyapatite ceramic-coated femoral stems in young patients A PROSPECTIVE TEN-YEAR STUDY. *Journal of Bone & Joint Surgery, British Volume*, 86(8), 1118-1123.
- Sivarasu, S., Beulah, P., & Mathew, L. (2011). Novel Approach for Designing a Low Weight Hip Implant Used in Total Hip Arthroplasty Adopting Skeletal Design Techniques. *Artificial Organs*, 35(6), 663-666.



- Slouf, M., Eklova, S., Kumstatova, J., Berger, S., Synkova, H., Sosna, A., Pokorny, D., Spundova, M., & Entlicher, G. (2007). Isolation, characterization and quantification of polyethylene wear debris from periprosthetic tissues around total joint replacements. *Wear*, 262(9), 1171-1181.
- Stops, A., Wilcox, R., & Jin, Z. (2011). Computational modelling of the natural hip: a review of finite element and multibody simulations. *Computer Methods in Biomechanics and Biomedical Engineering*, 15(9), 963-979.
- Suárez-Vázquez, A., Hernández-Vaquero, D., Del Valle López-Díaz, M., & Pérez-Coto, I. (2011). Distribution of periprosthetic osteolysis in the hip: A study using magnetic resonance. *Revista Española de Cirugía Ortopédica y Traumatología (English Edition)*, 55(3), 193-203.
- Taylor, M., Bryan, R., & Galloway, F. (2013). Accounting for patient variability in finite element analysis of the intact and implanted hip and knee: a review. *International journal for numerical methods in biomedical engineering*, 29(2), 273-292.
- Topoleski, L., Ducheyne, P., & Cuckler, J. M. (1998). Flow intrusion characteristics and fracture properties of titanium-fibre-reinforced bone cement. *Biomaterials*, 19(17), 1569-1577.
- Traina, F., De Fine, M., Di Martino, A., & Faldini, C. (2013). Fracture of Ceramic Bearing Surfaces following Total Hip Replacement: A Systematic Review. *BioMed Research International*, 2013.
- Tudor, A., Laurian, T., & Popescu, V. M. (2013). The effect of clearance and wear on the contact pressure of metal on polyethylene hip prostheses. *Tribology International*, 63(0), 158-168.
- Varini, E., Cristofolini, L., Traina, F., Viceconti, M., & Toni, A. (2008). Can the rasp be used to predict intra-operatively the primary stability that can be achieved by press-fitting the stem in cementless hip arthroplasty? *Clinical Biomechanics*, 23(4), 408-414.
- Vendittoli, P.-A., Amzica, T., Roy, A. G., Lusignan, D., Girard, J., & Lavigne, M. (2011). Metal ion release with large-diameter metal-on-metal hip arthroplasty. *The Journal of arthroplasty*, 26(2), 282-288.
- Verdonschot, N., & Huiskes, R. (1997). The effects of cement-stem debonding in THA on the long-term failure probability of cement. *Journal of Biomechanics*, 30(8), 795-802.
- Viceconti, M., Brusi, G., Pancanti, A., & Cristofolini, L. (2006). Primary stability of an anatomical cementless hip stem: A statistical analysis. *Journal of Biomechanics*, 39(7), 1169-1179.
- Waanders, D., Janssen, D., Mann, K. A., & Verdonschot, N. (2011). The behavior of the micro-mechanical cement–bone interface affects the cement failure in total hip replacement. *Journal of biomechanics*, 44(2), 228-234.

- Xie, Y., Li, H., Zhang, C., Gu, X., Zheng, X., & Huang, L. (2014). Graphene-reinforced calcium silicate coatings for load-bearing implants. *Biomedical Materials*, 9(2), 025009.
- Yildiz, H., Chang, F. K., & Goodman, S. (1998). Composite hip prosthesis design. II. Simulation. *Journal of biomedical materials research*, 39(1), 102-119.
- Yoo, J. J., Yoon, P. W., Lee, Y.-K., Koo, K.-H., Yoon, K. S., & Kim, H. J. (2013). Revision Total Hip Arthroplasty Using an Alumina-On-Alumina Bearing Surface in Patients With Osteolysis. *The Journal of Arthroplasty*, 28(1), 132-138.
- Younesi, M., & Bahrololoom, M. (2010). Optimizations of wear resistance and toughness of hydroxyapatite nickel free stainless steel new bio-composites for using in total joint replacement. *Materials & Design*, 31(1), 234-243.
- Zhang, H., Brown, L., Blunt, L., & Barrans, S. (2008). Influence of femoral stem surface finish on the apparent static shear strength at the stem-cement interface. *Journal of the mechanical behavior of biomedical materials*, 1(1), 96-104.
- Zhang, Y., Sun, M.-j., & Zhang, D. (2012). Designing functionally graded materials with superior load-bearing properties. *Acta Biomaterialia*, 8(3), 1101-1108.
- Zivic, F., Babic, M., Grujovic, N., Mitrovic, S., Favaro, G., & Caunii, M. (2012). Effect of vacuum-treatment on deformation properties of PMMA bone cement. *Journal of the Mechanical Behavior of Biomedical Materials*, 5(1), 129-138.

## LIST OF PUBLICATIONS

- Oshkour, A. A., Talebi, H., Shirazi, S. F. S., Yau, Y. H., Pramanik, S., Tarlochan, F., & Abu Osman, N. A. (2015). Parametric study of radial functionally graded femoral prostheses with different geometries. *Meccanica*, (In Press).
- Oshkour, A. A., Talebi, H., Shirazi, S. F. S., Yau, Y. H., Tarlochan, F., & Abu Osman, N. A. (2014). Effect of Geometrical Parameters on the Performance of Longitudinal Functionally Graded Femoral Prostheses. *Artificial organs*. (In Press).
- Oshkour, A. A., Abu Osman, N. A., Bayat, M., Afshar, R., & Berto, F. (2014). Three-dimensional finite element analyses of functionally graded femoral prostheses with different geometrical configurations. *Materials & Design*, 56, 998-1008.
- Oshkour, A. A., Pramanik, S., Shirazi, S. F. S., Mehrali, M., Yau, Y. H., & Abu Osman, N. A. (2014). A comparison in mechanical properties of cermets of calcium silicate with Ti-55Ni and Ti-6Al-4V alloys for hard tissues replacement. *The Scientific World Journal*, 2014, 9.
- Oshkour, A. A., Talebi, H., Seyed Shirazi, S. F., Bayat, M., Yau, Y. H., Tarlochan, F., & Abu Osman, N. A. (2014). Comparison of Various Functionally Graded Femoral Prostheses by Finite Element Analysis. *The Scientific World Journal*, 2014, 17.
- Oshkour, A. A., Abu Osman, N. A., Yau, Y. H., & Tarlochan, F. (2013). Design of new generation femoral prostheses using functionally graded materials: a finite element analysis. *Proceedings of the Institution of Mechanical Engineers, Part H: Journal of Engineering in Medicine*, 227(1), 3-17.
- Oshkour, A. A., Abu Osman, N. A., Davoodi, M. M., Yau, Y., Tarlochan, F., & Bayat, M. (2013). Finite element analysis on longitudinal and radial functionally graded femoral prosthesis. *International journal for numerical methods in biomedical engineering*, 29(12), 1412-1427.
- Oshkour, A. A., Abu Osman, N. A., Yau, Y. H., Tarlochan, F., & Pramanik, S. (2013). Internal-external circumferential crack behaviour in the cement layer of total hip replacement. *Fatigue & Fracture of Engineering Materials & Structures*, 1-17.
- Oshkour, A. A., Davoodi, M. M., Abu Osman, N. A., Yau, Y. H., & Tarlochan, F. (2013). Finite element analysis of circumferential crack behavior in cement-femoral prosthesis interface. *Materials & Design*, 49, 96-102.